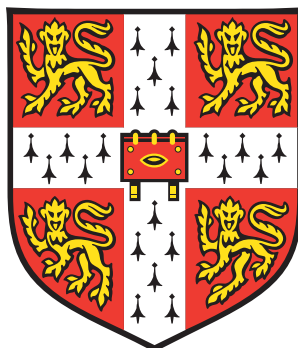


# ON THE PLASMONIC PROPERTIES AND DYNAMIC INTERACTIONS OF NANOSTRUCTURED AFM TIPS



Alan Sanders  
Robinson College  
PhD Thesis



A thesis submitted for the degree of *Doctor of Philosophy*  
Supervisor: Jeremy J. Baumberg  
Submitted: July 2015

**NanoPhotonics**  
Centre

**EPSRC**  
Engineering and Physical Sciences  
Research Council

## Declaration

---

The work presented in this thesis was carried out at the Nanophotonics Group in the Cavendish Laboratory, University of Cambridge between October 2011 and July 2015. This dissertation is the result of my own work and includes nothing which is the outcome of work done in collaboration except where specifically indicated in the text. It has not been submitted in whole or in part for any degree at this or any other university, and is less than sixty thousand words long.

*Alan Sanders*

## List of Talks, Posters and Publications

---

### Publications

- A. Sanders et al., “Facile fabrication of spherical nanoparticle-tipped afm probes for plasmonic applications”, Particle & Particle Systems Characterization **32**, 182–187 (2015)
- F. Benz et al., “Nanooptics of molecular-shunted plasmonic nanojunctions”, Nano letters **15**, 669–674 (2014)

### Conference Presentations

- A. Sanders et al., “Towards robust correlated measurements of dynamic plasmonic gaps in the sub-nm regime”, in Quantum plasmonics 15 (Mar. 2015)
- A. Sanders et al., “Au nanoparticle-tipped afm probes for plasmonic applications”, in Photon14 (Sept. 2014)
- A. Sanders et al., “Electrochemical fabrication of aupd-tipped afm probes for plasmonic applications”, in Cavendish graduate student conference (Dec. 2013)
- A. Sanders et al., “Revealing the quantum regime in tunnelling plasmonics”, in SPP6 (May 2013)
- A. Sanders et al., “Revealing the quantum regime in tunnelling plasmonics”, in Cavendish graduate student conference (Dec. 2012)

## Acknowledgements

---

This project would not have been a success without the support of countless people and financial bodies over the last four years. I would first and foremost like to thank Prof. Jeremy Baumberg for giving me the opportunity to undertake this project and for supporting me throughout. His guidance, enthusiasm, wealth of knowledge and endless supply of ideas kept me on target and made this project what it is today.

I have also greatly benefitted from the support of many talented researchers over the years, without whom the work could not have been achieved. In particular, I am grateful to three post-docs who became heavily involved in the tips project and whose expertise and advise has been invaluable. I am thankful to Dr. Matthew Hawkeye for introducing me to the ongoing tips project and helping me gain proficiency in electronics and plasmonics. I would like to thank Dr. Richard Bowman for giving me new insights into the principles of optics and optomechanical design and for assisting in the design and construction of the custom microscope platform. I am finally indebted to Dr. Liwu Zhang, under whose supervision I ventured into electrochemistry.

I would like to thank Lars Herrmann and Daniel Sigle for providing numerical simulations to support my experimental claims, and Anna Lombardi and Lee Weller for performing supplementary tip measurements using their newly developed tuneable laser systems. I am also grateful to Prof. Javier Aizpurua and Dr. Ruben Esteban for their helpful discussions whilst attending conferences.

My work has also been supported by both the Nanophotonics and Cavendish Laboratory support staff. I would like to thank Anthony Barnett for his help in designing mechanical parts and for their prompt machining, Colin Edwards for keeping all computer systems running, and Angela Campbell for her administration of this project. Thanks to Chris Summerfield, Gary Large, Kevin Mott, and Nigel Palfrey for their machining of the microscope used to conduct all optical work and to Barry Shores and Huw Prytherch for their assistance in designing the integrated electronics. I am grateful to EPSRC for funding this project and to NanoTools GmbH, for their cooperation in providing spherical Au tips for experimentation.

Lastly, my time in Cambridge would not have been the same without the fantastic Robinson College MCR community and the Cambridge University Taekwondo club, in whose company I have spent many hours outside of work. I would especially like to thank Dr. Peter Smielewski for everything he has taught me. I would finally like to acknowledge the rest of the Nanophotonics group, specifically those in plasmonics, who have provided many useful discussions and made the group a great place to work over the last four years.

---

## Abstract

---

### On the Plasmonic Properties and Dynamic Interactions of Nanostructured AFM Tips

*Alan Sanders*

Plasmonics, the confinement of light to nanometric dimensions in the form of optically-driven collective oscillations of conduction electrons, enables strong, local field enhancements, which can be exploited to realise nano-optics and nano-spectroscopy. However, the onset of quantum mechanical effects serves as a fundamental limit to plasmonic confinement in what has recently become known as the quantum regime of plasmonics.

In the present work, a dual AFM tip approach to form sub-nm plasmonic cavities is adopted to investigate the quantum regime of plasmonics and to determine, in particular, the relationship between conductance and plasmonics, a theme of great interest in the field. The technology required to reliably form sub-nm plasmonic cavities between AFM tips is further developed. A custom optical microscope with an ultra-stable nanopositioning platform has been entirely designed and optimised to facilitate experiments. Light scattering from both single and gap-coupled nanostructures can be measured over a broad wavelength range using a novel dark-field spectroscopy technique utilising a supercontinuum white-light laser.

This experimental system has been exploited to fully characterise the optical response of both sharp and spherically nanostructured Au AFM tips in order to understand their plasmonic properties. Additional spherical Au nanoparticle-tipped AFM probes are fabricated using apex-selective pulsed electrodeposition to demonstrate a simple method for introducing localised surface plasmons into a robust tip geometry. Hyperspectral imaging is utilised to optically characterise single nanostructures and identify localised surface plasmons. Spherical Au tips, with their nanoparticle-like apex geometry, are found to exhibit a radiative plasmon resonance between 600–700 nm, not present in sharp Au tips, leading to a 30× improvement in Raman scattering efficiency compared with sharp Au tips.

Finally, plasmonic interactions between two AFM tips are studied and the transition between coupled and charge transfer plasmons is dynamically observed. Simultaneous measurement of the d.c. current, applied force and optical scattering as tips come together is used to determine the effects of an optical conductance in a plasmonic nano-gap. Critical conductances are experimentally identified for the first time, determining the points at which quantum tunnelling and conductive charge transport begin to influence plasmon coupling. This is a step towards fully understanding the relationship between conduction and plasmonics and the fundamental, quantum mechanical limitations of conventional plasmonic coupling.

# Contents

---

<b>1</b>	<b>Introduction</b>	<b>1</b>
1.1	Project Outline . . . . .	4
<b>2</b>	<b>Theoretical Background</b>	<b>7</b>
2.1	Plasmons . . . . .	7
2.1.1	Electromagnetic Waves . . . . .	8
2.1.2	Bulk Plasmons and the Optical Properties of Metals . . . . .	10
2.1.3	Surface Plasmons . . . . .	13
2.2	Plasmon Coupling . . . . .	21
2.2.1	Classical Models of Plasmonic Coupling . . . . .	23
2.2.2	The Dynamical Optical Response of Plasmonic Dimers: Transitioning from Capacitive to Conductive Plasmonic Coupling . . . . .	27
2.3	Plasmons in Tips . . . . .	37
2.3.1	The Electromagnetic Response of Tips . . . . .	39
2.3.2	Challenges associated with Tip Plasmonics . . . . .	42
2.3.3	Tip Modification, Nanostructuring and Optical Antenna Tips . . . . .	44
2.4	Conclusions . . . . .	46
<b>3</b>	<b>Electrochemical Fabrication of Spherical AuNP-Tipped AFM Probes</b>	<b>49</b>
3.1	Electrochemical Deposition . . . . .	50
3.1.1	Experimental Electrodeposition of Au . . . . .	52
3.2	Initial Fabrication of Spherical AuNP-Tipped AFM Probes . . . . .	54
3.2.1	Dependence of Tip Morphology on Voltage and Underlying Nucleation Mechanisms . . . . .	57
3.2.2	Decontamination of Tip Surfaces and Post-Fabrication Processing . . . . .	60
3.3	Conclusions . . . . .	61
<b>4</b>	<b>Microscope Design for Simultaneous Measurements on Plasmonic Tips</b>	<b>63</b>
4.1	Mechanical Design . . . . .	63
4.2	Optical Design . . . . .	65

---

4.2.1	Confocal Localisation of Spectra . . . . .	69
4.2.2	Characterisation of Microscope Performance . . . . .	72
4.3	Electronics Design . . . . .	76
4.4	AFM Design: Measurements of Force . . . . .	80
4.4.1	Calibrating the AFM . . . . .	82
4.5	Scanning Capacitive AFM Tip Alignment . . . . .	83
4.5.1	Mechanism for Alignment of Two Opposing Tips . . . . .	83
4.5.2	Numerical Modelling and Experimental Measurements of Scanning Capacitance Tip Alignment . . . . .	86
4.5.3	Experimental Alignment of Tips using Scanning Capacitance AFM . . . . .	91
4.6	Conclusions . . . . .	94
<b>5</b>	<b>Understanding and Applying Single Tip Plasmonics</b>	<b>95</b>
5.1	Optical Characterisation of Nanostructures using Hyperspectral Imaging . . . . .	95
5.2	Understanding Plasmons in Spherical Nanoparticle Tips . . . . .	97
5.2.1	Interpreting the Spectral Response of Metallic Tips . . . . .	100
5.2.2	Implications of Spherical Metallic Tip Plasmonics . . . . .	102
5.3	Improved Field Enhancement of Spherical Au Nanoparticle Tips . . . . .	103
5.4	Conclusions . . . . .	107
<b>6</b>	<b>Plasmon Interactions in Tip Dimers</b>	<b>109</b>
6.1	Experimental Measurements of Dynamic Tip Dimers . . . . .	109
6.1.1	Non-Optical Properties of a Nano-Tip Dimer Gap . . . . .	111
6.2	Plasmonic Coupling Between Tips . . . . .	114
6.2.1	Sharp Tip Dimer Interactions . . . . .	114
6.2.2	Spherical Tip Dimer Interactions . . . . .	116
6.3	Quantum Effects in Sub-nm Gaps between Spherical-Tipped AFM Probes . . . . .	119
6.3.1	Observations of Quantum Charge Transport in Plasmonic Cavities . . . . .	120
6.4	Conclusions . . . . .	126
<b>7</b>	<b>Conclusions and Outlook</b>	<b>129</b>
7.1	Outlook and Future Directions . . . . .	131
<b>Appendices</b>		<b>133</b>
<b>Bibliography</b>		<b>149</b>
<b>List of Symbols</b>		<b>165</b>
<b>Acronyms</b>		<b>167</b>



# Chapter 1

## Introduction

Windows of the Robinson College chapel. Metallic nanoparticle impurities historically led to the vibrant colours associated with stained glass.

Optics has always been one of the primary branches of applied science, used to probe and extract information from many physical systems. By studying the way light interacts with a material its properties can be discerned. This is the main principle behind optical microscopy and spectroscopy. Conventional optics, solely based upon the use of light, however, is held back by a fundamental limitation. The finite momentum of the photon restricts the spatial confinement of light to its wavelength. Since the discovery of the diffraction limit in 1873, much work has been done trying to circumvent its imposed limitations and retrieve information from sub-wavelength dimensions. Whilst the diffraction limit is firmly fixed for freely propagating photons it can be broken at an interface, where waves can acquire evanescent character. Such surface waves can exist with wavelengths far below those of photons and aid in the extraction of optical information from nanoscale sources. By understanding the electromagnetic behaviour of waves on an interface, optics can be brought down to nanoscale dimensions.

Nanophotonics, or nano optics, is the name given to the progression of optics into the sub-wavelength domain - the understanding and application of light beyond the diffraction limit. Electromagnetic fields surrounding an object on these sub-wavelength length scales are said to be in the *near-field* domain as opposed to the conventional *far-field*. To achieve this level of localisation, nanophotonics exploits light-matter interactions. Matter polarised by an external electromagnetic field can generate its own polarisation fields with much smaller degrees of localisation. These fields are determined both by the incident field and by the physical characteristics of the matter. By this mechanism the optical properties of metals on the nanometre scale become particularly interesting through the excitation of plasmons.

Plasmons are the quanta of collective oscillations of optically-driven free electrons, the study of which is known as plasmonics. By transferring optical energy into plasmons on the surface of a metal the limits of optical confinement can be overcome, allowing light to be strongly confined to sub-wavelength dimensions in the form of a surface charge density oscillation, as shown in Figure 1.1. For this reason plasmonics is sometimes known as “*metal optics*”. Surface plasmons maintain the same frequency as their photonic excitation, however their wavelength is far below the diffraction limit. The result is a highly concentrated energy

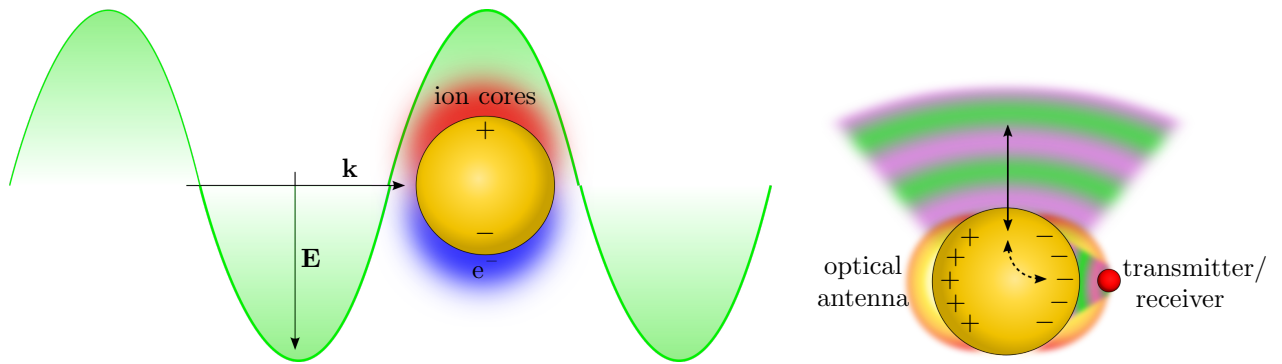


**Figure 1.1: Diagram of a localised surface plasmon in a AuNP.** Electrons move to screen the external field from the AuNP. The charge density at the electromagnetic poles of the surface greatly enhances the local field. AuNPs are therefore considered to be optical nano-antennae. The electric field from a near-field transmitter is coupled via an antenna into far-field radiation. By reciprocity, far-field radiation can be received in the near-field.

density at the poles of the charge oscillation on the metal surface. Charge accumulates at the surface, thus the electric field surrounding a strongly confined plasmon becomes significantly enhanced. This resonant near-field enhancement is one of the defining features of plasmons and forms the basis for nearly all applications of plasmonics to date.

Plasmonic phenomena has been known for over a century, however limited experimental access to metallic nanostructures restricted its study and application until technology advanced. The advent of modern microscope technology and nanostructure synthesis reignited the field and, over the course of the last 40 years, has led to the development of many novel nanotechnologies, including enhanced vibrational spectroscopies [1, 2] and near-field optical microscopy [3–8]. The most widespread of these technologies exploit the local field enhancement around a plasmonic metallic nanostructure or the more intense “hot spots” formed between coupled plasmons in many nanostructures in order to efficiently interact with matter on the nanoscale. In the vast majority of plasmonic developments, noble metal nanostructures are used as their highly mobile electrons mean they are especially good at sustaining surface plasmons in the visible region of the electromagnetic spectrum. By utilising these surface plasmon resonances, fields can be both transferred to and extracted from sub-wavelength dimensions containing nano-absorbers and nano-emitters, such as molecules and quantum dots (Figure 1.1). Such structures supporting plasmons which readily couple with light have since become known as optical nanoantennae, in analogy with conventional metal radio wave antennae [9].

Sensing has become the primary application of plasmonic nanoantennae. Surface-enhanced Raman scattering (SERS) can be used to enhance weakly interacting<sup>1</sup> inelastic (Raman) scattering from vibrating molecules [10] by a factor of  $|E/E_0|^4$ , where  $|E/E_0|$  is the field enhancement at the location of the molecules placed in the vicinity of plasmonic nanostructure.

<sup>1</sup>Only 1 in  $10^7$  photons inelastically scatter from the bonds in a vibrating molecule.

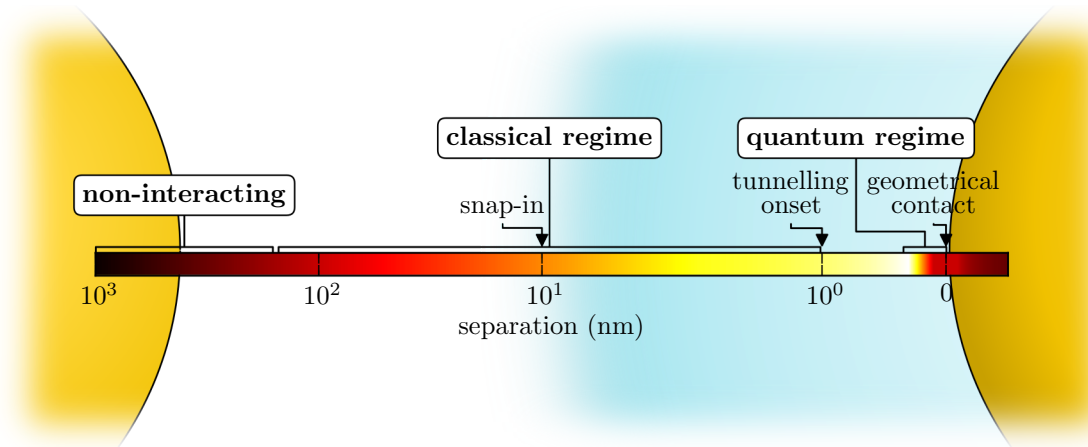


**Figure 1.2: Regimes of plasmonic interaction.** The diagram shows the coupling strength between two plasmonic particles across the full range of characteristic separation dimensions. At distances greater than the particle radius plasmons are uncoupled. Classical mode coupling begins at separations below the particle radius. Many nanoscale phenomena, such as capillary surface tension (AFM snap-in) occur at these characteristic separations in ambient conditions. Once the separation transitions to below 1 nm quantum mechanical effects begin to become important. The quantum regime is the point at which these effects significantly effect plasmonic interaction.

Scanning near-field optical microscopy (SNOM) is a similar technique by which near-field light is collected through a sub-wavelength-size aperture, a process that can be similarly boosted through use of a plasmonic aperture. The culmination of these developments is the recent ability to measure light scattering from just a few molecules within a single hot spot [11].

Realistically, however, fields can only be enhanced so far. By continuing to push the boundaries towards robust single molecule plasmonic sensing, intuition suggests that plasmonic systems must become increasingly smaller to confine light into even smaller volumes and further increase the localised near-field enhancement. Inevitably though, the characteristic dimensions of the nano-gaps sustaining the hot spots, or the particles themselves, becomes sufficiently small that quantum mechanical effects, such as quantum tunnelling, ballistic transport and non-locality, are no longer negligible and begin to adversely affect confinement (Figure 1.2). Plasmonics in these quantum mechanically-limited regimes currently only has a limited understanding due to difficulties in reliably accessing sub-nm length scales as well as understanding how to model each regime. To a certain extent this is primarily caused by difficulty fabricating structures with such small characteristic features. Few reports have therefore conclusively shown the influence of quantum effects on plasmonic performance and it remains an extremely topical and relatively new area of plasmonics that still requires exploring.

The ideal way of experimentally mapping the quantum regime is to use precisely positioned individual nanoparticles coming closer together and transitioning from classical to quantum to contacted interaction regimes. Though possible in many ways, the dynamic control and precise positioning of a sub-nm cavity between two nanoparticles is not a trivial task. While there

are methods for controlling nanoparticle positions, difficulty arises as to what measurements are then possible. A rich amount of fundamental physics exists within sub-nm gaps that can strongly influence plasmonic behaviour, therefore a system must be carefully designed to enable measurement of each significant effect. Sensitive measurements of charge transfer and forces, not compatible with individual nanoparticle experiments, are required to probe both plasmonic and quantum mechanical effects. Consequently, precise nanopositioning of an electrically contacted nanoparticle with force sensitivity is required in order to experimentally access and improve the understanding of the quantum regime of plasmonics.

AFM probes are appealing devices as a means of controllably progressing into sub-nm cavities whilst simultaneously making the necessary measurements to understand the quantum regime, though a plasmonic tip apex structure is a necessity. Metallic tip structures at a glance are promising plasmonic probes as characteristic apex dimensions readily fall well below the diffraction limit. Furthermore, a clear advantage of tip systems is the maturity of the many surface science techniques used for characterising nanoscale topology, forces and electronic properties. Techniques such as scanning tunnelling microscopy (STM) [12] and atomic force microscopy (AFM) [13] have formed the foundation of surface analysis studies since their inception. By combining AFM probe-based techniques with optical measurements further insight into quantum mechanical effects in plasmonic systems can be gained. This was the approach adopted by Savage et al. to initially reveal this domain [14] and remains the case throughout this project.

---

## 1.1 Project Outline

---

The primary purpose of this project is to demonstrate robust measurements of plasmonic gaps in the sub-nm regime, at the point when quantum effects become important, building upon the work conducted by Savage et al. [14]. A significantly modified microscope design is employed compared to that used by Savage et al. in order to incorporate a larger range of possible measurements and potential experiments. By using a combined atomic force-optical microscope and two opposing, plasmonic tips, plasmons can be dynamically probed using multiple, simultaneous, correlated measurements. A large amount of time and effort has been dedicated to the design and construction of a microscope capable of making simultaneous measurements of the electronic, force and optical signals on a plasmonic tip dimer in order to better understand the quantum regime of plasmon coupling. Both the microscope technology and the sample fabrication technology are heavily developed to enable robust measurements on sub-nm gaps and improve upon the current standards of experiment.

A prerequisite of all experiments is the availability of plasmonic AFM tips with radiative plasmon resonances, the simplest geometry of which is a spherical tip apex. Spherical AuNPs

mounted onto two conductive AFM tips are used to dynamically form plasmonic nano-gaps. Though studies using commercially available spherical Au tips are still carried out, the sensitivity of measurements in the sub-nm regime requires more robust and controllable probes. Despite the widespread use of tips in metal optics techniques, the application of nanostructured tips for improved performance is a relatively recent idea. Little work has been reported on the modification of the sharp tip geometry and nanostructuring a spherical apex remains complex and expensive. To address these issues, a new fabrication technique using electrodeposition is developed as a simple method for producing spherically nanostructured metallic tips. The optical response of both sharp and spherical metallic tips is then characterised using a selection of techniques developed to identify the plasmons supported by each structure. Tips are then applied to Raman scattering to demonstrate the improvements when using nanostructured tips.

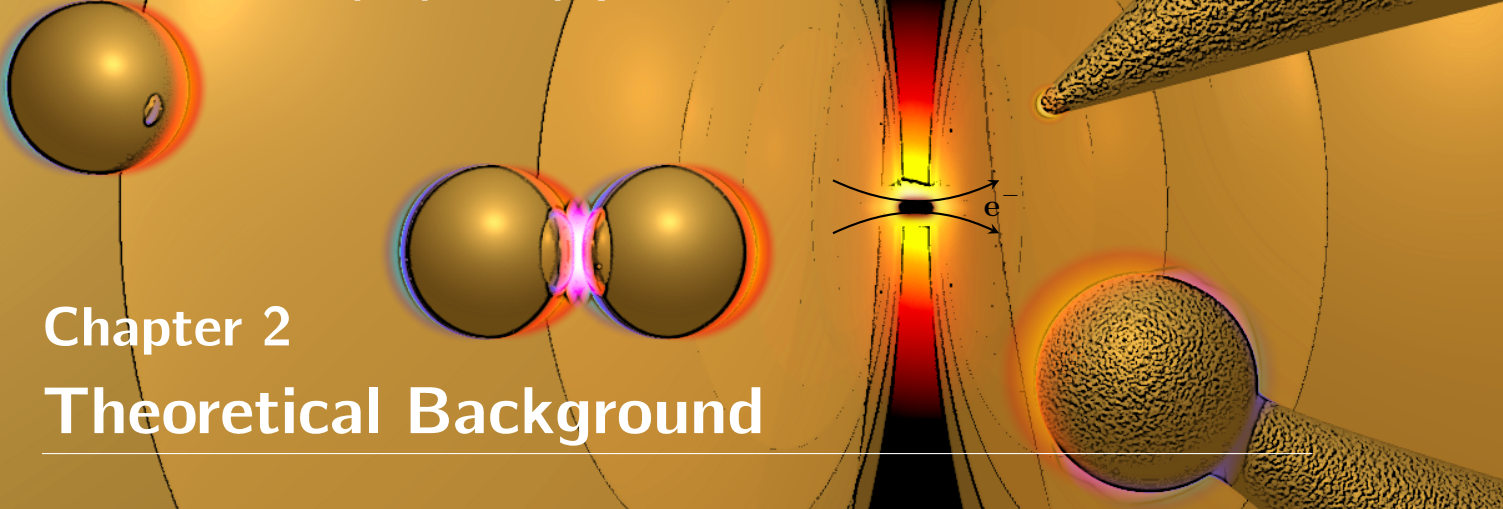
Finally, with all experimental components in place, interactions between two coupled tips are investigated, progressing into the domain of sub-nm plasmonic gaps. Current experiments in the quantum regime surpass previous experimental efforts and build upon the proposed theoretical foundations emerging in recent years to show that conductance is the dominant factor in determining the fundamental degree to which light can be confined. I show that a set of critical conductances exist which define the boundaries between each of the quantum regimes.

This report necessarily begins with the theoretical background required to understand plasmons and the relevant plasmonic phenomena within the scope of this project. The previous uses of tips for plasmonics, along with their current understanding, are detailed to motivate their use in experimental plasmonics. The experimental work carried out in this project is discussed in three parts:

- the production of spherical-apex plasmonic AFM tips by electrochemical nanostructuring
- the design and construction of a microscope capable of making stable measurements on an AFM tip dimer in the sub-nm regime
- experiments performed using combinations of plasmonic AFM tips in the microscope

These results are broken down into understanding the plasmonics of individual spherically-nanostructured tips followed by understanding the coupling between two tips as their separation progresses into the sub-nm quantum regime and below.





## Chapter 2

# Theoretical Background

As previously stated, light can be confined below the diffraction limit by exploiting plasmons. Transferring energy from a diffraction-limited photonic field into collective oscillations of conduction electrons enhances the electric field on the surface of a metallic nanostructure with nanoscale localisation. It is through the understanding and application of this phenomenon that nano-optics and sub-wavelength confinement is made possible. This chapter deals firstly with a theoretical description of electromagnetic fields and the optical properties of metals. From this basis the concept of a plasmon can be introduced and the different kinds of plasmons defined, illustrating how they interact within different spatial regimes. Through this behaviour, the study of charge transfer in plasmonic systems, specifically quantum charge transport, is addressed. Finally, the plasmonics of metallic tips is discussed in preparation for the experiments described in later chapters studying plasmon interaction through each of the characteristic spatial regimes.

### 2.1 Plasmons

Plasmons are a direct solution of Maxwell's equations at the boundary between a dielectric and a metal. Despite existing on length scales from 100 nm down to around 1 nm, the high free electron density of metals mean energy levels still retain their characteristic continuous conduction bands and quantisation effects can be ignored.<sup>1</sup> Hence, classical theory is able to accurately describe physical phenomena until the characteristic length scale drops below  $\sim 0.5$  nm and a phenomenological approach using Maxwell's equations forms the basis of the mathematical description of plasmons.

<sup>1</sup>A higher density of states means that energy levels are more closely spaced, hence metals with a large free electron density appear to have an energy continuum as opposed to discrete energy bands or levels at room temperature.

### 2.1.1 Electromagnetic Waves

Maxwell's equations universally describe the classical, dynamical behaviour of electromagnetic (EM) waves, representing the foundations of electromagnetism. In their macroscopic, differential form, describing EM fields in matter, they are given by,

$$\nabla \cdot \mathbf{D} = \rho_{\text{ext}}, \quad (2.1\text{a})$$

$$\nabla \cdot \mathbf{B} = 0, \quad (2.1\text{b})$$

$$\nabla \times \mathbf{E} = -\frac{\partial \mathbf{B}}{\partial t}, \quad (2.1\text{c})$$

$$\nabla \times \mathbf{H} = \mathbf{J}_{\text{ext}} + \frac{\partial \mathbf{D}}{\partial t}, \quad (2.1\text{d})$$

where  $\mathbf{E}$  is the electric field,  $\mathbf{B}$  is the magnetic flux density,  $\mathbf{D}$  is the electric displacement field,  $\mathbf{H}$  is the magnetic field,  $\rho_{\text{ext}}$  is the free (volume) charge density,  $\mathbf{J}_{\text{ext}}$  is the free current density and  $t$  is time. The charge and current densities refer to only the external contributions from free charges, related to the internal contributions from bound charges via  $\rho_{\text{tot}} = \rho_{\text{ext}} + \rho_{\text{int}}$  and  $\mathbf{J}_{\text{tot}} = \mathbf{J}_{\text{ext}} + \mathbf{J}_{\text{int}}$ .  $\mathbf{D}$  and  $\mathbf{H}$  are introduced to include material dependencies and describe macroscopic fields, and are defined by,

$$\mathbf{D} = \epsilon_0 \mathbf{E} + \mathbf{P}, \quad (2.2\text{a})$$

$$\mathbf{H} = \frac{1}{\mu_0} \mathbf{B} + \mathbf{M}, \quad (2.2\text{b})$$

where  $\mathbf{P}$  is the polarisation (dipole moment per unit volume),  $\mathbf{M}$  is the magnetisation, and  $\epsilon_0$  and  $\mu_0$  are the permittivity and permeability of free space, respectively. For linear media, microscopic and macroscopic fields are related through the constitutive relations,

$$\mathbf{D} = \epsilon \epsilon_0 \mathbf{E}, \quad (2.3)$$

$$\mathbf{H} = \frac{1}{\mu \mu_0} \mathbf{B}, \quad (2.4)$$

from which  $\epsilon$  and  $\mu$  are defined as the relative permittivity and permeability used to describe the electromagnetic properties of the medium.

The displacement field arises due to polarisation of a material in response to an applied field and is related to the internal charge density by  $\nabla \cdot \mathbf{P} = \rho_{\text{int}}$ . Conservation of charge means that  $\nabla \cdot \mathbf{J} = \partial \rho / \partial t$ , which requires that  $\mathbf{J} = \partial \mathbf{P} / \partial t$  (a result also achievable by differentiating Eq. 2.2a). The final equation of importance is the relationship between the electric field and the current density, given by,

$$\mathbf{J} = \sigma \mathbf{E}, \quad (2.5)$$

where  $\sigma$  is the conductivity. These few relations are sufficient to understand the behaviour of electromagnetic waves in media.

Propagation of EM waves within a medium is governed by a wave equation relating both the spatial and temporal changes of a wave. Combining Eq. 2.1c and Eq. 2.1d leads to the general wave equation for EM waves in the time domain,

$$\nabla(\nabla \cdot \mathbf{E}) - \nabla^2 \mathbf{E} = -\varepsilon \varepsilon_0 \mu \mu_0 \frac{\partial^2 \mathbf{E}}{\partial t^2} - \mu \mu_0 \mathbf{J}, \quad (2.6)$$

describing the propagation of an EM wave in a given medium. In the absence of both charge and current Eq. 2.6 reduces to,

$$\nabla^2 \mathbf{E} = \varepsilon \varepsilon_0 \mu \mu_0 \frac{\partial^2 \mathbf{E}}{\partial t^2}, \quad (2.7)$$

describing a wave propagating in both space and time with a velocity  $v = 1/\sqrt{\varepsilon_0 \varepsilon \mu_0 \mu}$ . In free space ( $\varepsilon = \mu = 1$ ) this is the speed of light  $c = 1/\sqrt{\varepsilon_0 \mu_0}$ , with light slowed when in media to  $v = c/\tilde{n}$  by a factor  $\tilde{n} = \sqrt{\varepsilon \mu}$  known as the refractive index.

In general  $\varepsilon$  is a complex quantity,  $\varepsilon = \varepsilon_1 + i\varepsilon_2$ , and depends on the frequency of the EM wave,  $\omega$ . Plasmons are a phenomenon resulting from this frequency dependence in metallic materials. The relative permittivity is therefore denoted  $\varepsilon(\omega)$  and is referred to as the material's dielectric function from this point onwards. The concept of a plasmon can be identified through this function alone. Equations are therefore simplified by setting  $\mu = 1$  and removing any magnetic contributions. Since  $\varepsilon(\omega)$  is a complex parameter with components  $\varepsilon_1 + i\varepsilon_2$ , the complex refractive can be expressed as  $\tilde{n} = \sqrt{\varepsilon(\omega)} = n + i\kappa$ , where  $n$  is the real part causing refraction and  $\kappa$  is the loss coefficient determining absorption in the medium. The complex refractive index and the dielectric function are then related via  $\varepsilon_1 = n^2 - \kappa^2$  and  $\varepsilon_2 = 2n\kappa$ .

The dispersive properties of a material are found by solving Eq. 2.6 with  $\varepsilon = \varepsilon(\omega)$ , describing the behaviour of a wave propagating through a non-magnetic, dielectric medium. For a propagating EM wave with frequency  $\omega$  and wave vector  $\mathbf{k}$  in space  $\mathbf{r}$  of the form,

$$\mathbf{E} = \mathbf{E}_0 e^{i(\mathbf{k} \cdot \mathbf{r} - \omega t)}, \quad (2.8)$$

Eq. 2.6 can be expressed in the frequency (Fourier) domain as,

$$\mathbf{k}(\mathbf{k} \cdot \mathbf{E}) - k^2 \mathbf{E} = -\varepsilon(\mathbf{k}, \omega) \frac{\omega^2}{c^2} \mathbf{E}, \quad (2.9)$$

where  $k = |\mathbf{k}|$  is the magnitude of the wavevector. The variable  $k_0 = \omega/c$  is sometimes used in Eq. 2.9 when all quantities considered are wave vectors. From this equation the propagation behaviour of EM waves in media can be described.

Solutions to Eq. 2.9 depend on the orientation of the wavevector with the field. Transverse

wave solutions ( $\mathbf{k} \cdot \mathbf{E} = 0$ ) yield the dispersion relation for light,

$$k = \sqrt{\varepsilon(\mathbf{k}, \omega)} \frac{\omega}{c} = \tilde{n} k_0. \quad (2.10)$$

Inserting this into Eq. 2.8 gives a general solution for light propagating through a dielectric medium,

$$\mathbf{E} = \mathbf{E}_0 e^{(-\kappa k_0 r)} e^{[i(n k_0 r - \omega t)]}. \quad (2.11)$$

The real component of the refractive index  $n$  slows the wave whereas the imaginary component corresponds to an exponential decay with characteristic length  $1/\kappa$ , representing loss within a medium.

Longitudinal wave solutions ( $\mathbf{k} \cdot \mathbf{E} = k|\mathbf{E}|$ ) result in  $\sqrt{\varepsilon(\mathbf{k}, \omega)}\omega/c = 0$ , hence solutions only exists for  $\varepsilon(\mathbf{k}, \omega) = 0$ . Both these conditions are important when describing plasmons in the bulk of a metal (only longitudinal plasmons are supported) and on the surface (both transverse and longitudinal plasmons supported).

Lastly, combining Eq. 2.3 with the differential of Eq. 2.2a, Eq. 2.5 and Eq. 2.8 yields a relation between a material's conductivity and it's dielectric function,

$$\varepsilon(\mathbf{k}, \omega) = 1 + \frac{i\sigma(\mathbf{k}, \omega)}{\varepsilon_0 \omega}. \quad (2.12)$$

Both quantities are able to describe the same physics from a different perspective. Since  $\text{Re}[\varepsilon]$  is related to both  $\text{Im}[\sigma]$  and  $\text{Re}[\tilde{n}]$ ,  $\text{Re}[\sigma]$  must therefore be related to  $\kappa = \text{Im}[\tilde{n}]$  and the attenuation of waves inside media. A large conductivity in a material corresponds to large transmission losses with decay attributed to the energy needed to move electrons at the surface of the material. Furthermore, the relation between  $\varepsilon(\omega)$  and  $\sigma$  becomes important when considering points of conductance in a plasmonic system and that plasmons exist as an oscillating current density induced by a time-varying polarisation.

Using the framework outlined so far the optical properties of metals can be deduced along with the existence of plasmons. The discussion begins with the Drude model for the optical response of metals [15], which is used to first predict the behaviour of plasmons. From there the distinction can be made between plasmons within the volume of a metal and those confined to the surface, which are of most interest in plasmonics.

### 2.1.2 Bulk Plasmons and the Optical Properties of Metals

The optical properties of a metal are dominated by the response of highly mobile, nearly-free electrons delocalised from the positive nuclei background. When light is incident on a metal, nearly free electrons at the surface are displaced in the opposite direction to the field. The field of the induced charge distribution therefore screens the electric field inside the metal.

Field penetration into the metal is strongly attenuated, with fields decaying exponentially over a characteristic ( $1/2e$ ) length known as the skin depth,  $\delta_m = c/2\omega\kappa$ .<sup>2</sup> The small values of  $\delta_m$  exhibited by metals means that they fall within the *perfect conductor* approximation (zero internal field) with transmission only possible through thin metallic films. An EM wave impinging on a metal is hence internally screened and reflected, giving metals their shiny appearance. A metal begins to show a more “dielectric-like” behaviour when the frequency of incoming light is high enough that electron inertia prohibits an instantaneous response, thus allowing field penetration. Such effects are seen in the visible region of the EM spectrum in the case of noble metals. Fields increasingly penetrate metals up until ultraviolet (UV) photon energies, at which point most metals become transparent. This is known as the *ultraviolet transparency*.

Since the dominating cause of these effects stems almost exclusively from nearly free electrons, as opposed to bound electrons,<sup>3</sup> the optical properties of metals can be classically described by the Drude model [15]. This model describes the motion of a free electron gas in response to an applied field. The equation of motion for a single free electron in a time-varying applied field is given by,

$$m\ddot{\mathbf{r}}(t) + m\gamma\dot{\mathbf{r}}(t) = -e\mathbf{E}(t), \quad (2.13)$$

where  $m$  is its effective optical mass,  $e$  its charge, and  $\gamma = 1/\tau$  its electron collision frequency, the inverse of the relaxation time,  $\tau$ . Using an effective optical mass as opposed to the actual electron mass incorporates band structure effects into the model. The electron collision frequency amounts to an effective coefficient of damping as in a mechanical oscillator. For a harmonic driving field, the induced oscillatory response of the free electrons induces a polarisation ( $\mathbf{P} = -ner$ , where  $n$  is the number density of electrons),

$$\mathbf{P}(t) = -\frac{ne^2}{m(\omega^2 + i\gamma\omega)}\mathbf{E}(t). \quad (2.14)$$

The resulting displacement field, obtained by substituting  $\mathbf{P}$  into Eq. 2.2a and using Eq. 2.3, defines the dielectric function of a metal,

$$\varepsilon(\omega) = 1 - \frac{\omega_p^2}{\omega^2 + i\gamma\omega}, \quad (2.15)$$

where  $\omega_p$  is the plasma frequency of the metal, given by,

$$\omega_p^2 = \frac{ne^2}{\varepsilon_0 m}. \quad (2.16)$$

---

<sup>2</sup>The skin depth is defined using  $1/2e$  rather than  $1/e$  to consider power instead of field.

<sup>3</sup>Optical properties derived from bound electrons are described by a Lorentz oscillator model.

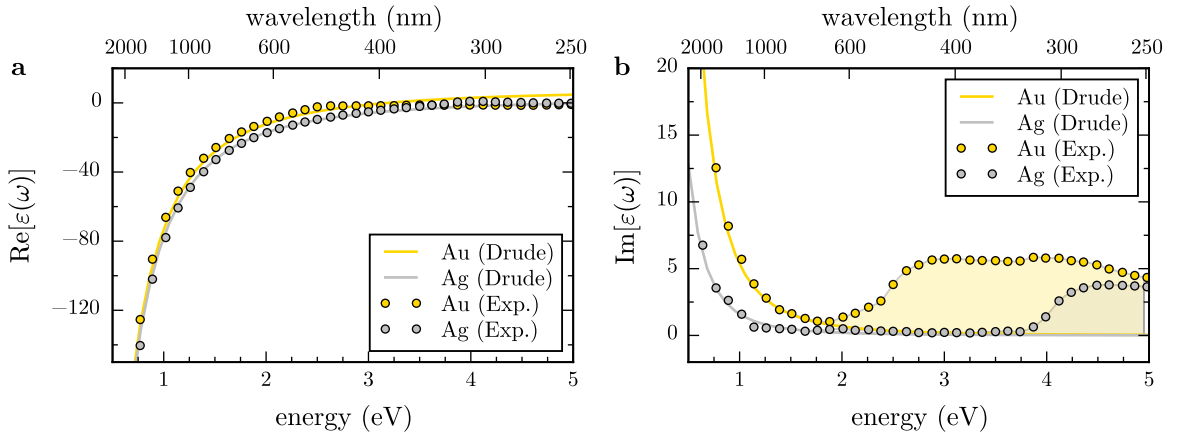


**Figure 2.1: Plot of the dielectric function, given by the Drude model, for Au and Ag compared with empirical data.**  $\varepsilon(\omega)$  is calculated using Eq. 2.17. The plasma frequency is calculated using Eq. 2.16. The parameters of the curves are  $n = 5.90 \times 10^{28} \text{ m}^{-3}$ ,  $m = 9.11 \times 10^{-31} \text{ kg}$ ,  $\gamma = 1/\tau = 1/1 \times 10^{-14} \text{ s}$  and  $\varepsilon_\infty = 8$  for Au and  $n = 5.86 \times 10^{28} \text{ m}^{-3}$ ,  $m = 9.11 \times 10^{-31} \text{ kg}$ ,  $\gamma = 1/\tau = 1/3 \times 10^{-15} \text{ s}$  and  $\varepsilon_\infty = 3$  for Ag. Empirical data (Johnson and Christy, 1972 [16]) is shown for comparison to illustrate the importance of interband transitions. Differences between the Drude model (solid lines) and experimental results (circles) are caused by interband transitions not included in the basic Drude formalism.

The optical properties of a metal can be discerned from the real and imaginary components of  $\varepsilon(\omega)$ . The plasma frequency defines the point at which a metal transitions into a dielectric. For  $\omega < \omega_p$ ,  $\text{Re}[\varepsilon(\omega < \omega_p)] < 0$  and a free electron gas remains metallic in character, with electrons moving to oppose an incident field. Once  $\omega > \omega_p$  the free electron gas, limited by inertia, cannot respond fast enough to the field and the metal becomes dielectric in character. In real metals, interband transitions increase  $\text{Im}[\varepsilon(\omega)]$  and Eq. 2.15 has to be modified to account for interband absorption caused by bound electrons through the inclusion of a constant  $\varepsilon_\infty$ . The dielectric function then has the form,

$$\varepsilon(\omega) = \varepsilon_\infty - \frac{\omega_p^2}{\omega^2 + i\gamma\omega}. \quad (2.17)$$

A plot of Eq. 2.17 is shown in Figure 2.1, along with empirical data, illustrating both why noble metals exhibit high quality, visible spectrum (400–700 nm, 1.5–3 eV) plasmonics, as well as the failings of the Drude model. Noble metals have  $\text{Re}[\varepsilon(\omega)] < 0$  and small  $\text{Im}[\varepsilon(\omega)]$  in the visible region, hence behave very similarly to an ideal free electron gas. The Drude model fails at higher energies as interband transitions are not included in the basic model. These transitions increase the absorption ( $\propto \text{Im}[\varepsilon(\omega)]$ ) and are significant for  $\lambda < 500 \text{ nm}$  in Au and  $\lambda < 300 \text{ nm}$  in Ag. A measure of the quality of a metal can be determined from its quality factor  $Q = |\text{Re}[\varepsilon]/\text{Im}[\varepsilon]|$ . The high  $Q$  of noble metals in the visible regions means they can easily respond to an incident field and screen it, behaving metallically.

The plasma frequency  $\omega_p$  in  $\varepsilon(\omega)$  not only describes a metal-to-dielectric transition but also dictates the frequency of the collective longitudinal mode of oscillation. By substituting Eq. 2.15 in the zero damping limit into the dispersion relations for transverse and longitudinal waves it is clear that transverse waves are only supported if  $\omega > \omega_p$  with a dispersion  $\omega^2 = \omega_p^2 + k^2c^2$ . However, a collective longitudinal oscillation is allowed at  $\omega = \omega_p$  since  $\varepsilon(\omega) = 0$  in the absence of damping. In this case the free electron gas is displaced from the ionic core background a distance  $u$  due to the applied field to form surface charge densities  $\sigma = \pm neu$ . The resulting depolarisation field is  $E = neu/\varepsilon_0$  and the motion of the free electrons is defined by,

$$nm\ddot{u} = -neE = -\frac{n^2e^2u}{\varepsilon_0}. \quad (2.18)$$

Simplifying this relation leads to,

$$\ddot{u} + \omega_p^2 u = 0, \quad (2.19)$$

hence  $\omega_p$  is considered the natural frequency of the system and the electrons resonate when driven at  $\omega = \omega_p$ . This is known as the bulk or *volume plasmon*. Since this is a longitudinal oscillation, however, light cannot couple with it. For this reason, volume plasmons cannot be excited and measured by means of optical techniques but require other experimental methods, e.g. electron energy loss spectroscopy (EELS) [17]. Optical plasmonic phenomena must therefore be a result of a different kind of plasmon.

### 2.1.3 Surface Plasmons

Surface plasmons (SPs), unlike bulk plasmons, are collective oscillations of conduction electrons tightly confined to the surface of the metal and therefore not necessarily restricted by the diffraction limit. The maximum magnitude of the wavevector is set by  $k_0 = 2\pi/\lambda$  with individual components restricted by  $k = \sqrt{k_x^2 + k_y^2 + k_z^2}$ . Consider Eq. 2.10 in the form,

$$k_x^2 = \tilde{n}^2 k_0^2 - k_y^2 - k_z^2. \quad (2.20)$$

If a wave propagates freely in all three dimensions then it remains diffraction limited and the propagation constant  $k_x < \tilde{n}k_0$ . However if one or more of its wavevector components become imaginary ( $k_{y,z}^2 < 0$ ) then it becomes possible that  $k_x > \tilde{n}k_0$ . This behaviour can occur at an interface, where surface waves take on evanescent character in the  $z$ -direction whilst propagating in the  $xy$  plane.<sup>4</sup> By coupling light into surface waves the diffraction limit can be beaten. Waves of frequency  $\omega$  can acquire wavelengths many times smaller than their excitation wavelength. The SP is one such case of this phenomenon and occurs at metal-dielectric interfaces. Unlike in a bulk metal, electrons displaced by an applied field at the

---

<sup>4</sup>Evanescent meaning imaginary  $k_z$  therefore exponentially decaying amplitude in the  $z$ -direction.

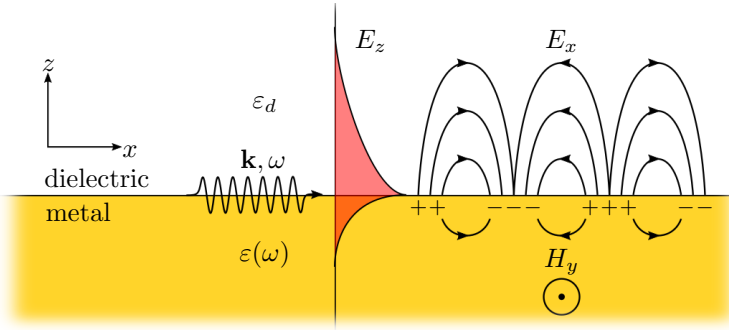


**Figure 2.2: Diagram of a surface plasmon polariton (SPP).** TM surface electron density waves (surface plasmons) couple with an evanescent wave originating from an EM wave to form a SPP. The SPP remains confined to the interface but can propagate across the surface.

surface of a metal feel a restoring force due to the positive nuclei background. Transverse fields impinging on the metal surface at an angle are then able to manipulate the electron motion. SPs can therefore be excited by light as well as by the longitudinal waves needed to excite bulk plasmons, forming polariton quasiparticles under strong coupling with photons.<sup>5</sup> This optical excitation is known as the surface plasmon polariton (SPP) and, as a result of it being optically accessible, is one of the most commonly studied plasmonic phenomena.

### Surface Plasmon Polaritons

An SPP is a propagating transverse magnetic (TM) wave confined to the surface of a metal - the bound state between a photon and a SP. The TM nature of the wave indicates that **E** has a component traversing across the interface as shown in the diagram of an SPP in Figure 2.2. No such solution exists for transverse electric (TE) surfaces waves (i.e. a component of **H** passing through the interface).<sup>6</sup> While confined in two dimensions to the planar boundary between a metal and a dielectric, the SPP can either propagate or become stationary as a result of interference. The latter stationary form of the SPP is similar to the localised surface plasmons, described later.

The SPP itself is described through its dispersion. A TM wave propagating in the  $x$ -direction along a metal/dielectric interface has a spatial field profile in a space  $\mathbf{r}$  given by  $\mathbf{E}(\mathbf{r}) = \mathbf{E}(z)e^{i\beta x}$  where  $\beta = k_x$  is the propagation constant. The magnetic field in this configuration is then  $\mathbf{H}(\mathbf{r}) = \mathbf{H}(y)e^{i\beta x}$ . Solving the wave equation across the metal-dielectric interface leads to the dispersion relation of a SPP, given by,

$$\beta = \frac{\omega}{c} \sqrt{\frac{\varepsilon_d \varepsilon(\omega)}{\varepsilon_d + \varepsilon(\omega)}}. \quad (2.21)$$

<sup>5</sup>Polaritons are the name given to quanta or quasiparticles of light-matter interactions. Strong coupling describes the point at which a quasiparticle is no longer distinguishable between its two constituent components.

<sup>6</sup>TE and TM are also known as *s*- and *p*-polarisations, respectively.

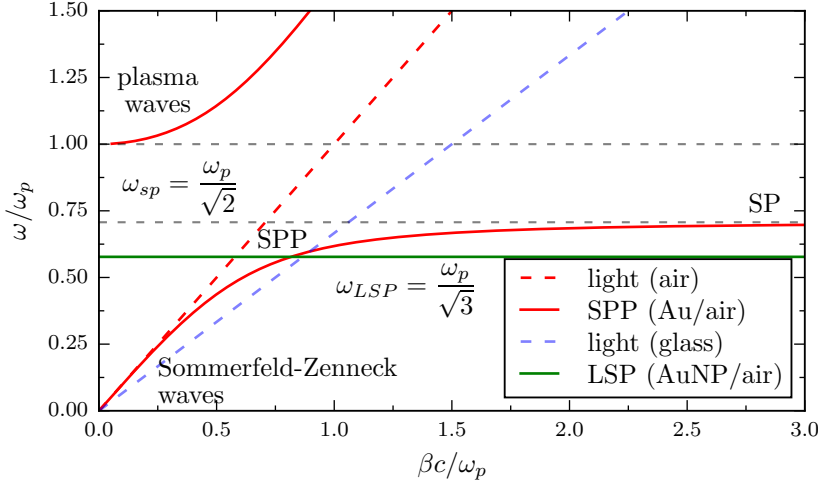


**Figure 2.3: Plasmon dispersion relations for the SPP and LSP.** The dashed lines indicate the dispersion of light in both glass and air (vacuum) along with the surface plasmon frequency. SPPs can be described as photon-like or plasmon-like depending on their point of excitation. SPPs excited with large  $k$  and  $\omega \approx \omega_{SPP}$  are considered plasmon-like while SPPs with low  $k$  are considered more photon-like. These have been known as Sommerfeld-Zenneck surface waves [18].

This dispersion is shown in Figure 2.3 along with the dispersion of light for both air and glass media. From the dispersion curve it is clear that SPPs cannot couple with light within the same medium as their dispersion curves do not cross. However, light from within a higher refractive index medium such as glass can generate evanescent waves and excite SPPs on a nearby metal/air interface. This method of coupling photons with surface plasmons, depending on the specific prism arrangement, is known as the Kretschmann (prism-metal-dielectric) or Otto (prism-dielectric-metal) configuration [19, 20]. Since a diffraction grating may also impart momentum onto a photon ( $k_x \rightarrow k_x + n\pi$ ) a metallic grating can launch SPPs along a planar metal-dielectric interface. This phenomenon was first observed in 1902 by Wood, dubbed as Wood's anomaly [21], and only explained via surface waves many years later [22].

Closer inspection of the curve highlights one of the major features of a plasmon. While SPPs retain the frequency of the excitation field, their wavelength is considerably smaller than the diffraction-limited wavelength of light. Depending on where on the curve the SPP lies it can be considered to be either more photon-like or more plasmon-like. For small  $\beta \approx k_0$  the SPP is similar to light grazing the interface (Sommerfeld-Zenneck waves)<sup>7</sup> whereas SPPs with large  $k$  become more plasmon-like and their frequency saturates at the surface plasmon frequency,

$$\omega_{SP} = \frac{\omega_p}{\sqrt{1 + \varepsilon_d}}. \quad (2.22)$$

<sup>7</sup>Sommerfeld-Zenneck waves are surface waves that appear throughout mechanics and electromagnetism that are confined to the interface between two different media.

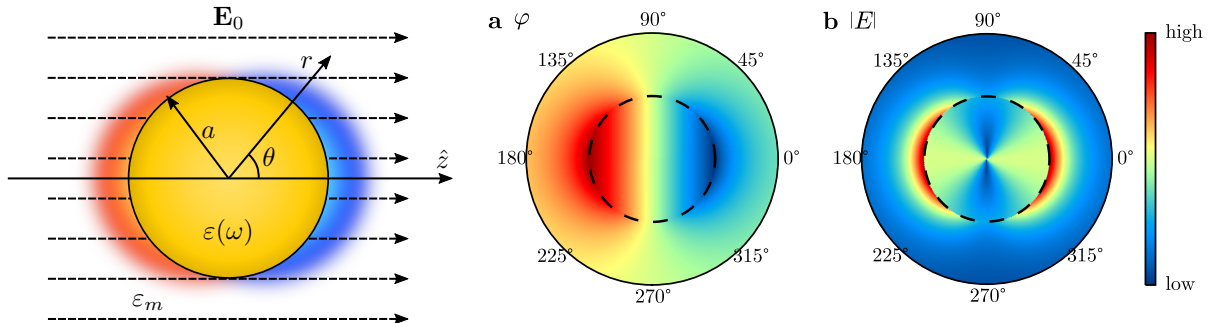


**Figure 2.4: A spherical metallic particle in an applied electric field.** The sphere is assumed to be in the quasistatic regime ( $a \ll \lambda$ ). The aura around the particle indicates the phase of the free electron oscillations in the plasmon. Calculations of (a) the potential and (b) the magnitude of the electric field for a spherical nanoparticle on resonance ( $\varepsilon(\omega) = -2\varepsilon_d$ ).

At this point the SPP can be considered electrostatic and becomes an SP. To some extent, SPs confined to a finite, continuous, non-planar surface, defining a metallic nanoparticle (MNP), can be considered to be the basis for localised surface plasmons (LSPs) or localised surface plasmon polaritons (LSPPs).

### Localised Surface Plasmons

LSPs are collective oscillations of conduction electrons confined within a fixed sub-wavelength spatial extent. These can occur on any nanoscale curved surface but the effects are strongest, and most well-documented, on the surface of a MNP. Free electrons are displaced from the nuclei in response to an applied field and form a surface charge distribution, polarising the particle. Coulomb interaction between the poles of the surface charge distribution results in a restoring force on electrons within the particle. This gives rise to a natural frequency of oscillation, leading to resonance when driven harmonically at the correct frequency. The particular resonant frequencies present in a particle depend on the particle geometry (supporting various multipolar surface charge distributions), its material properties and the dielectric properties of the surrounding medium, which each modify the electron restoring forces. Each different multipolar charge distribution is considered to be a unique LSP mode, identifiable by its optical resonance [23].

The simplest form of a LSP is the dipole resonance of a spherical MNP. Assuming the sphere radius  $a \ll \lambda$  (the wavelength of light), the particle is considered to be in the quasistatic regime, where electrons move instantaneously in response to the incident field and their phase is ignored. Electrostatics, rather than electrodynamics, is applicable to solve this problem with an electrostatic potential,  $\varphi$ , described by the Laplace equation,  $\nabla^2\varphi = 0$ . A general

solution in a spherical geometry is of the form [24],

$$\varphi_{l,m_l}(r, \theta, \phi) = \sum_{l=0}^{l=\infty} \sum_{m_l=-l}^l [A_l r^l + B_l r^{-(l+1)}] P_l^m(\cos \theta) e^{im_l \phi}, \quad (2.23)$$

where  $l$  is the degree of spherical harmonic and  $m_l$  its order,  $A_l$  and  $B_l$  are constants and  $P_l^m(\cos \theta)$  are associated Legendre polynomials. For a sphere of radius  $a$  and dielectric function  $\varepsilon(\omega)$  in a dielectric medium described by  $\varepsilon_d$  the solution is fixed by boundary conditions, reducing to [25],

$$\varphi = \begin{cases} -\frac{3\varepsilon_d}{\varepsilon(\omega) + 2\varepsilon_d} \mathbf{E}_0 \cdot \mathbf{r} & r \leq a \text{ (inside)}, \\ \left( -1 + \frac{\varepsilon(\omega) - \varepsilon_d}{\varepsilon(\omega) + 2\varepsilon_d} \frac{a^3}{r^3} \right) \mathbf{E}_0 \cdot \mathbf{r} & r > a \text{ (outside)}. \end{cases} \quad (2.24)$$

For a metal sphere the potential (plotted in Figure 2.4a) describes an induced dipolar surface charge distribution. The description is simplified by defining the dipole moment,

$$\mathbf{p} = \varepsilon_0 \varepsilon_d \alpha \mathbf{E}_0 = 4\pi \varepsilon_0 \varepsilon_d a^3 \frac{\varepsilon(\omega) - \varepsilon_d}{\varepsilon(\omega) + 2\varepsilon_d} \mathbf{E}_0, \quad (2.25)$$

where the polarisability,  $\alpha$ , incorporates the frequency dependent behaviour and is defined as,

$$\alpha(\omega) = 4\pi a^2 \frac{\varepsilon(\omega) - \varepsilon_d}{\varepsilon(\omega) + 2\varepsilon_d}. \quad (2.26)$$

The outside potential is then expressed as,

$$\varphi_{out} = -\mathbf{E}_0 \cdot \mathbf{r} + \frac{\mathbf{p} \cdot \mathbf{r}}{4\pi \varepsilon_0 \varepsilon_d r^3}. \quad (2.27)$$

This is simply the potential of an induced dipole superimposed onto the incident field. The electric field inside and outside of the sphere is calculated using  $\mathbf{E} = -\nabla \varphi$  and given by,

$$\mathbf{E} = \begin{cases} \frac{3\varepsilon_d}{\varepsilon(\omega) + 2\varepsilon_d} \mathbf{E}_0 & r \leq a \text{ (inside)}, \\ \mathbf{E}_0 + \frac{3\mathbf{n}(\mathbf{n} \cdot \mathbf{p}) - \mathbf{p}}{4\pi \varepsilon_0 \varepsilon_d} \frac{1}{r^3} & r > a \text{ (outside)}, \end{cases} \quad (2.28)$$

where  $\mathbf{n} = \mathbf{r}/r$  is the radial unit vector, and shows a similar dipolar phenomenon as seen in Figure 2.4b.

Provided that the quasistatic approximation remains valid, the electrostatic result is simply multiplied with a harmonic time dependence to describe electrodynamic behaviour. Hence, an EM wave induces a coherent, oscillating dipole moment  $\mathbf{p} e^{i\omega t} = \varepsilon_0 \varepsilon_d \alpha(\omega) \mathbf{E}_0 e^{i\omega t}$ . The be-

haviour of electrons in the spherical MNP at optical frequencies, described using the dielectric function  $\varepsilon(\omega)$ , is then simply incorporated into  $\alpha(\omega)$ . For a good metal  $\text{Re}[\varepsilon(\omega)] < 0$  and the denominator in Eq. 2.26 undergoes resonance at the Fröhlich condition when,

$$\text{Re}[\varepsilon(\omega)] = -2\varepsilon_d. \quad (2.29)$$

This corresponds to excitation of a collective oscillation of conduction electrons on the surface of the sphere - the dipolar LSP. Its magnitude in real metals is restricted by damping of the electron motion leading to a Lorentzian-shaped resonance band - the dipolar surface plasmon resonance. Its relationship with  $\varepsilon_d$  means that the resonant frequency can be tuned by varying the external dielectric medium. As seen in Eq. 2.28, the field from the induced dipole moment of the plasmon is superimposed onto the incident field, leading to a resonant field enhancement both inside and outside the surface of the sphere. This is the single most useful property of a plasmon, and one that is heavily exploited in sensing and sensor developments.

In the Drude model, with  $\varepsilon(\omega)$  given by Eq. 2.17, the Fröhlich condition is satisfied when,

$$\omega_{\text{LSP}} = \frac{\omega_p}{\sqrt{1 + 2\varepsilon_d}}, \quad (2.30)$$

which evaluates to  $\omega = \omega_p/\sqrt{3}$  for a MNP in vacuum. As can be seen in Figure 2.3, the flat dispersion of a LSP mode means it crosses the light line at a single point. Light of the correct frequency therefore readily couples with LSPs without the need for SPP momentum matching mechanisms. In general, the optical spectrum of a MNP can contain a number of multipolar plasmon modes for which the resonant frequencies are given by [26],

$$\omega_l = \omega_p \sqrt{\frac{l}{\varepsilon_d(l+1) + 1}}, \quad (2.31)$$

where  $l$  denotes the charge distribution of a specific spherical harmonic mode ( $l = 1$  for dipole,  $l = 2$  for quadrupole, etc.). However, these modes only exist outside of the quasistatic regime in larger MNPs or more complex geometries. For nobles metals, such as Au and Ag, the fundamental  $l = 1$  mode occurs in the visible region of the EM spectrum ( $\lambda = 520$  nm for Au and  $\lambda = 360$  nm for Ag in vacuum or air [24] and redshifted in the presence of other media [27]), leading to them often being the plasmonic metal of choice. Additionally, the polarisability changes with MNP geometry due to differing restoring forces acting on the surface charge distribution. Changes from a spherical shaped MNP therefore lead to tuning of the LSP resonance across the visible spectrum. This geometrical dependence is well known [28–30] and has been exploited in many applications over the past decade, e.g. infrared (IR) photothermal therapy [31–33].

The larger the separation between opposing poles of surface charge, the weaker the restoring force. A larger particle, or similarly an elongated particle (a nanoellipsoid or nanorod), will therefore have lower energy resonances. Simple changes can be made to the theoretical (quasistatic) model to account for an ellipsoidal geometry, and thus somewhat understand the geometrical dependencies incorporated into the polarisability. Insertion of a geometrical correction to the polarisability leads to the definition [24, 34],

$$\alpha_i(\omega) = 4\pi a_1 a_2 a_3 \frac{\varepsilon(\omega) - \varepsilon_d}{3\varepsilon_d + 3L_i(\varepsilon(\omega) - \varepsilon_d)}, \quad (2.32)$$

where  $i$  is the index of each anisotropic axis with a geometrical factor,

$$L_i = \frac{a_1 a_2 a_3}{2} \int_0^\infty \frac{dq}{(a_i^2 + q)\sqrt{(q + a_1^2)(q + a_2^2)(q + a_3^2)}}. \quad (2.33)$$

The resonance condition along each axis then becomes,

$$\text{Re}[\varepsilon(\omega)] = -\frac{1 - L_i}{L_i} \varepsilon_d. \quad (2.34)$$

By increasing the size of an axis, decreasing its associated geometrical factor, the resonance condition decreases from  $\varepsilon(\omega) = -2\varepsilon_d$ , redshifting the resonant LSP frequency. The more elongated the particle becomes, the larger the redshift until the restoring force is weakened to the point that each LSP no longer exists.

## Optical Observation of Surface Plasmon Resonances

Depending on the microscopic dipole moment of excited plasmons, their fields can be radiative and hence macroscopically observable. This depends on the geometry of the plasmons time-varying charge distribution. Antenna-like dipolar plasmons bear similarity with the Hertzian dipole, an infinitesimal oscillating current source which both absorbs and radiates EM waves. The relationship between the current,  $\mathbf{I}(t)$ , carried by the dipole of length  $d$  and the radiative electric field around it is given by [35],

$$\mathbf{E} = \frac{ik\mathbf{Id}\eta_o}{4\pi r} e^{-ikr} \left[ \hat{r} \left( \frac{1}{ikr} + \frac{1}{(ikr)^2} \right) 2 \cos \theta + \hat{\theta} \left( 1 + \frac{1}{ikr} + \frac{1}{(ikr)^2} \right) \sin \theta \right], \quad (2.35)$$

The radial behaviour of the electric field around an object can be split into three distinct regimes - the *near-field* or Fresnel regime and the *far-field* or Fraunhofer regime. At short distances the  $(kr)^{-2}$  term dominates to form the near-field but quickly falls off with increasing distance. The remaining  $(kr)^{-1}$  term defines the far-field. The boundary between the near-field and the far-field is defined as the point at which  $kr = 1$  where  $r = \lambda/2\pi$  (hence why

sub-wavelength optics deals with the near-field).

Plasmons similarly have the ability to both resonantly absorb and scatter incident fields. The absorbance and scattering cross sections determining interaction with a spherical MNP are given by [36],

$$\sigma_{\text{scat}} = \frac{k^4}{6\pi} |\alpha|^2 = \frac{8\pi}{3} k^4 a^6 \left| \frac{\varepsilon(\omega) - \varepsilon_d}{\varepsilon(\omega) + 2\varepsilon_d} \right|^2, \quad (2.36a)$$

$$\sigma_{\text{abs}} = k \text{Im}[\alpha] = 4\pi k a^3 \text{Im} \left[ \frac{\varepsilon(\omega) - \varepsilon_d}{\varepsilon(\omega) + 2\varepsilon_d} \right]. \quad (2.36b)$$

Since  $\sigma_{\text{scat}} \propto V^2$  and  $\sigma_{\text{abs}} \propto V$ , absorption dominates in smaller particles whilst larger particles scatter more strongly. The extinction cross section, commonly used in spectroscopy, can be calculated using  $\sigma_{\text{ext}} = \sigma_{\text{scat}} + \sigma_{\text{abs}}$ . The size of each cross-section, i.e. the spatial extent over which light interacts with the MNP, depends on  $\alpha$  and is increased on resonance. Hence, MNPs optically appear strongly coloured and much larger than they actually are.<sup>8</sup>

For example, when on resonance with the dipolar LSP, both cross sections are enhanced by the polarisability resonance from the geometrical particle size to the  $\mathcal{O}(500 \text{ nm})$  scattering size. The increased size of the cross-section is comparable to the wavelength of light, meaning LSPs efficiently couple with photons in the far-field. The LSP mediates energy transfer between the near-field and the far-field and acts to match the electromagnetic modes of nanoscale absorbers/emitters, such as phonons (Raman) and radiative energy levels (quantum emitters, fluorescence), with those of a diffraction-limited photonic mode via an oscillating charge density [37]. A plasmonic MNP is often therefore described as an *optical antenna* in a similar manner to a device that converts between radio waves and an electrical current is named a radio antenna [9, 38]. LSP modes which readily couple with the far-field are then sometimes referred to as *antenna modes* and become important when designing resonant structures for specific sensing applications.

Whilst the quasistatic approach is useful to first demonstrate the field enhancing capabilities of a MNP, the description breaks down once the size of the particle becomes closer to the excitation wavelength. Retardation effects result in phase differences between the incident field and the induced electron currents across the particle, which strongly influences the radiated fields. At this point Mie theory (electrodynamics) [39] is required to describe the spectral response of spherical MNPs, providing a more general description of their optical response. Using this approach the spectrum of a MNP can be decomposed into superimposed multipoles, arising from the existence of higher order LSP modes in larger MNPs with finite dipole moments. The spectral response of spherical AuNPs of varying sizes is shown in Figure 2.5,

---

<sup>8</sup>Consider that  $\sigma_{\text{scat}}$  for a AuNP is enhanced  $100\times$  on resonance, meaning it's area cross-section is  $\sqrt{100/\pi} = 6\times$  wider than it's radius, hence why a 50 nm AuNP looks like a 300 nm green sphere when imaged.

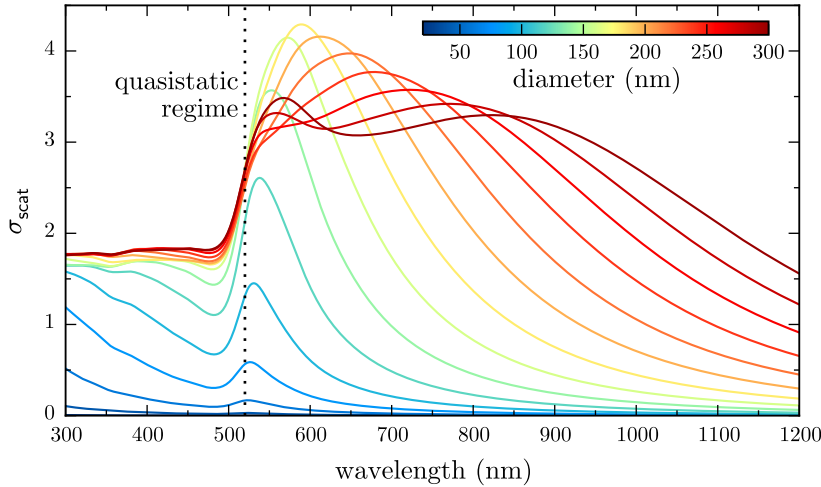


**Figure 2.5: Mie scattering cross-sections for AuNPs of increasing diameter.** The 520 nm resonance position of the dipolar LSP mode of a AuNP in the quasistatic approximation is indicated by the dotted line. The resonance stays at 520 nm until  $d > 80$  nm then redshifts. The emergence of higher order modes following a similar behaviour is seen once  $d > 100$  nm.

demonstrating the redshift and broadening of lower order modes with increasing particle size and the excitation of higher order modes.

To summarise, by utilising the particle material, geometry and polarisation anisotropy, its LSPs can be tuned across the entire UV–NIR spectrum to tailor to individual applications. However, even when exciting on resonance, a single particle can only provide a relatively small field enhancement ( $|E/E_0| \sim \mathcal{O}(5 - 10)$ ). An alternative approach to exploiting LSPs is therefore to couple the fields of many plasmons together. Through coupling, the confined fields in nanometric-size gaps between MNPs can be enhanced by many more orders of magnitudes.

## 2.2 Plasmon Coupling

Both the resonant field enhancement and the confinement of a surface plasmon can be improved by bringing a second surface plasmon into close proximity. Similar to coupled harmonic oscillators and dipoles, plasmons couple together via Coulomb forces, forming normal modes of oscillation. The charge distributions of the resulting normal modes depend sensitively on the particle separation and are strongly confined to the dielectric space between metallic surfaces where charges strongly interact. These normal modes are therefore more generally known as *gap plasmons* and lead to tuneable plasmon resonances [40, 41] and significant increases in field enhancement, enabling single molecule spectroscopy [42, 43].

Coupled plasmons are a feature of many metallic nano-systems with closely spaced metal-dielectric interfaces, including metal-insulator-metal (MIM) and insulator-metal-insulator (IMI)

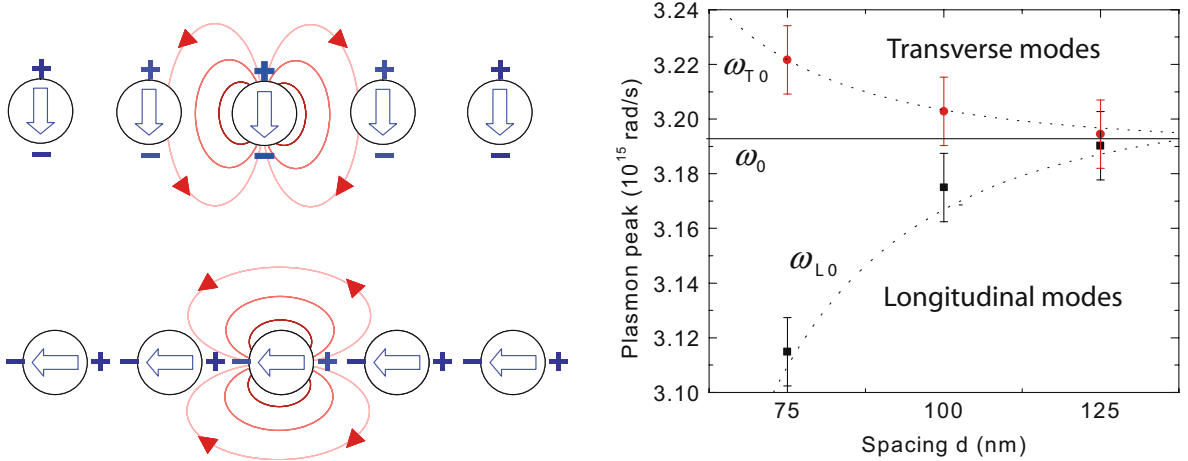


**Figure 2.6: Experimental and theoretical plasmon coupling.** Dipolar plasmons in chains of spherical AuNPs couple depending on field orientation [24] (left). Experimentally measured plasmon resonance energies in coupled AuNP chains show the gap-dependent tuning due to coupling [45] (right). The dotted line corresponds to a  $r^{-3}$  point dipole model.

waveguides [24, 44] and systems containing multiple MNPs [40, 41, 45–49] or nanoparticles-on-mirror (NPoM) [42, 50–54]. For the purposes of this work, discussion is restricted to the ideal case of coupled LSPs between two closely spaced MNPs, closely representing the experimental system, though the description of coupling is valid for many other cases involving SPs. Furthermore, in each example of coupled systems, the physics can be reduced to interactions between neighbouring charge distributions. Understanding the simple dimer system is therefore important to fully understand more complex geometries.

In the simplest description, the Coulomb interaction between free electrons in adjacent MNPs introduces an additional coupling force, pulling charge towards the gap between metallic surfaces. A greater amount of charge accumulates on the gap-facing metallic surfaces. As particles move closer together this force grows, more strongly confining the charge and increasingly polarising the gap region. The resonance frequency of the individual plasmon mode shifts from  $\omega_0$  by  $\Delta\omega$  depending on the strength of coupling. The sign of  $\Delta\omega$  depends on whether coupling is attractive or repulsive. Similar to coupled oscillators, the two coupling configurations (normal modes) along each axis are the in-phase and anti-phase modes. Light generally drives the free electrons of two sub-wavelength particles in phase, resulting in only an observable bonding configuration. Plasmons excited in phase along the dimer axis experience an attractive coupling force, redshifting with decreasing interparticle separation, whereas plasmons excited in phase perpendicular to the dimer axis experience repulsive coupling, blueshifting with decreasing interparticle separation. Compelling evidence for each of these modes has been seen many times, with particularly good results found using chains of AuNPs [45], as shown in Figure 2.6. In almost all cases, it is the in-phase coupled plasmons oriented along the dimer axis that are of interest.

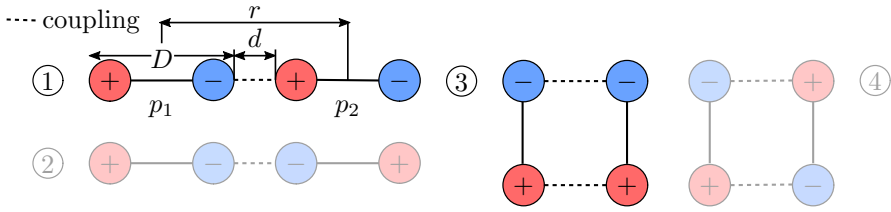


**Figure 2.7: Diagram of dipole interactions.** The distance between dipoles of length  $D$  is  $r$  with an edge-to-edge separation  $d$ . Configurations 1 and 3 are comparable with plasmon coupling as a result of sub-wavelength structures being driven by a single external light field. Configurations 2 and 4 are generally unphysical or non-radiative in plasmon dimers without asymmetry or phase retardation.

The primary effect of plasmon coupling orientated across the dimer gap is increased confinement of the electric field to the dielectric gap medium, leading to much larger field enhancements that can be exploited for sensing. For a strongly confined gap mode there is very little field in the metal with almost all field confined to a small mode within the gap [55]. This is known as a plasmonic ‘hot spot’. Through this mechanism alone the field enhancement can be increased by more than an order of magnitude [56, 57]. Hence, in recent years, the interests of the plasmonics community have shifted from individual plasmonic nanostructures to coupled systems in order to maximise nano-optical performance. This has led to the progression into sub-nm plasmonic cavities, the study of which is a focus of this project. The development of a theoretical model for such small systems begins with the classical models of plasmon coupling with additional complexity added until quantum mechanical effects become apparent.

### 2.2.1 Classical Models of Plasmonic Coupling

Two analytical classical models exist to describe plasmon coupling. The first and simplest model continues the description of the dipole plasmon present in small (quasistatic) MNPs and introduces dipole-dipole interactions. The second model of plasmon hybridisation is more complex and successfully models higher order modes of charge oscillation.

#### Dipole-Dipole Model

In its simplest case, interactions between dipolar plasmons in small MNPs appear similar to dipole-dipole interactions [45, 46, 58–60], exhibiting the same behavioural dependence on separation and relative orientation with respect to the incident field. Examples of some commonly considered dipole-dipole interaction geometries are shown in Figure 2.7. In each situation the electric field incident on a dipole  $\mathbf{p}_1$  is perturbed by the presence of a second dipole  $\mathbf{p}_2$  a distance  $r$  away, whose fields (described by Eq. 2.28) are superimposed onto the incident field

at the location of  $\mathbf{p}_1$ . The result is in an effective field given by,

$$\mathbf{E}_{\parallel}(\mathbf{p}_1) = \mathbf{E}_{0,\parallel} + \frac{\mathbf{p}_2}{2\pi\epsilon_0\epsilon_d r^3}, \quad (2.37a)$$

$$\mathbf{E}_{\perp}(\mathbf{p}_1) = \mathbf{E}_{0,\perp} - \frac{\mathbf{p}_2}{4\pi\epsilon_0\epsilon_d r^3}, \quad (2.37b)$$

where  $\parallel$  and  $\perp$  denote the orientation of dipoles relative to the dimer axis. The sign of the second term in each equation determines the effect of coupling whilst its strength falls as  $r^{-3}$  [61]. The polarisability of the MNP is modified by this additional interaction field, changing the frequency at which it becomes resonant. For two dipoles aligned end-to-end ( $p \parallel r$ ) and driven in phase, coupling is attractive (increased  $\mathbf{E}$ , Eq. 2.37a), leading to a decrease (redshift) of the resonant frequency. Conversely, the interaction between two dipoles aligned side-by-side ( $p \perp r$ ) is repulsive (decreased  $\mathbf{E}$ , Eq. 2.37b), causing an increase (blueshift) of the resonant frequency. These describe the in-phase interactions between two dipole.

Anti-phase configurations, as shown in Figure 2.7, behave in the opposite manner to the in-phase counterparts as the direction of the Coulomb force reverses. These configurations are often ignored in quasistatic dimers since light only drives in-phase oscillations. Phase retardation across the larger dimer particles can break the coupling symmetry and allow excitation of anti-phase modes, however they still have no net dipole and remain non-radiative. Electron-based techniques such as EELS are instead used to probe these ‘dark’ modes. Using EELS with AuNP chains, the validity of the dipole approximation was confirmed, showing good agreement with the experimental data shown in Figure 2.6 [45].

The dipole-dipole model is only an approximation to actual plasmonic coupling and does not adequately account for the spatial charge distribution. It can be somewhat improved by taking into account the finite particle size. Since the internal restoring force within particles, scaling as  $D^3$ , contributes to the potential, the interaction energy goes as  $(r/D)^{-3}$  as opposed to  $r^{-3}$  [62]. Furthermore, this quantity is redefined to better represent a dimer using the gap width,  $d$ , as  $(d/D) = (r/D) - 1$ . The resonant wavelength shift due to attractive coupling can then be approximated using a “plasmon ruler” equation [62, 63],<sup>9</sup>

$$\frac{\Delta\lambda}{\lambda_0} = a \exp \left[ -\frac{(d/D)}{\tau} \right], \quad (2.38)$$

where  $a$  is the coupling strength and  $\tau$  is a decay constant. In essence, this model describes an interesting phenomenon - that plasmon coupling is scale invariant. Dimers comprised of larger particles interact more strongly for the same separation than smaller dimers. However, their relative shifts depend on how the gap size compares with the particle size. In recent years this relation still shows good agreement with experimental data but the approach remains limited

---

<sup>9</sup>The exponential approximates a more complex power law [64].

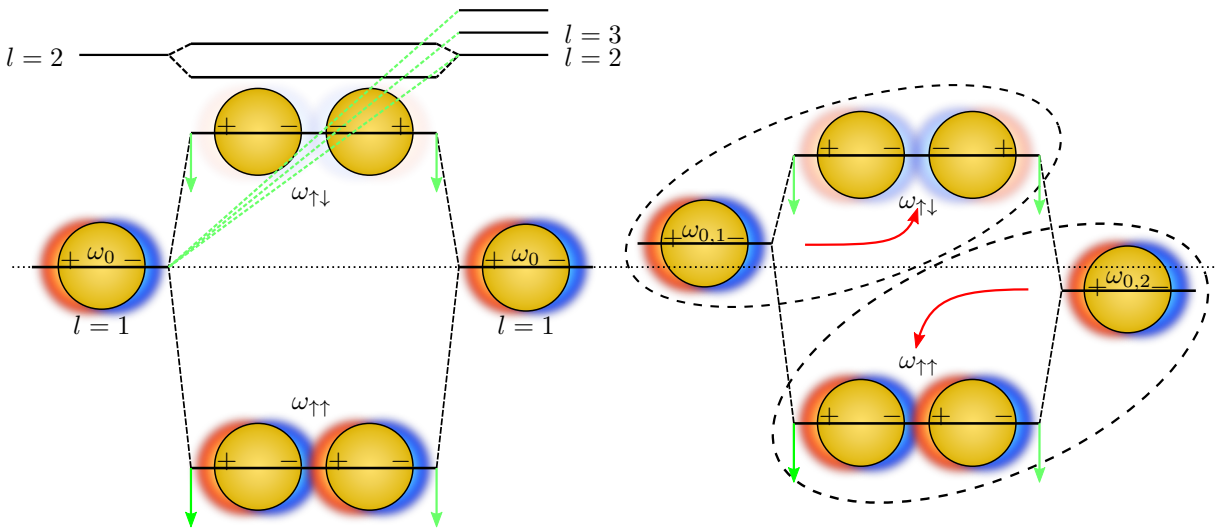


**Figure 2.8: Diagram of plasmon hybridisation between coupled plasmons in a nanoparticle dimer.** Plasmons are coupled along the dimer axis. Coupling leads to bonding and anti-bonding modes for each set of interacting  $l$  modes (left). Interaction with higher order  $l$  modes lowers the overall energy of lower order coupled modes (green lines). Only the bonding ( $\omega_{\uparrow\uparrow}$ ) mode in the symmetric (homo-)dimer has a net dipole moment and is therefore observable. Cancellation of the net dipole moment means the anti-bonding ( $\omega_{\uparrow\downarrow}$ ) mode remains optically dark. On the contrary, asymmetry in a (hetero-)dimer means both modes stay bright (right). In this case, the lower and higher energy individual modes shift to form the bonding and anti-bonding hybridised modes, respectively. This diagram is adapted from [65].

to describing only dipolar modes in simple geometries [47].

### Plasmon Hybridisation

A slightly more complex model, known as plasmon hybridisation, was developed to more generally explain the formation and behaviour of coupled modes [26, 65, 66]. In this model, plasmon resonances are mechanically modelled as resonant oscillations of an incompressible fluid confined within an equilibrium geometry [26]. The plasmon resonances of a more complex particle geometry are then solved by decomposing it into coupled resonances of two simpler particle geometries [26, 66]. This is done in analogy with the ideas underpinning molecular orbital hybridisation and the hybridisation of quantum energy states. Using this logic, the theory equally describes the plasmon resonances of two coupled simple particle geometries [65] or a particle coupled with its image charge in a surface [67]. Under these circumstances, the multipolar modes of each of the individual dimer particles energetically split into two hybridised modes representing the bonding (in-phase) and anti-bonding (anti-phase) configurations. This behaviour is shown in Figure 2.8.

Unlike the dipole-dipole model, plasmon hybridisation is capable of predicting higher order multipolar modes in a coupled dimer system as well as dealing with more complex geometries. It is therefore valid for describing larger dimer geometries and smaller gap sizes. As with dipole-

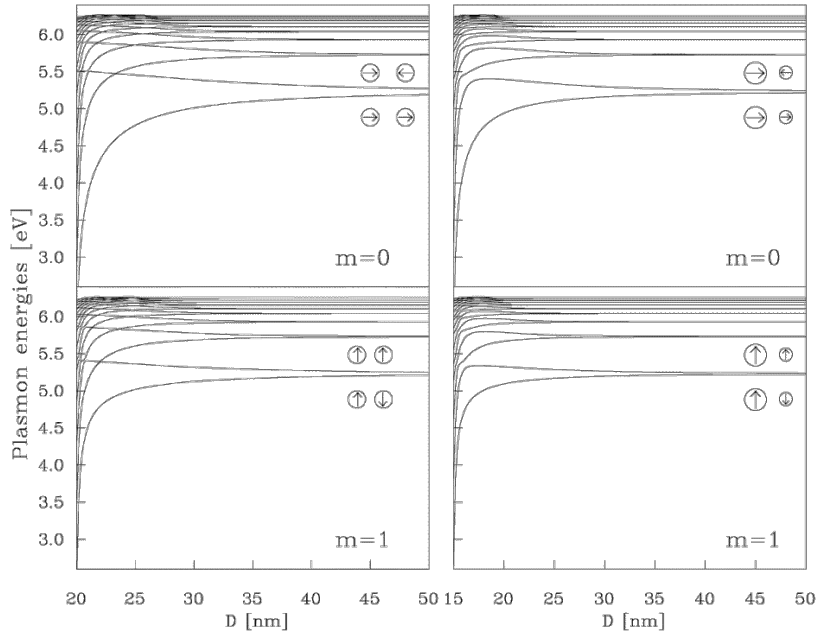


**Figure 2.9: Hybridised plasmon energy shifts for spherical AuNP dimers.** Homodimer (left) and heterodimer (right) plasmon energies are calculated in both the axial (top) and transverse (bottom) coupling configurations. Spheres are 10 nm in diameter in the homodimer and 10 nm and 5 nm in the heterodimer.

dipole interactions, the bonding and anti-bonding hybridised modes redshift and blueshift from their initial mode positions, respectively, upon decreasing the separation. These shifts in the plasmon energies are shown in Figure 2.9. However, the addition of higher order modes to the classical description of plasmon coupling, and their interaction with adjacent modes of similar energies, modifies the rates of each mode's shift, as shown by the green lines in Figure 2.8 [65]. These interactions leads to a further redshift of each affected mode, though only in the case of small gaps or larger particles once higher order modes are excited.

In each classical approach it is the resulting dipole moment of each coupled mode that dictates its radiative properties. The in-phase bonding mode exhibits a large dipole moment and strongly couples with light whereas the anti-phase anti-bonding mode has no net dipole moment in a symmetric system and thus remains dark. This remains the case until the anti-bonding dimer mode acquires a finite net dipole moment through particle asymmetry (difference material, size or shape), at which point it becomes more radiative and hence experimentally observable using optical methods. Alternatively, local excitation of specific charge distributions using EELS allows for measurement of dark modes [68, 69]. Should both bonding and anti-bonding modes be bright and gaps decrease enough that a blueshifting anti-bonding mode approaches on a higher order redshifting bonding mode, an anti-crossing will occur and modes exchange symmetry. This causes anti-bonding modes to eventually redshift into geometrical contact.

Whilst each of the previously described analytical models has found some success in de-

scribing experimentally observed plasmon coupling in simple systems, their approaches are limited in scope. Neither model directly calculates electrodynamics and solves the actual electromagnetic problem. Instead, they use analogies to similar electromechanical systems to provide a useful insight into the mechanism of plasmon coupling. The electrodynamics of a particular plasmonic problem are now often solved using computationally demanding, numerical techniques, in which the electrodynamics are solved at each boundary within a system.

## 2.2.2 The Dynamical Optical Response of Plasmonic Dimers: Transitioning from Capacitive to Conductive Plasmonic Coupling

Using modern numerical simulation techniques, such as the boundary element method (BEM) and finite-difference time-domain (FDTD) approaches, the full separation-dependent optical response of a plasmonic dimer has been calculated as particles transition from non-interacting to coupled through into geometrical contact [55]. In these calculations, the lowest order plasmons hybridise, redshift and more intensely scatter as the separation decreases, with higher order modes eventually emerging. Classically, this leads to a large number of modes being present in nanometre-size gaps. The lateral confinement of the field between particles of radius  $R$  separated by a gap of width  $d$  is estimated as  $w = \sqrt{Rd}$  [55]. As higher order modes become more intense, scattering from lower order modes decreases. Despite this, their field enhancement continues to rise [70]. These plasmons become so confined that they no longer couple with the far-field. This behaviour continues until particles are nearly touching into geometrical contact.

Once touching, bonding hybridised plasmons abruptly transition into charge transfer plasmons (CTPs) - charge oscillations spread across the full extent of the connected dimer. These are widely observed in geometrically contacted or overlapping plasmonic systems [46, 71]. A dipolar CTP emerges at lower energies (considered to be the equivalent of a monopolar dimer

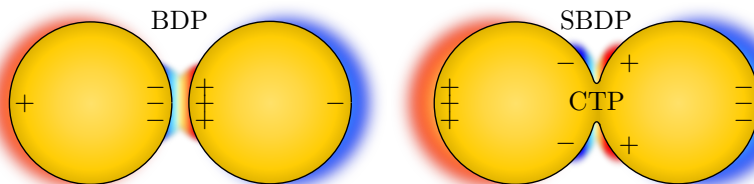


**Figure 2.10:** Diagram showing the emergence of charge transfer and screened bonding dimer plasmons on geometrical contact in a nanoparticle dimer. The field generated by the bonding dimer plasmon (BDP) is screened from the gap by the conductive contact, forcing capacitive coupling to the outer crevices in the form of the screened bonding dimer plasmon (SBDP). The dominant charge oscillation is then the charge transfer plasmon (CTP) through the conductive bridge and across the whole structure.

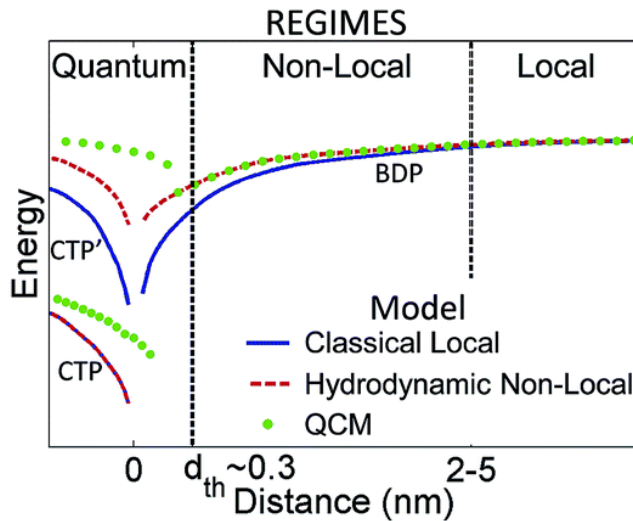


**Figure 2.11:** Calculated plasmon energies of a spherical AuNP dimer as a function of gap separation using a number of computational models [75]. The classical local approach is valid for separations greater than 2 nm. Below this non-locality smooths the gap and adequately describes mode behaviour until 3 Å. At this point quantum models must be used. Figure taken from [75].

mode) as screened coupled plasmons are expelled out of the gap, transitioning into higher order CTPs due to their similar charge distributions [55, 72–74]. Their resonances blueshift, diminishing in intensity and broadening in width as a result of significantly increased currents. The lower energies of CTPs are associated with a spatially larger dipole, as shown in Figure 2.10, suggesting they should blueshift with increasing particle overlap. Their broad width compared with capacitively coupled plasmons is caused by dissipation in the junction and can be linked with behaviour described by Eq. 2.12.<sup>10</sup>

Classical predictions of plasmon coupling break down in small, sub-nm gaps where the continuum of excited higher order modes redshift to a singularity as  $d \rightarrow 0$ , and the field enhancement increases infinitely. This behaviour is completely unphysical and is rectified once non-locality and quantum mechanical effects are considered. A comparison of the models taking these effects into account is shown in Figure 2.11. Quantum mechanical effects begin to affect plasmon coupling under two conditions - either the particles become sufficiently small that non-local quantum effects (finite, non-negligible electron wavefunction spill-out from the particle) become important or the gap size decreases to scales on which quantum tunnelling and non-locality of the gap surfaces can no longer be ignored.

The non-local electron spill-out from metal surfaces smooths the gap geometry and consequently the spectral trends. The redshift into contact is heavily reduced compared with classical predictions since electrons move further into the metal on approach, suppressing cou-

<sup>10</sup>For a spherical MNP dimer with a bonding hybridised dipolar plasmon (BDP) the corresponding CTP modes are typically labelled as the CTP and CTP'. The CTP' is often labelled as the screened bonding dipolar plasmon (SBDP) due to similarities in charge distribution.

pling [75]. Smoothing of sharp edges in the gap prevents a continuum of higher order modes, which become harder to excite, leaving only the most fundamental dimer modes. Screening of the coupled modes and the emergence of CTPs prior to geometrical contact are predicted only once quantum charge transfer effects are accounted for. The onset of quantum tunnelling means charge is transported across the gap without requiring geometrical contact. This is soon after followed by a quantum conductive charge transport regime prior to returning to a classical description of plasmonics. These two effects, due to their significance in sub-nm dimer gaps, are considered in more detail.

### Quantum Charge Transport: Electron Tunnelling and Ballistic Transport

The quantum charge transport properties of a system consisting of two reservoirs of free electrons separated by a potential barrier are determined by comparing the height of the potential barrier to the Fermi energy of each reservoir. For two metals separated by an insulating gap the potential barrier will, in general, be larger than the Fermi level. Classically, electrons with energies below the potential barrier cannot reach the other side. Electrons can only conduct through via quantum tunnelling, in which electrons incident on thin barriers have a finite probability of passing directly through the barrier as opposed to going over it. This is shown in Figure 2.12.

The potential barriers and transmission probabilities of a tunnel junction between two reservoirs of Au are shown in Figure 2.13. In a simplistic model, the potential layout is considered as a 1D rectangular barrier and the tunnelling probability increases exponentially with decreasing barrier width,  $d$ , going as  $T = e^{-\beta d}$ , where  $\beta$  is a decay parameter [76].<sup>11</sup> Many different mathematical descriptions of this phenomena exist [77, 78], especially after the invention of STM, that predict the conductance and resulting current density as electrons tunnel

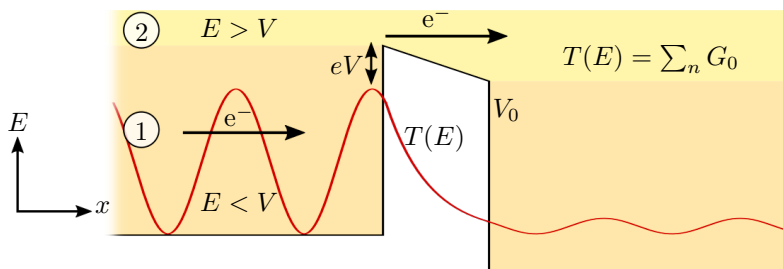


**Figure 2.12: Diagram of quantum charge transport between two reservoirs of free electrons.** If the Fermi energy of electrons is below the barrier potential (1) then there is a finite transmission probability  $T(E_F)$  of tunnelling through the barrier. If the Fermi energy becomes larger than the potential barrier (2) then electrons are free to move through a quantised number of conducting channels of conductance  $2e^2/h$ .

<sup>11</sup>For a simple rectangular barrier of height  $V_0$  the transmission  $T = |t|^2$  is given by,  $T = e^{-2\sqrt{\frac{2m}{\hbar^2}(V_0-E)}d}$ .

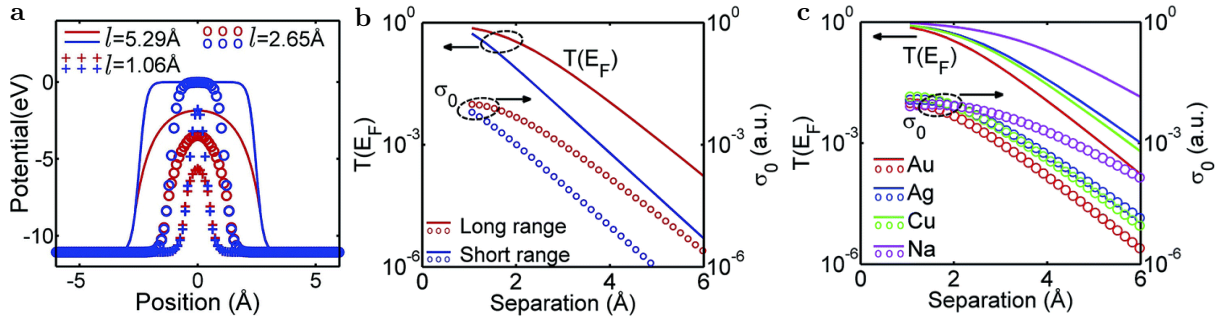


**Figure 2.13: Potential barrier shapes for various gap widths and tunnelling transmission probabilities as a function of separation and material [75].** Calculated potential barrier shapes between two Au particles as a function of separation (a) with corresponding transmissions (b). The inclusion of long-range image charge interactions is compared with a simple short-range barrier model. Realistic barrier shapes are more rounded than the simpler rectangular assumption. Overlap between rounded potential edges decreases the barrier height with reduced separation. Tunnelling increases exponentially as the gap width reduces, with increased tunnelling caused by the smaller rounded barriers. Transmission depends on the work function of a material with differing transmission probabilities at a given separation (c).

through an arbitrary potential landscape. This is in part due to the large number of parameters that influence tunnelling (e.g. work function, barrier potential, barrier shape, applied bias, temperature, charge hopping [78]) and the extension of it into 3D gap morphologies, however the exponential decay is always present.<sup>12</sup> The current density is therefore expected to follow [79],

$$J = J_0 e^{-\beta d}, \quad (2.39)$$

where  $J_0$  is a saturation current density. This behaviour holds for large gap sizes but begins to fail in small ( $2 \text{ \AA}$ ) gaps where the rectangular barrier shape assumption no longer holds (Figure 2.13a,b). The barrier height begins to decrease with separation on overlap of the rounded edges. Tunnelling then becomes even more likely as the separation decreases. Since the transmission depends on the Fermi energy of free electrons in a material and the potential of the barrier region in between, different materials have different tunnelling responses. For example, tunnelling is far stronger in Na than in Au (Figure 2.13c) [75]. Finally, the current generated by tunnelling depends on the number of tunnelling channels available in a junction and the transmission coefficient of each channel [80].

Once the barrier falls below the Fermi level (at  $\sim 1\text{--}2 \text{ \AA}$ ), provided that the contact is short enough that motion is ballistic (no scattering), conduction electrons can move freely between the two reservoirs via a number of discretely quantised, 1D conduction channels under the application of an applied bias. This bias in the plasmonics case stems from the field induced by light. Each channel has a transmission probability  $T(E_F) = 1$  and a conductance given

<sup>12</sup>At least within a low bias approximation, which is generally valid in the context of this thesis.

by  $G_0 = 2e^2/h$ , the conductance quantum [81]. The total conductance depends only on the number of open channels, a quantity depending typically on the width of the conductive region or the atomic scale contacts between reservoirs. This results in a conductance described by the Landauer formula<sup>13</sup> [81],

$$G = \frac{2e^2}{h} \sum_n T_n(E_F) = nG_0, \quad (2.40)$$

where  $n$  is the number of transmission channels. Though still firmly in a quantum domain, ballistic transport is a form of conductive contact as opposed to a tunnelling phenomenon. Classical behaviour is only recovered if the length of the constriction increases to the point at which electrons begin to scatter or the width increases to allow many channels. In this event, the conductance is classified as diffusive with a conductance given by  $G = \sigma A/d$ .

### Quantum Charge Transport in Plasmonic Nanogaps

The effects of quantum charge transport were first predicted in small ( $R < 2\text{ nm}$ ) NaNPs using full quantum mechanical, time-dependent (TD) density functional theory (DFT) [80]. Since these calculations consider the behaviour of each electron, they are currently limited in complexity to small systems containing less than 2000 electrons. Quantum effects in larger metallic nanostructures are predicted by the quantum corrected model (QCM), a classical model which includes the effects of non-locality and uses an effective gap dielectric function that takes conductivity into account. Quantum effects are then predicted by inserting pre-calculated conductivity values from TDDFT [70]. Both the QCM and TDDFT show agreement on the effects of tunnelling and conduction on plasmon coupling in NaNPs, with QCM predictions of the plasmon energies in a AuNP dimer shown in Figure 2.11.

In numerical simulations, the onset of tunnelling creates a conductive bridge through which electrons can transmit during each half optical cycle. Tunnelling electrons neutralise some of the accumulated surface charge on the gap-metal interfaces, lessening the local capacitive interaction and reducing the rate of redshift. Coupled plasmons begin to be expelled from the gap and the field enhancement drastically falls [70, 80]. This is the screening effect and signifies entry into the *crossover* regime [80]. At these separations, typically  $5\text{ \AA}$  in Na, the barrier remains above the Fermi level. Screening prevents the formation of an arbitrarily large charge density around the gap and the divergence of plasmon resonances, preparing the gap for a progressive transition into conductive contact.

The conductance provided by quantum tunnelling is too small to excite CTPs, hence only screening is initially observed. Once the gap size reduces to the point at which the potential barrier falls below the Fermi level a dimer transitions into a conductive state where  $T(E_F) = 1$

---

<sup>13</sup>Full derivation of the Landauer equation and quantised conductance is found in the appendices.

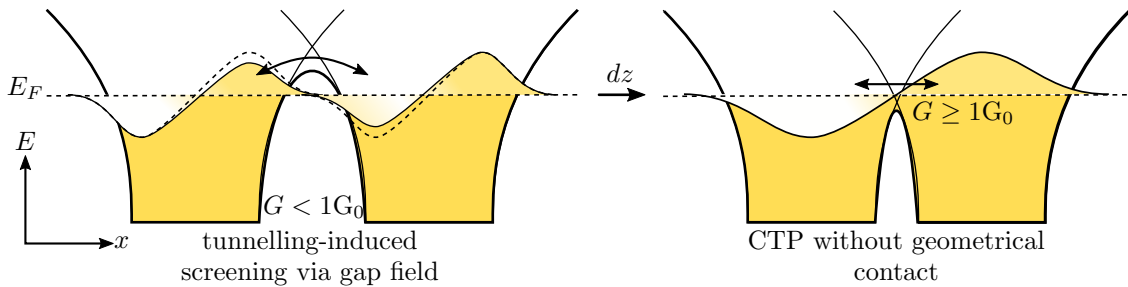


**Figure 2.14: Diagram of the charge transfer process in a nanoparticle dimer.** The electron density is represented by the filling of the particle potential wells. Electrons are considered non-local and spill out from the gap surfaces. Long-range image charge interactions also further round the potential barrier. Tunnelling at large distances neutralises optically-driven charge accumulation on gap surfaces, reducing coupling. At smaller separations the particle Fermi level can become greater than the gap potential barrier, permitting conduction instead of tunnelling. This is the origin of gap current and CTP excitation.

and conductances are given by Eq. 2.40. This is the *conductive* or *CTP* regime, in which the free flow of electrons permits a large current through junction and enables CTP excitation [80]. A diagram showing this changeover in conduction mechanisms is shown in Figure 2.14, similar to DFT calculations presented in [80]. The increased current progressively screens and ultimately decouples gap plasmons, which blueshift into higher order CTPs. The fundamental CTP appears near to geometrical contact once the conductance rises sufficiently [70, 82]. Similar effects are seen in classically calculated AuNP dimers connected by a conductive bridge to mimic molecular linkers [72, 73].

A critical gap width for such quantum conductive effects is found between 1–2 Å for NaNPs with a similar transition occurring in AuNP dimers for gaps between 1.06 Å and 2.65 Å [75], as shown in Figure 2.13a. Though quantum simulations considered only small NaNPs it is proposed that larger nanoparticle dimers could enter the quantum regime at greater separations as larger nanoparticles have more closely spaced energy levels (reduced quantum size effects) and therefore more available conductance channels [80]. The QCM seemingly reproduces this effect with conductive effects occurring in  $R = 25$  nm AuNP dimers at similar 2–3 Å separations, despite the lower rate of tunnelling between Au surfaces.

A simple estimation of this critical distance is given in [14], when simulating a tip dimer with spherical Au apices. The conductive regime is said to dominate once the charge stored in a plasmon becomes less than the charge involved in charge transfer, i.e. the fraction of conductive charge is greater than 50%. The tunnelling conductivity in a rectangular barrier model is,

$$\sigma(d) = \frac{3k_e e^2}{4\pi h} e^{-2k_e d}, \quad (2.41)$$

where  $k_e = \sqrt{2m\varphi}/\hbar$  is the electron wavenumber at the work function,  $\varphi$ . The distance at

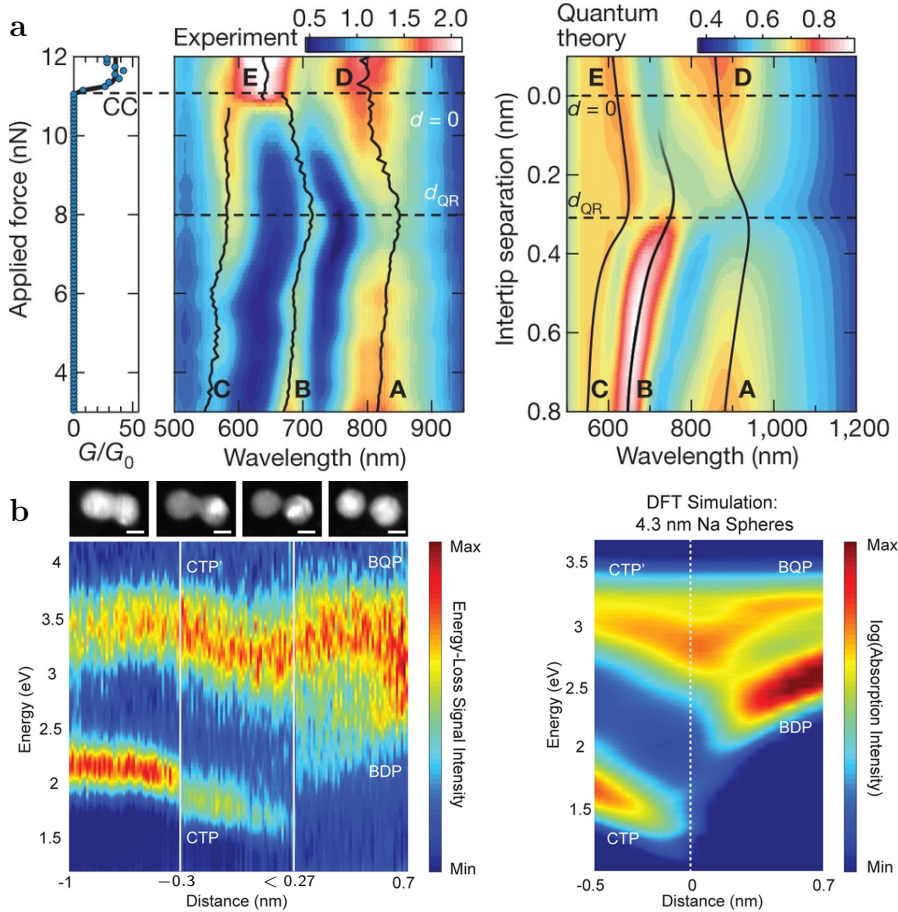


**Figure 2.15: Examples of experimental measurements showing the quantum regime of plasmonic coupling through direct monitoring of the plasmon resonances.** (a) Super-continuum dark-field scattering measurements of two 300 nm diameter spherical Au tips in a dimer configuration with reducing separation, transitioning below 1 nm and into the quantum regime [14]. (b) EELS measurements of 10 nm AgNPs being induced closer together by the electron beam [82].

which this leads to a majority of charge transfer is calculated as,

$$d_{QR} = \frac{1}{2k_e} \ln \left[ \frac{3k_e \lambda \alpha}{2\pi} \right], \quad (2.42)$$

where  $\lambda$  is the wavelength of the plasmon and  $\alpha = 1/137$ , the fine structure constant. Evaluating this for Au ( $\varphi = 4.8$  eV) at an 850 nm plasmon wavelength yields a critical separation of 1.6 Å with a conductivity of  $3.3 \times 10^3$  S m<sup>-1</sup>. If instead the larger conductivity from DFT is used, the equation predicts a critical gap size of 3.6 Å, similar to the 3.1 Å found in QCM spectra.

Experimental evidence of quantum transport effects in plasmonic gaps has recently been found using optical spectroscopy [14, 83, 84], EELS [82], SERS [84], photoluminescence [85] and third-harmonic generation measurements [86]. Optical scattering measurements from

a dynamic spherically-tipped Au AFM probe dimer clearly show the spectral signatures of quantum effects and generally agree with QCM simulations. Two coupled plasmon resonances begin to weaken during the final 7 Å of the approach into contact (Figure 2.15a) [14]. Distances are determined by comparing with QCM spectra. Coupled modes blueshift upon decreasing past a 3 Å critical separation and begin to regain intensity whilst a new mode strengthens going into contact. Further experimental agreement is found in EELS measurements on 10 nm AgNP dimers, brought together under the influence of the electron beam (Figure 2.15b) [82]. In this system the dimer exhibits simultaneous CTP excitation and coupled mode screening once  $d < 3 \text{ \AA}$ . The agreement between both experiments, the QCM and DFT calculations reinforces the idea that quantum tunnelling screens plasmon coupling and the rising conductance after ballistic conductive contact leads to the rise of CTPs.

A small number of other recent experiments have also now began to report effects attributed to conduction and quantum tunnelling. Alkanedithiol molecules of various lengths have been used to discretely tune the gap separation of AuNP dimers, with attenuation and blueshifting of the BDP with molecules smaller than pentanedithiol [83]. Similar results are found when using intercalating surface-assembled monolayers (SAMs) [79]. Further investigations into sub-nm plasmonic gaps have also shown behaviours attributed to quantum tunnelling, though inferred from properties depending on the field enhancement as opposed to direct measurement of SPRs. A decrease in signal intensity in both the SERS peaks [84] and photoluminescence [85] in nano-gap systems, for example, are signatures of quantum tunnelling screening the coupled plasmon field.

Finally, theory has begun to predict the variability of quantum regime plasmonics with gap morphology, showing that atomic rearrangements can dramatically alter the plasmonic response [87]. This is theoretically demonstrated in 16 Å faceted NaNPs dimers in various configurations, shown in Figure 2.16. With flat surfaces aligned the conductance is maximised, with a CTP and a fast blueshift seen as early as 5 Å. In contrast, with facet vertices aligned, a CTP only begins to emerge after contact between atoms. Screening in this arrangement is observed earlier at around 6 Å, likely due to tunnelling only having to neutralise a small surface area. The facets demonstrate an atomic lightning rod effect that increases the field in the gap whilst minimising the conductance. All other configurations average to the expected result predicted using a spherical particle model. This demonstrates that experiments can in some sense become limited by surface roughness or even atomistic surface defects.

### Limits of Critical Behaviour in Conductive Plasmonic Nanogaps

Both the screening-induced blueshift and CTP excitation require a conductance threshold to be surpassed in order for these effects to occur. Thresholds have been defined for a dimer containing a classical conductive linker, where the gap between particles of radius  $R$  has a

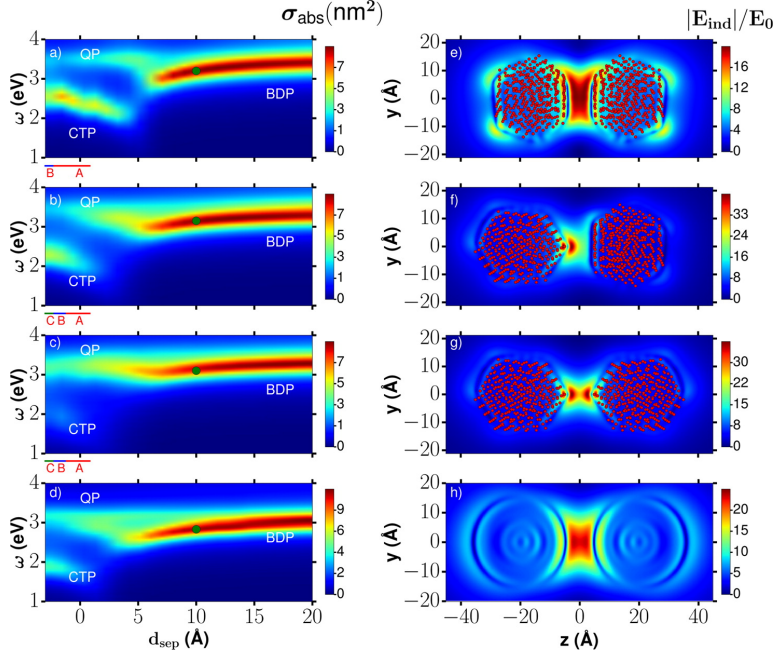


**Figure 2.16: TDDFT calculations of 16 Å faceted NaNP dimers arranged with different facet alignments [87].** Aligned facets leads to the smallest field enhancement and the earliest onset of charge transfer effects at 5 Å. Vertex alignment results in an atomic-scale lightning rod effect and increased field localisation. CTP excitation is more difficult in this configuration, occurring at 0 Å, due to the small contact but screening is made easier for the same reason, occurring at 7 Å. The figure is taken from [87].

width  $d$ , conductivity  $\sigma$ , and linker radius  $a$  [72, 73]. The blueshift of screened gap plasmons occurs at low conductances with a critical conductance for the dipolar bonding plasmon given by,

$$G_{\text{SBDP}} = 2\epsilon_0\omega_{\text{BDP}} \frac{a^2}{d}, \quad \left( \sigma_{\text{SBDP}} = \frac{2\epsilon_0\omega_{\text{BDP}}}{\pi} \right). \quad (2.43)$$

Reducing the conductance to a conductivity by removing a factor of  $\pi a^2/d$  shows that screening is intrinsically independent of geometry and depends only on a critical conductivity. Experiments maintaining a fixed geometry whilst increasing the gap conductivity using fractional mixing of similar conductive and insulating SAMs have succeeded in showing a blueshift of coupled plasmons with an estimated  $2G_0$  threshold [88], as shown in Figure 2.17. A similar  $2G_0$  threshold is also found in theoretically considered 1 nm dimer linkers [72].

A second, much larger, threshold exists for CTP formation, occurring at,

$$G_{\text{CTP}} = \epsilon_0\omega_{\text{CTP}} \frac{R^2}{d}, \quad \left( \sigma_{\text{CTP}} = \frac{\epsilon_0\omega_{\text{CTP}}}{\pi} \left( \frac{R}{a} \right)^2 \right). \quad (2.44)$$

Unlike screening, CTP formation depends not only on the conductivity but also the junction geometry. The geometrical factor ( $R/a$ ) represents the ratio between the total charge in the

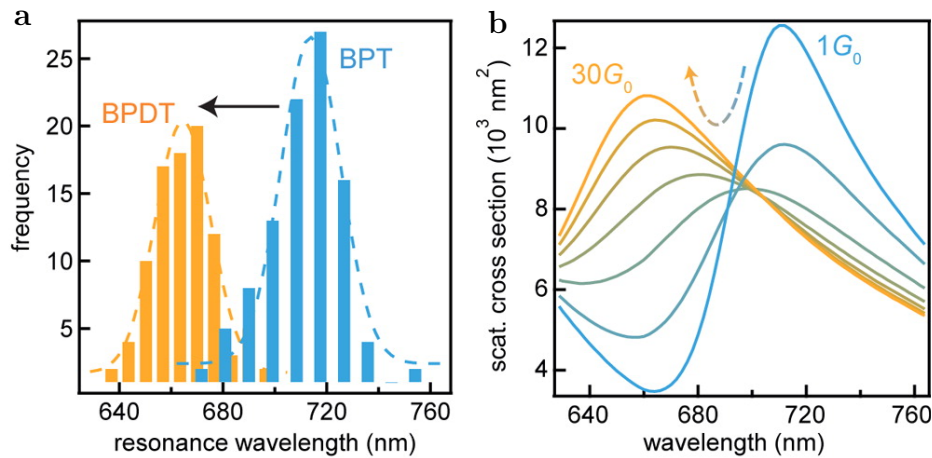


**Figure 2.17: Experimental and theoretical scattering spectra of 80 nm AuNP on a planar Au mirror separated via variable conductance molecular spacer layer [88].** Variable conductance molecular SAMs are formed from fractional mixing of BPT (insulating) and BPDT (conductance). The blueshift and attenuation of the coupled plasmon begins at  $2G_0$  with the screened mode emerging once  $G > 5G_0$ .

particle and the amount which can pass through a gap with fixed conductivity. Hence, a small, nanometre-scale but highly conductive junction between particles can accommodate sufficient current to maintain a CTP. This has been experimentally demonstrated in AuNP dimers separated by hollow spacer molecules and linked by a Au thread during exposure to high power laser pulses [74, 89].

Interestingly, qualitative agreement between QCM calculations and full quantum mechanical calculations suggest that the quantum nature of the system is of little importance. Even though the QCM uses a classical, resistive gap with conductance values characteristic of quantum transport, quantum effects on gap plasmons are accurately replicated. This implies that, despite the quantum nature of such small gaps, the effects on plasmon coupling only depend on the amount of charge transfer and not the mechanism by which it occurs. This links together work done using particle positioning [14, 82] with studies of interacting plasmonic system coupled with molecular linkers [79, 83, 88]. Quantum tunnelling and quantised conductance still remain interesting cases, however, since both forms of conduction are unavoidable once gap sizes decrease below 0.5 nm. This is why the point at which the electric field is expelled from the gap is described as the quantum limit to plasmon confinement [14]. For this reason, it is important to fully understand the relations between plasmonic hot spots and sites of (quantum) charge transfer.

Although charge transfer effects have been shown in previous reports by varying the conductivity of a fixed gap, there has yet to be a report showing the optical response of a dynamic dimer structure correlated with its electronic response. It is the aim of this project to successfully determine the relationship between electronic and plasmonic phenomena using a dual plasmonic nano-tip dimer. Metallic nano-tips are a plasmonic geometry currently receiving

significant attention from the plasmonics community. In order to use nano-tips to determine the effects of quantum charge transfer on plasmonics, their supported plasmons must first be described.

## 2.3 Plasmons in Tips

Significant efforts have been made to advance nanoscale surface characterisation by developing new optical tools and integrating optics into existing nanoscale topological measurements. Metallic tips were investigated due to the widespread use of scanning probe microscopies (SPMs), such as AFM, and STM. The similarity in size between metallic nanostructures and the sub-wavelength-size apex of tips initially suggested that visible plasmons would be expected, enabling resonant near-field enhancement. Prior to any spectral characterisation studies to understand their near-field response, tips were applied in combined SPM-optical microscopes to achieve sub-wavelength localisation and enhancement of optical signals. As the next logical step from SERS and SNOM, the sharp apex of tips were exploited to develop the spin-off techniques of tip-enhanced Raman scattering (TERS) [90–93] and apertureless scanning near-field optical microscopy (a-SNOM)<sup>14</sup> [94–99]. These are also known collectively as tip-enhanced near-field optical microscopy (TENOM).<sup>15</sup>

The concept for TENOM was first proposed in 1985 [100] but it was not until 2000 that reports first emerged using tips to enhance Raman spectroscopy [90–93]. All measurements were carried out in inverted microscopes with either an AFM [90–92] or STM [93] mounted on top. Two of the initial measurements suggested a lower-limit Raman enhancement of  $\sim 10^4$  [90, 91], hence a field enhancement of around 10. A third independent measurement utilising evanescent wave excitation obtained a field enhancement of 80 [92]. Since then Raman enhancements in the region of  $10^7$ – $10^9$  have been measured [101].<sup>16</sup>

Whilst SERS enhancement factors have also increased significantly in recent years, the TENOM approach remains popular since the tip can be scanned across a sample. For this reason, techniques such as TERS are widely considered to become the successors of SERS. However, for this to be the case, the optical response of metallic nano-tips must be well understood and they require the capability to controllably and reproducibly enhance the near-field. Since the use of tips for observing fundamental plasmonics is also a central part of this project it is beneficial to understand the underlying concepts and mechanisms of TENOM.

<sup>14</sup>Also known as scattering scanning near-field optical microscopy (s-SNOM).

<sup>15</sup>These are also sometimes known as field-enhancing near-field optical microscopy (FENOM) since apertured techniques do not necessarily exploit plasmonic enhancement as much.

<sup>16</sup>A clear distinction is made between the field enhancement,  $|E/E_0|$ , and the Raman enhancement,  $|E/E_0|^4$ , when stating enhancement factors. In the literature the terms “field enhancement” or “enhancement factor” are generally used interchangeably between the magnitude of the near-field and the improvement in Raman scattering efficiency.

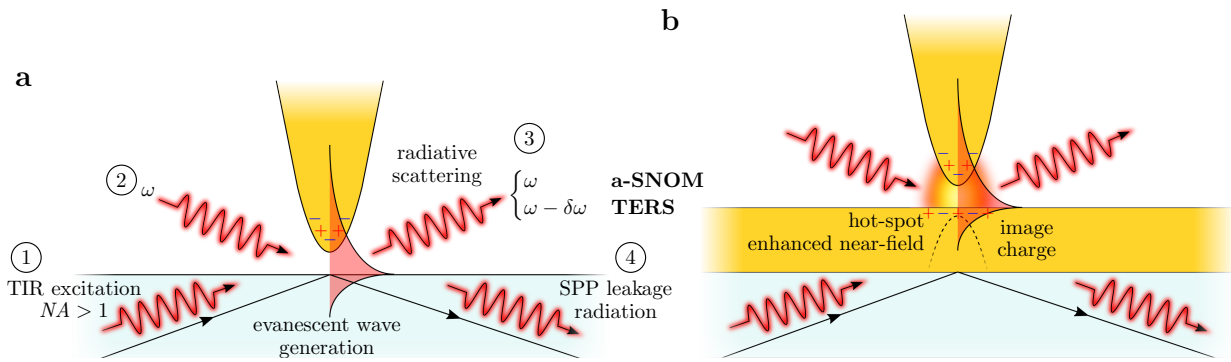


**Figure 2.18: Concepts of TENOM.** Basic TENOM systems constitute a tip and a sample (left). Tips can perturb evanescent surface waves, generated by high-NA TIR, and scatter them into the far-field (1 → 3) [102, 103]. Photons illuminating the tip can induce a weak dipole localised to the tip apex, which can scatter the near-field (2 → 3). More recent TENOM arrangements employ a metallic substrate to couple with the tip and further localise the field into a “hot spot” (right). Coupling of plasmons between the tip and the substrate can be achieved by exciting SPPs on the substrate using evanescent waves (1) or by focusing light onto the gap (2). Both mechanisms lead to scattering of light from the gap into the far-field (3). SPPs launched onto the planar metallic surface (either via the tip or evanescent waves) can radiatively decay into  $NA > 1$  (1, 2 → 4) [104].

Figure 2.18 shows the general approaches to TENOM. TENOM is ideally classified as a local excitation approach as opposed to a local scattering approach [105], though the two are not independent. In the tip scattering approach the non-radiative near-field, comprising evanescent waves, is perturbed by the presence of the tip, leading to scattering into radiative modes. In the tip excitation approach, the tip is resonantly excited to induce a large, local, near-field enhancement and used as a sub-diffraction-limited light source, from which localised scattering can be measured. This process can be much more efficient than the pure scattering approach but depends on the optical antenna properties of the tip. In both cases, the resolution of scattering images is sub-diffraction limited and set by the size of the tip radius ( $\sim 50$  nm).

To optimally exploit light scattering from nanoscopic tips, tip-based systems have been generally designed in either the side-illumination or bottom-illumination configuration (photon paths shown in Figure 2.18), setting the collection and, more importantly, the tip excitation geometry. Side-illumination has been used successfully in a number of cases [11, 103, 106, 107] but suffers generally from far-field scattering overshadowing the near-field. More complex optical techniques, such as using polarisation-resolved or interferometric approaches, are then required to overcome this. Bottom illumination, the more dominant design, utilises evanescent waves generated by  $NA > 1$  illumination undergoing total internal reflection (TIR). TIR results in minimal background scatter outside of the illumination aperture with only the near-field scatter collected. Collection is achieved using either the central  $NA < 1$  aperture of the high  $NA$  illumination objective [108–113] or a secondary low NA objective [114–116]. Whilst this does require that both the sample and any metallic substrate are optically trans-

missive, evanescent wave generation can excite SPPs in both a metallic substrate and the tip once brought within the near-field. For these reasons, it is important to consider the optical geometry when interpreting any presented TENOM results.

### 2.3.1 The Electromagnetic Response of Tips

The electromagnetic response of tips can be broken down into individual components that constitute the enhancement mechanism. The two main optical components are the lightning rod effect and a resonant plasmon contribution for metallic tips [117–119]. Each component is maximised when the incident field is along the tip axis [120]. The plasmonic component has been the focus of study in recent tip-based work, however progress in sharpening tips has also led to increases in the lightning rod component. Both components are important to consider when attempting to understand optical measurements involving tips.

Regardless of plasmonic behaviour, metallic tips intrinsically exhibit a lightning rod effect under the application of an applied field, instilling a non-resonant component of near-field enhancement. From the definition of the electric field  $\mathbf{E}(\mathbf{r}) = -\nabla\varphi(\mathbf{r})$  it is clear that its strength strongly depends on geometry, with field lines perpendicular to the equipotential conductor surface. The more curved a surface, the more compressed the field lines become around its equipotential surface due to the accumulation of surface charge.<sup>17</sup> A simple model, calculated by solving Laplace's equation for a tip-shaped electrode, shows this behaviour in Figure 2.19. Consequently, even without a plasmonic component, sharp tips provide a promising platform for localised near-field enhancement.

The expected plasmonic component also arises from the curvature of the metal-dielectric interface at the tip apex. Curvature allows for both SPP excitation and localisation at the apex due to adiabatic nanofocussing [37, 44, 121–124]. This can lead to plasmons appearing in the predicted spectra of tips, however none possess an antenna-like geometry to efficiently couple with light. Strong, antenna-like LSPs are unlikely to be excited at the apex of a sharp tip

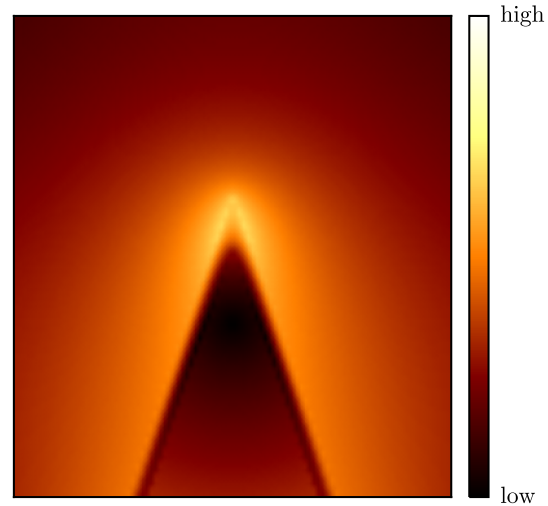


**Figure 2.19:** Calculated magnitude of the electric field around a tip showing the lightning rod effect. Compression of the field lines around the sharp corner of an equipotential surface leads to a localised, non-resonant field enhancement. Poisson's/Laplace's equation is solved for a tip structured electrode with a surface charge distribution separated by some distance from a planar metal counter electrode of the opposite surface charge.

<sup>17</sup>Since  $E \propto 1/r^2$  the electric field is larger in regions of smaller curvature.

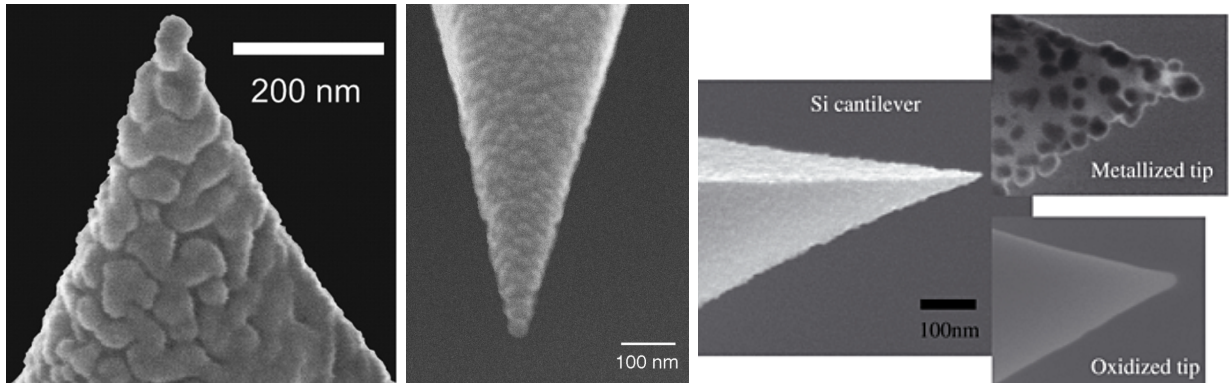


**Figure 2.20:** SEM images of metallised tips exhibiting random nanostructures. Images are taken from [112] (left), [116] (middle) and [134] (right). Each SEM shows randomised grains deposited using evaporation. These are thought to enable LSP excitation if located at the apex.

since lack of a second metal-dielectric interface prevents the formation of a pole of opposite charge to the apex. Thus, there can be no strong restoring forces or dipole moment. The extended size of the typical tip structure ( $\sim 20 \mu\text{m}$ ) prevents any potential low-order antenna-like plasmons from existing. Calculations for shorter, truncated, tip geometries (nanocones or nanoellipsoids) show visible-NIR LSPs [125, 126] as in nanopyramids [127, 128], however these redshift and diminish with increasing tip length<sup>18</sup>, leaving only the smooth response of the lightning rod effect, increasing towards the IR, for realistic tip shapes [118, 129].<sup>19</sup> The standard, sharp metallic tip geometry therefore makes for a poor *plasmonic* optical antenna unless any optically-dark SPP modes can be accessed.

Evanescence waves are capable of exciting some of these modes, with evidence for localised apex plasmons found through resonant scattering of evanescent waves [102, 103, 130], resonances in the TERS background [131, 132] and depolarised scattering images [112]. The addition of a degree of nanostructuring also allows for more localised plasmons [108, 112, 133, 134]. Spectral resonances between 600–800 nm, attributed to SPPs, have been observed in scattered evanescent waves from the surface of a prism by a Au tip with a W tip giving a comparatively flat spectrum [102]. Shifts of  $\sim 75$ –100 nm have been observed between Ag and Au tips with a  $\text{Si}_3\text{N}_4$  underlying tip material, redshifting resonances by  $\sim 30$  nm compared with solid metallic tips [103, 130]. This dependence on both the tip metal and underlying material has been highlighted numerous times due to the prevalence of the two dominant tip geometries of sharply etched metal tips and metallised (metal-coated) non-metallic tips.

<sup>18</sup>LSPs are supported only when a nanostructure is smaller than the wavelength of light, allowing light to drive in-phase collective oscillations of conduction electrons. Phase retardation occurs in larger nanostructures and higher order LSP modes dominate. In nanostructures larger than the focus, the case for almost all standard SPM tips, collective oscillations are no longer possible, leaving only weak LSPs at point of curvature and SPPs which disappear as the nanostructure size is increased due to growing losses [118].

<sup>19</sup>The apparent sharpness of the apex increases with wavelength as the field becomes larger relative to the apex curvature. Thus the lightning rod effect is greater at longer wavelengths [118].

Surface roughness imparted onto metallised tips by the coating procedure is likely to introduce localised plasmonic components which light can couple to, mimicking small 10–50 nm MNPs [112]. Similar behaviour has been used to explain the origin of SERS in rough metal films [1, 2]. Each grain acts as a point at which photons couple and plasmons radiate, hence a grain located at the apex can plasmonically enhance and scatter the near-field. This behaviour is of importance in metallised dielectric tips coated using evaporation<sup>20</sup> [108, 112, 134] or chemical reactions [133], some examples of which are shown in Figure 2.20. Even with the frequent application of TENOM, there have been very few spectral measurements of scattering from tips from which to better understand tip plasmonics. Optimum tip parameters, such as coating thickness, for maximum field enhancement are still being debated and characterisation of performance is still carried out using TERS [135].

### Coupling with Metallic Substrates

An alternative strategy for maximising the field enhancement is to couple tips with a planar metallic substrate and form a plasmonic MIM cavity to better localise light, as in Figure 2.18b [44, 114, 116, 132, 136–138]. In this instance, a weakly-excited dipole in the tip can induce an image dipole in the metallic surface to form a more strongly-confined coupled mode in the gap. Specifically, pairing a Au tip with a Au substrate greatly enhances the field localisation and strength, more so than when paired with a Pt surface [136] or a non-metallic surface [139]. This is attributed to better optical polarisability of the Au substrate. In these cases the Raman enhancement has been shown to rise to  $\sim 10^6$ – $10^9$  [116]. Coupling can be achieved by either exciting the tip dipole or through SPP excitation on the underlying metallic substrate [114, 116]. Unlike the coupling between MNP plasmons, theory suggests that the coupling between a Au tip and a Au surface only minimally shifts the gap resonance ( $\Delta\lambda \sim 10$  nm), likely due to the reduced dipole moments in tips [139].

One final tip-based plasmon excitation mechanism of interest within the scope of current work is electrical excitation. Similar to the use of EELS in electron microscopy, tunnelling electrons can be used to excite plasmons in an STM geometry. Electrical excitation circumvents some of the limitations of the single wavelength excitation as electrons need only to have sufficient energy  $eV$  that a portion transferred to the conduction electrons is enough to excite plasmons with frequencies  $\hbar\omega \leq eV$ . Light emission via electrical excitation is also background-free since there is no illumination source. Using tunnelling current excitation, light has been observed from both the tip-substrate gap [131, 132] and the interface between the metal substrate and its underlying dielectric [104]. Broad resonances, which redshift with decreasing tip-substrate separation, are found superimposed onto TERS spectra when operating in an STM configuration [131, 132]. Light detected from metal-glass interfaces is leakage

<sup>20</sup>Evaporation conditions used to roughly nanostructure a tip are similar to when depositing metal islands.

radiation from SPPs on the metal-air interface. Since light cannot leak from SPPs at the metal-air interface, these emission must be scattering from MIM gap plasmons between the tip apex and the surface. It is thought that 95% of the emission is due to SPP excitation rather than LSP excitation [104].

### 2.3.2 Challenges associated with Tip Plasmonics

Since the first measurements of tip enhancements and plasmons, techniques such as TERS and a-SNOM have become widespread. However, they are not currently reliable enough to be considered as a standard technique. Difficulty controlling the tip near-field is both a result of the irreproducibility of the tip geometry and a lack of understanding of the optical processes governing the enhancement, leading to large variations between reported field enhancements and TERS contrasts. A selection of these, reported between 2000 and 2011, are shown in Figure 2.21, showing the variability of TERS. The current challenges with TENOM are therefore improving the reproducibility of the near-field enhancement between tips [112, 113, 140] and achieving a better understanding of the tips themselves [118].

Factors determining the efficiency of TENOM include experimental excitation/collection geometry, tip sharpness, surface metal morphology, material influences and tip/apex orientation. From Figure 2.21 it is clear that sharper STM tips result in larger field enhancements than metallised AFM tips and comparative studies have shown similar trends [109, 141, 142]. Intuition suggests that the lightning rod effect must play a significant role in the near-field enhancement process. Theory showing drastic increases in the lightning rod effect after only small increases in sharpness (20 nm to 10 nm) gives some evidence towards this [118, 135], potentially explaining the varying measured field enhancements over time and between experiments. However, sharpness-induced enhancements can only be improved to a point as recent theory indicates the existence of a quantum limit set by nonlocal effects [143].<sup>21</sup> Understanding how to optimise the plasmonic component in tips is therefore a priority.

Materials choice, as with much of plasmonics, heavily influences any plasmonic behaviour. Ag tips generally outperform Au tips under visible light, although these claims highly depend on the underlying tip material and metal morphology. Only the metal and its morphology are important in solid STM tips and thickly metallised AFM tips, where plasmon energies are insensitive to any potential underlying materials. On thinly coated (< 40 nm) AFM tips, plasmons are tuned by the metal film thickness [129] and the refractive index of the underlying tip material. Tuning can vary drastically between materials such as Si, SiO<sub>2</sub>, and Si<sub>3</sub>N<sub>4</sub> [115, 142]. These high index materials can shift plasmon resonances into the infrared and out of resonance with the pump laser frequency. Careful consideration must therefore be given when

---

<sup>21</sup>Field enhancement saturates as the potential around any finer structural imperfections becomes smoothed due to electron spill-out (non-locality).

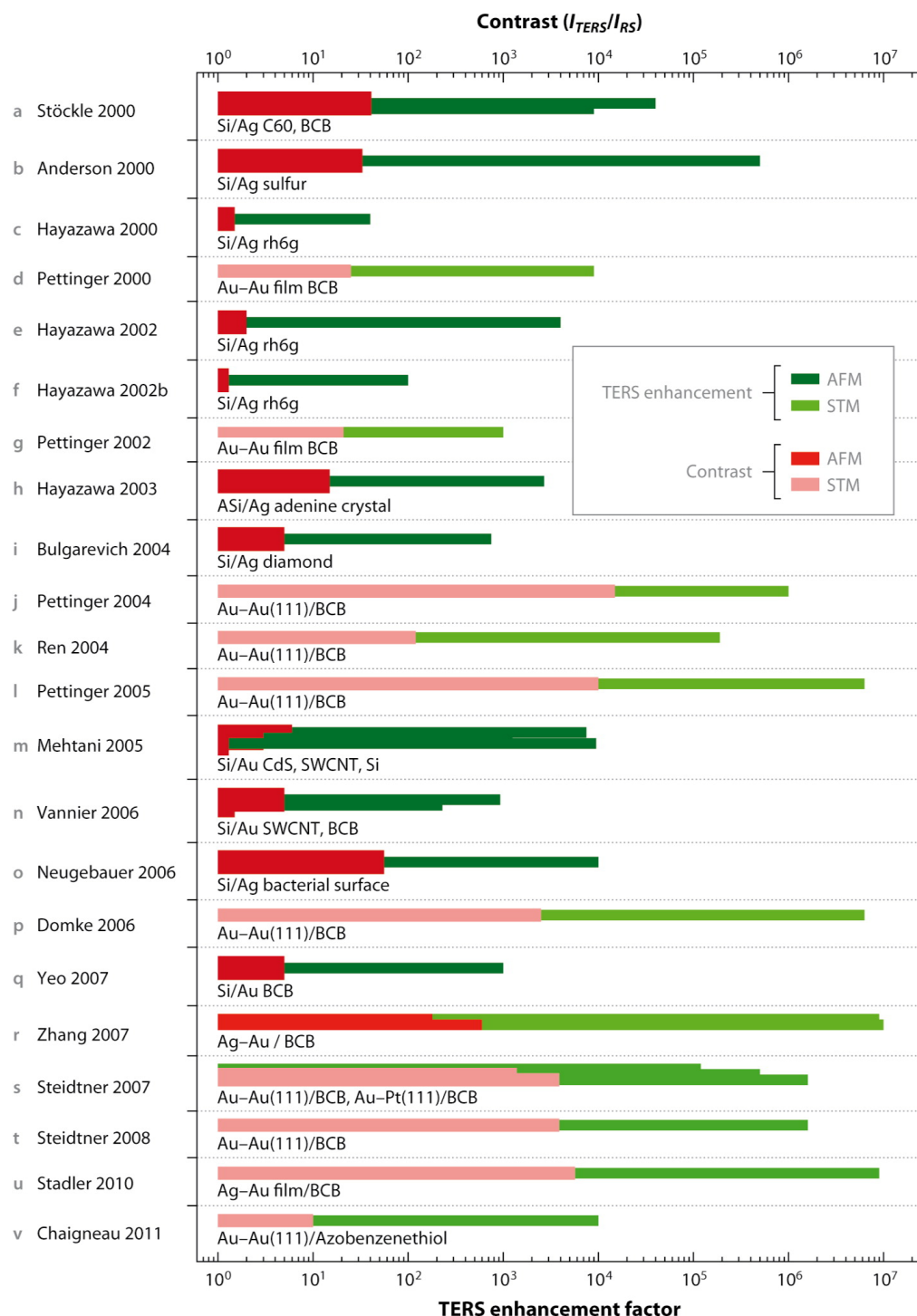


**Figure 2.21: Comparison of TERS field enhancements and contrasts reported between 2000 and 2011 [101].** STM tips, likely due to their increased sharpness, outperform AFM tips. Ag tips outperform Au tips. Larger enhancements are observed in systems where there is an underlying thin, noble metallic film. Statistical correlations still remain somewhat weak, showing the current variability in TERS experiments, attributed to the irreproducibility of enhancing tips.

pairing a tip with a laser [109, 110, 134, 144].

A large amount of variability stems from surface metal morphology. Reliance on randomised apex geometries, as shown in Figure 2.20, for LSP excitation greatly limits reproducibility. Furthermore, this granularity is rarely taken into theoretical account when attempting to explain TENOM. The orientation of the tip, along with the roughened apex, with respect to the sample and the incident excitation field is also known to influence near-field enhancement [109, 112].

Finally, variability between similar measurements can stem simply from differences in tip placement, optical setup, whether coupled with a mirror, and the specific illumination/collection geometry or optics used. As tips are rarely characterised there is little traceability between measurements from which to systematically determine the relevant causes for difference. It is highly likely, however, that geometrical limitations are the current dominating limitation restricting the progress of TENOM, leading to research into new tip geometries with better optimised, well-known optical responses.

### 2.3.3 Tip Modification, Nanostructuring and Optical Antenna Tips

The mode mismatch caused by the size difference between diffraction-limited light and the nanometre scale results in a 3–4 order of magnitude coupling efficiency loss [123]. As described previously, a LSP can act as an optical antenna with the ability to effectively modify the local density of electromagnetic states. In this way, freely propagating, far-field optical radiation can be efficiently converted into localised near-field evanescent modes and vice versa [9, 105]. Evidence suggests that sharp metallic tips, in their standard form, are not particularly good optical antennae, with most modes unresponsive to radiative fields. To improve their coupling efficiency, standard sharp tips have been modified or nanostructured to introduce the necessary plasmon states [145]. Whilst previously achieved by roughening the metal surface, more reliable and reproducible methods have been developed in recent years to controllably nanostructure the tip and engineer the optical response.

Gratings imprinted onto the side of tips can transform the apex into a nanoscale, single wavelength light source as SPPs excited on the grating propagate to the apex and re-radiate on 10 nm length scales [146, 147].<sup>22</sup> Far-field illumination remains spatially separated from the apex, suppressing background scatter and allowing only near-field scattering from the apex to be measured, producing background-free TERS signals [37, 123].

Nanostructuring of the tip apex has been investigated in order to engineer and tune an optical antenna precisely at the apex. Tips are structured with distinct, sub-wavelength-sized metallic features in order to create the necessary antenna-like LSPs to enable far-field excitation in the visible region of the EM spectrum. Etching [148, 149], focussed ion beam (FIB)

---

<sup>22</sup>Single wavelength operation results from adiabatic nanofocussing of only a single  $\lambda = 800$  nm mode.

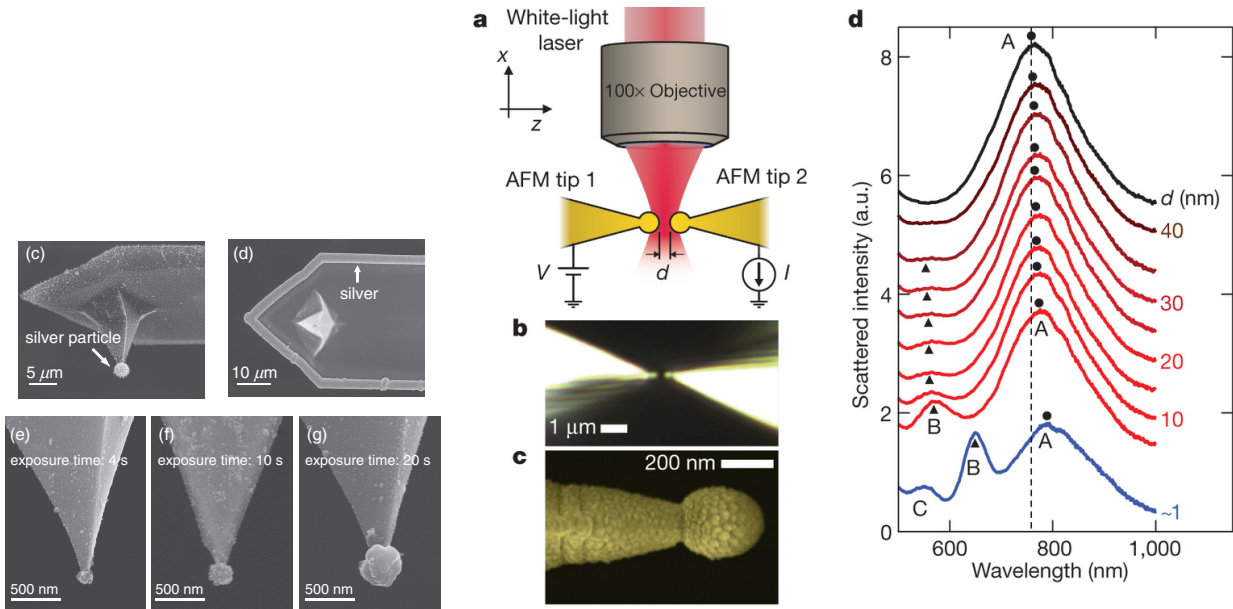


**Figure 2.22: Examples of spherical tip fabrication and surface plasmon resonances.** (left) Photochemically fabricated AgNP-on-Si tips for TERS [156]. Field enhancement is increased  $\sim 20\times$  compared with sharp Ag tips when using 488 nm illumination with a 1.4 NA objective in an inverted microscope. (right) Experimental evidence of LSPs in 50 nm Au-coated, 150 nm radius spherical AFM probes (NanoTools B150) [14]. The large radius minimises sensitivity to axial tip-tip alignment, increases scattered signal levels, and supports higher-order plasmonic cavity modes in the visible spectrum. Resonances are excited using a supercontinuum laser source in a side-illumination configuration. Separation-dependent coupling between two spherical tips confirms plasmonic behaviour.

machining [150–152], selective deposition [153], MNP pickup [154], and nanostructure grafting [155] have all been successfully used to nanostructure optical antenna tips, though each process is complex and time consuming. Scattering resonances in the visible-NIR spectrum have been directly measured on a subset of these [152, 153] while other reports use improvements in the field enhancement as a measurement of antenna quality [149, 155, 156]. In such cases the field enhancement can be improved by an order of magnitude through LSP excitation [150, 151, 156].

Lack of a strong plasmonic contribution from sharp Au metallised tips to TENOM is further evident from direct comparison with Au nano-tip probes. A Si tip with the apex replaced by a Au nanocone outperforms a standard Au AFM tip by 120% in the side illumination geometry [155]. Similarly, cutting the Au coating off past the apex also enables LSPs [153]. Each of these modifications is carried out using FIB machining and is therefore highly controllable, though costly in time and resources.

The simplest geometry to impart onto a tip apex is a sub-wavelength metal sphere. By doing so the tip gains LSPs similar to those in an isolated spherical MNP. The specific modes depend on the sphere material and geometry along with the attachment method since the base

tip structure determines the local adjacent dielectric medium. Coupled plasmons between two spherical Au tips have been previously observed in the far-field [14], but no characterisation has yet been done. Additionally, a  $20\times$  increase in field enhancement and improved spatial resolution has been measured when using a photochemically-fabricated AgNP-on-Si tip compared with a sharp Ag tip [156]. These demonstrate that spherical metallic tips have the potential to improve TENOM if they can be fully understood.

To date there are very few reported methods of simply nanostructuring a tip without the need for FIB, electron microscopy or complex chemistry, justifying the study of how to produce good plasmonic tips. A simple approach for chemically producing plasmonic tips is explored and developed, specifically targeting the spherical tip apex geometry. Other than their successful application in TERS and fundamental plasmonics studies, the origin of LSPs in spherical tips has not yet been fully investigated. Very little work has been done to reliably produce, characterise and understand the optics of spherically nanostructured tips. Furthermore, there is still additional work needed to similarly investigate the optical response of sharp tips, comparing them directly with nanostructured tips in both fundamental studies and near-field enhancement applications.

## 2.4 Conclusions

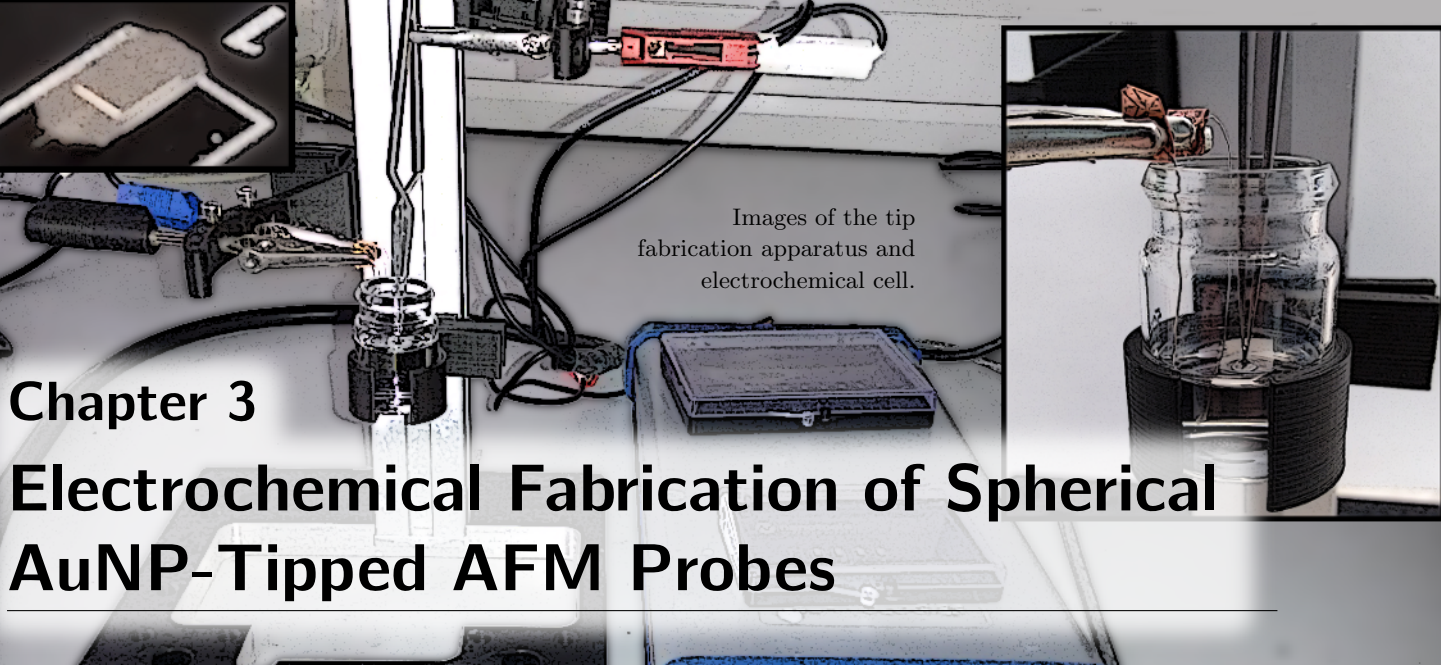
The coupling of plasmons in metallic nanostructures is now widely exploited in order to enhance and confine optical fields on nanometric scales. In order to maximise enhancement, the characteristic scales of these gap structures are rapidly approaching the sub-nm level where quantum mechanics can no longer be ignored. As recent results have shown, charge transfer in such small gaps can lead to the emergence of new plasmonic phenomena and a break down of classical field confinement. This regime must therefore be well understood if the characteristic size of plasmonic devices are to continue decreasing.

The effects of electron tunnelling and charge transfer in sub-nm plasmonic gaps have only been touched upon in recent years and still require significant investigation. To this extent, tips whose plasmons readily couple with light provide a useful platform for dynamically studying the fundamental plasmonics of nanogaps. Their well-developed experimental geometries for topological measurements form the basis of microscopes integrating optics and tip-based surface techniques. By using such a setup, quantum effects in coupled plasmonic systems can be further investigated by controllably reducing a gap into the sub-nm regime.

To date there have been no direct correlated measurements between plasmon resonances and quantum transport effects. Tunnelling has been inferred from direct measurements of plasmon resonances without electronic measurements [14, 82] and from variables influenced by the gap field enhancement, which in some cases provide electronic measurements [79, 83,

84, 86]. The effects of quantum charge transport can be better understood with correlated electrical and force measurements. By using an experimental geometry related to AFM these measurements become possible.





## Chapter 3

# Electrochemical Fabrication of Spherical AuNP-Tipped AFM Probes

As discussed in the previous chapter, nanostructuring a tip can create the necessary geometry and electromagnetic interfaces to support antenna-like plasmons. This enables coupling with far-field light and can improve the plasmonic performance of such tips. Consequently, this also means that excited plasmons scatter into the far-field and are therefore experimentally observable. This is a crucial property when using tips to measure fundamental plasmonics. Because of this, one of the major aims of this project is to produce robust nanostructured, plasmonic tips. The spherical geometry is targeted for its simplicity.

Fabrication of spherical tips has previously been achieved by mounting single nanoparticles onto the apices of tips. This concept has been reported numerous times over the last decade [157], beginning with the use of fibres as mounting structures [158–161] and progressing onto the use of SPM tips [134, 156, 162–164]. Whilst mounting nanoparticles onto SPM tips is more difficult than with fibres the additional capabilities of the SPM tip have made such tips desirable. However, these tips typically require complicated assembly processes to precisely secure a single nanoparticle at the apex of the tip, greatly increasing their fabrication time and costs. More recent methods have attempted to address the complexity issue by directly depositing nanoparticles onto the apex by exploiting localised chemical reactions. Nevertheless, these techniques have still been limited by cost or required specialist equipment [160, 163], incompatible with SPM probes [149, 159] or subject to limitations in nanoparticle growth, either in size [165] or material [156]. Non-metallic spherical tips on AFM probes have been created using methods such as vacuum-processing diamond-like carbon growth (NanoTools B-series). These nano-tips can then be made plasmonic through evaporation of a metallic coating. Even in recent years it still remains a challenge to simply and efficiently produce spherically nanostructured tips.

Electrochemical deposition is highly suited to the tip geometry because of the large d.c. field enhancement localised at the sharp apex point. Due to its significantly reduced radius of curvature, the equipotential surface resulting from an applied voltage leads to the compression of field lines at the tip apex. This strongly increases the field amplitude in the vicinity of

the tip apex and is known as the lightning rod effect. Under such conditions the rate of electrochemical reactions is significantly increased around the tip apex. By exploiting this localised field enhancement it is possible to grow a spherical MNP directly onto the tip apex. Whilst use of the lightning rod effect for electrochemical growth has been used to grow dense forests of MNP [166, 167] it has yet to be applied to the fabrication of single MNPs at a tip's apex.

Selective growth of MNPs onto the apices of tips is difficult using traditional methods of electrochemical deposition but can instead be achieved by using single-pulse, high-field electrochemical growth. This chapter describes the process of pulsed electrodeposition for apex-selective nucleation and growth of AuNP AFM tips. The process of electrochemistry is first described followed by discussion of the method by which spherical AuNP-tipped AFM probes are produced.

## 3.1 Electrochemical Deposition

Electrochemistry is defined as the study and application of chemical reactions occurring on the surface of an electrode that are either caused by or generate an electrical current. Electrochemical growth, or electrodeposition, is a method for depositing a solid material from solution. In general, this requires two electrically connected electrodes, submerged in an ionic solution (electrolyte), with a potential difference. Depending on the electrode potential, and how it compares with the energy required to activate a specific chemical reaction between ionic species, ions are either removed or created at the electrode-electrolyte interface through the addition or removal of electrons, respectively. Connecting electrodes allows excess electrons donated at the anode to transfer and fill the electron deficit at the cathode. An electrochemical cell reaction is therefore split into two half-reactions - electron capture and electron generation. These reactions are known as *oxidation* and *reduction*, which combine to form an overall *redox* reaction. Oxidation occurs at the anode whilst reduction occurs at the cathode. The current flow between electrodes at a given potential therefore measures the underlying reaction rate while electrode potentials set the possible redox reactions. Thus, electrochemistry is a powerful technique, containing an in-built method of directly monitoring the state of the chemical process.

Each oxidation and reduction reaction has an associated standard potential,  $E^\circ$ , characterising the potential required to add or remove an electron from the chemical species. Chemical species with highly negative standard potentials can readily donate electrons and are known as reducing agents. Chemical species with highly positive standard potentials are more likely to be reduced and are therefore known as oxidising agents. In general, having  $E^\circ < 0$  means the chemical species is highly likely to dissociate into ions, while  $E^\circ > 0$  means a chemical

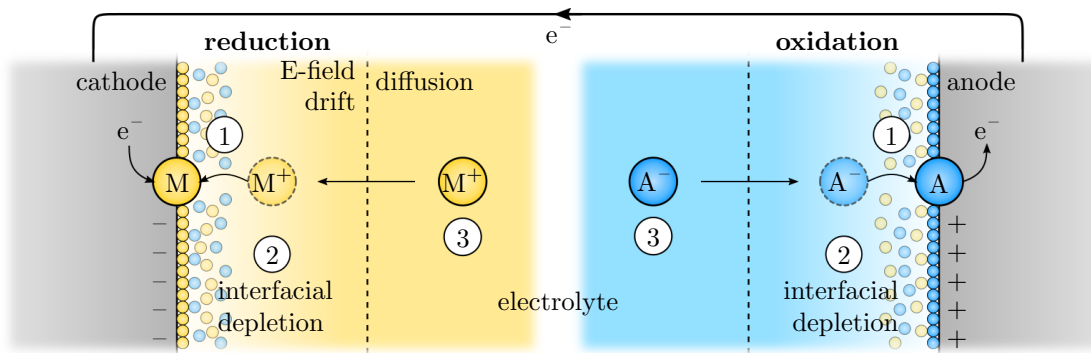


**Figure 3.1: Diagram of the electrodeposition process over time.** Two electrodes are submerged in an ionic solution. Depending on the potential, ions can either be oxidised or reduced at each electrode interface, generating a current between electrodes. Metallic ions initially at the interface are reduced on short time scales (1). Nearby ions drift to the surface following the field lines. Each charged electrode attracts a diffuse layer of unreacted, oppositely charged ions, partially screening the local field. Depletion of ions in the vicinity of the surface (2) creates a concentration gradient. Further growth is limited by mass transport (mainly diffusion) (3).

species is more likely to be found in a charge neutral or lesser charged state. Electrons move to equilibrate an in-built potential set by the difference between standard potentials at each electrode,  $V_{\text{cell}} = E_{\text{ox}}^{\circ} - E_{\text{red}}^{\circ}$ , and the resulting current can be used to power an external load.<sup>1</sup> This is the origin of the battery effect.

Electrodeposition is an opposite effect caused by either applying a voltage across a cell containing metal ions (standard electrodeposition) or by using a reducing agent (electroless deposition) [168]. If both half-potentials are overcome a redox reaction is activated. Metal ions from the solution are reduced onto the cathode surface, via a half-reaction,



in which  $n$  electrons are reacted with an  $n$ -oxidation state metal ion as a complimentary oxidation occurs at the anode. This is the basis of electroplating. Only electrode-based electrodeposition is discussed here in the context of electrodepositing onto tips.

A potential difference,  $V_{\text{cell}} = E_{\text{ox}}^{\circ} - E_{\text{red}}^{\circ}$ , needs to be applied to correctly bias the cell to overcome the activation energies of half-reactions at each electrode. Metallic ions situated at or near the cathode interface are then reduced whilst electrolyte ions on the anode surface oxidise. The rate of these reactions is set by a number factors, including the rate of charge transfer, nucleation and crystallisation [168]. This is the point at which reduced ions form adatoms on the surface after charge transfer and must either join with other adatoms to form a critically

<sup>1</sup>Consider a battery constructed of a Zn cathode and Cu anode in a  $\text{Cu}_2\text{O}/\text{Zn}_2\text{O}$  electrolyte and connected via a salt bridge. The half-reactions are  $\text{Cu}^{2+} + 2e^{-} \longrightarrow \text{Cu}$  ( $E^{\circ} = 0.339$  V) and  $\text{Zn} \longrightarrow \text{Zn}^{2+} + 2e^{-}$  ( $E^{\circ} = -0.76$  V) with an overall reaction  $\text{Zn} + \text{Cu}^{2+} \longrightarrow \text{Cu} + \text{Zn}^{2+}$ . The potential of this reaction is  $\phi_{\text{Cu}} - \phi_{\text{Zn}} = 1.099$  V.

stable nucleus, crystallise into a specific growth morphology or find an energetically favourable growth location. Excess surface charge accumulated at the electrode surface (unreacted metal ions from the solution and dissociated cathode ions) attracts a more diffuse layer of oppositely charged ions. This is known as the *electrical double layer* and partially screens the local potential, reducing the externally observed field and slowing down the rate of reaction [169].

After the initial surface reactions the rate of reaction becomes influenced by mass transport - the arrival of either ions or electrons at each electrode interface. The rate of ion movement towards the interface can be categorised into three types of mass transport: diffusion, migration and convection. The electric field and electrophoretic mobility determines the migration (drift) current whereas local ion concentration sets the diffusion flow. Convection occurs if there is a thermal gradient in the cell. The main effects considered in this work as the dominant mass transport mechanisms are diffusion and migration. During mass transport, nearby ions follow a trajectory to the electrode surface set by the field lines of the cell potentials and the concentration gradients pointing to locations of high electrochemical activity and local ion depletion. The extent of the ion depletion region around a growth is known as its diffusion zone and becomes important when two expanding diffusion zones overlap. Under these situations mass transport becomes divided between two competing growth sites, stunting growth. The overall rate of an electrochemical reaction (its rate determining step) will be limited by whichever of the previously discussed effects is slowest since each process occurs in series.

Electrodeposition is often described in terms of an *overpotential*,  $\eta = E_{\text{applied}} - E^{\circ}$ , that is the difference between the in-built potential of an electrolytic solution and the applied potential across it. In this case,  $E^{\circ}$  is defined for the reduction of a metal ion onto an electrode of the same metal. Deposition of this metal will only occur once the applied potential is more negative than  $E^{\circ}$ , i.e.  $\eta < 0$ . This describes the potential at which enough adatoms form critically stable nuclei on the metal surface. The more negative the overpotential the faster charge transfer, nucleation and drift will occur and therefore the faster the reaction will occur. However, favourable interactions mean that some metals deposit easier onto electrodes made of other materials. Reduced adatoms are able to find energetically favourable locations to grow without the need to form critical nuclei. In this case, deposition can begin even if  $\eta > 0$ . This is known as *underpotential* deposition and is useful to consider if a slow, controlled growth is desired.

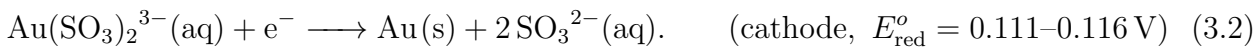
### 3.1.1 Experimental Electrodeposition of Au

Electrodeposition is the process used to fabrication spherical Au AFM tips by exploiting the sharp profile of the tip apex. The dynamics of deposition depend heavily on the potential (electric field), the exposure time, the electrode/cell geometry and the solution. In experimental electrochemistry, a potentiostat is used to apply or measure a controlled potential

between two electrodes and the solution whilst also measuring the current through the cell. A reference electrode with a well-known potential is used to determine the individual potential of the working (active) electrode relative to the solution. The most fundamental reference electrode is the standard hydrogen electrode (SHE) since the dissociated of hydrogen is defined as  $E^\circ = 0 \text{ V}$  [168], however, due to its complex setup, many other alternatives exist, including the saturated calomel electrode and the Ag/AgCl electrode. Potentials referenced using these other electrodes are often quoted relative to a SHE using the known reference potential. In the simplest of cells, reference electrodes can be in principle ignored and the counter electrode is used as a potential reference point.

Au can be deposited using one of the many available precursor solutions. A simple precursor is  $\text{AuCl}_3$  but it is not particularly widely used. A large number of solutions are cyanide based (e.g.  $\text{AuCN}$ ), which pose significant health risks. Sulphite-based solutions ( $\text{Au}(\text{SO}_3)_2^{3-}$ ) on the other hand are less hazardous at the cost of deposition quality. One of the most widely used sulphite-based Au precursors is the commercial ECF60 solution from Metalor. A smooth quality of the deposition morphology is typically achieved by slowly depositing at low potentials and using additives, such as brightener, to achieve smoother coatings [170]. However, when depositing nanostructures, additives are not necessary since the amount of Au deposited is typically very small. Additionally, ECF60 is water soluble [171], simplifying dilution for control over the Au ion concentration.

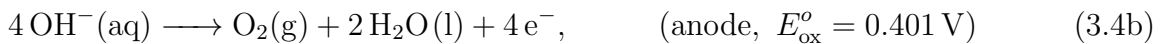
Since the actual composition of ECF60 is proprietary it's exact redox reaction is unknown. Known information includes it being a sulphite-based Au precursor consisting of 0.05 M Au and 0.24 M  $\text{Na}_2\text{SO}_3$  at a pH of 9.5 [171]. The expected reduction reaction for a sulphite-based Au precursor is [172],



The redox reaction is expected to be satisfied by oxidation of the  $\text{SO}_3^{2-}$  species, however complementary water splitting reactions are also expected at higher potentials. Two sets of half-reactions for the water splitting are [173],



and,



both resulting in a redox reaction of  $2\text{H}_2\text{O(l)} \longrightarrow 2\text{H}_2\text{(g)} + \text{O}_2\text{(g)}$ . The standard potential of Eq. 3.3a is  $E_{\text{ox}}^{\circ} = -1.23\text{ V}$  ( $E_{\text{red}}^{\circ} = 1.23\text{ V}$  for Eq. 3.4a). In general, both these reactions occur simultaneously with a build up of  $\text{H}^+$  at the anode and a build up of  $\text{OH}^-$  at the cathode. Using this solution, significant growth occurs once  $V < -0.6\text{ V}$ , as has been experimentally determined, with an increase in the number of reactions once  $V < -1.23\text{ V}$ .

## 3.2 Initial Fabrication of Spherical AuNP-Tipped AFM Probes

Selective nucleation and growth of a single nanoparticle at the apex of an AFM tip requires using pulsed electrodeposition, a much less common method. The reason for this is that standard methods are designed to produce an even metallic coating rather than growth at a single point. For tips, growth must initially be completely field dependent, taking advantage of the lightning rod effect at the apex, but not over sufficient time that smoothing of the apex curvature takes place, reducing the apex field and diverting growth around the resultant neck. By applying a high potential in a short pulse all metallic surface ions are immediately reduced. Charge transfer in this domain can be considered instantaneous and nucleation readily takes place. Accumulation of surface charge therefore does not occur and thus the double layer never forms. Growth in this regime is limited only by mass transport.

A simple method is used to successfully demonstrate that a spherical AuNP can be electrochemically grown at the apex of a metallic AFM tip. Conductive coatings are required for the electrochemical reaction, therefore Au- and Pt-coated AFM tips are used (BudgetSensors

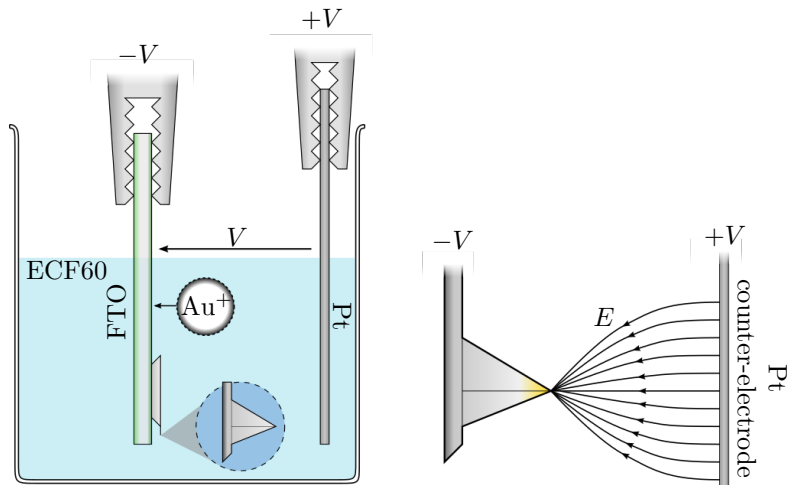


**Figure 3.2: Experiment geometry for pulsed electrochemical deposition of Au onto an AFM tip.** Electrochemical cell for growth of Au onto the apex of an AFM tip. Termination of field lines at tip apex due to the lightning rod effect enhances localised electrochemical growth for single NP growth.

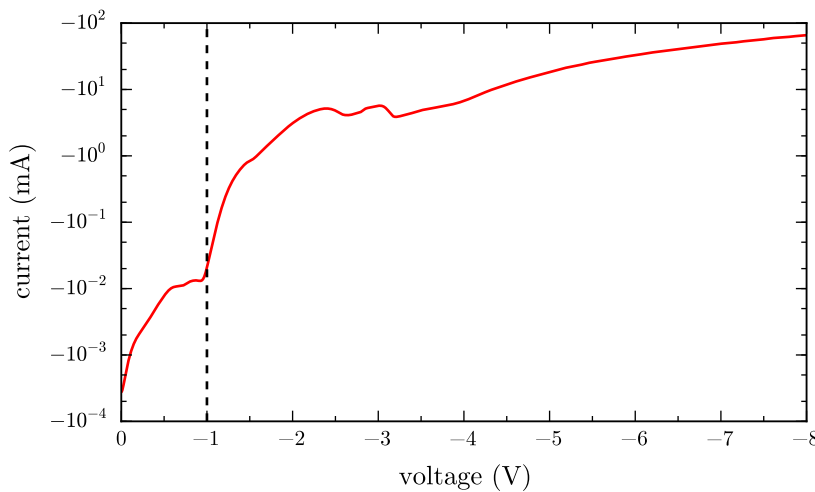


**Figure 3.3: Linear sweep voltammetry of a single AFM cantilever in ECF60.** The AFM probe is held by an Al clamp cathode out of solution, replacing the standard FTO electrode to show growth characteristics of only the tip. The remaining geometry is the same as in Figure 3.2.

GB/E series). The adhesion of molecular layers can prevent deposition of Au therefore tips must be cleaned thoroughly prior to deposition. Tips are pre-treated with 20 min O<sub>2</sub> plasma to remove organic contaminants from the surface prior to growth. A simplified two-electrode system (AutoLab PGSTAT 302N potentiostat) is employed for growth since both cell geometry and electrodeposition solution are kept the same between fabrications. AFM probes are attached to fluorine-doped tin oxide (FTO) conductive glass, used as a working electrode, opposite a Pt wire counter-electrode, spaced 10 mm apart (Figure 3.2). FTO glass is cleaned through sonication in 10 min steps using de-ionised (DI) water, ethanol and finally acetone. Metalor ECF60 is used as the electroplating solution with no additives. Simultaneous fabrication of both Au and Pt tips can be carried out by contacting multiple tips, closely spaced side-by-side on the same FTO surface.

Linear sweep voltammetry of a single AFM tip in ECF60 (Figure 3.3) shows that substantial Au growth starts at around -1 V. This is larger than what is usually expected in ECF60. Differences are attributed to the potentials being referenced to the counter electrode instead of the solution, thus increasing the required potential difference. Further increases in growth are attributed to the activation of water splitting reactions, confirmed by the generation of bubbles at each electrode at higher potentials. An increase from theoretical reduction potentials can also be caused by temperature which factors into the reaction thermodynamics [168]. The current inevitably becomes limited by mass transport causing the observed saturation at highly negative potentials.

A single high-voltage pulse is applied to nucleate and grow a single AuNP at the tip apex. Due to the large field amplitude at the tip apex, field lines from across the cell terminate at the apex, inducing ions to drift towards the tip apex prior to undergoing reduction (Figure 3.2b).

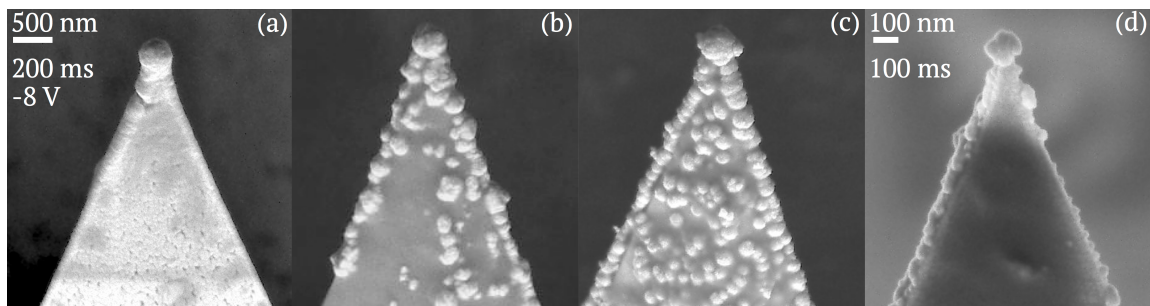


**Figure 3.4: Comparison of AuNP-tipped AFM probes, fabricated on various base structures using  $-8\text{ V}$  pulses of different lengths.** The first three tips were produced simultaneously using a 200 ms pulse on (a) a commercial Pt tip with no pre-treatment, (b) a plasma-treated Pt tip, (c) a plasma-treated Au tip. (d) Duplicate spherical tip produced separately on a plasma treated Pt tip using a 100 ms pulse.

Multiple combinations of applied voltage and pulse times are investigated to optimise growth parameters. Growth of Au onto the AFM tip is confirmed by current dynamics, revealing a 2–3 ms initiation followed by relaxation to continuous diffusion-limited growth within a few 10s of milliseconds. Scanning electron microscopy (SEM) imaging, carried out on a LEO GEMINI 1530VP FEG-SEM Scanning Electron Microscope, is used to characterise the resulting growth morphology.

SEM images of four tip samples fabricated at  $-8\text{ V}$  are shown in Figure 3.4, three of which were fabricated simultaneously on one FTO glass slide, to show the effects of tip pre-treatment and exposure time in the applied field. These images demonstrate that spherical AuNP tips can be reliably fabricated using the proposed electrodeposition procedure. AuNP growth diameters between 150–450 nm are achieved using 100–200 ms pulses across the electrochemical cell on both Pt and Au tips. Evidence of growth localisation to the high field regions is clearly exhibited by the formation of spherical AuNPs at the tip apex. The morphologies obtained differ with and without plasma pre-treatment. Using tips as supplied leads to a smooth sphere at the tip apex, resulting from the lightning rod effect, followed by a broad neck and semi-uniform Au coating across the exposed surfaces of the tip (Figure 3.4a). Plasma treatment removes organic contamination and can also oxidise the surface [174, 175]. Removal of contaminants prevents growth at defect sites. The formation of an insulating metal oxide layer prevents growth on surfaces, limiting growth only to sharp regions with a small radius of curvature (Figure 3.4b–d). These regions remain conductive and the electric field is large and highly localised. Because Au is more difficult to oxidise than Pt, the shielding effect is different for plasma-treated, Au-coated AFM probes, which exhibit significant localised nanoparticle growth on all exposed surfaces (Figure 3.4c). Longer pulse times result in bigger diameters of spherical AuNP, as shown in Figure 3.4b and Figure 3.4d. A 200 ms pulse leads to a spherical AuNP on the Pt tip with a diameter of  $\sim 450\text{ nm}$  (Figure 3.4b), while the diameter of the AuNP is 150 nm with a 100 ms pulse (Figure 3.4d).

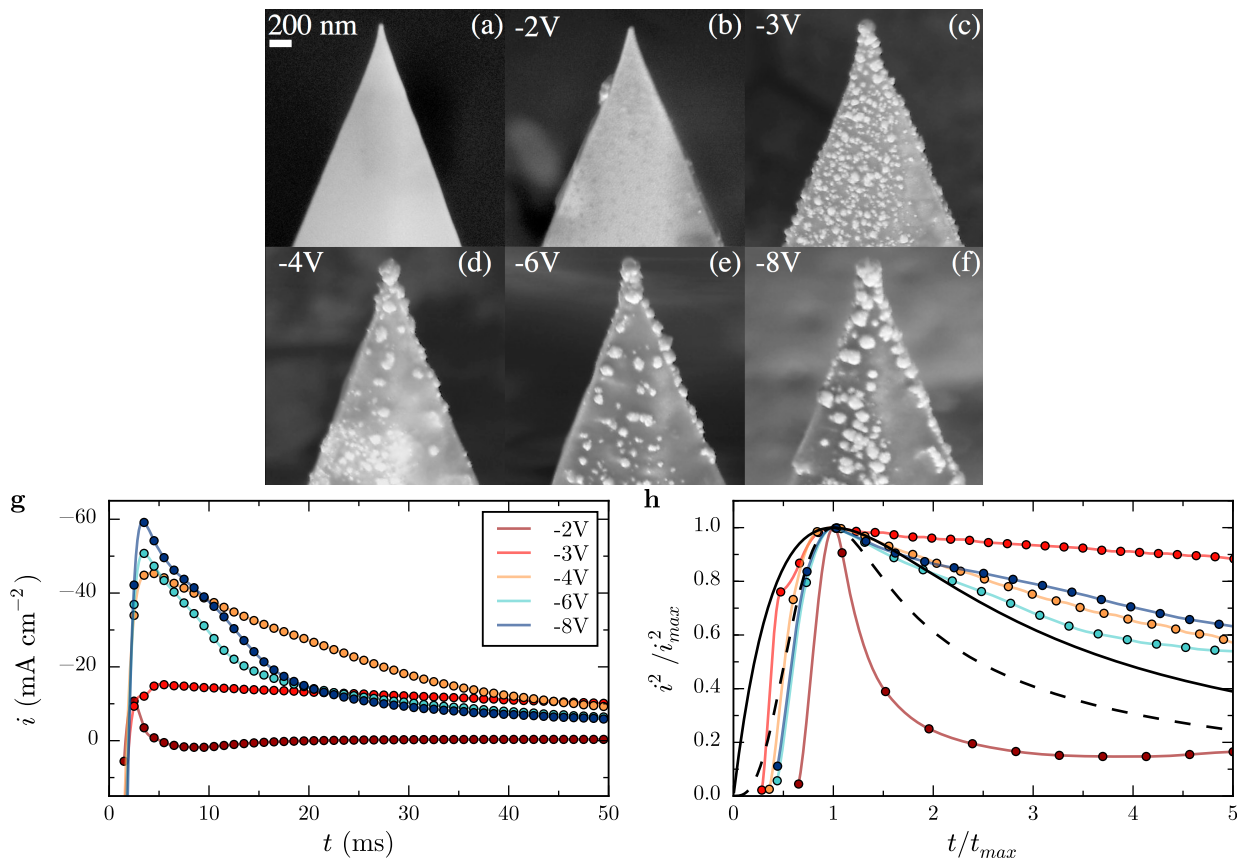


**Figure 3.5: Voltage dependence of pulsed electrodeposition onto Pt tips.** Comparison between a standard Pt AFM tip (a) and AuNP growth on plasma-treated Pt tips (b-f) using 150 ms pulses for voltages between  $-8$  and  $-3$  V and a 500 ms pulse at  $-2$  V. This shows the change in deposition mechanism as the magnitude of applied field strength is increased, with no spherical growths at voltages more positive than  $-3$  V irrespective of exposure time. (g) Current transients from current traces measured during fabrication of tips shown in (b-f), offset by the saturation current density ( $-10$ ,  $-31$ ,  $-34$ ,  $-78$ ,  $-142$   $\text{mA cm}^{-2}$ , respectively). (h) Variable-independent reduced current transients (coloured lines) measured at various applied voltages during fabrication compared with theoretical curves for progressive (dashed) and instantaneous (solid) nucleation current transients [176].

### 3.2.1 Dependence of Tip Morphology on Voltage and Underlying Nucleation Mechanisms

To investigate the dependence of fabricated tip morphology on the pulsed voltage across the electrochemical cell, the growth of AuNP on Pt tips at different applied voltages is further studied. SEM images of such fabrications along with corresponding current transients are shown in Figure 3.5. Images show that apex-selective growth occurs only once the voltage is more negative than  $-3$  V. This voltage dependence is attributed to changes in deposition mechanism with field strength. At low voltages ( $V \geq -2$  V), electrodeposition forms smooth film coatings (Figure 3.5b) similar to direct-current electrodeposition. Under these conditions

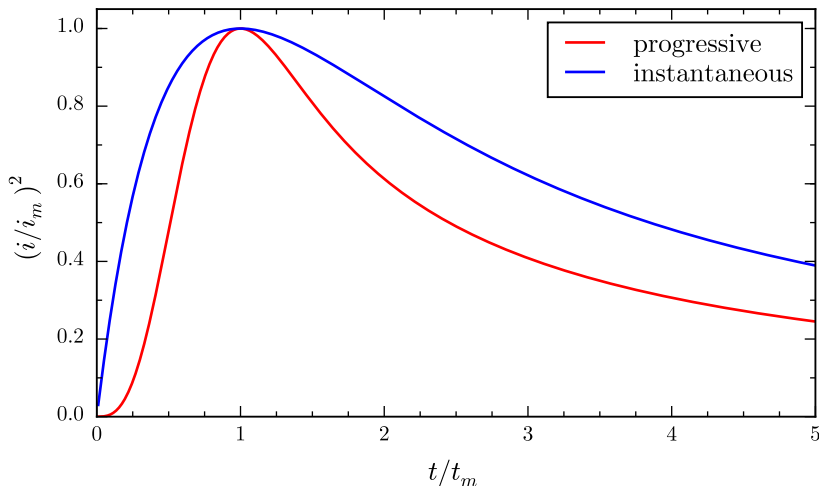


**Figure 3.6: Reduced current transients for the two extremes of nucleation as predicted by the Scharifker-Hills (SH) model [176].** The normalised current,  $(i/i_m)^2$ , is plotted as a function of time normalised to the maximum,  $t/t_m$ . Dashed lines show reduced transients from linear transitions between instantaneous nucleation, assuming instantaneous nucleation occurs first then decreases.

growth is dominant over nucleation and the field profile caused by the lightning rod effect is eventually evened out, yielding smooth rounded tips. Even with 500 ms exposure time no apex-selective growth is observed despite the charge transfer being equivalent to AuNP tip growths at more negative potentials.

The electrodeposition morphologies on tips fabricated at potentials more negative than  $-2\text{ V}$  can be roughly understood by considering that overpotential as the boundary for nucleation. Additional insight can be provided by further considering the most common nucleation mechanisms known from AuNP growth on planar electrodes [176]. These are progressive and instantaneous nucleation. During progressive nucleation, nuclei form at a time  $t$  then grow, increasing the size of the diffusion zone around them, thereby preventing further nucleation within that zone. At the end of progressive nucleation there are many nuclei of different sizes due to the different times at which they each originally nucleated. During instantaneous nucleation all nuclei are formed at  $t = t_0$  and then grow at the same rate until their diffusion zones overlap. The overlap of diffusion zones stunts growth as the finite ion flow is split between the two nuclei. For a sparse distribution of nuclei the end result is a set of equally sized particles. For more standard electrodeposition the current transients for progressive and instantaneous nucleation are given in the Scharifker and Hills (SH) model by,

$$\left(\frac{i}{i_{\max}}\right)^2 = \frac{1.2254}{t/t_{\max}} \left[1 - e^{-2.3367(t/t_{\max})^2}\right]^2, \quad (3.5)$$

and,

$$\left(\frac{i}{i_{\max}}\right)^2 = \frac{1.9542}{t/t_{\max}} \left[1 - e^{-1.2564(t/t_{\max})}\right]^2, \quad (3.6)$$

respectively, where  $t_{\max}$  is the time at which the current density maximises at  $i_{\max}$ . Usually the transition to instantaneous nucleation occurs after reducing the potential by only 0.2 V from the onset of progressive nucleation potential [177], however this behaviour has not been investigated on short time scales or at large, negative potentials where conditions are severely different and the assumptions used to develop the SH model break down.

Increased nucleation is observed at  $-3$  V where spherical tip growth is initiated under a progressive nucleation mechanism. Some preferential growth is exhibited at the tip apex but a strong diffusion boundary has not yet formed, as evidenced by the large number of nucleated particles and variation in particle size (Figure 3.5c). For more negative voltages ( $V \leq -4$  V) nucleation becomes more selective, leading to cleaner surfaces and improved apex localisation (Figure 3.5d-f). This is due to a transition to instantaneous nucleation, in which a fixed number of particles nucleate at selected active sites upon application of a field [178]. This occurs preferentially at sharp edges where the field is highest. Further selectivity may occur through depletion of ions in the vicinity of the growing tip, preventing additional growth sites. This helps to produce an isolated AuNP at the tip apex. Increasing the magnitude of the voltage increases the number of active sites available for nucleation and more of the tip surface surpasses the field threshold for instantaneous nucleation. Hence, using less negative voltages while still remaining in an instantaneous nucleation regime minimises the number of active nucleation sites, leading to cleaner spherical growth at the tip apex.

A changeover in nucleation mechanisms is also observed in current transients (Figure 3.5g)<sup>2</sup> as the shape distinctly changes when decreasing the voltage below  $-2$  V. The largest change in transient shape occurs at  $-3$  V, indicating the onset of shorter time-scale nucleation. Elongation of the transient time is likely caused by contribution to the current from progressive particle nucleation throughout the exposure. Much sharper, short time-scale current transients are observed for potentials more negative than  $-4$  V, supporting the hypothesis of an instantaneous nucleation mechanism since the fast current decay indicates the saturation of all active sites, leaving only diffusion-limited growth.

The influence of instantaneous nucleation for isolated AuNP tip growth is further evident in comparisons to theoretical (SH model) reduced current transients for diffusion-limited progressive and instantaneous nucleation (Figure 3.5h). Reduced current transients are normalised to  $(i/i_{\max})^2$  and plotted against  $t/t_{\max}$  to remove variable dependencies, where  $i_{\max}$  and  $t_{\max}$  represent the peak current and corresponding time. In general, for less negative deposition potentials ( $-2$  V), nucleation resembles more closely progressive nucleation and growth, while at more negative potentials ( $V < -4$  V) it resembles more closely instantaneous nucleation.

<sup>2</sup>Current measurements are interpolated to create a smooth line through data points. Transients are analysed by first making a quadratic interpolation of experimental data points before data reduction to extract the reduced current transients. This approach is used due to the limited number of points available in the peak region.

This correlates well with the SEM images shown in Figure 3.5d-f. Variations from theory occur due to the variable field profile present across the tip leading to localised instances of both progressive and instantaneous nucleation contributing to the overall current. It should be known that the SH model is built upon assumptions such as random nucleation and provides valid results only for the limiting cases of only progressive or instantaneous nucleation, for which the validity fails in such a selectively grown system [179].

A simple model can be developed from SEM images and current transients. Whilst the large surface area of the FTO glass likely dominates the behaviour of the current density, SEM images do indeed show localised changes in the morphology of the tip. When the apex of the tip has a field profile above the threshold for instantaneous nucleation, a single particle may nucleate at the apex and quickly grow. As it nucleates quicker than the rest of the tip its diffusion zone increases to prevent other particles nucleating nearby. This leads to a clean single AuNP growth at the tip apex. If the threshold for instantaneous nucleation is not met then many smaller particles form around the apex (Figure 3.5c). On the other hand if too much of the tip nucleates instantaneously (very large overpotentials) then the chance for a clean growth is also heavily reduced (Figure 3.5f) since many particles nucleate around the apex prior to the expansion of substantial diffusion zones. The choice of voltage is therefore imperative to ensuring selective growth of a single AuNP at the apex.

### 3.2.2 Decontamination of Tip Surfaces and Post-Fabrication Processing

After each batch of fabrications, tips are imaged using SEM to study surface morphology. Characterisation is necessary to determine the specific apex morphology but leads to contamination issues. Exposure to the electron beam is known to deposit layers of carbon onto samples. Despite washing tips in DI water and ethanol after deposition to remove any leftover chemical films, the surface of the tip inevitably contains carbon contamination after imaging. To ensure good electrical contact, AuNP tips must be cleaned before use. Although plasma cleaning is used to remove organics from the surface before fabrication it can oxidise the surface. Submerging tips in piranha solution ( $3\text{ H}_2\text{SO}_4 : 1\text{ H}_2\text{O}_2$ ) for 10 min proves to be an effective method for removing organics from the surface of the Au without introducing any adverse surface layers.<sup>3</sup> Though it can still oxidise or hydroxylate surfaces this is to a lesser extent compared to plasma treatment. Tips treated with piranha solution electrically contacted more often than tips left untreated after SEM imaging.

The activity of piranha solution degrades over time with some indication that small vol-

<sup>3</sup>Piranha solution is a strong oxidising agent and works via  $\text{H}_2\text{SO}_4$  quickly dehydrating organics.  $\text{H}_2\text{SO}_4$  and  $\text{H}_2\text{O}_2$  react to create oxygen radicals which oxidise the remaining carbon molecules into elemental carbon. The overall result is the decomposition of organic matter into carbon,  $\text{CO}_2$  and water.

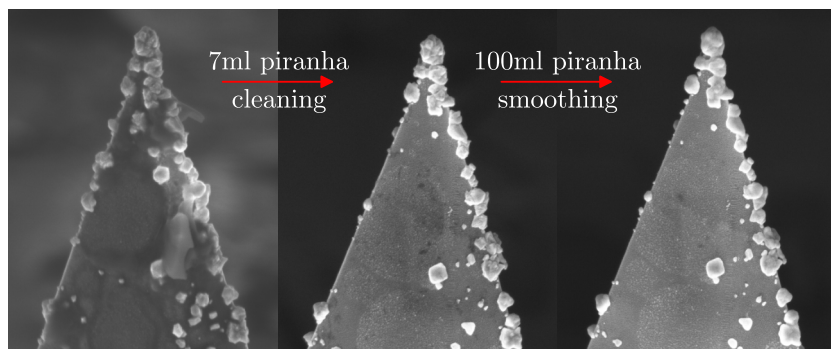


**Figure 3.7: Post-processing effects of piranha solution.** Low volume and temperature piranha solution removes organics from the Au surface while large volumes at 120 °C smooth the surface.

umes of the solution loses effectiveness after only 15 min. During its initial stages, the piranha reaction is extremely exothermic with temperatures reaching up to 120 °C. The overall temperature of the solution is determined by the volume of solution used. The heat generated in larger volumes takes longer to dissipate, maintaining a higher average solution temperature. The morphology of tips can be somewhat adjusted by exposing tips to piranha solution with varying temperatures and exposure times. Tips cleaned in small (5 ml) volumes show no changes in morphology whereas those treated in a large (100 ml) volumes are found to have smoothed surfaces (Figure 3.7). This effect is attributed to the increased solution temperature enabling surface atom rearrangement into more energetically favourable configurations. No comparison is made with other high-temperature solutions, such as boiling water, since the cleaning of tips is also desired. Should a fabrication fail, or their morphology damaged, Pt tips can be returned to their original state by using Au etching solution (Sigma standard Au etchant) to remove any deposited Au. This effectively reduces the effective cost per successfully nanostructured tip.

### 3.3 Conclusions

By using electrochemical deposition, the simple fabrication of spherical metallic tips has been successfully demonstrated. Tips can be fabricated within a short period of time and with high throughput using pulsed electrochemical deposition, exploiting the sharp tip geometry to nucleate and grow a single nanoparticle at the apex. Though simple and cheap compared with many other techniques, control of growth morphology quality still presents issues. The many free variables in the system are problematic for morphology control and are yet to be fully understood and optimised. As a result, there is currently little ability to predict the size and shape of nanoparticles. Nevertheless, the deposition process succeeded in its original purpose of providing spherical AuNP tips for plasmonic applications that can be electrically

contacted to measure charge transfer through a plasmonic nanogap.

Several advantages emerge from apex-selective single nanoparticle electrochemical growth. The capability for simultaneous nanoparticle growth on many tips ensures a high throughput process, while morphology and size is controlled by voltage and time. This provides a viable method for producing tips capable of expanding the user-base of plasmonics and furthering research into applications of TERS and SNOM. Furthermore, the spherical nanoparticle growth method introduced here is not restricted to specific metals, and many different composite systems can be created with this apex-localised growth technique. For example, silver nanoparticle tips could give a large optical response and field enhancement under visible illumination (although oxidation is sometimes an issue). This technique could therefore become a simple route to effectively improve TENOM across a broadband wavelength range.

## Chapter 4

# Microscope Design for Simultaneous Measurements on Plasmonic Tips

AFM tip experiments are performed in a custom-built microscope for optical spectroscopy with simultaneous force and electronic measurements. The microscope is fully automated<sup>1</sup> and capable of running a variety of experiments, primarily to study the optical response of tips. Its primary function is to take the tips of two opposing AFM probes, align them into a tip-to-tip dimer geometry and demonstrate nm-scale precision spatial control. Using such a setup, the plasmonic behaviour of both individual and coupled tip systems can be investigated. In this chapter the principles behind the operation and design considerations of the microscope system are discussed in depth, with sections split between the mechanical and optical design of the microscope followed by integration of the electronics and AFM module for force measurement.

## 4.1 Mechanical Design

To gain insight into the behaviour of realistic metallic nanostructures, along with any chemical treatments or potential ‘real world’ applications, requires experiments be carried out in ambient conditions. Measurement of the physical properties of two nanostructures on the sub-nm scale in ambient conditions is a difficult challenge. For a microscope to be able to perform such measurements requires many careful considerations, the result of which is a compact experimental platform resistant to both vibrations and thermal effects.

The most important parts of any microscope are the sample stage and objective lens. For stable optical measurements these have to be locked together and mechanically referenced in a symmetric configuration to prevent mechanical or thermal drift between the sample of interest and the focal spot of the source. The short mechanical reference distance in an inverted microscope design provides the best stability and the microscope platform (Figure 4.1) is designed based on this concept. Mechanical drift is minimised by maintaining a close reference

<sup>1</sup>A custom Python application used to control the microscope and all experiments

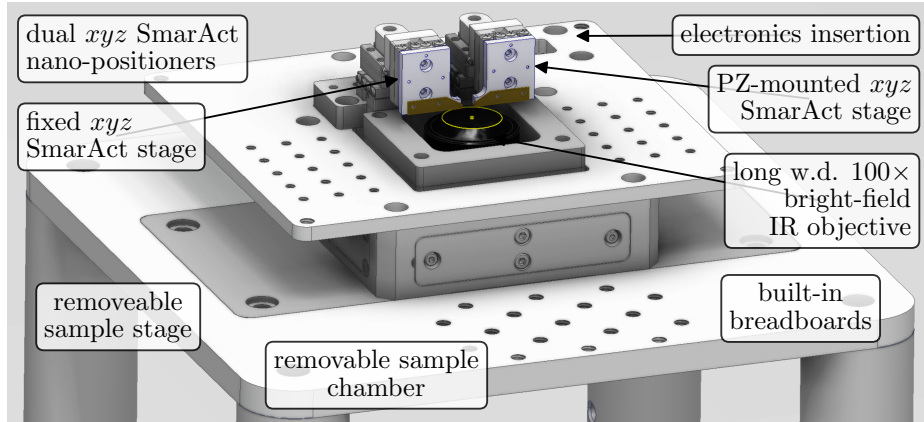


**Figure 4.1: Mechanical design of the microscope.** The main features of the inverted microscopy platform are highlighted, including two independent nanopositioners, one with piezo control, situated on a removable breadboard plate above the focus of an objective. Breadboard holes enable the mounting of optomechanics close to the sample. The top plate features a sealed lid with gas inlets for environmental control.

point between the sample and the objective. In this case the sample stage is tightly potted into a top plate from which the objective is screwed so that any vibrations between sample and objective occur in phase. Thermal drift is minimised by exploiting symmetry such that any expansion is around the objective and that all mechanical plates expand at the same rate. Cast aluminium is used for plate construction for its lower coefficient of thermal expansion compared to regular aluminium, whilst still remaining cheap and easily machinable compared to steel or titanium. The overall microscope platform is constructed 200 mm above the table on 1.5" diameter steel posts. The 200 mm height maintains stability without the need for cross-linking and is spacious enough to accommodate optics. The microscope platform and all important optics are mounted onto an anti-vibration stage to reduce vibrations. All optics are mounted in either cage or lens tube, held 5 mm off the table and locked together, for stability.

The typical experiment sample setup is shown in Figure 4.2a. Samples are mounted onto either of two 3-axis slip-stick translation stages with 12 mm of travel and fine piezo control (SmarAct GmbH, 2× SLC-1720-S with MCS), of which one is mounted onto a 3-axis piezo translation stage (PI GmbH, PI-733.3CD) for finer motion control. The top platform design is modular and easily removable, with a tight-fitting socket precise enough to relocate the sample stage to within 10  $\mu\text{m}$  after removal. Multiple adapters are used to mount different samples onto the stage. A cover slip holder is used for nanoparticle characterisation while AFM chip holders (Figure 4.2b) are designed to mount tips. AFM probe mounts are made from machinable glass-ceramic (MACOR, Corning inc.) in order to prevent thermal expansion (good coefficient of thermal expansion  $\alpha_{T,\text{MACOR}} = 9.3 \times 10^{-6} \text{ K}^{-1}$ , compared to other machinable materials'  $\alpha_{T,\text{aluminium}} = 23.1 \times 10^{-6} \text{ K}^{-1}$ ,  $\alpha_{T,\text{titanium}} = 8.6 \times 10^{-6} \text{ K}^{-1}$  or  $\alpha_{T,\text{ABS}} = 30.4 - 73.8 \times 10^{-6} \text{ K}^{-1}$  [173]) and to electrically insulate the mounts from the nanopositioners. The

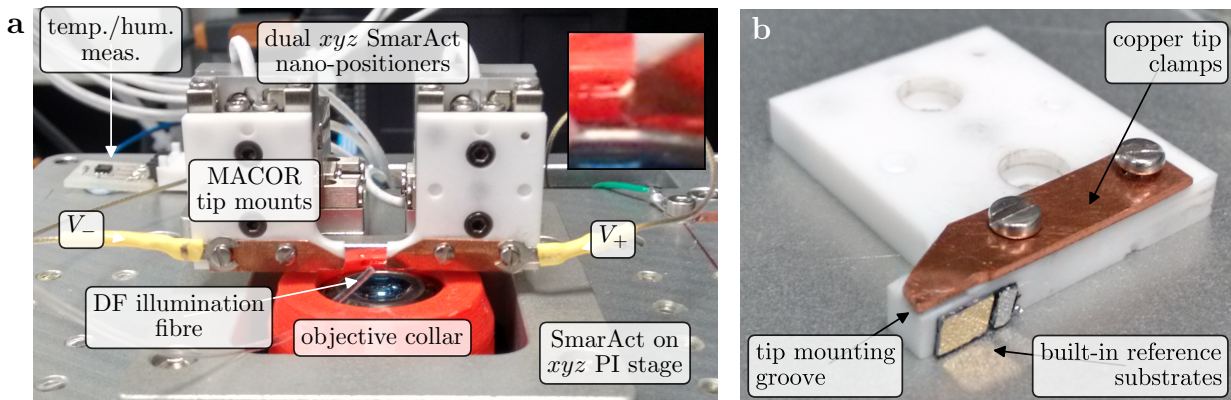


**Figure 4.2: Design of the dual tip microscope stage.** Images are annotated with the key design features incorporated into the sample stage. (a) Design of the dual tip mount stage and dark-field illumination mechanics. Each nanopositioner with tip mount clamp is connected to an external electronic circuit. A 3D-printed, plastic collar is attached to the objective, holding a 1 mm diameter optical fibre for dark-field side-illumination. A temperature and humidity sensor is attached to the back of the plate for environmental monitoring when the chamber is sealed. (b) Design of the tip mounts. Tips are placed in a rectangular groove in the insulating MACOR plate and held in place by an angled Cu clamp. Electrode solder tags are screwed down onto the clamp to electrically contact the tip. Mirror substrates are stuck onto the bottom of the mount to provide an easily accessible, in-situ spectral referencing point for incident illumination.

copper clamps holding the AFM probes are contacted to enable biasing of the junction between tips and measurement of the current through the junction.

The grounded experimental chamber is sealed to control the gas environment (switchable between a line containing air bubbled through water and a nitrogen line to control humidity) and act as a Faraday cage to reduce electromagnetic interference (EMI) incident on the sample. The chamber is equipped with a low pressure, one-way valve and a needle valve to control gas flow. Silencers are attached to the gas inlets with a foam surround to prevent air currents. The presence of a sealed chamber is enough to stabilise the sample against external air currents and help maintain a constant thermal equilibrium around the sample. A low magnification basic microscope, constructed from a small CCD, is attached to the roof of the chamber to aid alignment of samples with the objective focus. Metal contacts connect the roof to the grounded base to form the Faraday cage. Optical windows on the sides of the chamber are used to insert secondary lasers perpendicular to the objective axis, used primarily with the AFM module. They also allow for external monitoring of the stage positions from the side.

## 4.2 Optical Design

Dark-field (DF) spectroscopy is the primary optical method used to study plasmonic nanosstructures, in which samples are illuminated at high angles with reflections filtered to collect only low-angle scattering from the focal plane. This microscope employs two kinds of DF mi-

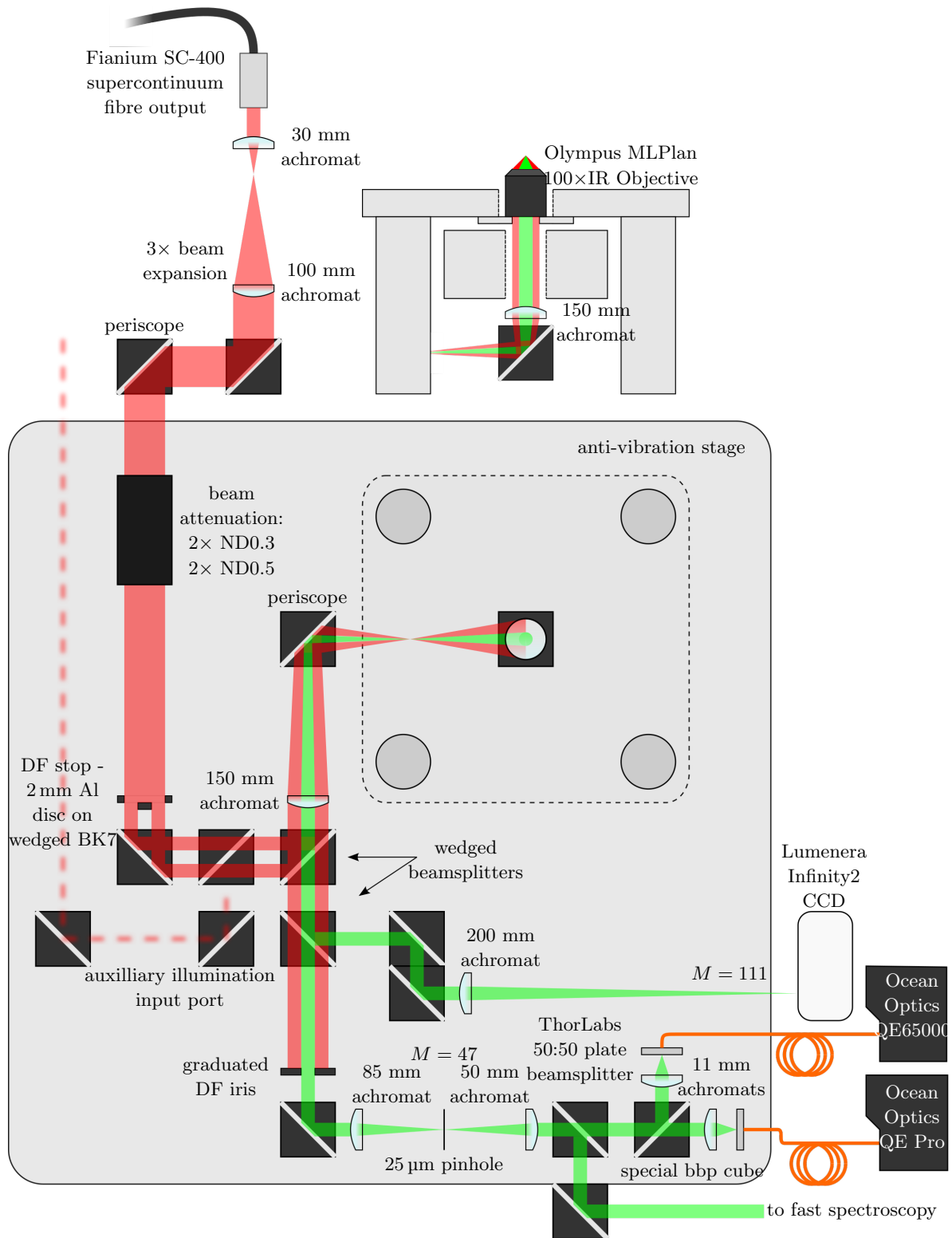


**Figure 4.3: Diagram of the full optical layout and specification of the microscope.**  
All optics are accounted for except for silver periscope mirrors, which transfer the beam between platforms of differing height.

croscopy - conventional DF imaging using a side-illumination fibre and supercontinuum (white light) laser DF spectroscopy.

The optical design employs the concept of reimaging spatial filters into the correct planes for efficient DF spectroscopy, leading to a compact design. Employing reimaging means that beams are not necessarily required to propagate exactly along the optical axis, minimising the number of long, empty beam lines, typically used for alignment. By reimaging the front and back focal planes of the objective, spatial and Fourier  $k$ -space filters are placed in the corresponding planes, ensuring optimum filtering performance and minimal aberration. A detailed schematic of the microscope platform and the surrounding optical bench layout, containing the specifications of all optics used, is found in Figure 4.3.

Both image and Fourier planes are set through careful placement of each set of lenses. The required minimum degrees of freedom for beam alignment are accounted for by mirrors placed in the focal and Fourier planes. Those in Fourier planes change the position of the beam without affecting its shape, whereas those placed in focal planes only change the beam shape without shifting the position in the objective focus.<sup>2</sup> The position and shape of the beam are therefore independently adjustable, greatly simplifying beam alignment. This advantageous technique results in a high beam quality, and, as a direct result of the lack of long, iris-containing beam lines, a compact microscope.

A long working distance objective is required for imaging and spectroscopy of tips. Additionally, a large numerical aperture (NA) is required to properly study nanostructures as it means light is collected across a large acceptance angle with a small focal length and large magnification. A bright-field (BF) long working distance IR objective (Olympus LMPlan 100 $\times$  IR, 0.8 NA) is used to access wavelengths above 700 nm, for which the more convenient DF VIS objectives (Olympus LMPlan 100 $\times$  BD) exhibit a sharp cutoff.<sup>3</sup> A DF illumination/collection configuration is necessary for imaging scattered light from a nanostructure. Since DF illumination is not supported on BF IR objectives, light needs to be brought in externally in a side-illumination geometry to image samples. A 3d-printed objective collar is used to hold a 1 mm diameter optical fibre  $\sim$ 1–2 mm from the sample, outside of the objective collection angle, to which a cold white LED is fibre coupled. The fibre is fed through a breadboard hole in the top plate and sealed so as to preserve the environmental chamber integrity. The fibre outputs a broad cone of light which illuminates samples over a large area.

Use of a ultra-high brightness supercontinuum laser source (Fianium SC-400, 4 W, 480–1750 nm) enables single nanostructure spectroscopy with exposure times around 10–50 ms. The beam is expanded to fill the back aperture of the objective and apertured into a ring to mimic DF illumination using a DF disc stop placed in a Fourier plane. The inner diameter of the ring is set at 2 mm and the outer diameter is set by the back aperture of the objective,

---

<sup>2</sup>Diagrams indicating the principles of beam alignment using reimaging are found in the appendices.

<sup>3</sup>A comparison of the two available 100 $\times$  objectives is found in the appendices.

in this case 3 mm. This technique is a pseudo-DF method denoted supercontinuum dark-field (SDF). To prevent laser damage to samples the incident power is heavily attenuated. Reflective neutral density filters totalling ND 1.6 (2.5% transmission) are placed in the beam line to reduce the initial incident power. The majority of the incident power is lost at the DF stop. Further attenuation results from the 10:90 (R:T) beamsplitter used to relay the laser into the microscope. At this point the total power integrated over the whole spectral range is reduced to 1 mW, as measured on a bolometer (Coherent, Inc.) behind the objective.<sup>4</sup> Whilst the power is seemingly low and comparable with high-brightness incoherent light sources, the focussing ability of the single mode laser results in an intense, diffraction-limited, white light focus not possible with incoherent sources. For an assumed broadband spot size around 1  $\mu\text{m}$  the focal intensity is  $\sim 10^5 \text{ W cm}^{-2}$ .

The incident light is apertured and reimaged directly onto the back focal (Fourier) plane of the objective, as opposed to aperturing close to the objective back aperture. This prevents diffractive artefacts in the conjugate plane of the collected light. The ring aperture means that the focus is illuminated only at high-NA as with conventional DF spectroscopy. Scattered light is then filtered by a DF iris placed in a Fourier plane in the return beam path to remove any signal contribution from reflected, high-NA illumination. Reimaging allows both the DF iris and stop to be located away from the objective for convenient access and easy adjustment. Alternative designs using optics mounted at the objective back aperture do not benefit from having the stop and iris in conjugate planes and may require motorised irises if not accessible by hand. For this experiment a simple graduated dark-field iris is sufficient for external use to filter the collected light signal.

Since incident power is not an issue, and in many cases requires significant attenuation, the microscope is optimised for efficient collection. The 10:90 beamsplitter used for laser input means only 10% of collected light is lost when returning back through the main microscope arm. Furthermore, all optics in the system are optimised for light between 500–1100 nm.<sup>5</sup> The angle-dependent Fresnel coefficients of the glass used in all optics components mean that *p*-polarised light is favoured during transmission throughout the microscope collection path.<sup>6</sup> A 90° turning periscope is placed after the first reimaging lens to reverse the linear polarisations of light so that the stronger *p*-polarisation component is orientated along the tip axis.

Subsequently, collected light is split into imaging and spectroscopy paths using a second (50:50) beamsplitter placed before the DF iris. CCD imaging is both used to align and characterise the laser focus and to centre samples onto the targeted laser illumination spot.

<sup>4</sup>Power characterisation found in the appendices.

<sup>5</sup>Broadband optimisation is achieved via exclusive use of Ag mirrors, Edmund Optics VIS-NIR AR coating on lenses, COMAR NIR and ThorLabs visible or visible-NIR coated beamsplitters.

<sup>6</sup>All beamsplitters have some degree of polarisation sensitivity due to Fresnel coefficients of the glass used. Reflectance can be a factor of 2 different between orthogonal linear polarisations. A comparison of polarisation-dependent reflectances is found in the appendices.

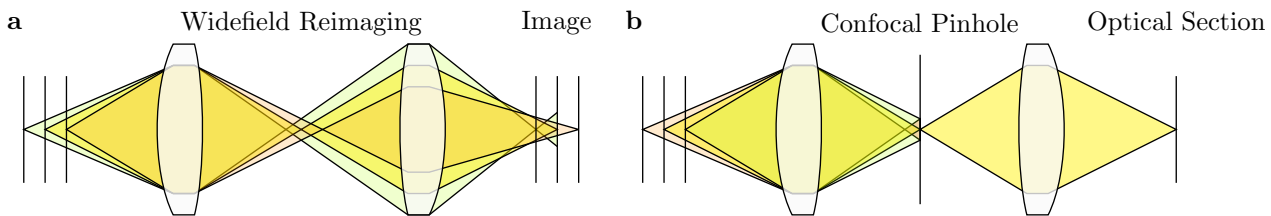


**Figure 4.4: Diagram of optical sectioning in confocal microscopy.** (a) Out of focus light from nearby focal planes leads to blurring and a decrease of resolution in images. (b) Images spatially filtered in the focal plane by a confocal pinhole localise light from only a select volume that is sufficiently focussed to pass through the pinhole aperture.

Sample imaging uses light collected from the scattered white side-illumination LED light to produce DF images whereas laser light is not DF-filtered in this path. Images are magnified  $111\times$ .<sup>7</sup> Light passing along the spectroscopy path is DF-filtered to remove any contributions to the scattering signal from reflected light. A graduated iris is used to remove the 2 mm outer-ring of the returning beam. The iris is placed in the image plane of the DF stop for the most accurate filtering and optimum performance. The two beamsplitters present before the DF iris are wedged to prevent ghost images, which transmit through the closed iris and create spectral artefacts. However, the 5 mm thickness of wedged beamsplitters means increased dispersion and the limited availability of broadband AR coatings results in reduced reflectance in the NIR. Additionally, the DF-filtering process only works to remove light reflected out at the same angle. Angled samples (such as the facets of tips) can reflect light into the low-NA collection, creating spectral artefacts. It is for this reason that the flat tip facets are even visible in a dark-field configuration.

#### 4.2.1 Confocal Localisation of Spectra

Since the laser focusses to a diffraction-limited spot on the sample, spectra are collected from a small sampling volume. This single mode input forms the first component of confocal localisation. Further spectral localisation is achieved by confocally filtering the image plane after the DF iris using a  $25\text{ }\mu\text{m}$  pinhole to collect light from only the central focal spot. Only light in focus on the pinhole may pass through it. By rejecting out of focus light the image becomes an optical section with a tighter depth of focus. The size of the pinhole sets both the lateral and axial width of the transmitted light and leads to both spatial masking and optical sectioning in the objective-sample plane, as shown in Figure 4.4. Spectra are therefore acquired from a localised sampling volume, as set by the location of the  $47\times$  demagnified pinhole image. The location of this spatial mask image in the objective focus is controlled by a mirror before the confocal filtering array. A slip-in small CCD is used to image the Fourier plane before and after confocal filtering to check pinhole alignment. Since the depth of focus

<sup>7</sup>Magnification is calculated by the ratio of focal lengths,  $M = f_2/f_1$ .

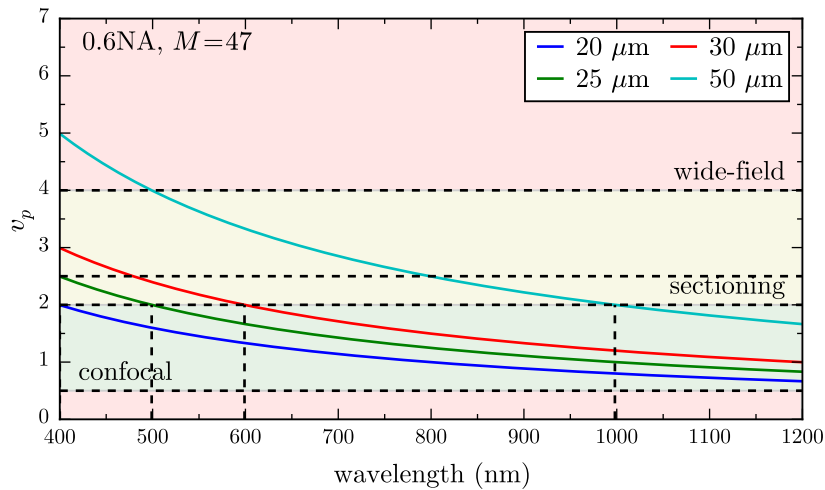


**Figure 4.5: Calculated optimum confocal pinhole size across the visible-NIR spectrum.** The detector width  $v_p$  determines the performance of confocal imaging, for which the characteristic detection regimes are highlighted. A 25  $\mu\text{m}$  pinhole is chosen for most experiments. Confocal performance is then achieved above 500 nm.

scales as  $M^2$  (or  $NA^2$ ) the placement of the pinhole along the beam path is not critical. Choice of pinhole diameter, however, is important.

Confocal filtering not only improves image contrast but also improves upon the wide-field, diffraction-limited resolution by up to a factor of  $\sqrt{2}$ , depending on pinhole diameter, at the cost of image brightness [180–183]. This stems from the removal of higher diffraction orders by the pinhole. The resolution of a microscope is often quantified using the Rayleigh criterion - the distance from the maximum of the point spread function (PSF) (expected to be an Airy function) to the first minimum [184]. A decrease in the Rayleigh criterion of diffraction-limited resolution is expected, going from  $r_{\text{lateral}} = 0.61\lambda/NA$  down to  $r_{\text{lateral}} = 0.44\lambda/NA$  at best. Decreasing the pinhole diameter therefore not only decreases the optical section thickness but also the minimum resolvable lateral distance to a certain extent.

For a realistic detector aperture the collection PSF is convoluted with its aperture function,  $D_p$ , giving an image PSF  $I = |h_1|^2(|h_2|^2 * D_p)$  [185]. The resulting resolution depends on a quantity  $v_p$ , the detector width, which can be related to the actual pinhole diameter,  $d_p$ , through [185],

$$v_p \geq \frac{\pi d_p NA}{M \lambda}. \quad (4.1)$$

The full-width half-maximum (FWHM) of the PSF retains the full,  $\sqrt{2}$  improvement if  $v_p \leq 0.5$ , but this leads to a significant loss in brightness. An increased resolution is still in effect until  $v_p \geq 4$ , at which point the wide-field behaviour is recovered. Practically,  $v_p \leq 2$  for optimal lateral resolution and  $v_p \leq 4$  for optimal depth resolution. Optimising for  $v_p = 2$  means that for a 0.6 NA,  $M = 47$  system (the spectroscopy collection geometry)  $d_p/\lambda \leq 43$ , i.e. 25  $\mu\text{m}$  at 500 nm and 55  $\mu\text{m}$  at 1100 nm. A plot of  $v_p$  across the visible-NIR spectrum for

a number of pinholes is shown in Figure 4.5, highlighting the relevant confocal regimes. For a given pinhole size that acts confocally in the visible, the intensity of some NIR wavelengths will be reduced since  $v_p$  drops below 1, however this loss is acceptable to maintain higher resolution in the visible region of the spectrum. A 25  $\mu\text{m}$  pinhole size is determined to be optimal in this microscope based on this analysis and the range of available pinhole sizes.

Once filtered only the spectral content of the beam is of interest rather than the image so strict adherence to conjugate planes is no longer necessary. The beam is split 50:50 into two signals, with one going to the benchtop spectrometers and the other to a fast spectroscopy path.<sup>8</sup> The benchtop spectroscopy signal is further split into linear *s* and *p* polarisation components using a broadband polarising beamsplitter cube (Melles-Griot 300–1100 nm). Broadband polarisers (Thorlabs 500–1500 nm) oriented along the *s* and *p* axes are placed at the cube output ports to increase the extinction. Each polarised signal component is then finally focussed into multi-mode fibres, using short focal length (11 mm) lenses to achieve a spot size smaller than the fibre core. 100  $\mu\text{m}$  fibre core is used instead of 50  $\mu\text{m}$  to reduce laser speckle in spectra since the confocal pinhole diameter already localises the signal. The spectral signal from each of the fibres is recorded using TE-cooled, benchtop spectrometers (Ocean Optics QE65000 and QE Pro) with integration times between 10–50 ms. The sensitivity of the Si detectors in the spectrometers drops off beyond 900 nm, imposing a limit to detectable signals of around 1100 nm. The supercontinuum laser imposes a 480 nm spectral short wavelength cut-off, resulting in an overall effective measurement window of 500–1100 nm.

Measured spectra are background-subtracted, to remove dark counts, and referenced to the spectral density of the supercontinuum illumination as transmitted through the microscope optics. Use of the intense supercontinuum source means low integration times below 20 ms are sufficient to near saturate the spectrometer for a high quality signal to noise. The high brightness of the supercontinuum laser at these exposures also means that the relative intensity contribution from external light sources is negligible. The coherence of the supercontinuum laser means that conventional referencing using scatter from a white diffuser to map the illumination spectral density is not possible. Instead, reflections from thin, reflective substrates attached underneath the piezo-mounted tip mount are used as a reference. Different substrates are used depending on the sample. For metallic samples the substrate is matched to the metal so only structural spectral features are observed. Otherwise either a Ag mirror or glass slide are sufficient for referencing as they provide relatively flat reflectances across the visible-NIR spectrum. The DF iris is kept fully open during reference acquisition to ensure the full spectral content of the incident beam is measured and to avoid introducing referencing artefacts. As optics are very rarely broadband between 500–1100 nm, all non-essential pathways are closed when acquiring spectra to prevent artefacts. Back reflections off lenses are

---

<sup>8</sup>The fast spectroscopy technique is developed and implemented but otherwise not used in any experiments in the current project. For this reason it's operation is omitted from this work.

found to superimpose a weak duplicate of the illumination spectrum onto spectra since the reflections are translated in  $k$ -space and are therefore not completely filtered by the DF iris.

### 4.2.2 Characterisation of Microscope Performance

During most experiments the power incident on samples is kept below 1 mW corresponding to a focal intensity of  $\sim 10^5 \text{ W cm}^{-2}$ . This is used to maintain sufficient signal quality whilst preventing damage or destructive changes to nanoscale Au samples (typically 50 nm Au coatings). Beam profiling, the study of the beam shape through the focal volume, is used to characterise beam propagation in the microscope and determine its ability to collect DF spectra. Profiling is carried out using focal scans of both light reflected from a Ag mirror and light scattered from an 80 nm AuNP, measured simultaneously on a CCD and a spectrometer. The CCD is used to laterally profile the beam through the focus while the spectrometer characterises the confocal profile and spectral distribution of the light. Both the illumination and collection pathways are profiled. The illumination pathway is profiled using the DF-filtered supercontinuum beam while one of the collection fibres is removed from its spectrometer and coupled to a 532 nm single mode laser in order to profile the collection pathway.

Figure 4.6 shows both the lateral focal spot on the CCD and relevant cross sections along the optical and focal axes for both the illumination and collection optics, along with depth-profiling using broadband-integrated spectra. Figure 4.6a shows the beam structure in the focus. The single mode fibre output exhibits the characteristic Airy profile expected of a Gaussian beam while the ring aperture of the supercontinuum beam leads to more power concentrated in the outer rings of the focal pattern (Figure 4.6b). The measured FWHM of the collection beam is  $(460 \pm 20) \text{ nm}$  with a beam waist ( $1/e$  width) of  $(540 \pm 20) \text{ nm}$ . The  $47\times$  demagnified image of the  $25 \mu\text{m}$  pinhole is expected to be  $530 \text{ nm}$ . The focal radius of a single mode Gaussian beam (the beam waist) is given by  $w_0 = \lambda/\pi NA$ , which results in a collection NA of  $0.62 \pm 0.02$ . Measurement of a Rayleigh criterion length of  $(530 \pm 20) \text{ nm}$  indicates the beam is focussed through  $0.61 \pm 0.02 \text{ NA}$ . Uncertainties on these calculations of the NA are small since the 532 nm wavelength is well known. Both calculations of the NA only partially agree due to beam focussing at the diffraction limit and both show a collection half-angle of  $(38.0 \pm 0.5)^\circ$ .

The axial cross section of beams (Figure 4.6c) shows the focussing of the high angle ( $0.64\text{--}0.8 \text{ NA}$ ,  $40\text{--}53^\circ$  incident angle) supercontinuum ring. The boundary between incident and collection beams is measured to be around 0.62 in both beam angle and spot size measurements since the DF iris diameter and the DF stop diameter are both set to 2 mm. The axial beam profile, however, measures the angle of light from the focus to below  $(21 \pm 1)^\circ$  ( $0.35 \text{ NA}$ ). This is likely caused by observation error due to the low intensities at high angles. After confocally filtering the depth of focus, as measured on the CCD beam profile, is on average  $4 \mu\text{m}$  across

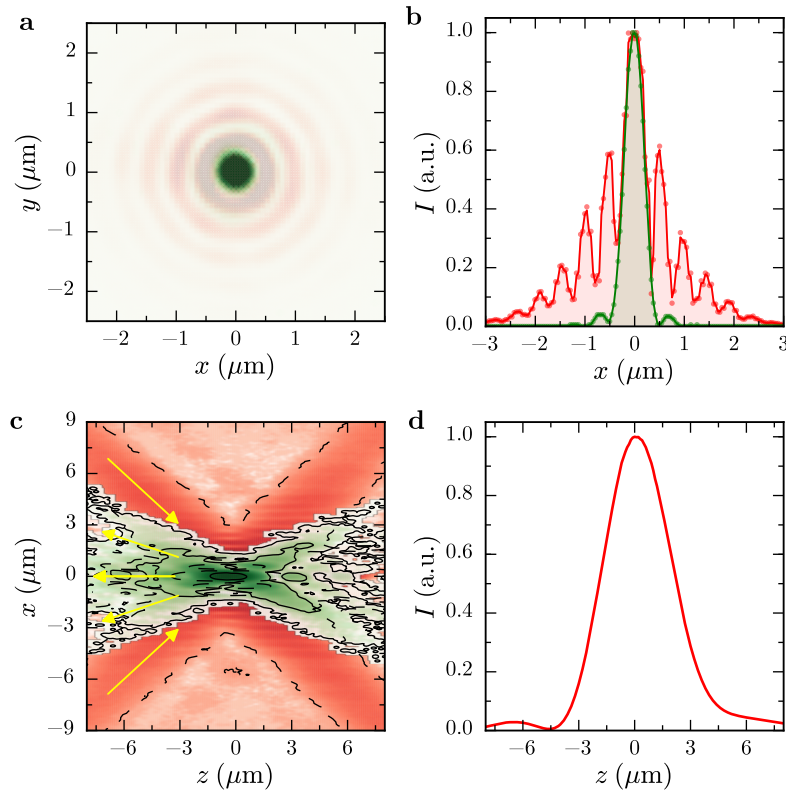


**Figure 4.6: Beam profiling of dark-field filtered supercontinuum illumination (red) and scattering collection (green) beam lines.** Supercontinuum laser light is reflected back from a Ag mirror in the objective focus to characterise the illumination pathway. The spectroscopy pathway is characterised by coupling a 532 nm laser into a single mode fibre and passing it through the collection optics with the DF-iris closed to 2 mm. The stated axial distance  $z$  is twice the displacement of the mirror to account for reflections to the focal plane. Lateral distances are calculated using the CCD array size and pixel dimensions. (a) Lateral beam profile of the illumination and collection focusses as measured on the CCD. (b) Intensity cross sections through the lateral beam profiles of the illumination and collection. (c) Axial cross section through the focus of illumination and collection beams. (d) Normalised summation of spectrometer counts of confocally localised supercontinuum light passing through the collection optics.

the supercontinuum wavelength range (Figure 4.6d).

Figure 4.7 shows the individual wavelength components that make up the integrated spectral signal in Figure 4.6d. As expected the depth of focus increases with wavelength. The depth varies from  $(2.8 \pm 0.1)$  μm at  $\lambda = 500$  nm to  $(6.4 \pm 0.1)$  μm at  $\lambda = 1100$  nm. The chromatic structure of the beam is non-linear and shows that the colour maxima for  $\lambda < 550$  nm and  $\lambda > 800$  nm occur slightly offset from the pinhole position. Overall this does not detract much from the measured spectra since intensity differences in the chosen focal plane are normalised with the reference spectrum.

Lateral localisation is more important to consider than axial sectioning. Scattered light from a sub-wavelength size nanoparticle provides a point source from which the PSF can be measured across a small, resonant bandwidth. By (raster-) scanning a strongly-scattering

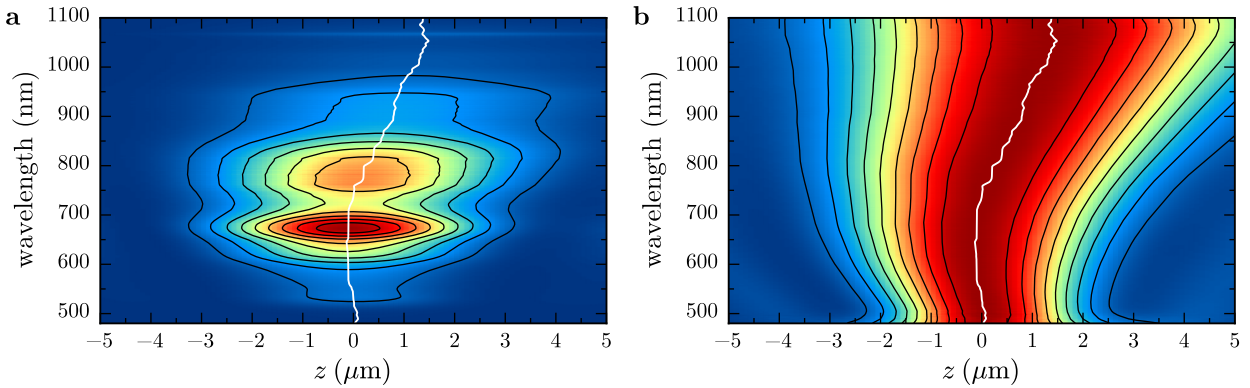


**Figure 4.7: Axial chromatic aberration at each wavelength through the objective focus.** The image in (a) is formed from spectra of the *s*-polarised component of a reflection from a Ag mirror scanned through the focus. An intensity plot normalised at each wavelength is shown in (b) to determine depth of focus. The white indicates the position of maximum signal along the optical axis for each wavelength and shows the distinctive bowing curve of chromatic aberration.

MNP under the beam its point scattering response is convoluted with the beam structure in the focus. The size of the confocal pinhole determines how much of this beam structure is laterally filtered prior to spectroscopy and thus, by measuring the scattering spectra, the actual PSF, as seen by the spectrometers, can be mapped across a broad range of wavelengths. It is this function that determines the specific locations from which spectra are collected and becomes particularly important when attempting to measure localised scattering from an extended nanostructure.

Figure 4.8 shows scattering profiles extracted from AuNP scans, demonstrating the effective spectral PSF for a range of pinhole diameters. 80 nm AuNPs on glass resonantly scatter at 550 nm due to excitation of the dipolar LSP. A single AuNP was chosen on which multiple scans were performed, changing and realigning the confocal pinhole in between each scan. Wavelength slices at the AuNP plasmon resonance (Figure 4.8a–c) show the effective lateral PSF. Without a pinhole in place the spectral PSF is a convolution of the focal beam profile shown in Figure 4.6a. The spectrometer sees the scattering from each of the concentric rings in the focus so localisation of spectral features to the beam centre cannot be guaranteed. Decreasing the pinhole diameter filters scattering from the focus and removes the contributions to spectra from the outer rings until spectra can only be acquired from the central spot. This guarantees localisation of observed spectral features to a finite-sized region. The FWHM of the scattering signals on resonance are  $(255 \pm 25)$  nm with the 25  $\mu\text{m}$  pinhole in place,  $(260 \pm 25)$  nm with the 50  $\mu\text{m}$  pinhole in place, and  $(300 \pm 25)$  nm without a pinhole. The FWHM at 900 nm for the case of the 25  $\mu\text{m}$  pinhole is 410 nm for reference. Due to the single AuNP being the only source of scattering in each of the scans the measured spectrum is the same for all pinholes (Figure 4.8e). Though the resolution is not improved by a great amount, use of the smaller pinhole does guarantee better spectral localisation, as seen by the presence

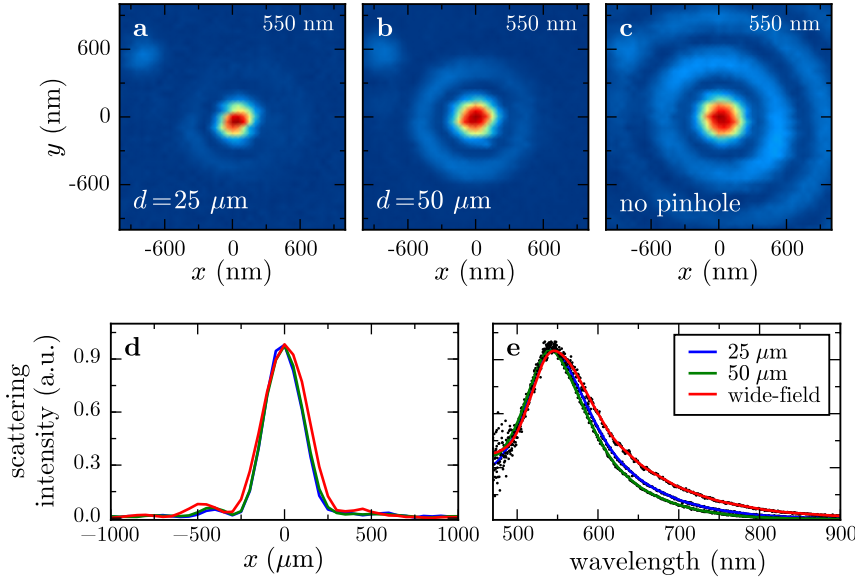


**Figure 4.8: Hyperspectral scans of a AuNP used to characterise the lateral PSF with different confocal pinhole diameters.** (a-c) Wavelength slices of AuNP scans on resonance using 25  $\mu\text{m}$  and 50  $\mu\text{m}$  diameter pinholes and finally no pinhole, respectively. (d) The extracted PSF from line profiles across images (a-c). (e) Spectra of imaged AuNPs at the scattering centroid location. Localisation is observed with reduced pinhole diameter as the concentric illumination rings are cut.

of only the central maximum in its PSF.

Fitting the centroid at every wavelength in the spectral data cube identifies lateral chromatic aberration in the microscope. This is an important parameter to consider when using hyperspectral imaging or when acquiring spectra. For example, if the chromatic aberration is systematic and fitted then a correction offset can be added to hyperspectral data cubes at each wavelength. Spectra from each pixel can then be further recombined into regular RGB images by integrating the spectra at each pixel with RGB pixel spectra.

Figure 4.9 shows the centroids of the PSFs across the plasmon resonance band for each pinhole diameter. Scattering centroids are extracted from each wavelength slice using discrete image moment analysis,

$$M_{ij} = \sum_x \sum_y x^i y^j I(x, y), \quad (4.2)$$

where  $i, j$  denote the moments of the  $x, y$  axes.<sup>9</sup> The position of maximum scattering is then given by,

$$(\bar{x}, \bar{y}) = \left( \frac{M_{10}}{M_{00}}, \frac{M_{01}}{M_{00}} \right). \quad (4.3)$$

<sup>9</sup>Note that the discrete image moments are based on the continuous moment theorem with moments given by

$$M_{ij} = \int_{-\infty}^{\infty} \int_{-\infty}^{\infty} x^i y^j f(x, y) dx dy.$$

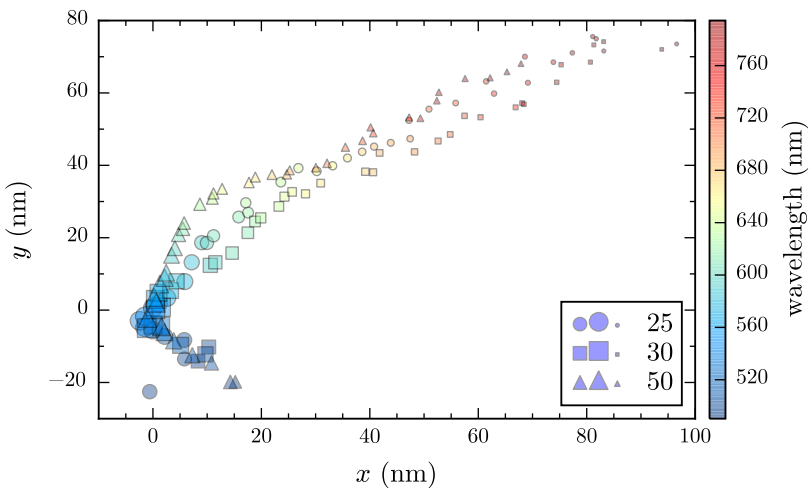


**Figure 4.9: Measurements of lateral chromatic aberration across the plasmon resonance scattering bandwidth of a hyperspectrally imaged AuNP.** The centroid position of the optical scattering is extracted from images at each wavelength. Changes in centroid position with wavelength signify chromatic aberration.

Displacements are scaled relative to the centroid position on resonance where the signal is highest. The centroid position drifts almost linearly by 80 nm in the  $x$ -direction and 80 nm in the  $y$ -direction. Since the pinhole only filters the outer rings of the PSF there is very little difference in the centroid positions between pinholes. As the range of centroid displacement in each direction is well below the diffraction limit and corresponds to only a few pixels offset in each image, the aberrations are not considered to negatively impact spectroscopy.

To summarise, a microscope platform has been designed to accommodate various sample geometries, specifically AFM tips. Single nanostructure spectroscopy is enabled by utilising an ultra-high brightness supercontinuum laser in a dark-field optical geometry, capable of measuring spectra between 500–1100 nm with short exposures, as low as 10 ms, allowing for time-efficient measurement of dynamic nanostructures. Beam profiling clearly shows that the supercontinuum dark-field technique works as expected and that spectra are collected from a small volume in the objective focus due to confocal localisation.

## 4.3 Electronics Design

By applying a voltage,  $V$ , and measuring the current,  $I$ , the conductance,  $G$ , of a conductive junction between tips can be determined using  $I = GV$ . Using this, quantum electronic transport can be measured and correlated with optical measurements to gain a sense of spatial separation and the extent of charge transfer across the gap.

The experimental chamber contains two triaxial connectors, one attached to each Cu tip clamp, to send and return electronic signals, permitting biasing and electrical measurement

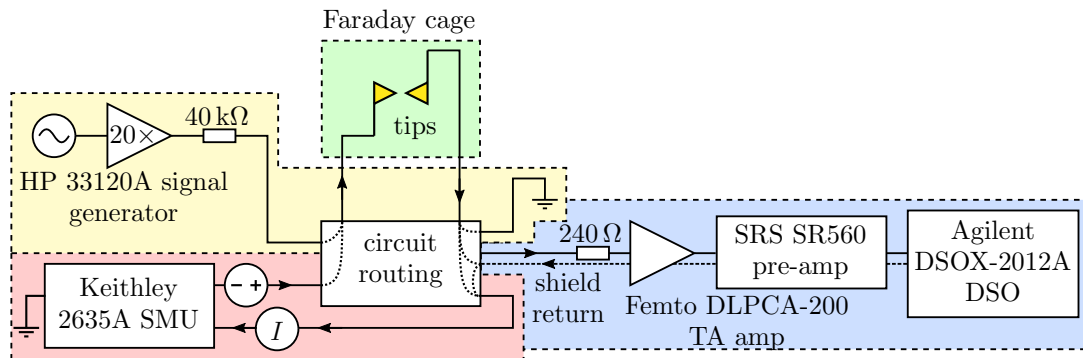


**Figure 4.10: Block schematic of the electrical circuit design.** The central routing box allows switching between a.c. and d.c. circuits and low- and high-bandwidth d.c. measurements. The a.c. circuit is used to align two AFM probes together while the d.c. circuit is used to measure spatially dependent signals from the gap between two AFM probes.

of the gap between AFM tips. Electronic signals are controlled and redirected using a control box, which attaches to the chamber triax cables. Electronics are split between an a.c. circuit that drives a resonant capacitive tip alignment procedure and a d.c. circuit for electrical measurements. The d.c. electronics are further split into low and high bandwidth measurement circuits. The low bandwidth ( $< 10$  Hz) circuit measures electronics continually over long time periods, typically giving spatial information linked to sample separation. The high bandwidth circuit operates on a trigger to capture single shot events on much shorter time scales. Both d.c. circuits are typically run simultaneously while the a.c. and d.c. circuits are manually switchable. A block schematic of this system is shown in Figure 4.10.

The a.c. circuit consists of a signal generator connected to a  $20\times$  voltage amplifier to drive the junction capacitance. This is used to resonantly drive an AFM cantilever into oscillation and align tips into a tip-to-tip dimer configuration. A  $40\text{ k}\Omega$  current limiting resistor is placed after the amplifier to prevent damage to the tip junction in the event of a direct conductive contact.<sup>10</sup> The return signal from the circuit is then terminated at ground. The separate d.c. circuit consists of a source-meter unit (SMU) circuit for low-bandwidth (sub-10 Hz) measurements with a switchable high-bandwidth measurement extension. The SMU (Keithley 2635A) is used to apply a voltage across the junction and measure the current. The switchable high-bandwidth path routes the current through a  $10^4\times$  gain transimpedance amplifier (Femto DLPCA-200) followed by a 1 MHz low-pass filtering stage (SRS SR560). The amplified voltage is measured on a digital storage oscilloscope (DSO) (Agilent DSOX-2012) with the shield becoming the return path of the current back to the SMU via the routing box.<sup>11</sup>

<sup>10</sup>The optimum resistance value is calculated using  $R = V/I_{\text{limit}}$  where  $V = 10\text{ V}$  typically and a safe current limit is  $I_{\text{limit}} = 250\text{ }\mu\text{A}$ . This gives a resistance of  $40\text{ k}\Omega$ .

<sup>11</sup>An alternative strategy for converting a current into a voltage is to pass the current through a well-known resistor and differentially amplify the voltage drop across the resistor. This was not used since the transimpedance amplifier was readily available and of a low noise specification.

The fundamental feature of the combined circuitry is their separability. The a.c. circuit is not required to be low-noise but the d.c. circuitry is used to measure low-level tunnelling currents. For the d.c. circuit to operate correctly it must be isolated from all other electronics. The a.c. circuit remains completely disconnected and held at ground when the d.c. circuit is engaged, and vice-versa. To achieve measurements of small, sensitive currents, reducing the noise level to a minimum is imperative. The noise floor at low bandwidths, along with the current range of the SMU, sets the minimum current which can be measured. The sub-10 Hz bandwidth of the SMU removes much of the noise during spatial measurements. Correct grounding of all electronic chassis to a single point (the SMU) shields EMI and prevents ground loops from inducing current offsets. Triax cabling is used with guarded connections where possible to prevent leakage currents.

A standard operating voltage between 10–50 mV is used to drive high quality tunnelling currents. Conductances greater than  $10^{-8}G_0$  are then clearly measured above noise. Using lower voltages means currents are only observable for larger tunnelling conductances, i.e. smaller gap widths, whilst higher voltages lead to larger overall currents and electrostatic interaction between tips, both of which should be avoided to prevent damage to the tip junction. To maintain good scan speeds the current range is restricted to 10 nA with a  $\pm 10$  pA error, since more accurate ranges have longer settling times. Limiting the current range is the dominant source of current measurement error as opposed to the noise floor.

Noise on the SMU is measured by varying a series resistance in place of the tip junction and taking the standard deviation of 20 measurements across a range of voltages in 10 mV steps. The open circuit noise measures  $\pm 10$  pA. Johnson noise for such a circuit is estimated to be around 1 pA. If current measurements are strictly limited by the current range then the percentage error of each range should be equivalent. This is not the case, with the percentage error increasing from  $10^{-3}\%$  to  $10^{-2}\%$  as the current decreases to the nA range, signifying the approach of the noise floor. Actual noise levels around  $\pm 100$  pA are found at 50 mV with a  $1\text{ M}\Omega$  ( $10^{-2}G_0$ ) junction resistance characteristic of conductances when passing through the quantum regime of plasmonics. Given the small percentage errors, circuit noise is not a problem for tunnelling current measurements.

Noise predominantly affects high bandwidth measurements, where it limits the conductance resolution and minimum trigger level for single shot measurements. High bandwidth noise typically originates from digital circuitry, e.g. switch-mode power supplies and powered relays. Power supplies are therefore covered in foil to shield EMI and manual toggle switches are used instead of remote-controlled relays. Applying a 1 MHz filter goes some way to reducing high bandwidth noise. Any more filtering smooths measurements too much.

The maximum allowed current is set to 250  $\mu\text{A}$  to prevent damage to contacted AFM tips. Upon surpassing this limit the SMU reduces the voltage to attenuate the current. A current

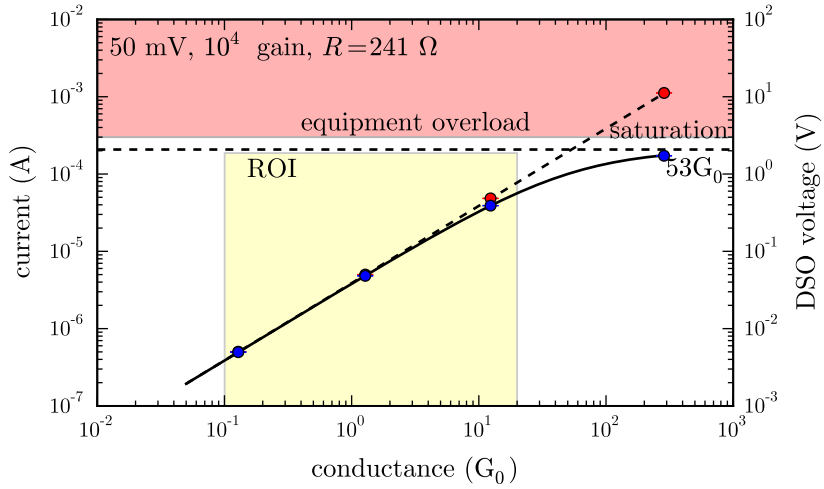


**Figure 4.11: Characterisation of electronic measurements based on junction conductance.** Solid lines show the calculated SMU currents and amplified voltages as a function of junction conductance under a  $50\text{ mV}$  applied voltage with a  $241\ \Omega$  current limiting resistor to prevent saturation (high bandwidth circuit). Dashed lines show the calculated current for the case without the current limiting resistor (low bandwidth circuit). Circles mark experimentally measured points using resistors in place of the tip junction.

limiting resistor is also included in the circuit to ensure a hardwired maximum and to prevent overloading of the DSO and transimpedance amplifier. The value of this resistor is calculated using,

$$R = \frac{AV}{0.95V_{\text{overload}}}, \quad (4.4)$$

where  $V$  is the operating voltage,  $A$  is the amplifier gain and  $V_{\text{overload}}$  is the minimum overload voltage for the circuit at a given voltage  $V$  (determined by whichever overload voltage is surpassed first, either the maximum transimpedance input current of  $5\text{ mA}$  pre-amplification or the maximum output voltage of  $5\text{ V}$ ). The pre-factor of  $0.95$  is chosen to prevent the current from getting close to overloading. For a  $50\text{ mV}$  bias and  $10^4$  gain the ideal resistance is  $175\ \Omega$  but for a  $10\text{ mV}$  bias with  $10^5$  gain it increases to  $350\ \Omega$ . To accommodate a range of voltages and both gain settings, a middle resistance of  $241\ \Omega$  is used, which provides some headroom for increasing the voltage at the lower gain. The calculated current and DSO voltage as a function of junction conductance for the low and high bandwidth circuits is shown in Figure 4.11. Excellent agreement with experimental current and voltage measurements taken with a set of resistors demonstrates the circuit behaves exactly as predicted.

The presence of the current limiting resistor means that measured circuit conductances,  $G_{\text{measured}}$ , contain a series resistance that needs to be taken into account. Junction conductances are calculated using,

$$G_{\text{junction}} = (G_{\text{measured}}^{-1} - R)^{-1}. \quad (4.5)$$

The maximum conductance value that can be measured is found by inverting the limiting resistance using  $G_{\max} = 1/R$ . For a 50 mV bias the conductance limit is  $53G_0$ . Conductances greater than this value are small compared to the series resistance and are therefore much harder to measure reliably. For this reason the range of interesting conductances ( $G < 20G_0$ ) is ideally kept to the linear part of the current curve by limiting the voltage and gain.

## 4.4 AFM Design: Measurements of Force

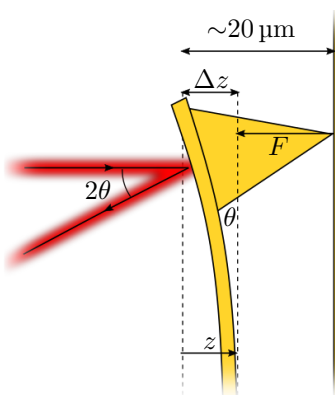


**Figure 4.12: Concept of contact mode AFM.** An applied force  $F$  bends the cantilever proportional to a linear displacement  $x$ . Light incident on the bent cantilever deflects at an angle  $2\theta$ .

An AFM module measures cantilever deflections as they flex under an applied force. The linear displacement of the cantilever,  $\Delta z$ , from its equilibrium position under an applied force,  $F$ , is simply given by,

$$F = k\Delta z, \quad (4.6)$$

where  $k$  is the stiffness or spring constant of the cantilever. Contact and tapping mode cantilevers are mostly used in experiments, for which  $k = 0.2 \text{ N m}^{-1}$  and  $40 \text{ N m}^{-1}$ , respectively. The change in angle caused by a linear displacement at the tip can be measured optically as a change in deflection angle of a laser focussed on the back of a reflective cantilever (Figure 4.12). The sensitivity of this technique has led to it being named atomic

force microscopy since atomic-scale forces cause measurable deflections, enabling topological imaging with nanoscopic resolution. For tip-tip dimers, force measurements become important as they dictate how tips come together and move through interfacial layers prior to electrical contact. A compact AFM module was thus constructed to monitor the tip-tip interaction forces during tip dimer measurements.

The AFM module consists of a compact optomechanical module, mechanically bolted onto the top plate of the microscope platform, and a separate 633 nm laser diode coupled together using a strain-relieved single mode fibre, as shown in Figure 4.13. Single mode fibre is used to produce a stabilised laser output. Light is focussed through an entry window in the experimental chamber onto the cantilever of a back-facing AFM probe during an experiment. The beam position is laterally offset on the focussing lens using a silver turning prism to focus on the cantilever at an angle so that reflections return through the AFM with the opposite lateral offset.<sup>12</sup> Light reflected back off the cantilever at a different angle in the

<sup>12</sup>An alternative to this approach allows use of a common beam path but requires two polarisers and a

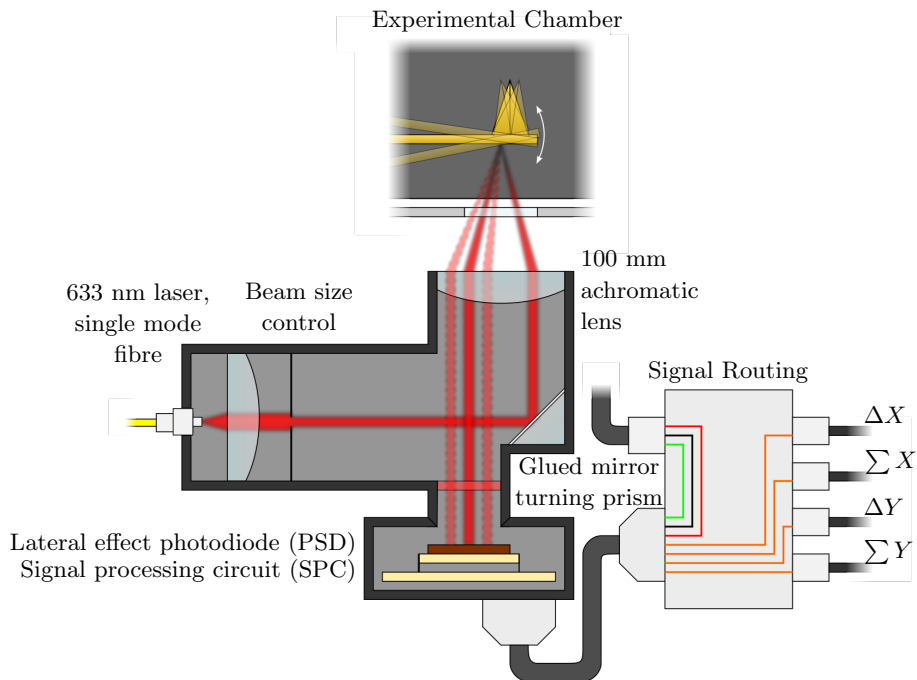


**Figure 4.13: Schematic diagram of the AFM module attached to the side of the microscope platform.** Incident light from a single mode fibre is focussed at an angle onto an AFM cantilever. Angled reflections from the cantilever are re-collimated into a laterally displaced beam whose position is detected on the PSD.

focal plane is laterally translated in Fourier space. This translation is measured using a fast lateral effect photodiode, also known as a position sensitive detector (PSD), where the beam position generates a current in each orthogonal direction. The PSD contains a signal processing circuit with a built-in transimpedance amplifier ( $10^5$  gain) to convert these small currents into voltages corresponding to the measurements  $\Delta x, y$  and  $\sum x, y$ . Voltages are recorded using a DAQ card (NI X-series).

Changes in the voltage output of the PSD correspond directly to motion of the tip and cantilever under an applied force. The position of the PSD is adjusted with zero force applied to the cantilever to zero the voltage. The lateral displacement of the returning beam is then calculated using,

$$ds_i = \frac{L_i}{2} \frac{\Delta V_i}{\sum V_i}, \quad (4.7)$$

where  $i$  is the lateral axis, either  $x$  or  $y$ ,  $L_i$  is the length of the detector along that axis (10 mm) and  $V_i$  is the voltage output at each end of the detector axis. The displacement can then be transformed into an applied force via a calibrated conversion.

The width of the cantilever and the radius of the input beam determines the minimum

---

quarter wave plate, leading to simpler alignment but a more costly design.

beam size. Cantilevers have a width of 50  $\mu\text{m}$  therefore the spot size in the focus must be less than this value. Since the input is a single mode Gaussian beam the spot diameter,  $2w_0$ , is given by  $2w_0 = 4\lambda f/\pi D$ , where  $f$  is the focal length and  $D$  is the collimated beam diameter. For  $\lambda = 633 \text{ nm}$  and a required spot size  $2w_0 < 50 \mu\text{m}$  the fraction  $f/D < 62$ . The focal length is restricted by the distance from the edge of the top plate, where the AFM module is mounted, to the cantilever through the chamber window. A 100 mm lens is chosen to accommodate the focal length constraint, which restricts the beam diameter to  $D > 1.6 \text{ mm}$ . This beam diameter is set by using a short focal length lens to collimate the single mode fibre output.

#### 4.4.1 Calibrating the AFM

The displacement of the tip under an applied force is related to the lateral translation of the beam on the PSD. By determining the tip displacement, the force applied to the AFM tip can be measured using Eq. 4.6. The transformation from tip displacement into a measured lateral displacement in Fourier space is linear in the current geometry and can be expressed as,

$$s = k_{x \rightarrow s} x, \quad (4.8)$$

where  $k_{x \rightarrow s}$  is the transformation constant. Each of the individual linear geometrical transformations required to convert the tip displacement into a measurable beam displacement in Fourier space (tip displacement to angular cantilever deflection to angular beam reflection to lateral translation on recollimation) are incorporated into this constant, which can be experimentally determined.

The simplest method of calibration involves pushing an AFM tip against a hard contact so that the displacement is known ( $\Delta z = z$ ). From there the beam translation is measured as a function of tip displacement and data can be fitted to determine  $k_{x \rightarrow s}$ . The force can then be estimated using Eq. 4.6. Whilst this is not ideal as the cantilever spring constant is still somewhat unknown, the method is simple. Therefore, for force measurements, the value of the cantilever spring constant is assumed from the AFM probe data sheet. The large tolerances on stiffness measurements mean that this approach is only sufficient to estimate the applied force on a nano-gap to within 50%.<sup>13</sup> Other methods of accurately measuring the cantilever spring constant do exist, as do methods to directly map the force to a measured signal, i.e.  $F = k_{s \rightarrow F} s$ , but add further complexity to experiments [186–194]. Since exact measurements of force are not crucial to current nanogap studies, the uncertainty is acceptable.

---

<sup>13</sup>The fractional uncertainty is given by  $\delta F/F = \sqrt{(\delta k/k)^2 + (\delta z/z)^2}$  for which  $\delta z/z$  is negligible compared with  $\delta k/k = \sim 0.5$ .

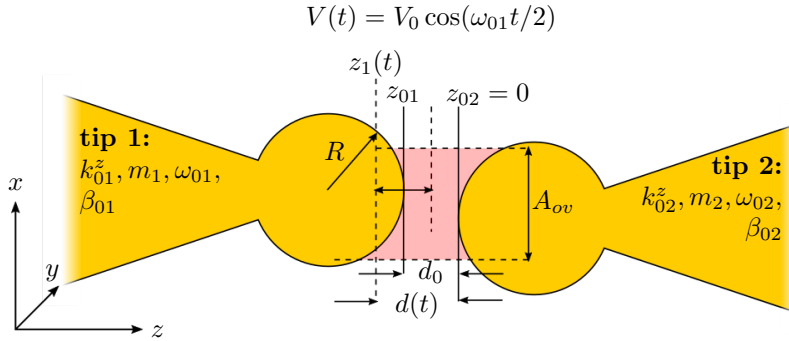


**Figure 4.14: Diagram of tip alignment parameters.** The position of one tip relative to the other is detected using a resonant scanning capacitance AFM technique. The gap is biased with an oscillating voltage to induce a resonant vibration of one of the AFM cantilevers. The amplitude of oscillation is sensitive to the gap size  $d$  and the area of overlap  $A_{ov}$  between tip features of characteristic size  $R$ . For sharp tips  $R$  is the apex radius whereas for nanostructured tips  $R$  is considered to be the feature size.

## 4.5 Scanning Capacitive AFM Tip Alignment

A significant challenge when attempting to recreate a plasmonic dimer using opposing AFM probes is the alignment of tips with the focussed laser spot in a symmetric tip-to-tip configuration. This capability is necessary to permit the majority of dual tip experiments and forms the first step to measuring the dynamical physical response of plasmonic tip dimer systems. For successful experiments the tolerance on the tip-to-tip alignment is less than  $\mathcal{O}(R_{\text{tip}})$ . Aligning tips using CCD imaging is limited by diffraction and therefore unsuitable. Initially this problem was solved using a non-linear capacitive alignment technique that required locking into the third harmonic of the driving signal [195]. Whilst functional in simpler systems, the technique was limited in its accuracy by the small pA level currents in the third harmonic mode and the extensive filtering and lock-in techniques required to measure these. A simpler approach is to simply use the AFM module optics to measure the oscillating cantilever deflection. This is more widely known as scanning capacitance mode AFM (SC-AFM) or scanning capacitance microscopy (SCM), and has been used in the past to measure the dopant levels in semiconducting substrates [196–200]. By utilising optical detection over direct electronic measurements tip alignment becomes segregated from the microscope electronic d.c. measurement circuitry and issues are no longer caused by noise leaking into the a.c. electronics.

### 4.5.1 Mechanism for Alignment of Two Opposing Tips

To a first approximation the metallic tips can be ignored and only the capacitive interaction between planar cantilevers is considered. Cantilevers are separated by a distance  $d(t) = z_1(t) - z_2(t)$  and coupled via the  $z$ -components of the long range, attractive, electrostatic

driving force  $F_{EL}^z$  and short range Van der Waals and repulsive tip-tip interaction forces  $F_{TT}^z$ . Each cantilever has an associated spring constant  $k_{0i}^z$ , mass  $m_i$  and resonant frequency of oscillation  $\omega_{0i} = \sqrt{k_{0i}/m_i}$ . When vibrated, cantilevers oscillate around an equilibrium position  $z_{0i}$ . The equilibrium separation between tips is then denoted by  $d_0 = z_{01} - z_{02}$ .

The equation describing motion in the  $z$ -axis of the two parallel cantilevers, denoted by  $i = (1, 2)$ , of spring constant  $k_i^z = k_{0i}^z + k_{TT}^z$ , coefficient of damping  $\beta_i^z = \beta_{0i}^z + \beta_{TT}^z$  and mass  $m_i$ , is given by,

$$m_i \frac{d^2 z_i}{dt^2} + \beta_i^z \frac{dz_i}{dt} + k_i^z (z_i - z_{0i}) = \pm (F_{EL}^z + F_{TT}^z), \quad (4.9)$$

where the sign of the force is positive for one tip and negative for the other. Assuming that alignment takes place at long range, tip-tip interactions can be ignored, therefore  $F_{TT}^z = 0$  and  $\beta_{TT}^z = k_{TT}^z = 0$ . The system is further simplified by assuming that one cantilever remains stationary by being stiff (tapping mode tip with  $k \approx 40 \text{ N m}^{-1}$ )<sup>14</sup> and always being off resonance ( $\omega_{01} \neq \omega_{02}$ ). This is usually satisfied in experiments where a stiff cantilever is required such that the optical probe is incident on the same sample area whilst under force. The apex separation is then restricted to  $d = z_1$  with an equilibrium separation  $d_0 = z_{01}$ . Under these conditions the motion reduces to that of a single tip,

$$m_1 \frac{d^2 z_1}{dt^2} + \beta_1^z \frac{dz_1}{dt} + k_1^z (z_1 - d_0) = F_{EL}^z(z_1, t). \quad (4.10)$$

This equation now describes the whole system rather than each individual tip with the main reference point between tips being the equilibrium separation  $d_0$ .

The remaining capacitive driving force exerted between tips is purely electrostatic and of the form,

$$F_{EL}^z(V, z) = \frac{1}{2} \frac{\partial C(z)}{\partial z} V^2(t), \quad (4.11)$$

where  $C(z)$  is the capacitance between the tips at a distance  $z$  and  $V(t)$  is the potential difference between tips. Under a parallel plate capacitor model the capacitance is  $C(z) = (\epsilon_0 A_{ov}/z) + C_{bk}$  for plates with  $A_{ov}$  area of overlap at a separation  $z$ , including a stray capacitance  $C_{bk}$ . Applying a harmonic driving force at a frequency  $\omega_s$ , described by  $V(t) = V_0 \cos(\omega_s t)$ , results in a nonlinear driving force, given by,

$$F_{EL}^z(z_1, t) = \left( \frac{-\epsilon_0 A_{ov} V_0^2}{4z_1^2} \right) [1 + \cos(\omega_p t)], \quad (4.12)$$

where  $\omega_p = 2\omega_s$  is the cantilever pump frequency. Substituting Eq. 4.12 into Eq. 4.10 gives

---

<sup>14</sup>This is based on data sheet values of almost all tapping mode tips.

the simplified equation of motion for the dual-tip system,

$$m_1 \frac{d^2 z_1}{dt^2} + \beta_{01}^z \frac{dz_1}{dt} + k_{01}^z (z_1 - d_0) = \left( \frac{-\varepsilon_0 A_{ov} V_0^2}{4z_1^2} \right) [1 + \cos(\omega_p t)]. \quad (4.13)$$

Driving at a pump frequency close to the cantilever resonance ( $\omega_p \approx \omega_{01}$ ) leads to a resonant oscillation between tips. For small oscillations around  $d_0$ , Eq. 4.13 can be Taylor expanded to first order into the form of the driven damped Mathieu equation with an approximate solution [201],<sup>15</sup>

$$z_1 \approx d_0 - |z_1^{off}| - z_{m1} \cos(\omega_p t + \varphi_1) \quad (4.14)$$

where,

$$z_1^{off} \approx \frac{\varepsilon_0 A_{ov} V_0^2}{4d_0^2 \langle k_{e1}^z \rangle}, \quad (4.15a)$$

$$z_{m1} \approx \frac{\varepsilon_0 A_{ov} V_0^2}{4d_0^2 \sqrt{(\langle k_{e1}^z \rangle - m_1 \omega_p^2)^2 + (\beta_{01}^z \omega_p)^2}}, \quad (4.15b)$$

$$\varphi_1 \approx \tan^{-1} \left( \frac{\beta_{01}^z \omega_p}{\langle k_{e1}^z \rangle - m_1 \omega_p^2} \right), \quad (4.15c)$$

in which  $\langle k_{e1}^z \rangle$  is the effective spring constant of the system,  $\langle k_{e1}^z \rangle = k_{01}^z - \varepsilon_0 A_{ov} V_0^2 / 2d_0^3$ , taking into account the time-averaged electrostatic interaction. From Eq. 4.15b and Eq. 4.15c it can be seen that both the oscillation amplitude and phase relative to the driving signal vary with the equilibrium separation  $d_0$ .

Although the model is for two parallel plates, it becomes applicable to tips in a dimer configuration once the separation is sufficiently low that the tip-to-tip capacitance dominates over all other capacitive contributions (such as the cantilever or tip facet interactions). In this regime, if the tips stray out of alignment the tip-to-tip distance increases and the capacitance decreases, reducing the tip oscillation amplitude and the phase, hence tips are aligned when both the amplitude and phase are maximised. Both these properties are readily measurable using optical cantilever deflection in the AFM module.

Whilst optical detection gives a better signal-to-noise and measures at higher bandwidths, it should be noted that the capacitive model was originally developed to show that a  $3\omega_s$  current signal can be used to align tips [195]. By driving the system with  $\omega_p \approx \omega_{01}$ , a mechanical parametric resonance is excited at  $2\omega_{01}$  (otherwise only the fundamental is excited

---

<sup>15</sup>Full derivation available in the appendix.

with resonant driving) and the current through the tip junction is given by,

$$I(\omega_s) \approx \omega_s C_0 V_0 \left( 1 + \frac{|z_1^{off}|}{d_0} + \frac{z_{m1}}{2d_0} e^{i\varphi_1} + \frac{C_{bk}}{C_0} \right) e^{i\frac{\pi}{2}}, \quad (4.16a)$$

$$I(\omega_p + \omega_s) \approx \frac{(\omega_p + \omega_s) C_0 V_0 z_{m1}}{2d_0} e^{i(\varphi_1 + \frac{\pi}{2})}, \quad (4.16b)$$

where  $C_0 = \varepsilon_0 A^{ov}/d_0$ . Non-linear oscillations in the tip capacitance result in parametric frequency mixing in the electronics with resulting signals at the sum and difference frequencies,  $\omega_p + \omega_s = 3\omega_s$  and  $\omega_p - \omega_s = \omega_s$  respectively. The signal at  $3\omega_s$  is background-free, as shown in Eq. 4.16b, and again depends on  $d_0$ . However, currents are  $\mathcal{O}(\text{pA})$  for acceptable driving voltages, therefore alignment only works over shorter ranges, and requires larger voltages to further boost the oscillation amplitude and low-noise detection electronics. Optical detection is advantageous as small oscillations at lower voltages are easily detectable, which protects the samples from damage caused by tapping between tips once the gap is small.

## 4.5.2 Numerical Modelling and Experimental Measurements of Scanning Capacitance Tip Alignment

### Numerical Modelling of Tip Alignment

Theoretical curves for the system response based on Eq. 4.13 for a typically used contact/tapping mode AFM probe dimer are solved numerically using an ordinary differential equation (ODE) solver.<sup>16</sup> Results are intended to *qualitatively* demonstrate the alignment technique. The following table summarises the parameters of the model for each tip:

	Tip 1	Tip 2
$k_0$ (N/m)	0.2	40
$\omega_0$ (kHz)	$2\pi.13$	$2\pi.300$
$\Delta\omega$ (Hz)	$2\pi.200$	$2\pi.200$
$r$ (nm)	20	20

**Table 4.1: Tip parameters used in numerical calculations.** The dimer is assumed to comprise of a dynamic contact mode AFM cantilever (tip 1) and a fixed tapping mode cantilever (tip 2).

The plate area is assumed to be  $\pi r^2$  where  $r$  is the radius of the tip, which is estimated to be 20 nm based on standard tip apex dimensions. Changing this value does not change the overall qualitative shape of the data. The mass of each tip is calculated from the resonance using  $m_i = k_{0i}/\omega_{0i}^2$ . The damping coefficient of each tip is given by  $\beta_{0i} = 2m\delta_i$  where  $\delta_i = \omega_{0i}/2Q_i$

---

<sup>16</sup>ODE in Numpy/Python

and  $Q_i = \omega_{0i}/\Delta\omega$  (a quantity which is verifiable by experiment). Only the damping coefficient of the vibrating tip matters at any given time due to the large difference in resonant frequencies. To maximise the detected response the system is studied around the resonance of the soft cantilever. The system spring constant is given by,

$$k_0 = (k_{01}^{-1} + k_{02}^{-1})^{-1}, \quad (4.17)$$

and the system mass is given similarly by,

$$m = (m_1^{-1} + m_2^{-1})^{-1}. \quad (4.18)$$

The forces acting on the tip are described by a capacitive driving force, described by Eq. 4.12, and an interaction force. The interaction force is described by,

$$F_i^z(z, d_0) = \begin{cases} -\frac{Hr_1}{6(z + d_0)^2}, & \text{if } d_0 + z > a_0 \\ -\frac{Hr_1}{6a_0^2} + \frac{4E\sqrt{r_1}}{3 - 3v^2}(a_0 - z - d_0)^{\frac{3}{2}}, & \text{if } d_0 + z \leq a_0 \end{cases} \quad (4.19)$$

where  $z$  is the tip position oscillating around an equilibrium position  $d_0$ ,  $a_0$  is the interatomic distance and  $H$  is the Hamaker constant [202–205]. The capacitive driving force depends only on the time-averaged tip separation whilst the interaction force depends on the oscillation amplitude of the tip around its equilibrium position compared with the gap separation since this eventually leads to tapping on the opposite tip.

The ODE algorithm computes the change in the cantilever position and velocity in time using their respective differentials,

$$\dot{z}_+ = \dot{z}_-, \quad (4.20)$$

$$\ddot{z}_+ = -m^{-1} [\beta_1^z \dot{z}_- - k_0^z z_- + F_{EL}^z(z_-, t) + F_i^z(z_-)], \quad (4.21)$$

where  $F_{EL}^z(z, t)$  is the capacitive driving force described in Eq. 4.12 and  $F_i^z(z)$  is the interaction described in Eq. 4.19. The tip motion is solved in time subject to stationary initial conditions for 100 AFM oscillation periods. The steady state harmonic properties of the waveform are extracted using a sinusoidal fit to the last 50 periods, when behaviour has stabilised. The modelled frequency response is determined by driving a spatially fixed tip dimer, separated by 100 nm, with a 10 V driving signal across a range of frequencies around  $\omega_s = \omega_{01}/2 = 2\pi.13 \text{ kHz}/2$ . The intertip separation is then varied while driving on resonance at various voltages to find the separation response.

## Experimental Measurements using Scanning Capacitance Microscopy

Experimental measurements of capacitive tapping mode tip interaction use the AFM optics on the microscope and monitor the position of the tip through the motion of the reflected laser beam. The backside of the softer cantilever of the pair is illuminated by the 633 nm laser beam. By resonantly driving an AFM tip electronically its oscillation generates a signal  $A \cos(\omega_p t + \phi)$  along one of the axes on the PSD. Lock-in detection is used in the software to remove noise and add phase sensitivity to signal measurements by referencing the oscillation to the driving signal. The NIDAQ device simultaneously acquires both PSD signals in each direction along with the driving signal from the function generator output. The second harmonic of the driving frequency,  $\omega_p$  is locked-in using the reference periodicity. The phase difference  $\phi$  is then measured relative to the reference phase.

Experimental measurements are performed on a tip dimer consisting of a 13 kHz,  $0.2 \text{ N m}^{-1}$  soft Au contact-mode AFM cantilever and a 300 kHz,  $40 \text{ N m}^{-1}$  stationary Au tapping mode AFM cantilever. The resonance frequency of the softer cantilever is determined prior to tip alignment at long range by scanning the driving signal frequency and measuring the cantilever response. The separation response is probed by aligning the soft tip to the position of maximum amplitude by laterally scanning the  $xy$  plane opposite the stiff tip. The soft tip is approached towards the stationary tip along the  $z$  axis and the cantilever response is measured. The rate of approach varies between 0.5–2 nm per step depending on how far apart tips are separated. The amplitude is monitored in real time and the tip is retracted once the signatures of tapping are detected. Quick retraction is necessary as tapping with a soft cantilever is unstable to effects such as snap-in and short-range attractive forces. There is also a high chance of damaging the metallic tip coating during contact. Judgement of the retraction point is subjective since the point of snap-in cannot be predicted but preserves the tip for multiple cycles. This approach-retraction cycle is repeated many times with a continuously reducing voltage until tapping is difficult to achieve without the oscillation immediately becoming unstable. This occurs once driving with less than 5–6 V.

## Comparison between Numerical Modelling and Experimental Scanning Measurements

Figure 4.15a shows the calculated frequency response for a dimer comprised of a stiff, tapping mode cantilever and a softer contact mode cantilever. From this the cantilever resonance can be clearly seen. The amplitude line shape matches the expected Lorentzian response of a damped resonator and oscillations transition between in-phase oscillation when driving at lower frequencies and anti-phase oscillation at higher frequencies. This is standard resonator behaviour as expected. The measured frequency response of a capacitively-driven contact mode AFM cantilever (Figure 4.15b) agrees well with the modelled response. The resonance frequency is higher than expected due to the tolerance range of real AFM cantilevers. One

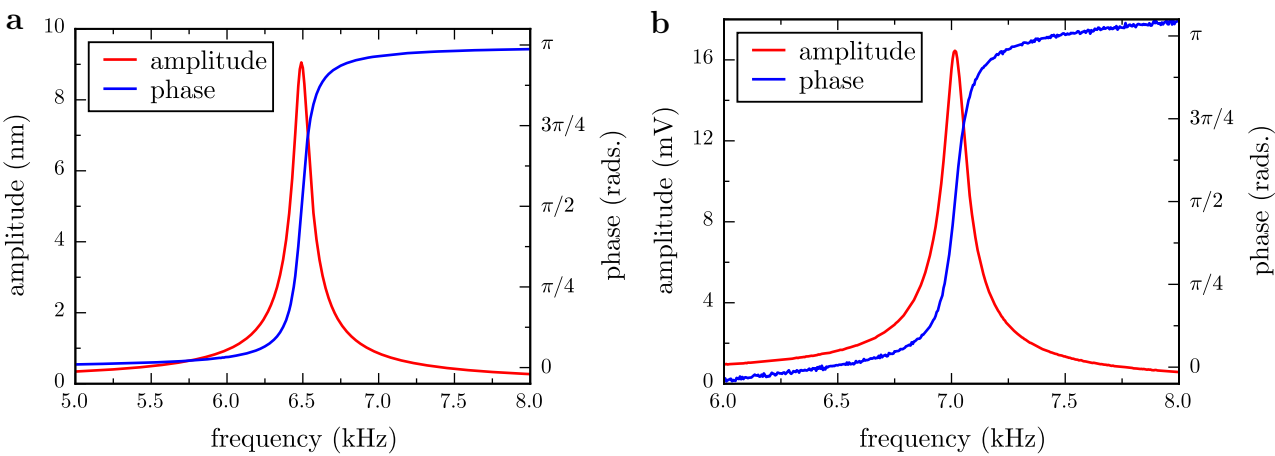


**Figure 4.15: Theoretical and experimental frequency response showing the amplitude and phase of a standard opposing AFM tip system.** The modelled tip junction (a) consists of a 13 kHz,  $0.2 \text{ N m}^{-1}$  soft tip and a 300 kHz,  $40 \text{ N m}^{-1}$  stationary tip, held at 10 V with a 100 nm intertip separation. Experimental cantilevers (b) are a 13 kHz,  $0.2 \text{ N m}^{-1}$  BudgetSensors ContGB Au tip and a 300 kHz,  $40 \text{ N m}^{-1}$  BudgetSensors TapGB Au tip, separated by  $\sim 1 \mu\text{m}$  and driven at 15 V.

noticeable difference is the linear gradient superimposed onto the phase response. This stems from time lags during acquisition which give a linear phase offset with increasing frequency.

The calculated separation response for the same contact/tapping-mode tip dimer is shown in Figure 4.16a. As the separation decreases the capacitance between tips increases and resonant oscillation is amplified. This amplification occurs until the amplitude is equal to the separation, at which point the system transitions into the tapping mode of AFM imaging. This is shown by the linear relationship of unity gradient between amplitude and separation, regardless of voltage. In this regime the oscillation is restricted by the gap width between tips, which limits the maximum possible amplitude. Calculations indicate that phase contrast only occurs once the oscillating tip comes into close proximity with the other tip. This onset of phase contrast occurs close to the point of maximum amplitude just before tapping. The phase is therefore a good indicator of the alignment between tips. Tips can be considered to be aligned once the centres of both the amplitude and phase overlap in a plane perpendicular to the two tips. The accuracy of these solutions becomes limited when the separation is reduced well into the tapping mode regime as the oscillation is difficult to sustain and surface (interfacial) forces begin to dominate, leading to the snap-in effect.<sup>17</sup> This instability is seen by the deviation of the amplitude from its linear decrease in the tapping regime followed by its rapid decay.

Figure 4.16b shows the corresponding experimental curve to the numerically calculated separation response. The expected capacitive increase in amplitude followed by a linear tap-

<sup>17</sup>Snap-in, also known as snap-to-contact, is an AFM phenomenon described in a later chapter as a result of capillary forces from a water meniscus in the gap.

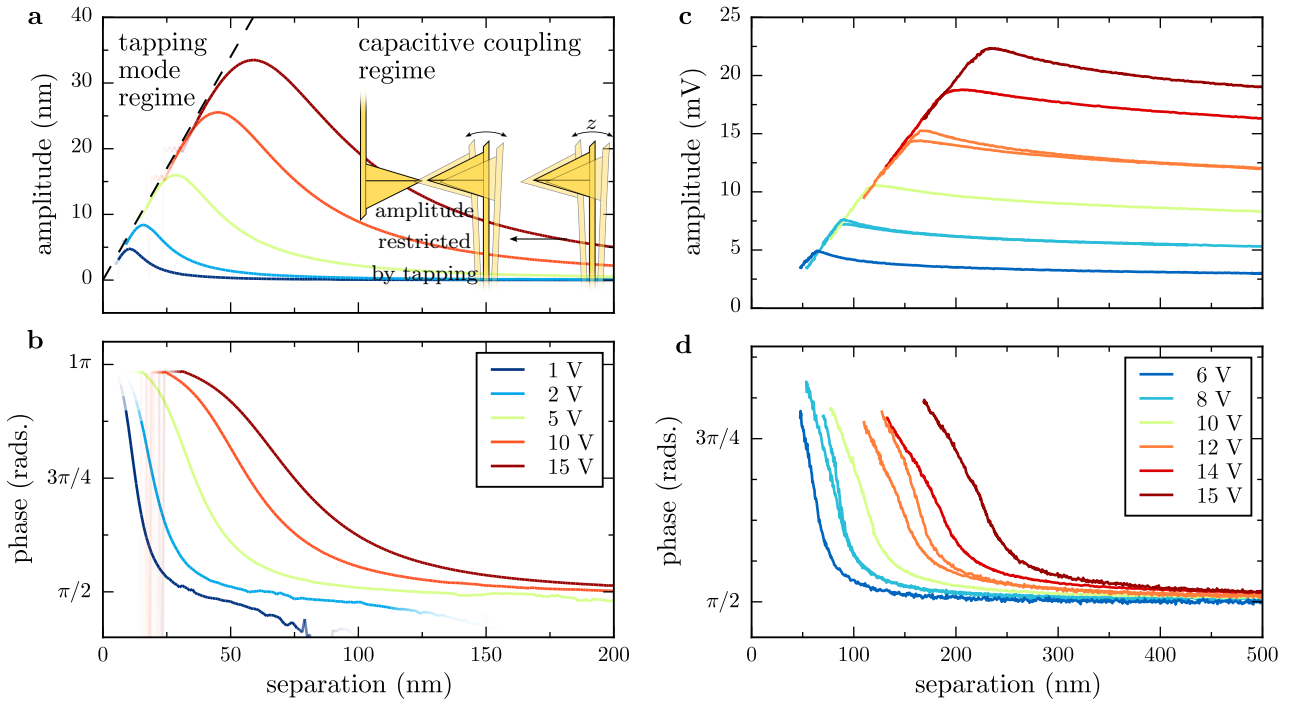


**Figure 4.16: Theoretical and experimental separation response showing the amplitude and phase of a standard opposing AFM tip system.** The modelled tip junction (a, b) consists of a 13 kHz,  $0.2 \text{ N m}^{-1}$  soft tip and a 300 kHz,  $40 \text{ N m}^{-1}$  stationary tip. The voltage across the modelled tip junction is varied while on resonance ( $\omega_s = 2\pi \cdot 6.5 \text{ kHz}$ ). The amplitude increases as the intertip separation is reduced. The dashed line shows the linear tapping regime of interaction. For separations below this limit, the hard surface restricts the amplitude to the gap between tips. A diagram of this is shown as an inset. Experimental cantilevers (c, d) are a 13 kHz,  $0.2 \text{ N m}^{-1}$  BudgetSensors ContGB Au tip and a 300 kHz,  $40 \text{ N m}^{-1}$  BudgetSensors TapGB Au tip. The same vibrating tip is approached and retracted with the voltage reduced between each approach cycle. The amplitude increases as the intertip separation is reduced until oscillation becomes restricted by the gap width.

ping mode regime is qualitatively found in the experimental data. Differences from numerical calculations, such as the less drastic capacitive amplitude increase, are likely due to the large extended shape of the tip and cantilever not taken into account in the simple model. The linear decrease is also less steep suggesting that only the upper region of the modelled curve is visible. The amplitude instabilities found in the calculations at small separations are also found in the experimental data. Repeat approaches after such an instability show different peak amplitudes with the differences attributed to misalignment after contact, changes in tip morphology or surface modification. Overall the cantilever behaviour qualitatively matches many of the trends predicted using a simple mathematical model solved using an ODE solver. As expected, the separation sensitivity of this technique makes it highly suited for tip alignment.

Another application for capacitive driving, demonstrated by Figure 4.16, is to use the long

range interaction to lock the positions of the tips relative to each other, using the separation-dependent amplitude response as a feedback mechanism in a PID loop.<sup>18</sup> Dynamic positioning and alignment between two tips can then be locked and maintained throughout an experiment to account for fluctuations due to either mechanical or thermal drift. Smaller separations can be locked by decreasing the voltage to reduce the amplitude up until the point at which the second harmonic signal becomes difficult to detect. The onset of tapping also limits the minimum achievable separation as the tip must remain oscillating. This technique could potentially become more useful if a stable plasmonic gap size is required for a long time whilst the contents or properties of the gap are modified.

### 4.5.3 Experimental Alignment of Tips using Scanning Capacitance AFM

By mapping the lateral amplitude and phase variations of the cantilever deflection on resonance, two opposing tips can be experimentally aligned. Alignment is carried out on resonance by laterally scanning the oscillating, soft cantilever tip over the stationary tip whilst reducing the separation. The location of the opposite tip is then determined by the position of maximum amplitude and phase. To prevent tip collisions due to entering the tapping regime, the voltage is reduced along with the separation. This allows only the minimum required signal for positional analysis. Unlike the phase, the amplitude signal varies smoothly over a longer range. As the intertip separation decreases, the amplitude centroid converges on the position of the opposing tip apex and the phase begins to increase and form a sharp peak. By iteratively following the lateral position of maximum amplitude the tips can be brought into alignment. This procedure is advantageous as it operates at long range in the non-contact regime, prior to the tapping mode regime.

Figure 4.17 shows a typical alignment scan at close range with peaks in both the amplitude and phase. At this point during the procedure the tips are considered to be well aligned. Tips are brought into alignment by identifying the position of these peaks. Since the tips are only symmetric along one axis, long range capacitive coupling is inhomogeneous and skewed until the distance between tips is small enough that the tip-to-tip capacitance dominates interactions. Gaussian fitting is therefore potentially inaccurate in determining the peak location. Calculating the centroid from discrete image moments, given by Eq. 4.2 and Eq. 4.3, provides a more accurate, and faster, way of centring the scanned tip on the opposing tip. The centroid position after each scan is tracked as the intertip separation decreases from larger distances ( $\sim 1 \mu\text{m}$ ) to around 100 nm as tips are brought into alignment. The centroids as a function of separation for a representative scan are shown in Figure 4.18.

---

<sup>18</sup>Proportional-integral-differential (PID) control loops are a form of feedback mechanism for stabilising a value at a preset target.

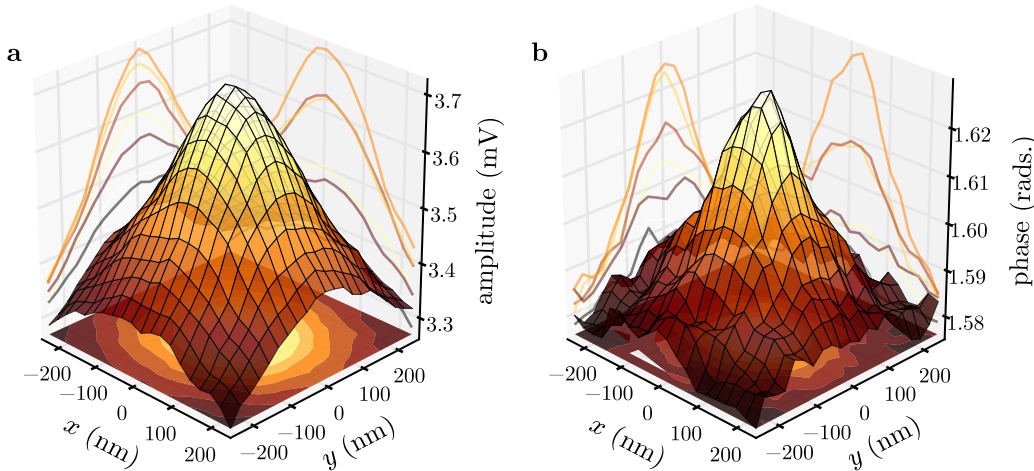


**Figure 4.17: Alignment scan of a soft Au AFM tip scanned laterally over a stiff Au AFM tip.** The soft tip is oscillating at 13 kHz (BudgetSensors ContGB) while the 300 kHz Au tip (BudgetSensors TapGB) remains static. Tips are separated by  $\sim 50$  nm and driven at 8 V, remaining in the capacitively coupled regime. Strong peaks are seen in both the amplitude and the phase of the soft cantilever oscillation. The tips are aligned in a tip-to-tip configuration when both signals are maximised.

Alignment is classified as the point at which the amplitude centroid is in agreement with the phase centroid. This criterion is chosen since the emergence of a peak in the phase signifies that the apex-apex capacitance dominates the response and because the phase centroid does not deviate significantly from its initial position (Figure 4.18a,b). The amplitude centroid, on the other hand, follows the point of maximum capacitive coupling, which depends on the overall tip and cantilever shape, the separation regime and the driving voltage. For example, most pyramidal AFM tips are asymmetric in one direction with different opening angles from the apex, hence the point of maximum capacitance occurs when the higher angle tip facets overlap. As the separation decreases the apex-apex capacitance begins to dominate since the relative capacitance contributions to the amplitude go as  $d^{-2}$ , hence the fractional change in the intertip separation is far greater than the fractional change in the cantilever separation. Upon surpassing this point the asymmetry is effectively removed, as shown in Figure 4.18a,b.

The accuracy of the alignment can be quantified from the FWHM of both the amplitude and phase peaks. The FWHM of both centroids shortly after passing the alignment threshold constrict to a similar length. This is inevitably limited by the feature size of the tip apex, such as the radius of a sharp or spherical tip apex. When studying spherical tips with 150 nm radii the FWHM remains much larger since the surfaces in close proximity are much flatter in comparison. As the FWHM reduces the uncertainty on the centroid position reduces down to a few nanometres, well within the tolerance levels of any dual tip experiment.

Alignment using this technique is limited to conductive tips for best results. Tips necessarily have to be conductive to generate a strong capacitive signal at the tip junction. Most

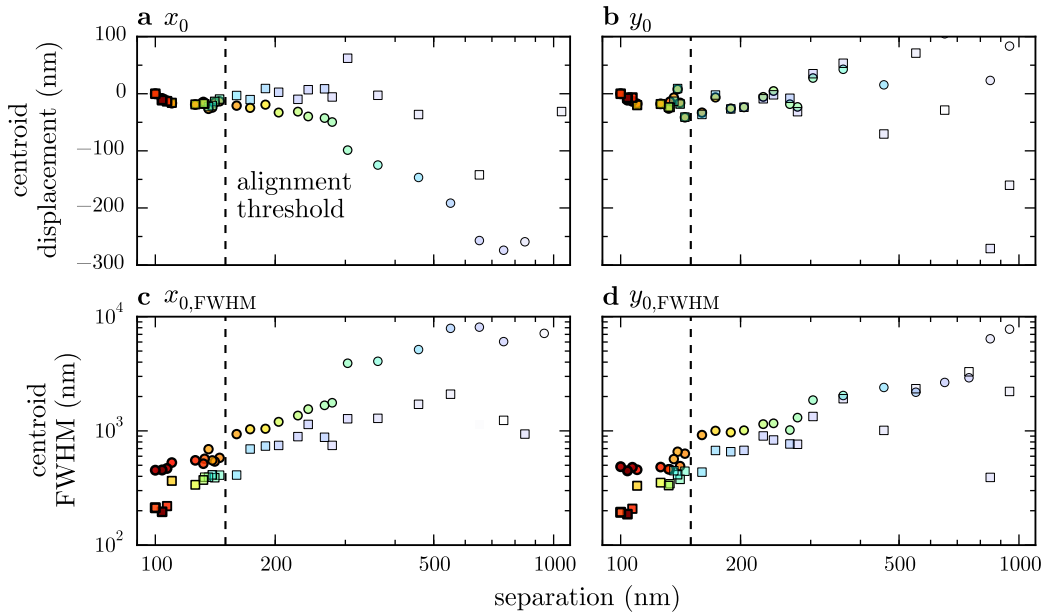


**Figure 4.18: Centroid tracking during approach and alignment of two sharp Au tips.** Amplitude (circles) and phase (squares) centroid positions relative to final alignment are shown in both the  $x$  (a) and  $y$  (b) directions. The centroid FWHM for the  $x$  and  $y$  amplitude and phase centroids are shown in (c) and (d), respectively. Marker colours indicate the strength of the peak in each alignment scan. A voltage of 8 V was maintained during each scan. The final separation is an estimate based on the eventual snap-in point and the onset of the tapping mode.

tips used with this technique have therefore been from Au or Pt AFM probes, though alignment of Si tips has been demonstrated at higher voltages since they are doped to dissipate static charge. Due to the improved signal quality when using optical detection compared to electronics, smaller oscillations can be used to align tips, which is good to maintain accuracy of alignment and reduce the risk of damaging tips. For a standard sharp Au tip dimer (one contact, one tapping mode cantilever) alignment has been carried out at voltages as low as 2 V for small tip separations. The PSD also offers at 400 kHz bandwidth compared with the 100 kHz bandwidth of available electronic lock-in amplifiers, allowing stiffer tips to be aligned on the occasion where a stiff dimer is needed. A demonstration of this high frequency alignment is shown in Figure 4.19 where a large voltage of 100 V was used to induce a sufficiently large oscillation for signal detection at 74 kHz.

To summarise, the capacitive alignment technique developed by Savage et al. [195] has been successfully adapted to use optical cantilever detection, as in AFMs, instead of electronic measurements of the tip junction. The technique is greatly improved, is less sensitive to other electronic systems integrated into the microscope, and has demonstrated the capability to align two tips to within a few nanometres of the target - less than the feature size of the tips. Both the frequency and spatial response have been studied, showing the tip separation dependence and the resulting alignment mechanism.

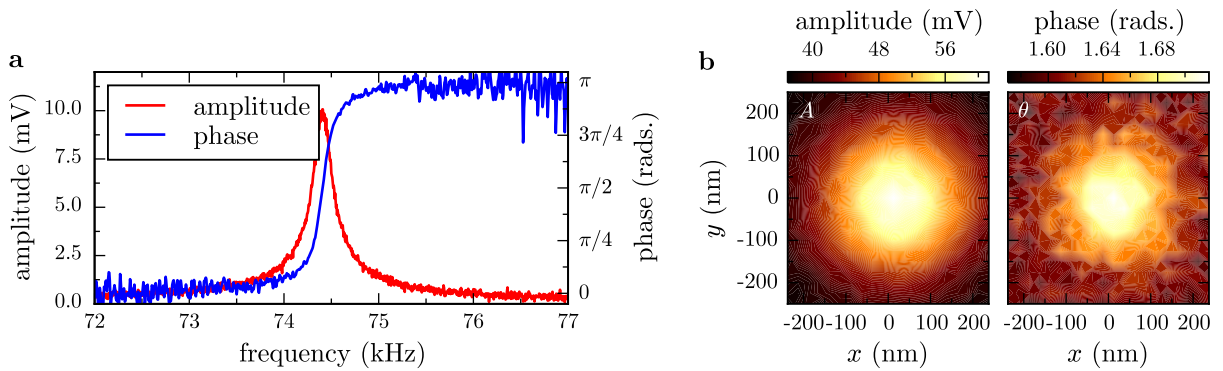


**Figure 4.19: High frequency alignment data for a tip dimer composed of two  $48 \text{ N m}^{-1}$  Au AFM tips.** Tips are separated by  $\sim 50 \text{ nm}$  and driven at  $120 \text{ V}$ . (a) Frequency response of the system. (b) Amplitude and phase alignment scans showing the expected peaks as the moving tip scans over the stationary tip.

## 4.6 Conclusions

A custom-built ultra-stable microscope platform, utilising supercontinuum dark-field spectroscopy, low-noise electronics and AFM, is built to accommodate spectral studies of both individual tips and tip dimers. The platform is stable to both temperature and vibration and able to take two tips and align them into a dimer configuration using a modified form of scanning capacitance microscopy. Performance characterisation shows spectral validity between  $500\text{--}1100 \text{ nm}$ , more broadband than standard optical microscopes, with confocal localisation enabling the study of more complex structures than point scatterers. The addition of fA level current and AFM force measurements results in a system capable of characterising a sub-nm plasmonic dimer system in far more detail than ever before possible.

## Chapter 5

# Understanding and Applying Single Tip Plasmonics

As discussed in the theoretical background (chapter 2.3) only a small amount of work has been done to characterise and understand tips prior to applying them as optical nanoantennae. Understanding plasmons in tips, specifically those which can couple with far-field light, has been one of the main motivations of this project. A hyperspectral imaging technique is applied to laterally map light scattering from a tip with confocally localised spectra to infer a local optical response and better study different tips. Understanding this response at the apex of single tips is of importance in determining their effectiveness as near-field enhancers and in understanding their coupling behaviour in the presence of another tip. In this chapter the spectra of single tips is discussed, studying both sharp and spherical-tipped Au AFM probes, along with their application in Raman spectroscopy.

## 5.1 Optical Characterisation of Nanostructures using Hyperspectral Imaging

Hyperspectral imaging encompasses a range of optical techniques which image using pixels comprised of a spectrum rather than an RGB colour value. This is advantageous over regular imaging as more quantitative information can be extracted from an image. Hence hyperspectral imaging techniques have become commonplace across many diverse fields, including microscopy [206, 207], astrophysics [208], remote sensing and geology [209, 210], food standards [211, 212], and medical imaging [213–215]. Within each of these fields, the features in an image are more clearly identified by their spectral signatures. In this instance, scanning confocal hyperspectral imaging is applied to optically characterise both sharp and nanostructured metallic tips and identify optical resonances originating from LSP excitation.<sup>1</sup>

<sup>1</sup>This technique has also been applied to other periodic, extended nanostructures that are not discussed within the context of this thesis.

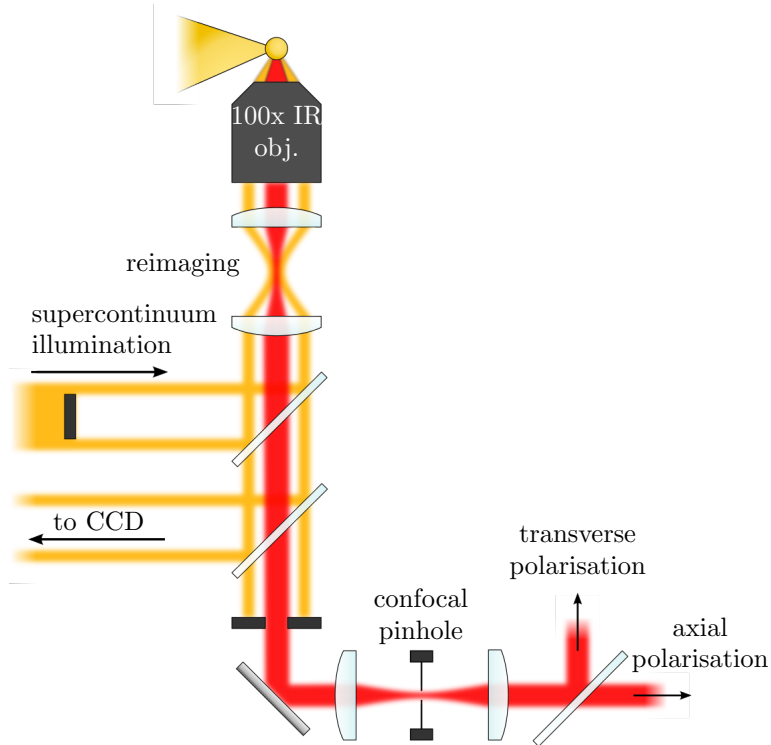


**Figure 5.1: Experiment configuration for hyperspectral imaging.** The laser is centered on the tip apex for imaging. The tip is scanned across the beam in a grid with spectra acquired at each position. The resulting image then contains 1044 colours at each pixel instead of the usual 3 (RGB).

Scanning confocal hyperspectral imaging falls under the category of spatially scanned imaging. Tips are scanned in a grid under the laser spot and the spectral content of the confocal sampling volume is measured at each point using a spectrometer instead of a photodiode or CCD. Images are then formed at a given wavelength or across a wavelength band. In this instance, using a spectrometer, each image pixel is digitised into 1044 bins between 400–1200 nm rather than the conventional 3 RGB colour bands.<sup>2</sup> This approach to hyperspectral imaging has previously been used to identify distributed plasmon modes in aggregated AuNP colloids [49] and to image SPPs [216]. By using this technique in the current microscope configuration, as shown in Figure 5.1, LSPs can be spatially identified with sub-diffraction-limited resolutions around 250 nm. Combining it with 80 nm AuNPs also enabled measurement of the microscope PSF and chromatic aberrations, as discussed in chapter 4.2.

Fast image acquisition is made possible by utilising the ultra-high brightness supercontinuum laser source and sensitive, TE-cooled, benchtop spectrometers with 10–20 ms integration times. Image acquisition is limited only by the integration time at each pixel and the ~30 ms movement time between pixels. The focal intensity is, on average,  $\sim 10^5 \text{ W cm}^{-2}$ , which is below the damage threshold for 50 nm metallic tip coatings. The illumination and collection

<sup>2</sup>The 0.8 nm wavelength resolution of spectra classifies this procedure as hyperspectral, as opposed to multi-spectral imaging in which images are formed using fewer, much broader, wavelength bands.

configuration is fixed using a preset reference intensity between different samples in order to more quantitatively compare images. Measured spectra of metallic nanostructures are normalised to a BF reflection spectrum of the same flat metal to show structural effects only, such as plasmons.

While not the fastest or most advanced method of acquiring hyperspectral images, spatial scanning is made efficient when used with a supercontinuum white-light source and images benefit from confocal localisation. Other imaging techniques, categorised under “spectral scanning”, “non-scanning” and “spatio-spectral scanning”, have been developed to more efficiently produce hyperspectral images under specific conditions. Spectral scanning involves wide-field imaging through either a range of bandpass filters [217], a tuneable liquid crystal filter [218, 219] or an etalon [220], which is appropriate if studying large areas or if confocal localisation is not required. Similarly, if optical sectioning is not necessary, samples can be imaged with a single direction line scan using an imaging spectrograph (monochromator with CCD) rather than using a two-dimensional grid scan [206]. Non-scanning or snapshot techniques are more complex and computationally demanding than scanning techniques as both spatial and spectral information are acquired in a single static measurement. Imaging is typically achieved using a computed tomography imaging spectrometer (CTIS) [221–224], in which a 2D dispersive grating placed in the Fourier plane results in spectrally separated images on the CCD. Spatio-spectro scanning is the most recent technique, developed in 2014, and involves diagonally scanning through the sample data cube where each point along an axis in the spatial image has a different wavelength [225].

Despite the potential improvements gained by using more advanced hyperspectral imaging techniques, spatial point scanning is deemed the most appropriate solution for tip characterisation, if only for simplicity and compatibility with dual-tip gap spectroscopy. Scan areas are typically small, benefit from confocal localisation, and image acquisition is not time-constrained since the microscope platform is stable.

---

## 5.2 Understanding Plasmons in Spherical Nanoparticle Tips

---

Hyperspectral images are taken of four different types of AFM probes to investigate the plasmonics of nanostuctured tips. AFM tips studied are Au- and Pt-coated standard AFM probes (BudgetSensors Au-coated AFM probes), spherical Au tips (300 nm Au-coated NanoTools B150 AFM probes) [14] and AuNP-on-Pt AFM probes, fabricated in-house using electrochemical deposition [226]. SEM images of a selection of these tips are shown in Figure 5.2. Fabricated tips are pre-treated where possible prior to use with piranha solution to remove

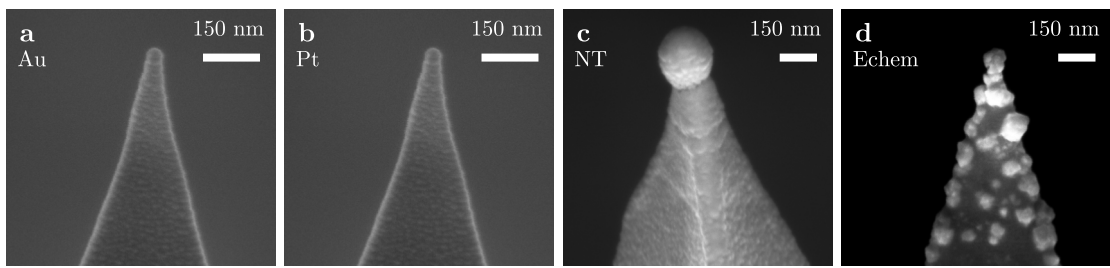


**Figure 5.2: SEM images of sharp and spherical metal tips studied using hyperspectral imaging.** Tips are (a) a sharp Au AFM tip, (b) a sharp Pt AFM tip, (c) a NT Au-coated spherical AFM tip and (d) an electrochemically deposited AuNP-on-Pt AFM tip.

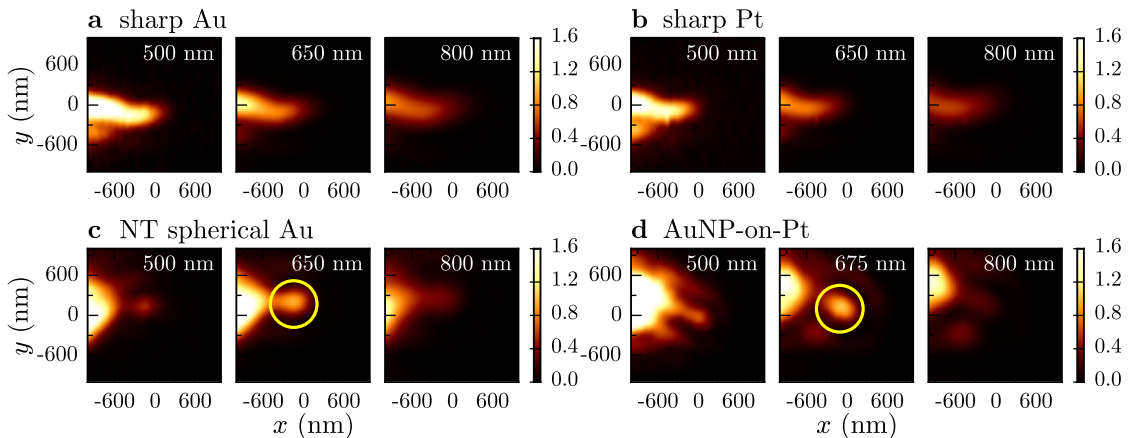


**Figure 5.3: Hyperspectral images of sharp and spherical metal tips at wavelengths of interest.** Images are of (a) a sharp Au tip, (b) a sharp Pt tip, (c) a NanoTools Au-coated spherical tip and (d) an electrochemically deposited AuNP-on-Pt tip. Collection polarisation is along the tip axis. Colour maps between slices all have the same normalisation. Resonant scattering from spherical apices is clearly seen in the hyperspectral images of between 600–700 nm and highlighted by yellow circles.

organic surface residue and, in some cases, smooth surface roughness.

Comparisons between spherical- and sharp-tipped metallic probes using hyperspectral image slices (Figure 5.3) show that spherical Au tips exhibit a characteristic red (600–700 nm) scatter, delocalised from the bulk tip. No similar localised scattering is seen for sharp Au or Pt tips in the visible spectrum, which have an overall weaker optical response. This delocalised apex scatter can also be clearly seen in wide-field DF imaging. The AuNP-on-Pt structure behaves very similarly to the Au-coated diamond-like-carbon spherical tip, likely because the 50 nm coating thickness is greater than the skin depth [129, 227]. Plasmons therefore see both as solid Au spheres. Differences in LSPs likely arise due to differences in neck material with Au-Pt and Au-Au neck boundaries.

Integrating spectra around tip apices better shows scattering resonances in spherical Au tips (Figure 5.4a,b), which are reliably present in all spherical-tipped AFM probes, both vacuum-processed and electrochemically deposited. These are attributed to direct LSP exci-

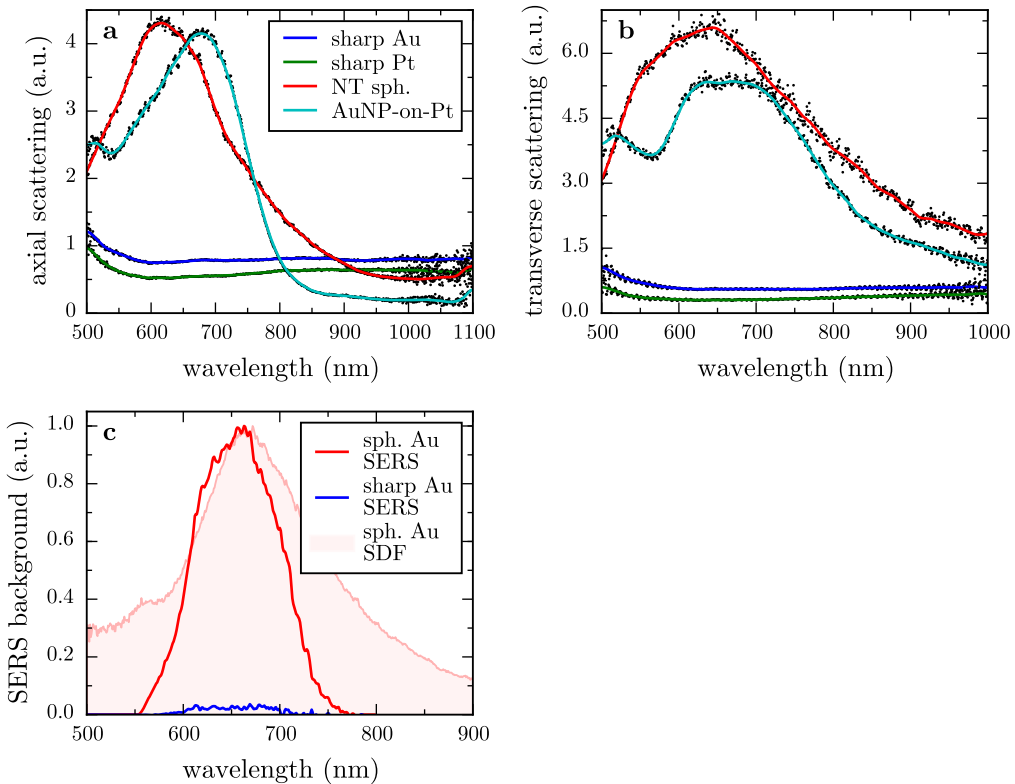


**Figure 5.4: Apex spectra of sharp and spherical metal tips.** Spectra are extracted from the hyperspectral images in Figure 5.3 by integrating pixels around the apex region in both the axial (a) and transverse (b) polarisations. A clear resonance between 600–700 nm is observed with spherical tips in both polarisations. Sharp metallic tips show comparatively flat spectra. Broadband tuneable SERS background measurements of both a sharp and spherical Au tip are integrated across excitation wavelengths spaced 10 nm apart (c) to confirm excitation of an LSP. Inelastic scattering of light from the tip apex is plasmonically enhanced in the near-field. The background spectrum is the SDF scattering spectrum of the spherical Au tip apex.

tation. SEM images confirm that this scatter correlates only with spherical Au tip shapes, or when a AuNP is securely attached at the tip apex with a sufficiently small neck joint. The response of sharp Au tips shows no similar plasmonic features while the slow rise in scattering towards the NIR is consistent with lightning rod scattering [118].

Broadband tuneable SERS [228] is used to confirm that the optical resonance seen in spherical Au tips is indeed a LSP by showing that the internal near-field is resonantly enhanced.<sup>3</sup> During plasmon excitation both internal and external fields are enhanced. The external field leads to strong enhancement of Raman spectra whereas inelastic scatter from electrons inside the metal surface is enhanced by the internal plasmonic field, forming the SERS background [229]. Broadband tuneable SERS is a technique capable of showing both of these components [228]. Hence, the near-field plasmon resonance can be calculated by integrating spectra of the SERS background acquired using a range of equally spaced excitation wavelengths. SERS

<sup>3</sup>Acquisition of broadband tuneable SERS measurements carried out by A. Lombardi.

background spectra are taken in 10 nm increments of the excitation wavelength and integrated between 500–900 nm. The resulting scattering spectrum, shown in Figure 5.4c, shows a distinct peak around the spherical Au tip scattering resonance, confirming it as a LSP resonance. Further, confirmation stems from direct observation of plasmon coupling between spherical tips, as has been previously reported [14], with results of the latest tip coupling experiments discussed in detail in the next chapter.

### 5.2.1 Interpreting the Spectral Response of Metallic Tips

LSPs in spherical Au tips are *radiative* antenna-like modes, similar to those in spherical AuNPs, that can efficiently couple far-field light into strong collective free electron oscillations without the need for SPP momentum matching. As with AuNPs, the signature of these plasmons is a distinct optical resonance indicating their large dipole moment, as seen in Figure 5.4. Such radiative LSPs form only when two close dielectric surfaces surround a metallic particle, allowing for the formation of confined multipolar surface charge oscillations with large dipole moments. Spherical metal tips retain some of the back hemisphere around the connection to the base tip apex (the neck), thus allowing the spherical apex surfaces to sustain similar plasmons. Sharp tips do not have this back surface, hence cannot support such resonances. Their metal-dielectric surface still, however, supports the launching of evanescent SPPs and a strong lightning rod component.

Partial loss of the backside spherical surface and the introduction of a conductive pathway in spherical tips significantly modifies restoring forces and provides a secondary surface for self-interaction. This makes spherical tips difficult to analytically describe. Numerical simulations of the near-field around spherical tips, computed using BEMAX, are instead employed to

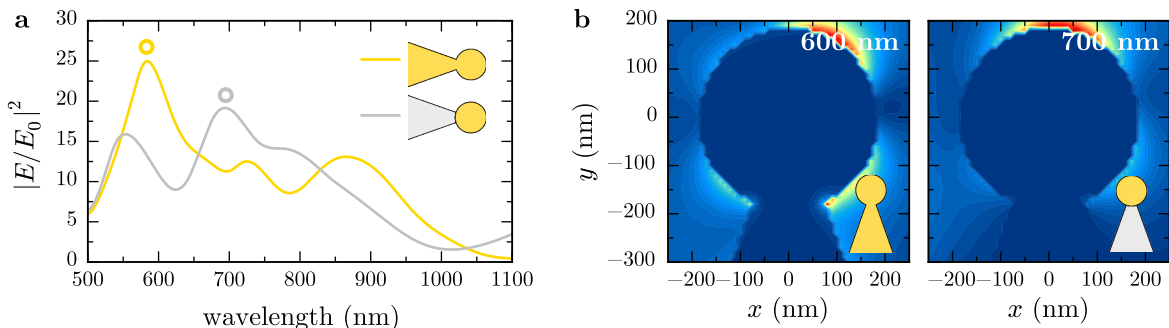


**Figure 5.5: Numerical simulations of the field enhancement around a spherical Au tip.** (a) Near-field spectra of spherical Au and AuNP-on-Pt tips, extracted from around the apex of the tip. (b) Near-field enhancement distributions of the two resonances highlighted by circles in (a). Simulated tips have a 300 nm spherical radii, 120 nm neck widths, 20° opening angles and 1.88  $\mu\text{m}$  lengths to best match typical experimental tip geometries. The field is a plane wave orientated along the tip axis.

better understand their response.<sup>4</sup>

Simulated spectra of the near-field around the apices of 300 nm spherical Au and AuNP-on-Pt tips with 120 nm neck diameters ( $d_{\text{neck}} = 0.4d_{\text{sphere}}$ ) are shown in Figure 5.5a. Tips are simulated with a length of 1.88  $\mu\text{m}$  to avoid truncation artefacts and incident fields are orientated along the tip axis. Strong modes appear for both tips between 550–700 nm similar to experiments. The peak positions of the strongest resonance in each tip approximately agree with experimental spectra. Near-field maps corresponding to the main resonance in each tip are shown in Figure 5.5b. The near-field at the dominant resonance in the spherical Au tip appears more quadrupole-like with a weaker dipole-like resonance occurring above 700 nm. Mie theory shows that visible frequency quadrupolar modes are more favourable in larger AuNPs once dipolar resonances shift into the NIR. A similarly structured mode to the AuNP quadrupole plasmon would be expected in 300 nm spherical Au tips between 500–600 nm. The neck geometry can also potentially short the pole of dipolar plasmons and reduce their confinement, with quadrupolar charge distributions becoming more favourable.

Similar plasmons are found in the AuNP-on-Pt tip except more blueshifted, with a 700 nm resonance appearing more dipole-like and a 550 nm resonance appearing more quadrupole-like. Electromagnetic coupling between Au and Pt surfaces is weaker than the interaction between two Au surfaces [136], hence plasmons in the spherical Au tip are less redshifted when attached to a Pt tip apex. The non-plasmonic Pt neck region also forms an additional boundary interface to better confine plasmons to the tip. As a result, the dipole-like mode exists nearer to the visible and becomes more favourable than the quadrupole-like mode and easier to couple to.

In order to directly compare the *plasmonic* behaviour of spherical Au tips with sharp Au

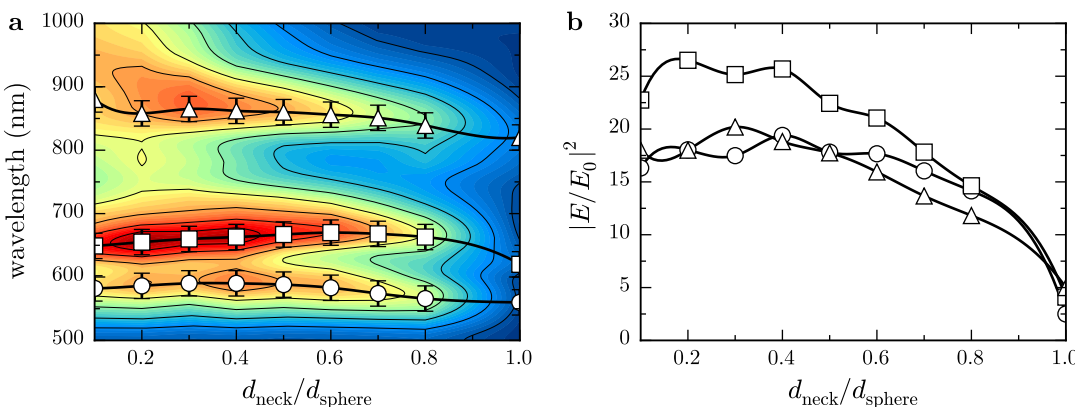


**Figure 5.6: Resonant wavelength and field enhancement dependence on the neck width.** The resonant wavelength (a) and field enhancement (b) for each of the resonances present in spherical Au tips as the neck width is varied between that of a spherical tip and a sharp tip. Tips have a 250 nm apex diameter, 1.88  $\mu\text{m}$  length, and 10° opening angle.

<sup>4</sup>BEMAX simulations carried out by D. O. Sigle.

tips, independent of the lightning rod contribution, the neck width is incrementally increased. In this manner, the simulated structure transitions from a AuNP attached to the apex of a sharp Au tip into a rounded tip geometry, similar in shape to a sharp Au tip, without the apex radius ever changing. The field enhancement and peak positions extracted from this morphology transition are shown in Figure 5.6. Resonances are insensitive to the neck width until it becomes greater than  $0.8d_{\text{sphere}}$ , explaining the robustness of observed spherical tip plasmons between different tip morphologies. A steady decrease in the field enhancement, however, is observed once  $d_{\text{neck}} > 0.4d_{\text{sphere}}$ , decreasing faster once  $d_{\text{neck}} > 0.8d_{\text{sphere}}$ . This supports the claim that sharp tips cannot sustain antenna-like LSPs.

### 5.2.2 Implications of Spherical Metallic Tip Plasmonics

The presented results demonstrate the importance of considering what plasmons might exist in a particular experiment and nanostructure geometry, and that it is vital to characterise nanostructures prior to their application in any further techniques. Without prior knowledge as to where in the visible spectrum plasmons are excited it is difficult to properly interpret any measurements, such as TERS spectra. Improved tip characterisation is crucial to understanding why such varied TERS enhancements are reported. Standard, wide-field microscopy is not a particularly effective tool for optically characterising tips. Confocal hyperspectral imaging, instead, provides a viable method for mapping the local scattering response with broadband tuneable SERS offering a unique way of optically characterising the near-field.

Exploiting visible LSPs in spherical tips also permits the use of a wider range of illumination configurations as the restriction to evanescent coupling is lifted. Regardless of plasmonics, the lightning rod effect will always play a role in the near-field enhancement process, giving sharp tips an initial advantage, but with careful optimisation of the spherical tip geometry, tips can be brought into resonance with a laser wavelength to maximise enhancement. Spherical Au tips in their current form are already quite well optimised for TERS due to being on resonance with the readily available 633 nm HeNe laser wavelength often used.

Plasmons in spherical tips have also been shown to readily couple with plasmons in other spherical tips [14] and would be expected to couple with image charges in a planar mirror, thus significantly increasing their near-field enhancement. In this situation, their resonances can be tracked as the tip approaches the surface and stopped on resonance with the incident TERS laser for maximum enhancement, for example at the common 785 nm excitation wavelength. For small gaps on the nanometre level, the plasmon mode will become strongly confined to the gap and its contribution to the near-field could outweigh the lightning rod effect. Exploiting radiative tip plasmons in this manner bridges the gap between the plasmonics involved in SERS and TERS. Some of the largest enhancement factors recently measured in plasmonic systems originate from radiative plasmons in AuNPs coupled with their image charge distribution in

a mirror [42, 43]. These systems repeatedly produce Raman enhancements of up to  $10^7$  with nanometric mode volumes, much like tips, demonstrating that plasmonic gaps can exhibit large field enhancement without requiring a significant contribution from the lightning rod effect. However, the static nature of the NPoM geometry lacks the ability to chemically map a surface. By coupling plasmons in spherical tips with their mirror charge, surfaces could be dynamically mapped with a potentially very large field enhancement.

This discussion on single tip plasmonics is concluded by performing one measurement specifically relevant to TENOM. To demonstrate the advantages of having prior knowledge of excited plasmons in tips, along with the advantages of using AuNP-on-Pt tips, a TERS measurement is performed directly after characterisation on resonance with a plasmon.

## 5.3 Improved Field Enhancement of Spherical Au Nanoparticle Tips

A result of spherical Au tips sustaining radiative LSPs is that their plasmonic contribution to the field enhancement can outperform the lightning rod contribution in sharp tips (assuming no near-field plasmonic excitation in sharp tips). The field enhancements for both sharp and spherical Au tips, more specifically AuNP-on-Pt tips, are determined in a side illumination configuration using Raman scattering.

SDF spectroscopy is used in conjunction with Raman spectroscopy in a modified version of the microscope platform, enabling both techniques (though not simultaneously). Tips are mounted opposite a second benzenethiol-coated sharp Au AFM tip in a tip-to-tip configuration

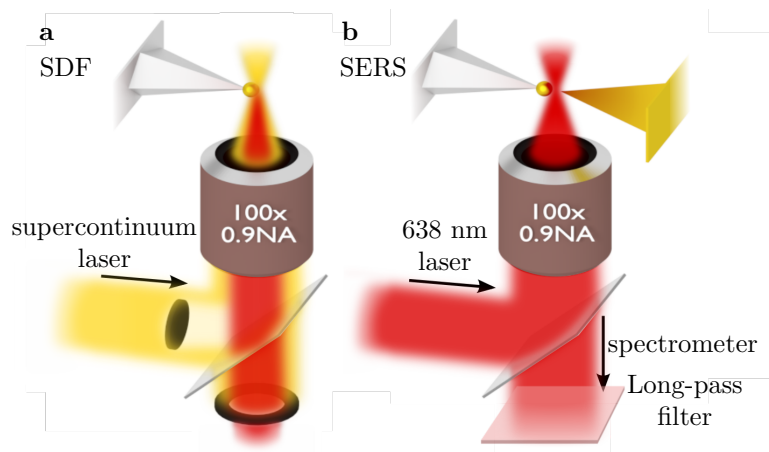


**Figure 5.7: Experimental geometry for dark-field spectroscopy and SERS measurements.** A 125 nm radius spherical AuNP grown onto a Pt-coated AFM tip is spectroscopically studied using a supercontinuum laser in a dark-field configuration (a). The tip is then brought within 1 nm of a benzenethiol-coated sharp Au tip under 638 nm illumination to measure SERS spectra (b).

tion, mimicking a plasmonic bow-tie antenna (Figure 5.7). This configuration is used to obtain good optical access to the intertip gap for spectroscopically probing its plasmonic properties. Benzenethiol (BTh) is used as a Raman marker for measuring the relative field enhancement of AuNP tips due to its strong Raman response and well-known spectra [179, 230]. BTh (VWR International Thiophenol for synthesis) is diluted to 5 mM solutions in ethanol (Sigma-Aldrich). A standard Au-coated AFM tip, for use as a SERS substrate, is prepared by coating a monolayer of BTh onto the surface. This is achieved by submerging it in 100 mM ethanolic BTh solution for 1 min followed by rinsing with ethanol and drying in nitrogen. This is repeated 5 times to ensure complete monolayer coverage. Tips used as plasmonic probes are not coated in BTh.

With the BTh tip retracted, a SDF scattering spectrum of the enhancing tip apex is acquired. After characterisation, the microscope optics are modified into a TERS configuration and the enhancing tip is aligned to the BTh tip using the capacitive alignment technique described in chapter 4.5.<sup>5</sup> Once aligned, the gap size is reduced to  $\sim 1\text{ nm}$ , limited by the thickness of the assembled BTh molecular layer, and illuminated through a  $100 \times 0.9\text{ NA}$  visible objective with  $3\text{ mW}$  ( $1.9\text{ MW cm}^{-2}$ ) of  $638\text{ nm}$  laser light incident on the gap, polarised along the tip axis. Scattered light is collected through the same objective and confocally localised. Raman spectra are filtered using a  $650\text{ nm}$  long-pass filter (Chroma) prior to dispersion in a spectrometer. Contact dynamics, measured using AFM, confirm that tips come into physical contact while separated by a BTh layer.

Near-field calculations for the spherical Au tip are computed for comparison with experimental results and to understand the enhancement mechanism. The near-field distribution at  $633\text{ nm}$  and the spectrum  $1\text{ nm}$  from the apex are calculated using the full electrodynamic boundary-element method [231, 232].<sup>6</sup> The spherical tip is modelled as a Pt cone with half-angle  $20^\circ$  with a  $250\text{ nm}$  diameter AuNP attached to its end. The neck diameter between sphere and tip is  $100\text{ nm}$ . The tip is illuminated with a plane wave polarised along the tip axis.

A  $250\text{ nm}$  diameter spherical AuNP-on-Pt tip, grown as described in chapter 3.2 ( $-8\text{ V}$ ,  $150\text{ ms}$  exposure), is used to demonstrate the augmented plasmonic properties of spherically nanostructured tips. Raman spectra of BTh molecules in the tip dimer gap are greatly enhanced by  $30\times$  when using a AuNP tip in place of a sharp Au tip (Figure 5.8a). As the same spectrometer is used for both broadband scattering spectra and SERS spectra, its restricted spectral resolution ( $300\text{--}1100\text{ nm}$  bandwidth), combined with the relatively broad laser diode linewidth, blurs the characteristic multiple Raman peaks of BTh between  $1000\text{--}1600\text{ cm}^{-1}$ . However the resulting observation of two broad peaks in this region affirms the presence of

<sup>5</sup>The optics are modified in the sense that the laser input is switched, filters are inserted and the dark-field iris is opened.

<sup>6</sup>Near-field calculations carried out by L. O. Herrmann.

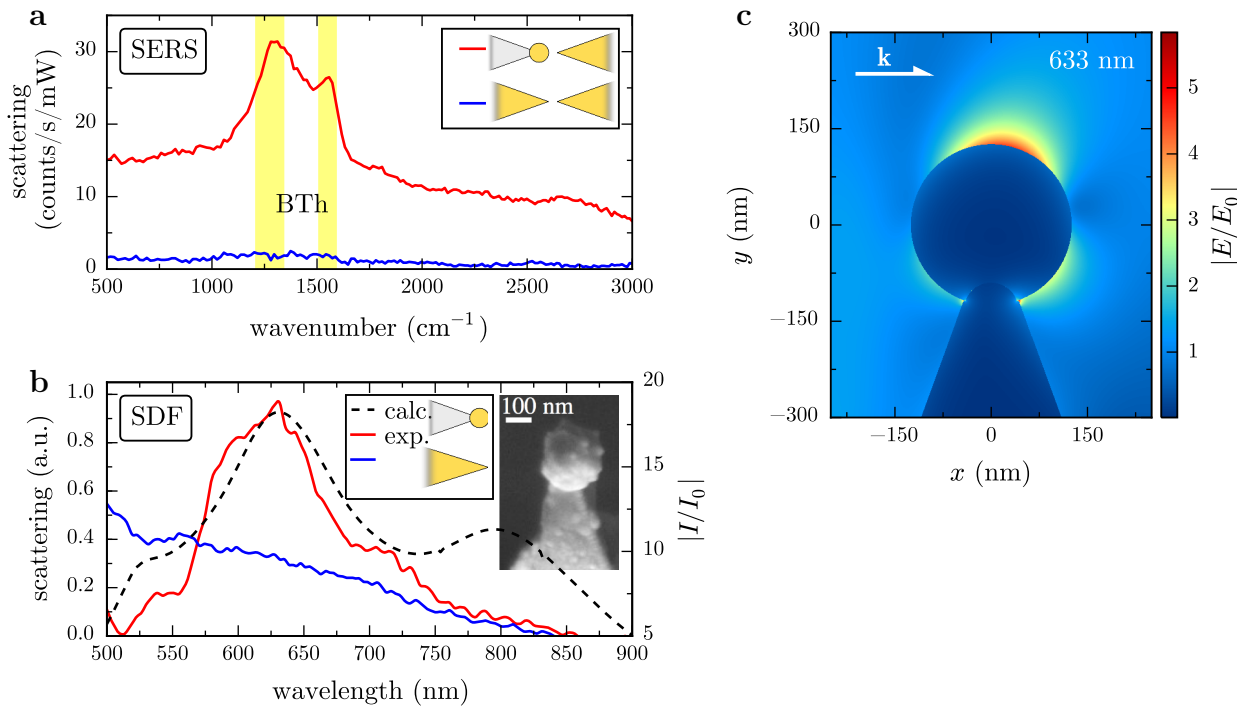


**Figure 5.8: Application of sharp Au and AuNP-on-Pt tips to enhancing Raman scattering.** (a,b) Comparative TERS and dark-field spectroscopy of sharp Au and AuNP tips. (a) Tip-enhanced Raman spectra of a benzenethiol-coated Au AFM probe brought close to the AuNP tip (red), compared to a sharp Au AFM tip (blue). (b) Dark-field optical scattering of AuNP (red) and sharp Au (blue) AFM tips, with calculated relative intensity enhancement 0.5 nm from the AuNP tip apex (dashed). The inset shows an SEM image of the 250 nm AuNP tip. (c) Calculated field enhancement profile for a 250 nm diameter AuNP at the end of a 1500 nm long Pt tip. The neck join is 50 nm wide and the tip is under longitudinally polarised plane wave illumination at 633 nm.

BTh in the gap between tips. Absence of an S-H peak around 2200 cm<sup>-1</sup> suggests good monolayer coverage. The background signal is also enhanced across a broad bandwidth, as is typical for SERS around a plasmon resonance [230].

SDF scattering spectra (Figure 5.8b), taken of individual tips prior to SERS measurements, show that the increased Raman enhancement when using a AuNP tip is due to resonant excitation of a LSP around 630 nm, not present in sharp Au tips. This is in good agreement with boundary element calculations of the near-field enhancement at the AuNP tip apex with a visible plasmon resonance observed across the AuNP (Figure 5.8b,c). Coupling between this LSP in the AuNP tip with a BTh-coated sharp Au tip forms a confined gap plasmon mode. Since coupling is between higher order modes in the sharp Au tip, shifting of this resonance as a function of gap size is weak [139, 233]. A relative SERS enhancement is estimated by taking into account the confinement and mode volume of a LSP in the gap in each case.

LSP mode volumes are estimated using a cylindrical gap mode model. The lateral width of a gap plasmon mode is calculated using  $w = \sqrt{R_{\text{eff}} d}$ , where  $R_{\text{eff}}$  is the effective radius of the particles,  $\sqrt{R_1 R_2}$ , comprising the plasmonic dimer and  $d$  is the width of the gap separating

particles [55]. This results in lateral mode widths of 4.5 nm for the sharp Au tip of 20 nm radius and 7.1 nm for the 125 nm radius AuNP tip. Assuming a cylindrical gap mode yields mode volumes of 15.7 nm<sup>3</sup> and 39.3 nm<sup>3</sup>, respectively. These define the near-field contribution to Raman scattering and a relative field enhancement is obtained using,

$$FE_{\text{rel}} = \frac{N_{\text{AuNP}}/V_{\text{AuNP}}}{N_{\text{tip}}/V_{\text{tip}}} \quad (5.1)$$

where  $N$  is the Raman signal counts and  $V$  is the mode volume. This evaluates to a relative SERS enhancement of 12. Since the LSP is laterally confined to only 7 nm within this gap the enhanced Raman signal is the result of scattering contributions from only a very small number of molecules. Lower limit absolute Raman enhancements are estimated using,

$$FE_{\text{abs}} = \frac{N_{nf}/V_{nf}}{N_{ff}/V_{ff}} \quad (5.2)$$

where  $N_{ff}$ , the number of counts obtained using only far-field laser light, is assumed to be 0.1 counts s<sup>-1</sup> mW<sup>-1</sup> from the noise levels since signals are below the signal to noise level and  $V_{ff}$  is assumed to be 25 000 nm<sup>3</sup> based upon the surface of a conical tip exposed to the focal volume of a diffraction limited spot ( $d = 412$  nm at  $\lambda = 638$  nm). This expression yields absolute, lower-bound Raman enhancements of  $1.9 \times 10^5$  for a 250 nm AuNP tip and  $1.6 \times 10^4$  for a sharp Au tip. Though absolute estimates are not as high as the expected 10<sup>7</sup>–10<sup>8</sup> enhancements reported in the literature [101], the relative SERS enhancement observed with the AuNP tip is indeed comparable to previously reported results [156].

These optical measurements confirm that AuNP tips provide increased field enhancement compared to sharp Au tips due to a strong LSP excitation. Lack of any strong peaks around 600 nm in dark-field spectra of sharp Au tips suggests that any plasmons present are weakly coupled and do not scatter strongly in this illumination geometry, resulting in a lower observed field enhancement. On the other hand, AuNP tips are well suited to high enhancements when illuminated at the appropriate plasmonic resonances. Whilst a number of plasmonic probes have been developed recently, several useful features are obtained here. By using standard AFM probes as a basis, these AuNP tips maintain their functionality as AFM probes for force microscopy. The metallic coating of these tips also allows for simultaneous electrical measurements whilst performing optical and AFM force measurements. These tips therefore function as standard electrical AFM probes with added plasmonic functionality. Furthermore, such tips also show excellent resistance to damage at the tip apex after multiple surface contacts, though surfaces do become deformed after heavy use. Their robust nature is attributed to the direct growth of the AuNP root across the pyramidal tip end. This is a significant improvement over currently-available commercial spherical AFM tips, in which spheres break

from the tip and adhere to the contact surface after only one or a small number of contact cycles. All of this is beneficial for creating a dynamically controllable plasmonic dimer on which to perform measurements in the quantum regime. Further applications of spherical metallic tips can be envisaged, for instance in plasmonic optical trapping [44] because the tips in the present geometry can conveniently act as a heat sink reducing the problematic optical heating observed, and resulting thermal damage.

## 5.4 Conclusions

---

Within this chapter it has been shown that spherical AuNP-tipped AFM probes are capable of supporting radiative LSPs in the red part of the visible spectrum that are not supported by the more conventional, sharp Au tips. These plasmons are clearly observed to exist at the apex of extended tip microstructures using scanning confocal hyperspectral imaging in the SDF microscope platform to locally probe the optical response. Broadband tuneable SERS is used to further confirm plasmonic behaviour in spherical Au tips. These techniques are ones that enable plasmon-dependent applications, such as TERS, to pre-screen nanostructured tips to better improve their reliability and reproducibility. The development of antenna-like plasmons in tips through nanostructuring, which readily couple to light without the need for momentum matching, is a step forward for TENOM. Furthermore, these modes determine what plasmonic phenomena are able to be experimentally observed, hence spherical tips can be used to dynamically investigate plasmonics.



# Chapter 6

## Plasmon Interactions in Tip Dimers

The final set of experiments discussed in this thesis are the product of each of the developments from previous chapters, utilising pairs of tips in the microscope platform to investigate the limits of plasmon coupling. Coupling between different tip morphologies is dynamically investigated to both confirm plasmonic behaviour in tips and increase understanding of the characteristic regimes of plasmon coupling, including the recently uncovered quantum regime. Through this work an improved interpretation of future results in sub-nm plasmonic gaps can be attained.

### 6.1 Experimental Measurements of Dynamic Tip Dimers

Dynamic interactions and separation-dependent phenomena between two tips are spectroscopically studied using an axial scanning approach. Tips are coupled with another tip in order to maximise optical accessibility to the gap. Although not representing the typical geometry used in TENOM this presents a more optimal geometry to explore plasmonic coupling on a more fundamental level. Tips are first aligned into the dimer configuration under the supercontinuum laser beam using the capacitive technique described in chapter 4.5. Alignment takes place with the laser illumination on to prevent spatial changes to the tip apices, caused by thermal expansion, from occurring post-alignment when spectroscopy is performed.<sup>1</sup> The tip of the stiffer cantilever of the pair is partially positioned in the laser spot and the tip of the softer cantilever is resonantly driven and used as the alignment probe, beginning at distances outside of the laser focus. Sufficient space is left after placement of the stationary tip to accommodate both tip apices equally under the laser spot once brought together. This level of positioning is subjective, with scattering intensity used to estimate an acceptable position for the stationary tip within the collection spot. Once alignment is complete the separation between tips is reduced from around  $\sim 300\text{ nm}$  to geometrical contact whilst undergoing measurement.

<sup>1</sup>This behaviour was briefly looked at, with laser-induced cantilever deflection being measured in tips. This suggested that the heat of the focus was causing mechanical deforming or bending of the AFM probe, moving the lateral position of the tip apex and misaligning the tip dimer prior to gap coupling experiments.

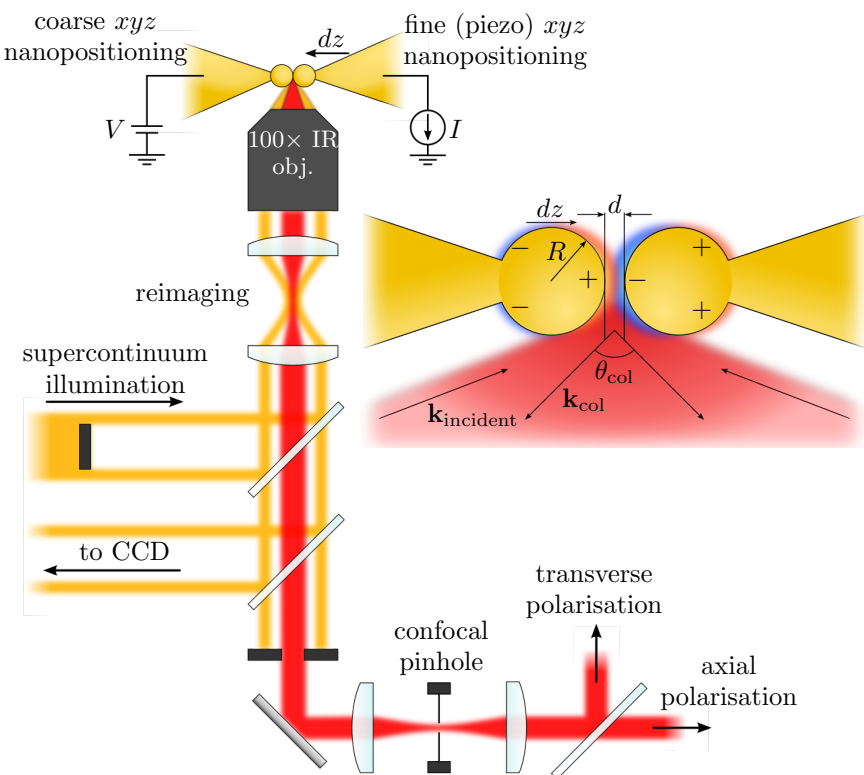


**Figure 6.1: Experiment configuration for axial tip scanning.** The laser is centred on the aligned tip dimer for gap spectroscopy. The soft cantilever approaches the stationary, stiff cantilever at a controllable rate  $dz \text{ nm s}^{-1}$ . A bias is applied across the tip junction and the current through the gap is measured. The soft cantilever faces the AFM module for force measurement via cantilever deflection. A diagram of tip dimer characteristics is shown as an inset. The diagram specifically shows the case for a spherical Au tip dimer, showing the antenna plasmon modes which couple together. Plasmonic coupling depends on both the gap size,  $d$ , and the particle radius,  $R$ . The illumination and collection angles, defining  $\mathbf{k}_{\text{incident}}$  and  $\mathbf{k}_{\text{col}}$ , are  $\theta_{\text{incident}} = \sin^{-1}(0.6 - 0.8NA)$  and  $\theta_{\text{col}} < \sin^{-1}(0.6NA)$ .

The tips used in experiments, whether commercial or fabricated in-house, are required to have clean metallic surfaces when studying gap plasmon interactions. Layers of insulating surface molecules prevent the gap from narrowing sufficiently to enter the quantum regime, therefore any layers deposited as either a byproduct of a chemical reaction or from carbon deposition in SEM need to be removed. This is done through either plasma cleaning or piranha treatment. To maintain cleanliness some experiments are performed in a nitrogen flow environment.

During scanning measurements on tip dimers, the stationary tip acts as the optical probe, staying fixed in the collection spot throughout the scan, whilst the other tip approaches at a rate of  $0.1\text{--}1 \text{ nm s}^{-1}$ . Approach speeds are continually adjusted and optimised during scanning to reduce the time interval between completion of alignment and achieving geometrical contact and minimise any potential lateral drift. Use of a stiffer cantilever ensures that the AFM tip remains fixed in its current position under the laser spot, even once under pressure from the

opposite tip. Measurements of the optical scattering, electronic conductance and applied force are taken at each point in the scan. The geometry of this experiment is shown in Figure 6.1. The approaching tip perturbs the near-field and interacts with the probe tip. Separation-dependent optical scattering is then collected through the objective collection aperture. Strong scattering of the intense supercontinuum source means 10–20 ms integration times are sufficient for a high quality signal to noise, therefore spectra acquisition does not affect the scan speed. Only light polarised along the tip dimer axis is reported in the context of this work in order to focus on the influence of charge transfer on coupled gap plasmons.

Simultaneous measurement of gap conductance and applied force supplement optical scattering measurements, enabling correlations to be made between characteristic gap properties to better interpret the relationship between charge transfer and plasmonic coupling.<sup>2</sup> Electronic properties are probed by driving with a d.c. voltage and measuring the current through the tip junction to determine its conductance. A bias of 50 mV is almost always used to achieve good signal quality in both low-bandwidth and high-bandwidth conductance measurements and to prevent spikes in the noise from setting off the high-bandwidth trigger. Larger voltages increase the electrostatic pull between tips, visible in force measurements, and the resulting high current upon contact would damage tips if not for the current limiting resistor. The smallest current range is fixed at 10 nA, with a sensitivity of 10 fA, since lesser ranges require longer settling times, slowing the scan rate. At 50 mV the smallest measurable conductance is around  $10^{-7}G_0$ .

The applied force is measured using optical detection of cantilever deflection by the AFM module. At each step in the scan the position of the returning laser beam is averaged for 100 ms to determine the mean cantilever deflection, and therefore the mean applied force, over the duration of electronics and optics measurements. Using this combination of measurements allows for a more informed interpretation of nanoscale gap behaviour than by measuring only the optical scattering, as was done originally [14].

### 6.1.1 Non-Optical Properties of a Nano-Tip Dimer Gap

Before studying the optical properties of nano-gaps it is beneficial to understand the range of physical phenomena that exist on each characteristic length scale present during scans that traverse from  $\sim 100$  nm to 0.1 nm. With tips well separated, only the separation and optical scattering are meaningful physical quantities. The optical scattering, if plasmonic in origin, is subject to a separation-dependent capacitive interaction. There is no current and no applied force until the separation reduces to below  $\mathcal{O}(10)$  nm. Below this point both the current and

---

<sup>2</sup>Each measurement is ran in parallel using multiprocessing in the experiment control method, with each taking a fixed amount of acquisition time. Multiprocessing not only allows data to be acquired around the same time but also decreases the overall measurement time.

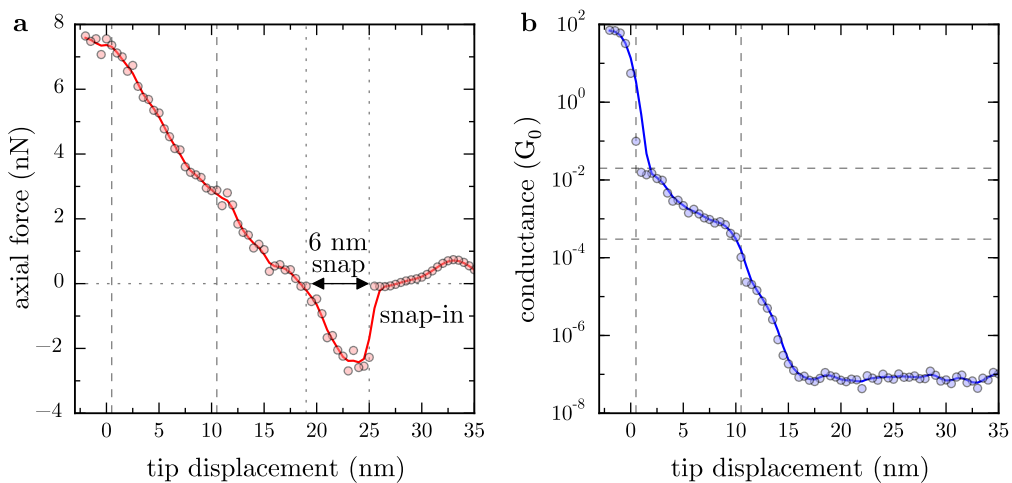


**Figure 6.2: Axial force and conductance measurements of a sharp Au tip dimer approaching into contact.** The characteristic AFM snap-in effect is seen in the axial force (a) as a discontinuous jump before the linear application of force in a soft contact regime. The tip apices snap together, reducing the separation to on the order of 1 nm, leading to the onset of quantum tunnelling, and finally conductive contact, upon further decreasing the gap separation (b). Dashed and dotted lines are added as guides to the eye showing different features in the scan, such as snap-in and conductance behaviour.

the force become instrumental in understanding the optical response. Due to the maturity of AFM, STM and molecular electronics there is already a wealth of information explaining both electronic effects and the forces expected on these length scales.

Figure 6.2 shows the conductance and axial force measurements from a typical scan once separation has passed below 10 nm. The force shows no features until there is a fast negative (attractive) jump in the applied force, showing that the tip has been pulled towards the opposing tip (Figure 6.2a). This is the signature of water in gap. The lack of a tunnelling current at this point shows that tips must still be separated by more than 1 nm. The actual extent of these snaps varies between scans depending on a number of factors, including the humidity, with some scans snapping in closer than 1 nm.

Since experiments are carried out in ambient conditions the surfaces of tips will always be coated in a thin film of water or nanobubbles. Even in a nitrogen environment, its presence is only reduced and not completely removed. When two surfaces come into close proximity a water meniscus forms between them, leading to strong capillary forces [234]. Hence, when the separation between the two tips reduces past the point of meniscus formation they are quickly pulled together [235]. This is known in AFM as the “snap-in” or “snap-into-contact” and occurs on separations  $\sim$ 5–30 nm [235, 236]. In the above scan the snap distance can be inferred from the displacement required to remove the applied force as 6 nm.

To prevent snap-in either a stiffer cantilever must be used (normally in tapping mode) [237] or the water meniscus has to be removed, which is usually achieved through liquid immersion AFM [236, 238, 239] or by using plasma treatment to remove hydrophobic contamination

[236]. In this instance, however, the water layer is advantageous. The presence of the meniscus prevents immediate electrical and geometrical contact and holds tips around 1 nm apart until further force is applied. Approach of the tips then occurs in much finer increments due to mechanical resistance from the water. This effectively splits a scan into three regimes - one in which the decreasing intertip separation is directly controlled, one after snap-in where cantilever displacement gradually pushes the tip through the water meniscus (soft interaction), and finally one in which force is applied directly to the opposite tip in geometrical contact (hard-wall contact).

The existence of the soft interaction regime enables sub-nm gaps to be studied with some degree of control since only a fraction of the applied cantilever displacement corresponds to a displacement at the apex. Instead, the meniscus is loaded with an applied force, leading to the linear reverse deflection observed in AFM force measurements. This can be seen in Figure 6.2a where 15 nm of cantilever displacement moves the apex  $\sim$ 0.8–0.9 nm (deduced from electron tunnelling measurements). The remaining 14.2 nm loads the gap with 8 nN of force, proportional to the cantilever's spring constant.

Use of soft AFM probes (contact mode cantilevers) means a greater spatial resolution in the sub-nm regime since force is applied more gently with cantilever displacement.<sup>3</sup> Softer cantilevers are also advantageous during tip alignment as they have larger oscillation amplitudes, and therefore lower voltages are needed to reach acceptable signal quality, and also lower bandwidth requirements (13 kHz as opposed to 190–300 kHz). For these reasons, along with those directly related to tip alignment capabilities (outlined in chapter 4.5), one tip in the dimer is usually a contact mode probe while the other tip, which must remain stationary under an applied force, is a stiffer tapping mode probe. Early experiments exclusively used contact mode cantilevers until determining that spectral changes could not be guaranteed to originate from the gap under the application of a large force.

Despite their usefulness in showing the relative motion of the tip, force measurements are somewhat limited in their information on the absolute separation. An estimate of the absolute separation is made possible by studying charge transfer in the gap. Electron tunnelling is the dominant charge transfer mechanism, occurring prior to conductive contact with the current due to tunnelling follows an approximately exponential decay with increasing separation. The conductance in STM is often stated to drop by approximately a factor 10 for every 1 Å away from conductive (approximately geometrical) contact. This relation permits deduction of the gap separation to a certain degree using the order of magnitude of the gap conductance.

Upon reducing the gap to below 1 nm electron tunnelling becomes detectable. Though the absolute value of the conductance for a given separation depends on the gap morphology the relative exponential conductance drop from geometrical contact still approximately holds

---

<sup>3</sup>Smaller  $k$  means larger  $x$  required for  $F = kx$  to meet the same target value.

for  $d > 2 \text{ \AA}$  [75]. This makes electron tunnelling a useful method for estimating the gap size to within  $\sim 0.1 \text{ nm}$ . Once the separation is greater than  $1 \text{ nm}$  the conductance drops to below around  $10^{-9}G_0$  and the corresponding current becomes difficult to measure without significantly raising the d.c. bias. For example, use of a  $50 \text{ mV}$  bias means a current on the order of  $1 \text{ fA}$ , which remains below the currently achievable noise level.

Figure 6.2b shows a typical conductance trace on approach. Once the separation decreases below  $1 \text{ nm}$  the conductance steadily increases with force from  $10^{-7}$  to around  $10^{-4}G_0$  as the tips transition through the soft interaction regime. At  $10^{-4}G_0$ , the rate of conductance increase slows, signifying the compacting of the meniscus into a single monolayer of water, which requires a greater force to displace. At  $10^{-2}G_0$  the separation is estimated to be similar in size to a single water molecule ( $2.75 \text{ \AA}$ ), which, when displaced, causes tips to quickly transition into geometrical contact, saturating with a contact conductance around  $100G_0$ . The displacement of this final gap layer and consequent relief of force on the tip is shown by a decrease in the force gradient during the transition into contact.

Each of the electronic and force measurements described in this section are instrumental in discerning the underlying phenomena occurring in sub-nm gaps. These measurements can then be correlated with optical spectra and used to interpret changes to plasmon coupling, especially changes that depend sensitively on gap morphology or dielectric medium. Using this information, more accurate physical models can be developed to further understand the quantum regime of plasmon coupling than what currently exist.

## 6.2 Plasmonic Coupling Between Tips

Plasmonic interactions between tips are studied using the dimer approach. Two AFM tips are dynamically brought together to form a single gap structure, mimicking a plasmonic dimer cavity, whilst the optical scattering, conductance and force are simultaneously measured. The resulting experiment geometry is shown as an inset in Figure 6.1. Both sharp and spherical Au tips are studied in a range of dimer permutations, in order to understand how plasmons in each tip couple. This is also compared with results from hyperspectral characterisation, indicating whether plasmons initially exist in such structures.

### 6.2.1 Sharp Tip Dimer Interactions

The first combination of AFM tips studied is a sharp Au tip interacting with another sharp Au tip. Hyperspectral characterisation indicates that sharp Au tips lack any observable LSPs. Similarly for dimer experiments, no observable coupling is expected despite the possibility that gap modes may exist. Reducing the separation between two sharp Au tips indeed shows no

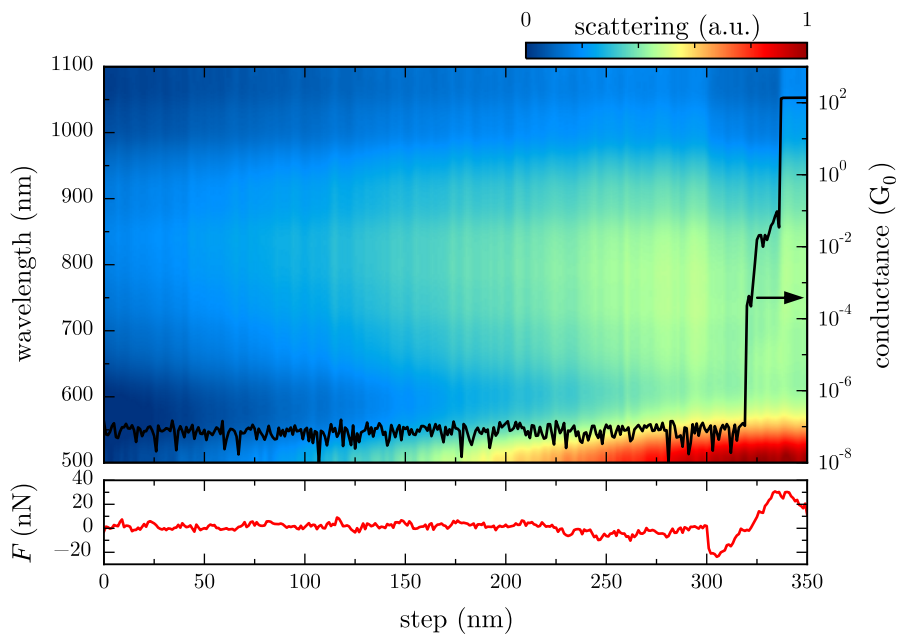


**Figure 6.3: Spectra of a sharp Au tip approaching a stationary sharp Au tip.** Sharp Au tips are BudgetSensors GB series AFM probes. There are no identifiable plasmon resonances initially in the system and no new modes appear with decreasing gap size. The lack of any shifting suggests that plasmons are not present in the system. The increase in intensity and its spectral shape are an artefact of adding more of the reflective tip facet into the confocal collection aperture.

resonances or coupled modes (Figure 6.3). Scattering increases are seen, however these do not shift with decreased separation or change with conductance. They are instead attributed to more of the reflective tip facet entering the confocal collection aperture as the tip is approached to the stationary tip. Spectral scattering increases also bear resemblance to the spectral density of the illumination and intensity changes correlate well with changes in the torsional force, further supporting this claim.

Tunnelling currents are observed to have no effect on scattering from the gap, despite reports suggesting that tunnelling electrons excite plasmons [104, 240–244]. The reason for this is the small 50 mV bias. The excitation condition  $\hbar\omega < eV$  is not satisfied for visible frequencies and hence only low energy SPPs in the IR could be excited.<sup>4</sup> Using higher voltages around 2 V would give a finite probability that an electron would excite an SPP, with intensity depending on the current through the junction and the collection geometry.<sup>5</sup> In the current geometry only localised gap modes could be observed since the system lacks a means of measuring SPP leakage radiation. Furthermore, reports detecting radiation from localised gap modes have used sensitive CCDs with long integrations. Hence, within this system when using 10 ms integration times, it is unlikely that tunnelling-induced radiation will be detected.

<sup>4</sup>For a 50 mV voltage the limiting frequency is  $7.6 \times 10^{13}$  rads, or  $\lambda = 24.8 \mu\text{m}$  deep in the IR.

<sup>5</sup>For a 2 V voltage the limiting frequency is  $3.0 \times 10^{15}$  rads, or  $\lambda = 630 \text{ nm}$ . Hence plasmons can be excited in the red frequencies of the visible spectrum and below.

The conclusions drawn from these experiments agree with those of individual sharp Au tip spectroscopy. Sharp Au tips do not show any evidence of supporting plasmons which readily couple with light and there have been no detected signatures of plasmon coupling between similar tips. However, both the gap geometry and previous spectroscopic (spectroscopy, TERS and electrical excitation) measurements on tips suggest that plasmons and gap modes can exist in such geometries. It can only be stated that, based on the measurements shown here, only radiative antenna-like plasmons can be seen in the far-field and that tips are not capable of supporting these. Further tests outside the scope of the work discussed in this thesis would be required to test for SPP excitation and how these effect the underlying mechanisms of TENOM.

In order to optically probe plasmon coupling in a sub-nm cavity between two tips, a tip geometry which couples with far-field light is required. Sharp Au tips are clearly inadequate for this purpose. For this reason the spherical tip geometry, with its visible wavelength plasmon resonances, facilitates the dynamic study of plasmonic coupling in nanoscopic gaps.

### 6.2.2 Spherical Tip Dimer Interactions

By using spherical Au tips the tip-tip system mimics the prototypical spherical AuNP dimer. It is through this arrangement that a controllable plasmonic dimer is recreated. The presence of radiative plasmons, discussed in chapter 5, enables the detection of gap modes as tips transition from the non-interacting regime at  $\sim 300$  nm through into the charge transfer regime before entering conductive contact. By utilising such a controllable plasmonic system, plasmon coupling can be better understood on a fundamental level and unravel the remaining questions regarding plasmonics in sub-nm gaps.

#### Spherical Tip Interactions with a Spherical Tip

The first configuration of spherical tips studied is that of a spherical Au tip approaching another spherical Au tip. In this instance the 600–650 nm LSPs of the individual tips interact and form observable gap modes. Representative scans of two approaching spherical Au tips are shown in Figure 6.4, in which plasmon resonances are dynamically followed from non-interacting to classically coupled. It should be noted that in previous microscope designs the short-range tip alignment meant that plasmons were only seen once in a coupled state near 750 nm [14]. Improvements to the range of the tip alignment technique using optical detection have allowed the full range of plasmon coupling to be studied.

Coupling between spherical tips appears very similar to that of a large nanoparticle dimer. Plasmons are initially uncoupled and only the single LSP of the probed tip is observed. Plasmons begin to interact at  $d \approx R_{\text{tip}} = 150$  nm as is classically expected, where  $d$  is estimated

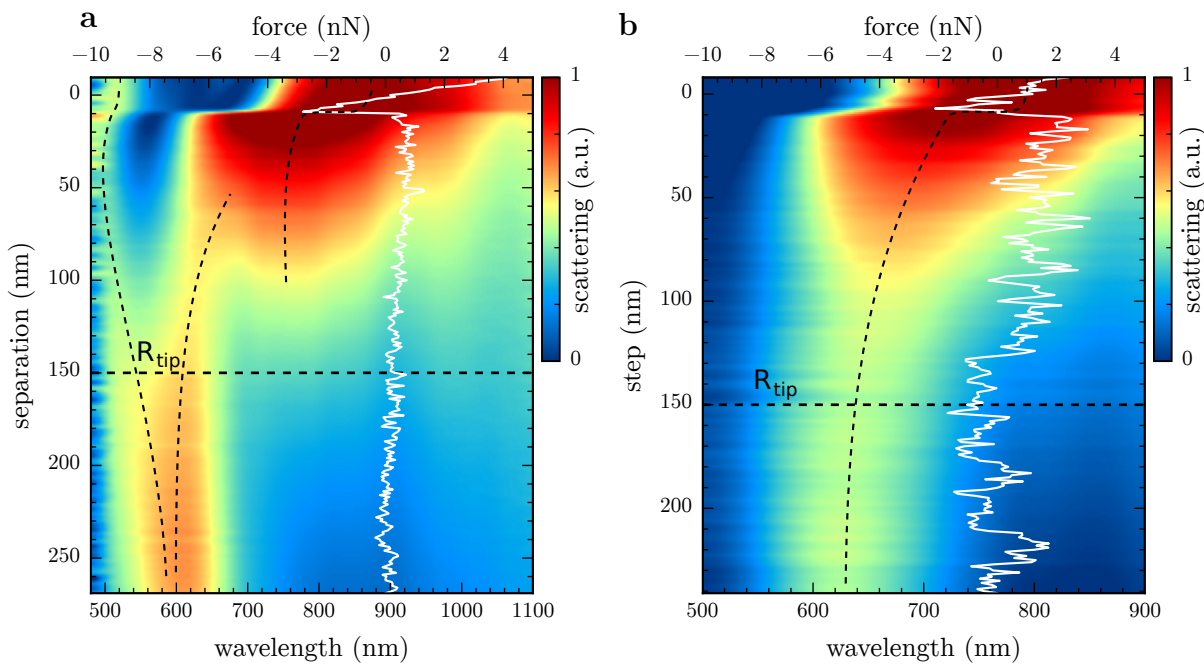


**Figure 6.4: Spectra of a spherical Au tip approaching a stationary spherical Au tip.** Spherical Au tips are Au-coated NanoTools B150 AFM probes. Two scans are presented in the classical interaction regime, showing similar phenomena. The separation is estimated based on known tip displacements to the point of snap-in. Guides to the eye are added to highlight mode behaviour. Horizontal dashed lines indicate the radius separation, at which point coupling is expected to begin. In both cases, but more clear in (b) with tips having similar initial LSPs, bonding hybridised modes form, which redshift with decreasing intertip separation (increasing coupling). With slightly dissimilar initial LSPs anti-bonding hybridisation can be seen as a blueshifting mode with decreasing intertip separation.

based on the point of snap-in. As the gap width decreases the individual plasmon modes increasingly couple together, redshifting monotonically and scattering increasingly. The initial plasmon mode at 630 nm redshifts to around 800 nm in each scan at the point of snap-in, where the separation is reduced to around 1 nm. Increased scattering is due to both increasing coupling and an increased amount of scattering metal entering the confocal sampling volume of the objective. Once the gap has decreased sufficiently ( $d \ll R_{\text{tip}}$ ) the confocal collection argument is negligible as the sampling volume becomes saturated, hence all further changes are due to plasmon coupling in the gap.

For large distances the rate of redshift is dominated by the increase in capacitive coupling as the separation decreases. In each scan a large abrupt redshift of the coupled mode correlates with snap-in. The large redshift on snap-in is due in part to two effects: the decrease in separation as the tip is pulled in by capillary forces and the increase in refractive index as the gap constitution transitions from air to water (and any material contained in the water meniscus). The intensity of the lowest order mode begins to decrease once the gap width decreases below 1 nm. This effect is attributed to the mode becoming increasingly confined

to the point of becoming non-radiative. Similar changes in mode intensity are often seen in classical simulations and occur well before the onset of any significant quantum effects [14, 75].

Slightly different classical coupling physics is observed when the dimer symmetry is broken. In some cases where initial tip resonances differ by  $\sim 50$  nm coupling is better described by a heterodimer model rather than a homodimer. Under the asymmetrical condition, anti-bonding modes can be excited due to phase retardation and are no longer dark since dipoles do not exactly cancel. Depending on which particle is probed, either the one supporting the lower or higher energy initial resonance, either a redshifting bonding mode or a blueshifting anti-bonding mode is observed to be the dominant gap resonance (see Figure 2.8 and [65]). The tip dimer probed in Figure 6.4a clearly exhibits both mode configurations and is a good representation of what is seen across many additional scans.

This effect has been documented previously [65] but never directly observed dynamically. The anti-bonding configuration is typically non-physical in most plasmonic systems since both particles are driven with the same phase of light. However, with larger particles, such as these 150 nm radius spherical Au tips, the phase symmetry is broken allowing anti-bonding hybridised plasmons to be excited. Both the blueshift and the later redshift at small separations are found in spherical tip scans, indicating the interaction and anti-crossing between the lower order anti-bonding mode and the higher order, adjacent bonding mode. The higher order bonding modes responsible for this are then seen after snap-in.

### Spherical Tip Interactions with a Sharp Tip

The interaction between the same spherical Au tip and a sharp Au tip is investigated with results shown in Figure 6.5. Despite the sharp tip perturbing the field around the spherical tip,

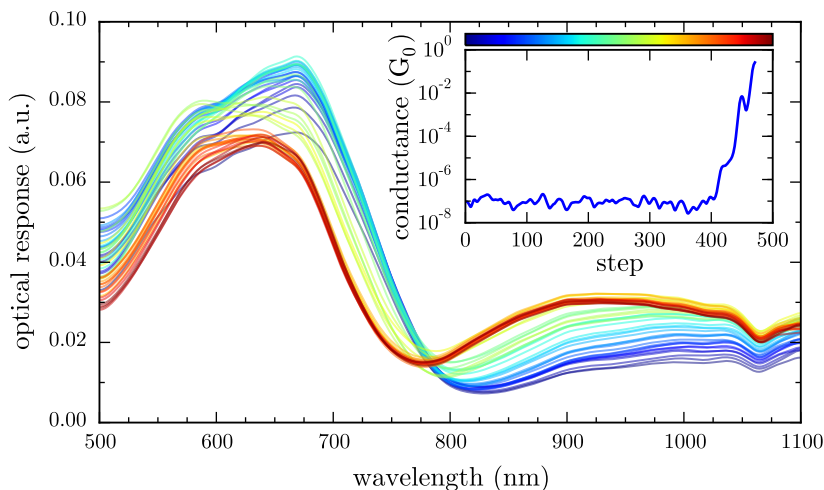


**Figure 6.5: Spectra of a spherical Au tip approaching a stationary sharp Au tip.** No coupling phenomena are observed due to the mismatch between plasmon modes.

acting as the optical antenna, no changes are observed in the spherical tip plasmon, suggesting that there is no interaction between sharp tips and spherical tip plasmons. This is in agreement with predictions that a sharp tip should not deviate the resonance of a planar surface [139, 233], for which the much larger tip could be considered. The tip acts as a point perturbation not strong enough to significantly modify the more distributed antenna-like response. This observation also supports the measurements shown in chapter 5.3, where the laser was assumed to stay on resonance with the AuNP tip as it approached the BTh-coated sharp Au tip.

## 6.3 Quantum Effects in Sub-nm Gaps between Spherical-Tipped AFM Probes

---

Quantum effects in plasmonic nanogaps become readily observable upon forming a sub-nm gap between spherical tip surfaces. By monitoring the electrical current simultaneously with the optical scattering the effects of quantum charge transfer can be directly inferred under the assumption that the conductance is similar at both d.c. and optical frequencies. Using this approach, the quantum limitations to plasmon coupling are observed in full for the first time. This section discusses the now readily attainable regime of plasmonics in sub-nm gaps. The investigation into the effects of quantum charge transport on plasmon coupling is the culmination of all previous developments to date, yielding some of the most interesting results of this project.

To briefly reiterate theory for separations below 1 nm gaps are expected to be in the tunnelling (crossover) regime, a progressive transition into electrical contact where classical theory fails due to the onset of quantum tunnelling. Gaps are characterised by a thin barrier between particles with a growing probability for electrons incident on the barrier to tunnel through it. Non-locality of electrons smears gap surfaces on the quantum level, and long-range interactions round the potential barrier in the gap. Tunnelling-induced charge transfer neutralises charge on the gap surfaces and reduces electromagnetic coupling. This decreases, and eventually halts, the rate of redshift and is otherwise known as the screening effect. Upon decreasing the separation past a critical gap separation (between 0.1–0.3 nm) time dimer passes through a critical conductivity threshold and enters the CTP (conductive) regime. In quantum simulations the threshold appears at the point where the increasingly overlapping barrier edges cause the central potential barrier region to drop below the Fermi level, creating a conductive constriction [80]. In QCM simulations all effects are attributed to an increasing quantum tunnelling current prior to conductive contact [14, 70, 75]. The increased currents below the critical separation cause gap plasmons to further decouple, blueshifting their resonances as they progressively transform into CTPs.

To date, estimations of a critical separation for the onset of conductive effects in larger AuNP dimers vary between 0.2–0.3 nm [14, 70, 75, 80, 82] depending on the specific dimer geometry and materials. However, this is by no means a fundamental quantity and therefore not the most appropriate standard by which to compare experiments. For example, a plasmonic nanogap fixed by a molecular spacer layer can exhibit conductive regime characteristics at much larger gap widths [79, 86]. The critical separation is simply the point at which rate of charge transfer overpowers capacitive interaction. A set of critical conductances should therefore exist for entry into each respective regime of quantum interaction, irrespective of gap size, that more fundamentally describe the effects of (quantum) charge transport on plasmon coupling.

As theory has previously suggested, critical conductances at optical frequencies are a more appropriate way of describing the regimes of charge transfer behaviour [73, 88]. Experimentally this proves incredibly difficult. In a sense, plasmonics is the only way of measuring an optical conductance since electronics cannot respond fast enough to measure currents at optical frequencies. One reason as to why charge transfer effects should be understood is therefore to enable the application of plasmonics as a method of measuring conductance at frequencies where current electronic technologies fail. At this time however, the d.c. current through the gap is measured as an approximation to the true electronic behaviour at optical frequencies and functions as a comparison with the effects seen optically. Using this, the current set of experiments explore the concept of critical conductances as the definitive way of interpreting charge transfer in plasmonic systems.

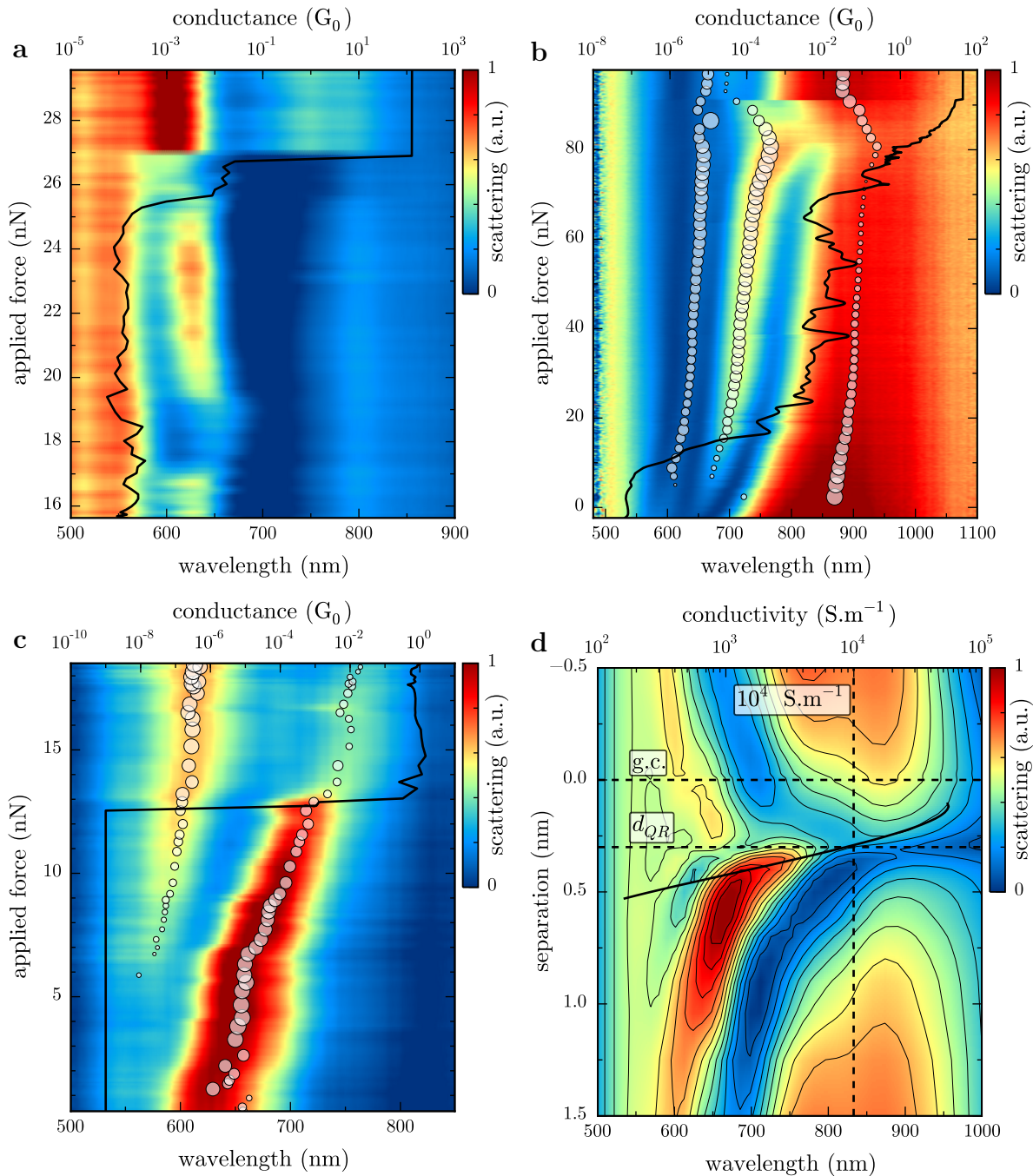
### 6.3.1 Observations of Quantum Charge Transport in Plasmonic Cavities

Figure 6.6 shows a selection of spherical Au tip dimer measurements showing both optical and electronic behaviour once in the sub-nm regime. Simultaneous quantum transport and SDF scattering measurements are presented as a function of the applied force compressing the gap. Each set of measurements exhibits the characteristic quantum regime transition between hybridised gap plasmons and charge transfer plasmons. However, comparison between sub-nm gaps formed in different tip dimers proves more difficult as the positions and shifts of plasmon resonances can behave very differently, regardless of any similar agreement between scans in previous coupling regimes. These differences are thought to originate from surface roughness or even smaller differences in nanoscale surface morphology that effect the way optics and electronics couple [80, 87].<sup>6</sup>

Figures 6.6a and 6.6b bear the closest resemblance to recent theory, showing both screening and CTP formation through the quantum regime (the original QCM spectra of sub-nm

---

<sup>6</sup>Changes in CTP position and intensity are said to originate from the touching profile of the dimer, indicating that the surface roughness may play a role with such large dimer surfaces [80, 87].



**Figure 6.6: Scans of multiple spherical tip dimers passing through the quantum regime and pushing towards geometrical contact.** Scans (a–c) show optical (SDF) scattering spectra as a function of the applied force on the gap with simultaneously measured conductance superimposed. The circles highlight the position of the peak with their size indicating the amplitude from a fitted model. Scans (a) and (b) use Au-coated NanoTools B150 spherical AFM probes to form a dimer while (c) uses electrochemically-fabricated AuNP-on-Pt AFM tips. Calculated QCM spectra of a spherical tip dimer as a function of separation, replotted from [14], is shown in (d). Simulated spectra show both coupled modes disappearing prior to geometrical contact (g.c.) at a critical separation  $d_{QR} = 0.31 \text{ nm}$ , shortly followed by the rise of CTP modes. Based on DFT calculations the critical conductivity is  $10^4 \text{ S.m}^{-1}$  ( $0.4 G_0 \text{ nm}^{-2}$ ). These effects are seen in experimental scans once the conductance surpasses  $2G_0$ .

gaps between spherical Au tips from [14] is replotted in Figure 6.6d with the DFT-calculated conductivity overlaid). Experimental plasmon modes appear at similar wavelengths to QCM predictions. Screening is indicated by a reduction in the rate of redshift and a decrease in scattering intensity. A blueshifting transition between coupled plasmons and emerging CTPs signifies the rise of stronger interparticle currents. The unseen fundamental CTP is expected to exist in the IR, outside the measurable spectral range of the current microscope, though the tip's neck joint may short this mode and prevent its existence. The behaviour of hybridised modes and higher order CTPs is thus used to interpret gap behaviour.

In both experiments, the redshift of each coupled mode becomes stunted with the onset of tunnelling, revealing that the conductance has risen sufficiently to begin screening gap coupling. The point of blueshift is less clear in Figure 6.6a due to the fast transition into geometrical contact. This jump is experienced in almost all scans and is attributed to a combination of the electrostatic pull between tips and a sudden decrease in mechanical resistance once the water molecules in the gap are displaced. The approach shown in Figure 6.6b is much more carefully controlled going into geometrical contact and provides a much clearer insight into the origins of the blueshift. The scan is likely the single most informative scan, containing many measurements in both the tunnelling and conductive regimes, including clear observation of discretely quantised conductance channels. It is at the transition between tunnelling and ballistic conduction, at around  $2G_0$ , that the blueshift of plasmon resonances begins to occur and tips enter the quantum conductive regime. This is in good agreement with the principles underpinning quantum theoretical models [80].

A better view of this transition is shown in Figure 6.7a with a linear conductance scale in order to closer inspect charge transfer behaviour. The turning point in the redshift of both coupled plasmons visually appears to occur at  $2G_0$ . Fitting spectra and extracting the behaviour of each individual mode provides a more quantitative analysis. The results of the fit are superimposed onto spectra in Figure 6.7a with fit parameters shown separately in Figure 6.7b. Mode positions approximately follow an exponential model as expected. At  $2 \times 10^{-3}G_0$  the plasmon redshifts, along with their amplitudes and widths, deviate from this model and becomes less pronounced, indicating entry into the tunnelling regime of plasmonics. Prior to this point the amplitude of the lower order mode is decreasing, likely due to increasing charge localisation. Upon passing through this first critical conductance at  $2 \times 10^{-3}G_0$  the amplitude is further screened and decreases faster. The higher order mode continues to gain intensity at this point, potentially from redistributed charge of the lowest order mode. Similar behaviour is found in the mode widths.

The second critical conductance occurs at  $2G_0$ , just after transitioning from tunnelling into a quantum conductive regime, i.e. once the Fermi level is above the gap barrier. Upon surpassing  $2G_0$  the resonance positions of both coupled plasmons begin to strongly blueshift

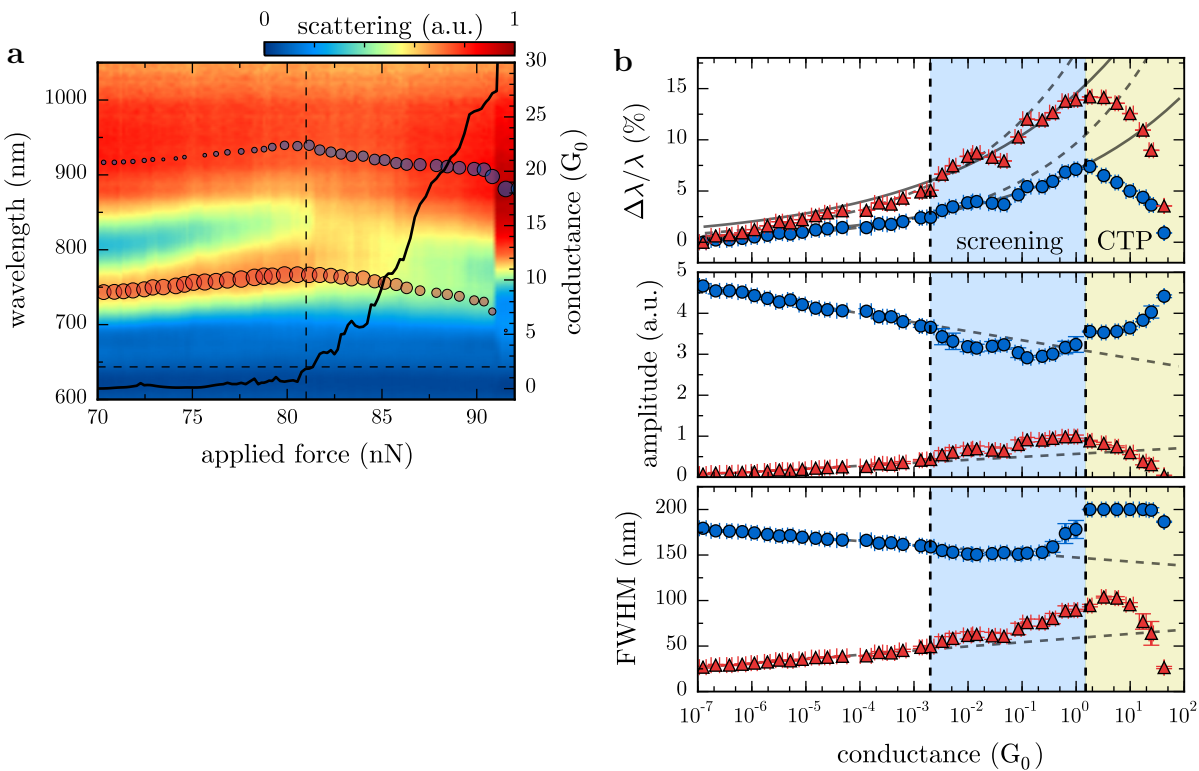


**Figure 6.7: Detailed analysis of a spherical Au tip dimer scan in the quantum charge transfer regime.** The scan shown in Figure 6.6b is replotted in (a) with a linear conductance scale to show quantised conductance stepping and its relationship with scattering spectra. Dashed lines indicate the point of blueshift at  $G = 2G_0$ . Peak positions in the fitted model are denoted by circles superimposed onto spectra with their size corresponding to the peak amplitude. The relative shifts, amplitudes and widths of each mode from fitted parameters are plotted in (b). Vertical dashed lines highlight the transitions into the tunnelling (crossover) regime at  $2 \times 10^{-3}G_0$  and the conductive regime at  $1.5G_0$ . Exponential curves are fitted to the wavelength shift for  $G < 10^{-3}G_0$  (dashed) and  $G > 2 \times 10^{-3}G_0$  (solid) to highlight the reduction in redshift caused by passing through the screening (tunnelling) threshold. Similar lines are plotted to show changes in the amplitude and width upon passing through  $2 \times 10^{-3}G_0$ .

into CTPs as current passes through the junction, quickly returning to their initial resonance positions prior to entering the tunnelling regime. During this transition the intensity and width of the lowest energy plasmon begins to increase, while the higher order plasmon attenuates into only a weak, blueshifted resonance. This CTP becomes fully developed during the final pull into geometrical contact.

Despite integer quantised conductance being observed in the early conductive regime, there is no obvious step-wise shifting of plasmon resonances. It would be intuitive to expect quantised current changes to discretise incremental blueshifts, however this appears not to be the case with the blueshift appearing smooth throughout. More experimental and theoretical data would be needed to properly understand this phenomenon.

Both sets of measurements at the focus of this discussion are not without their issues,

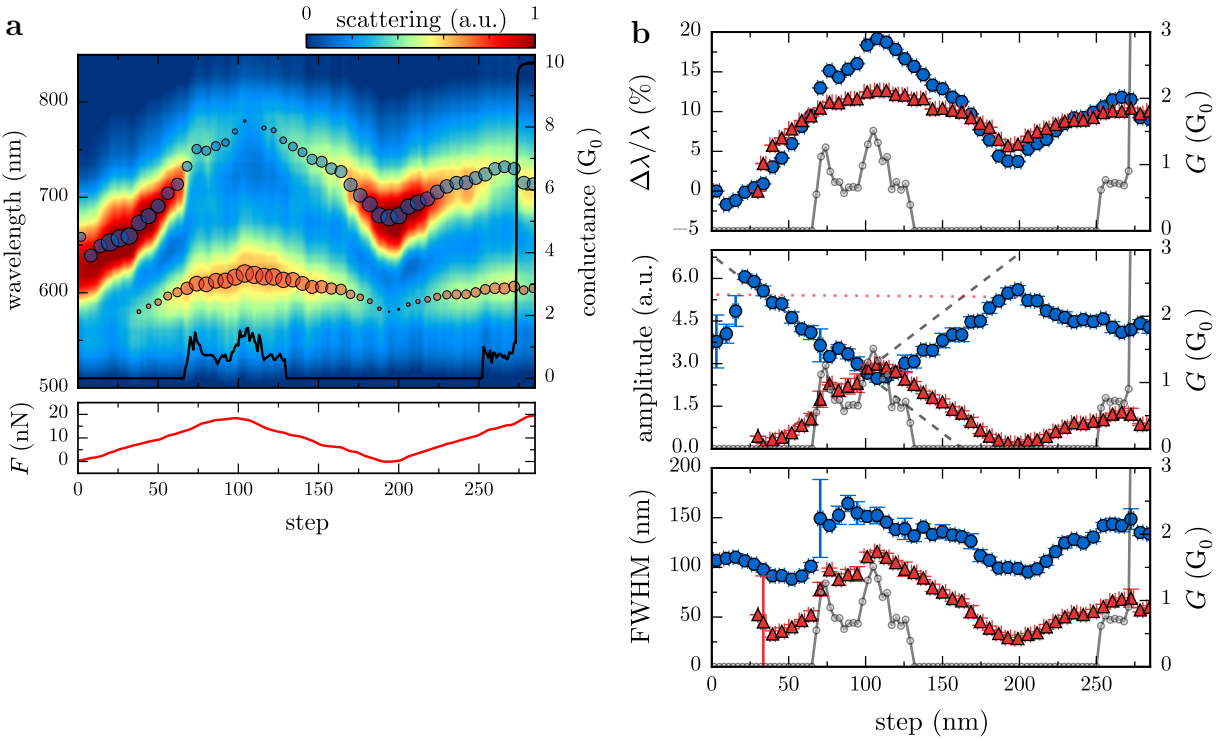
however, when compared with both theory and previous experimental results. Figure 6.6a shows variations in both the position and intensity of the 600 nm mode, which are attributed to changes in the torsional force on the gap, corresponding to a rotational motion of the tip. The mode also does not appear to shift as much as expected. The intensities of the final two modes when in contact are also reversed compared with QCM predictions. Figure 6.6b looks remarkably closer to theory.

Figure 6.6c shows a somewhat different phenomena to previous scans, though still in line with expectations and bearing an interesting similarity with higher order plasmons in QCM spectra. Tips in Figure 6.6c are highly asymmetric AuNP-on-Pt tips, smoothed using piranha solution. Both cantilevers have  $40 \text{ N m}^{-1}$  spring constants, hence the force resolution during approach is limited. Prior to tunnelling a higher order mode begins to emerge. The transition into contact is quick, with few to zero points at any given conductance, ending initially with a stable  $0.75\text{--}1.5G_0$  contact. The initial LSP resonance quickly diminishes with the rise of the conductance without blueshifting and the higher order resonance gains intensity. The screening here is another example of entering into a tunnelling regime but without sufficient current to enter into the conductive regime and form CTPs.

After the initial conductance increase, the tip is immediately retracted to test for reproducibility, as shown in the extended scan plot in Figure 6.8a. This is made possible by the robustness of electrochemically fabricated tips, with their solid AuNP apices. Attempting this with commercial, spherical Au tips results in the spherical apex separating from the neck due to adhesion forces. A second approach of the tip immediately after retracting out of contact demonstrates the same phenomenon until the conductance rises above  $2G_0$ , at which point both modes blueshift. Changes in the redshift and amplitude gradient show the effects of surface morphology as retraction introduces a small degree of misalignment. This changes the conductance channels in the local electronic landscape and how they interact with the plasmon field.

A detailed mode analysis of plasmon resonances is shown in Figure 6.8b. Shifting of plasmon resonances behaves as expected. Upon increasing the conductance up to the  $1G_0$  level there is a visible reduction in the rate of redshift caused by screening. Once the conductance abruptly rises above  $2G_0$  in the second approach there is a clear blueshift in the lowest order mode, alluding to a similar critical conductance. An interesting feature in this instance is that the extracted amplitude of the initial mode linearly decreases during approach at exactly the same rate as the new mode emerges. In a sense, charge is conserved and simply switches to a more favourable mode as the gap width decreases and tunnelling rate increases.

To summarise, each of the presented three scans shows agreement with recent theoretical concepts that predict the effects of quantum mechanical charge transfer on plasmon coupling. Four different plasmonic regimes related to charge transfer can be identified: classical coupling



**Figure 6.8: Detailed analysis of the extended electrochemically-fabricated spherical AuNP-on-Pt tip dimer scan.** An extended plot of the scan shown in Figure 6.6c is plotted in (a), demonstrating reproducibility in approaches. The applied force trace represents separation changes between tips, with tips approached, retracted and then finally approached into geometrical contact. Peak positions in the fitted model are denoted by circles superimposed onto spectra with their size corresponding to the peak amplitude. The relative shifts, amplitudes and widths of each mode from fitted parameters are plotted in (b). Reduced rates of redshift are found in the  $G \sim 1G_0$  regions with a discontinuous blueshift seen after the  $G > 2G_0$  transition. Linear rates of amplitude variation are revealed from peak fits after removing the width contribution from the peak intensity. A dotted red line shows the constant sum of the amplitudes. The FWHM of each mode initially increases with conductance.

in the absence of charge transfer, a quantum tunnelling regime, a quantum (ballistic) conductive regime and, finally, a classical conductive regime. Tunnelling is responsible for screening whereas conductive contact leads to the progressive formation of CTPs. Critical conductances for entering the tunnelling regime and the quantum conductive regime are observed in each case in the vicinity of  $2 \times 10^{-3}G_0$  and  $2G_0$ , respectively. This is the first time conductance values have been experimentally correlated with optical spectra using a dynamic approach to plasmon coupling.

Critical conductances are expected to hold outside of the quantum regime similar to the previously defined screening and CTP conductance thresholds [72, 73]. Comparison with previously explored systems shows excellent agreement, supporting the idea of critical conductances. Blueshifts of the BDP, forming the SBDP, begin to be seen in small  $2G_0$  conductive contacts in both theoretical models [72, 73] and experimental NPoM systems when AuNPs

are separated from a Au mirror by a blended SAM of variable conductance [88]. Observation of the same threshold conductance in two very different experimental systems provides strong evidence for the fundamental nature of critical conductances. Using this information, the plasmonics of a sub-nm plasmon system can begin to be better characterised and quantified with the aim to finally exploit plasmonics to measure optical conductivities.

## 6.4 Conclusions

---

Multiple different combinations of tips in a dimer configuration are used to probe plasmon coupling. Sharp Au tips exhibit no obvious plasmon resonances under far-field illumination and no gap mode coupling is observed with other sharp or spherical Au tips. This is caused by the lack of an antenna-like geometry in sharp tips. Plasmons excited at the apex of spherical Au tips, on the other hand, interact and form coupled modes. The behaviour of these modes is as expected, with similarity to plasmons in AuNP dimers. The inherent asymmetry between the large spherical tip structures leads to more complex scattering spectra wherein anti-bonding modes are no longer dark. Their spatial evolution into gap modes is something not previously seen before within a single plasmonic system.

To conclude experimental work, tip dimers are used to investigate the quantum regime of plasmonic coupling, specifically the effects of quantum charge transport. Using this approach, the development of the quantum regime is dynamically observed. Critical conductances are estimated for the onset of each characteristic effect using direct correlations between optical spectra and current measurements. Measurements agree well with theoretical principles. Though no quantitative measurements, such as temperature, voltage or power dependences, are made to guarantee the exact mechanisms of charge transport, quantum tunnelling and ballistic conductance are the most likely mechanisms. Further investigation could quantify this, although charge transfer phenomena are not expected to depend on the specific conduction mechanism. Comparison with tip dimers coated in different molecular layers of varying conductivities would add further understanding into the effects of charge transfer and forms the basis of future experiments on this topic.

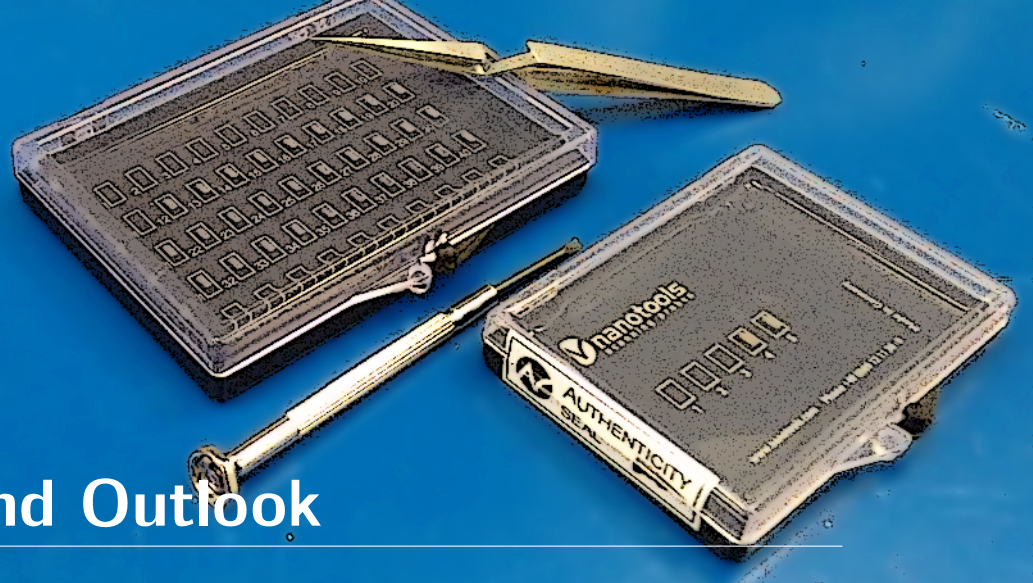
In summary, the existence of two distinct regimes of quantum charge transport have been detected in sub-nm plasmonic cavities. These are:

- The tunnelling regime (also known as the crossover regime), wherein electrons tunnelling through the gap barrier screens the local capacitive interaction between opposite gap surfaces, reducing plasmon coupling strength and slowing the associated redshift to a halt.
- The conductive regime, where strong currents at  $G_0$ -level conductances heavily attenuate

gap plasmons and lead to the previously observed blueshift transition into charge transfer plasmons.

Though numerous theoretically predictions and experiments have been reported in recent years, this is the first time that correlated experimental measurements between plasmon resonances and conductance have been performed to understand quantum effects in plasmonic systems.





## Chapter 7

# Conclusions and Outlook

This project has focussed on the understanding and application of tips for plasmonics, with the aim to use tips to further understand the recently revealed sub-nm regime of plasmonic coupling. Though the initial motivation was to investigate the quantum regime of plasmonic coupling, the project diversified into studying the optical differences between sharp and spherical tips using techniques such as hyperspectral imaging and plasmon coupling, the development of an electrochemical method as an alternative approach to producing spherical tips and the application of plasmonic tips for TERS. Finally, spherical tips were applied to investigate quantum effects in the sub-nm plasmonic coupling regime. Work was therefore split between three core areas: development of plasmonic tips, design and construction of a custom microscope for tip experiments, and ultimately performing experiments on combined tip systems.

Failure to observe any plasmonic behaviour in the far-field optical spectra of sharp Au AFM tips, despite their prominence in many near-field enhancing techniques, led to the investigation into nanostructured tip geometries. By nanostructuring an AFM tip, some of the well-known antenna-like properties of isolated plasmonic nanoparticles are transferred into the AFM probe form factor. Knowing that the particular tip nanostructure and optical geometry set which plasmons are radiative, and can therefore be experimentally observed, the spherical geometry was chosen for its simplicity. Both commercially-available spherical Au tips, used in previous tip plasmonics experiments, and AuNP-on-Pt tips, fabricated in-house using a newly developed pulsed electrodeposition procedure, are studied. Pulsed electrodeposition was chosen for its ability to exploit the sharp apex of AFM tips and quickly produce nanostructured tips. The technique was developed from its initial conception through to beginning the optimisation of each parameter in order to improve the process reliability and gain control of the tip morphology. Due to time constraints and the significant effort required to complete other aspects of this project, controllable electrochemical growth of spherically-tipped AFM probes was only partially optimised but produced enough samples to facilitate experiments. Further work is still needed to understand the exact mechanism by which nanoparticles nucleate and grow at and around the apex and optimise each growth parameter. Achieving this would enable a large number of varied studies into the application of plasmonic tips for TENOM - a

direction of research only touched upon in current work.

The optical study of AFM tips and the continued probing of dynamic plasmon coupling through each interaction regime necessitated the design of a custom microscope capable of combining the function and stability of two opposing AFM devices with a platform for broadband dark-field spectroscopy. The novel design and robust performance of the microscope has been discussed at length and quantified where appropriate. The comprehensive design of the dual-tip platform meant experiments could implement optical, electronic and force measurements for a more complete characterisation of plasmonic systems than is capable in many other experimental setups. Specifically, the combination of hyperspectral imaging and scanning capacitance microscopy enabled the alignment of AFM tips to each other and to the focus of the incident beam, resulting in a highly reproducible plasmonic dimer arrangement. Additionally, the modular design of the microscope and its array of possible measurements make it adaptable and extensible for many other (future) experiments. Within the scope of this project its main use has been to perform experiments on AFM tips.

Observations of strong optical resonances in spherical Au tips were attributed to radiative localised surface plasmon excitation - a feature not found in sharp metallic tips. The agreement between apex spectra extracted from hyperspectral imaging, broadband tuneable SERS and dynamic plasmon coupling experiments confirm that spherical metallic tips support antenna-like plasmons similar to those in individual nanoparticles, while sharp metallic tips remain unresponsive to light. The spherical Au tip LSP conveniently exists at the commonly used HeNe wavelength leading to enhanced Raman scattering efficiencies,  $30\times$  that of a sharp Au tip. This improvement is a step towards better exploiting controlled nanostructuring of tips for more enhanced and reliable sensing, and promoting radiative approaches to TENOM. However, direct comparison with evanescent excitation methods has not been performed and conclusions remain speculative for the time being.

The final sets of measurements used pairs of spherical Au tips to target the sub-nm coupling regime. The onset of quantum effects on plasmonic coupling was investigated in ambient conditions, surpassing the earlier experiments performed by Savage et al. [14]. The addition of tunnelling conductance and gap force measurements greatly increased the amount of information extracted from the dimer system to better understand the physics of sub-nm gaps. The robust design of the microscope platform enabled many successful scans through the quantum regime. Measurements showed both the screening of coupled plasmons followed by their transformation into CTPs, correlated with the onset of quantum tunnelling and ballistic transport. Observations are in general agreement with the principles underlying recent quantum theoretical descriptions of the quantum regime though further theoretical affirmation of these results is still required. Results strongly suggest the existence of critical conductances which determine the points at which key effects are seen in the quantum regime, a feature

which should be further investigated in this and many other systems.

## 7.1 Outlook and Future Directions

---

The experiments carried out have both demonstrated the appeal of nanostructured tips and expanded upon the rich regime of quantum plasmonics for further exploration. This project concludes at a pivotal point at which sub-nm gaps can reliably be probed using a newly-developed microscope platform. Within the current experimental system there is still scope for many further projects and many questions regarding the effects of quantum mechanics on plasmonics still require answers. Experimental parameters, such as temperature, humidity (gap water content), gap chemical composition (monolayers on tips) and applied bias (non-linear electrical control of coupled plasmons), are currently controllable but investigations into their effects on quantum-scale plasmonic gaps have yet to begin. Other parameters, such as pressure (vacuum), would require some adaptation but investigations remain possible.

Even in its current state the microscope platform could be used to perform a range of new and interesting experiments. Use of an electrical excitation mechanism has yet to be tested but is a realistic aim that could yield interesting results and background-free spectroscopy. Coating tips in both conductive and insulating molecules could be an effective method for determining critical conductances, with direct comparison to recent NPoM systems involving gap spacers [42, 54, 83, 88]. Coupling a tip with its mirror charge in an opposing cantilever is also a potential route for dynamically testing plasmonic interactions with molecular spacers. Each of these would provide a new insight into plasmonics on a fundamental level.

Though all results presented within this project focus on large, spherical Au tips, the developed tip fabrication and characterisation techniques are not limited to a specific metal or geometry. It would be interesting to measure and quantitatively compare the scattering response and field enhancement of spherical tips with carefully controlled sphere and neck sizes to validate theoretical predictions, and grow other sphere materials such as Ag, Cu or Al, if such materials electrochemically deposit in a similar manner to Au. A small amount of work was started, with some success, applying pulsed electrodeposition to deposit metal nanostructures other than Au on other conductive AFM tips, such as highly-doped Si. If successful this would facilitate the production of plasmonic probes resonant across a wide range of visible-NIR frequencies.

Finally, more controllable confirmation of quantum effects in plasmonic systems could become possible using 2D electron gases (2DEGs), the systems initially used to discover quantised conductivity [245, 246], and those currently being explored for plasmonics at THz frequencies [247–249]. By gating a biased 2DEG a region can be electrically depleted to form a 1D constriction through which ballistic transport occurs. Thus, by gating a plasmonic 2DEG,

it could be controllably depleted to pass through both capacitively coupled and conductive regimes.

To conclude, the recently accessible boundary between the capacitive coupling and charge transfer regimes of plasmonics has been successfully probed and continues to display a wealth of interesting physics. Dynamically controlling the particle positions of an AFM tip dimer has become a powerful experimental technique for the study of such physics. Since smaller gaps, blended with molecular electronics, have begun to become experimentally attainable, the results of these latest experiments are expected to be of great interest to the general plasmonics community. From the point of view of fundamental plasmonics, they provide an insight into a largely unknown regime of plasmonics whilst from an applied aspect they indicate both the limitations of plasmonic sensing and a potential new method for measuring electronic transport at optical frequencies.

# Appendix A

## Supplementary Theory

---

### A.1 Mie Theory

---

Mie theory [39] is used to calculate the scattering cross section of MNPs outside of the quasistatic regime. In Mie theory, solutions for EM scattering from a spherical particle are given as a superposition of spherical waves generated by electrical and magnetic multipoles. The amplitude of each electrical and magnetic multipole of order  $l$  is given by,

$$a_l = \frac{M\Psi_l(Mx)\Psi'_l(x) - \Psi_l'(Mx)\Psi_l(x)}{M\Psi_l(Mx)\xi'_l(x) - \Psi_l'(Mx)\xi_l(x)}, \quad (\text{A.1a})$$

$$b_l = \frac{\Psi_l(Mx)\Psi'_l(x) - M\Psi'_l(Mx)\Psi_l(x)}{\Psi_l(Mx)\xi'_l(x) - M\Psi'_l(Mx)\xi_l(x)}, \quad (\text{A.1b})$$

respectively, where  $x = n\pi D/\lambda$  is the size parameter,  $n$  is the refractive index,  $D$  is the particle diameter,  $M = (\varepsilon/\varepsilon_d)^2$ ,  $\Psi_l$  and  $\xi_l$  are  $l$ -order Riccati-Bessel and Hankel functions, respectively, and  $l$  is the degree of spherical harmonic (multipolar distribution). The extinction and scattering cross sections are then calculated using the multipolar expansion,

$$\sigma_{\text{ext}} = \frac{2\pi}{k^2} \sum_{l=1}^{\infty} (2l+1) \text{Re}[a_l + b_l], \quad (\text{A.2a})$$

$$\sigma_{\text{scat}} = \frac{2\pi}{k^2} \sum_{l=1}^{\infty} (2l+1) (|a_l|^2 + |b_l|^2). \quad (\text{A.2b})$$

The results of scattering calculations for AuNPs are shown in the main text.

### A.2 Quantum Charge Transport

---

One of main discussions of this work is the effect of quantum charge transport on plasmon coupling. Both quantum tunnelling and ballistic transport are qualitatively described in the

main text for simplicity. The following section shows the relevant mathematical derivations of the simplest cases of quantum tunnelling and ballistic transport.

### A.2.1 Quantum Electron Tunnelling

Electron tunnelling is predicted by the time-independent Schrödinger equation for an electron impinging upon a simple rectangular potential barrier, in which,

$$-\frac{\hbar^2}{2m^*} \frac{d^2\psi(x)}{dx^2} + V(x)\psi(x) = E\psi(x), \quad (\text{A.3})$$

where  $m^*$  is the effective electron mass,  $V(x)$  is the local potential (either zero or the barrier height  $V_0$  depending on the region) and  $E$  is the electron energy. A propagating electron incident on the barrier with a wavefunction  $\psi = e^{ikx}$  has an energy given by,

$$E = \frac{\hbar^2 k^2}{2m^*}. \quad (\text{A.4})$$

Inside the barrier the wavefunction decays as  $e^{-\beta x}$  where,

$$\beta^2 = \frac{2m^*}{\hbar^2}(V_0 - E). \quad (\text{A.5})$$

The transmission probability of the electron passing through the barrier is calculated in the WKB approximation as [76],

$$T(E) = \exp \left\{ -2 \int_0^{d_0} \beta(x) dx \right\}, \quad (\text{A.6})$$

$$= \exp \left\{ -2 \left[ \frac{2m^*}{\hbar^2}(V_0 - E) \right]^{\frac{1}{2}} d_0 \right\}, \quad (\text{A.7})$$

where  $d_0$  is the barrier width. Though assuming a simple rectangular barrier, Eq. A.7 shows the characteristic exponential dependence of electron tunnelling.

### A.2.2 Ballistic Conduction

A 1D constriction between two charge reservoirs of length  $L$  and width  $W$  can be described as either diffusive if  $l, l_\phi \ll L, W$ , ballistic if  $l, l_\phi \gg L, W$ , or quasi-ballistic if inbetween, where  $l$  and  $l_\phi$  are the mean free path and phase coherence length, respectively. Conductance in the diffusive regime is as classically expected,  $G = \sigma_{2D}W/L$ . In the ballistic regime, however, it

inherits quantum properties as is thus given by the Landauer formula,

$$G = \frac{2e^2}{h} T(E_F), \quad (\text{A.8})$$

where  $T(E_F)$  is the transmission coefficient of an electron at the Fermi level. This is derived from the current flowing through a barrier between two biased reservoirs, whereby the Fermi levels are related via  $E_{F,L} - E_{F,R} = eV$ . The leftwards current through a barrier is given by,

$$I_L = 2e \int_0^\infty f(E(k), E_{F,L}) v(k) T(k) \frac{dk}{2\pi}, \quad (\text{A.9})$$

where  $f(E, E_F)$  is the Fermi-Dirac function and the wavevector of an electron can be related to its energy via  $dE = \hbar v dk$ . Converting Eq. A.9 to an energy basis and adding the rightwards current yields,

$$I_L = \frac{2e}{h} \int_{E_L}^\infty [f(E(k), E_{F,L}) - f(E(k), E_{F,R})] T(E) dE. \quad (\text{A.10})$$

In the small bias limit<sup>1</sup> the Fermi-Dirac function is expanded as a Taylor series into,

$$f(E(k), E_{F,L}) - f(E(k), E_{F,R}) \approx eV \frac{\delta f(E(k), E_F)}{\delta E_F}. \quad (\text{A.11})$$

Substituting this into Eq. A.10 yields the integral,

$$I_L = \frac{2e^2 V}{h} \int_{E_L}^\infty \left[ -\frac{\delta f}{\delta E} \right] T(E) dE. \quad (\text{A.12})$$

At low temperatures  $\delta f/\delta E \rightarrow \delta(E - E_F)$  and the integral evaluates to,

$$I_L = \frac{2e^2 V}{h} T(E_F), \quad (\text{A.13})$$

from which the conductance  $G = I/V$  is derived to be,

$$G = \frac{2e^2}{h} T(E_F). \quad (\text{A.14})$$

With the barrier still in place this corresponds to a tunnelling conductance with  $T(E_F) < 1$ . The point at which the barrier disappears ( $E_{\text{barrier}} = E_F$ ) gives rise to  $T(E) = 1$  and opens up a single quantised conductance channel. Adding additional  $n$  sub-bands into the constriction continues to increase the conductance by its quantum,  $2e^2/h$ , and thus the conductance of a

---

<sup>1</sup>Large biases are ignored

1D *conductive* junction can be expressed as,

$$G = \frac{2e^2}{h}n. \quad (\text{A.15})$$

## Appendix B

# Supplementary Experimental Details

---

### B.1 Supplementary Optical Details

---

Features, design justifications and optical theory not essential to the main text are detailed here, including notes on reimaging, choice of objectives and polarisation optimisation. The concept of reimaging, and its effect on beam alignment, is shown in Figure B.1. The ray diagrams show that the beam position in the focus can be adjusted by changing the angle of a mirror placed in the Fourier plane (in the case of the microscope the mirror directly after the DF stop). The shape of the beam, dictated by its angular distribution in Fourier space, is controlled by tilting a mirror in a focal plane (the mirror in the focus of the reimaging arm). The two mirrors provide independent control over the two main beam properties.

The choice of objective was determined by the overall range over which a reference spectrum from a Ag mirror is valid. Two long working distance objectives suitable for single nanostructure spectroscopy were characterised for use in the microscope: a VIS and an IR objective. The raw reflectance spectrum of the supercontinuum laser measured using each objective is shown in Figure B.2. The short wavelength cut-off at 480 nm is due to the supercontinuum laser. The VIS objective clearly outperforms the IR objective below 625 nm, though both objective counts are large enough to maintain a good reference signal. Overall, references using the VIS objective only extend marginally more below 500 nm. However, the

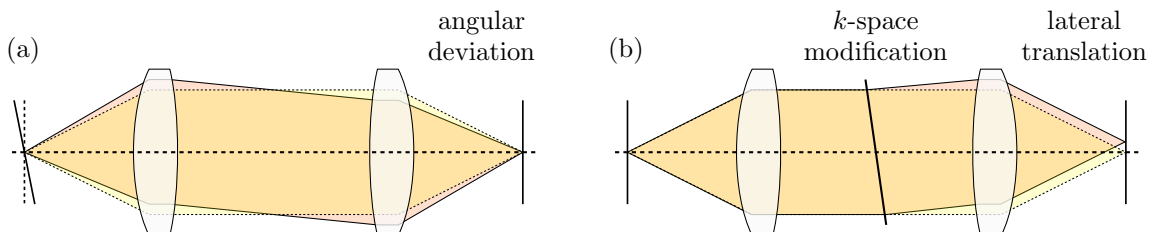
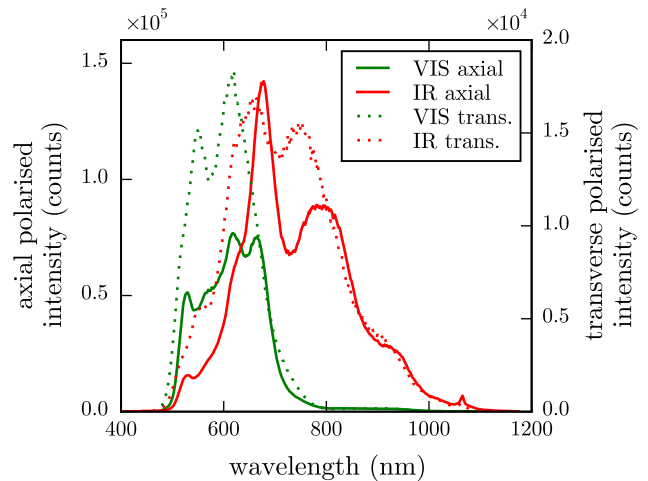


**Figure B.1: Concept of reimaging for beam alignment.** (a) Adjusting the angle of the beam in a focal plane does not change the position of the focus in the image (front focal) plane but changes the position in the Fourier (back focal) plane. (b) Adjusting the angle of the beam in a Fourier plane translates the position of the beam in the image plane without changing its angular components.

**Figure B.2: Spectral comparison between VIS and IR objectives.** The VIS objective is an Olympus  $100\times 0.9$  NA MPlan BD dark-field objective whereas the IR objective is an Olympus  $100\times 0.8$  NA MPlan bright-field objective.



700 nm cut-off of the VIS objective means that it is not suitable for spectra in the NIR with referencing only valid up until 900 nm whereas the IR objective extends to 1100 nm. The gain in spectral range means that the IR objective is chosen despite its lack of dark-field illumination for imaging.

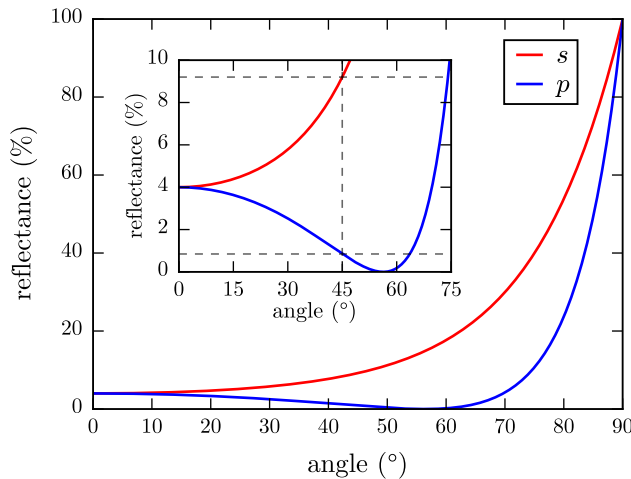


**Figure B.3: Reflectance as a function of angle of incidence for glass-air interface.** Reflective is calculated from the fresnel coefficients. The refractive index of glass is assumed to be  $n = 1.5$ . The inset shows a zoomed segment at low reflectances.

splitter limits current polarisation resolved measurements.

Consideration was given when designing the optical layout to account for intensity differences in each linear polarisation. Reflection and transmission of an EM wave incident on an interface between two refractive media at an angle is governed by the Fresnel equations [35]. As shown in Figure B.3, there is a large difference in reflectance between linear polarisations at higher angles of incidence. The microscope is designed such that the *s*-polarisation corresponds to light polarised along the tip axis, maximising its transmission to the spectrometers. Leakage of the *s*-polarisation into the weaker *p*-polarisation signal at the polarising beam-

## B.2 Supplementary Electronics

The schematic circuitry of the microscope electronics is shown in Figure B.4, corresponding to the simpler block diagram shown in the main text.

## B.3 Software Lock-In Derivation

To lock into only the signal component at the reference frequency  $\omega_r$ , a reference wave needs to be computed. The first step in the lock-in process is to mathematically construct a single frequency waveform at the correct harmonic using the supplied reference signal. The reference signal is typically of the form  $A \sin(\omega_{rs}t + \phi_r)$ , but the algorithm will also work with any periodic function since it triggers off a rising position edge. When  $\sin(\theta) = 0$  and the gradient is positive ( $\cos(\theta) = 1$ )  $\theta = 2n\pi$ . Hence the rising edge trigger points  $t_i$  occur at,

$$\theta = \omega_{rs}t_i + \phi_r = 2n\pi. \quad (\text{B.1})$$

Trigger times are fitted against the number of triggers (number of periods) since the start of the signal using,

$$t_i = \frac{1}{\omega_{rs}}(2n\pi - \phi_r) = \frac{2\pi}{\omega_{rs}}n - \frac{\phi_r}{\omega_{rs}}. \quad (\text{B.2})$$

A complex reference wave of the form  $e^{ih(\omega_{rs}t + \phi_r)}$ , where  $h$  is the harmonic of the reference frequency  $\omega_{rs}$  required to lock into the frequency  $\omega_r$ , is constructed from the  $t_i = mn + c$  fit using,

$$\omega_{rs} = \frac{2\pi}{m}, \quad (\text{B.3})$$

$$\phi_r = \frac{mc}{2\pi}. \quad (\text{B.4})$$

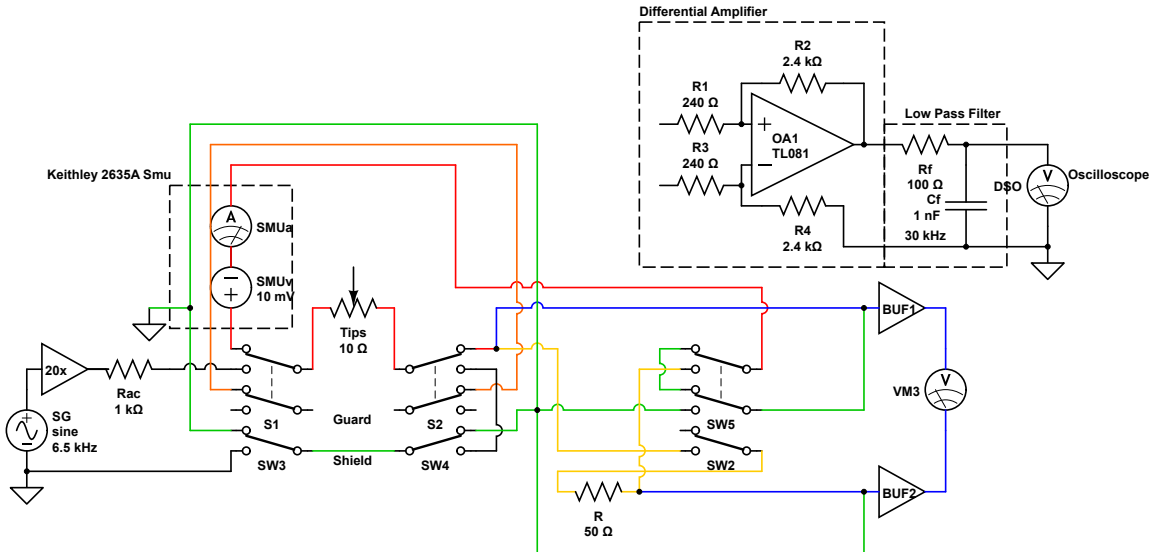


**Figure B.4: Schematic of the electrical measurement circuit.** The central routing box allows switching between a.c. and d.c. circuits and low-and high-bandwidth d.c. measurements. The a.c. circuit is used to align two AFM probes together while the d.c. circuit is used to measure spatially dependent signals from the gap between two AFM probes.

The frequency component of the signal at  $\omega_r = h\omega_{rs}$  can be extracted using Fourier analysis,

$$Z_s(\omega_r) = \frac{2}{t} \int_0^t Z_s(t) e^{-ih(\omega_{rs}t+\phi_r)} dt. \quad (\text{B.5})$$

Discretising this not a programmable form results in,

$$Z_s(\omega_r) = \frac{2}{n} \sum_0^n Z_s(t_n) e^{-ih(\omega_{rs}t_n+\phi_r)} \quad (\text{B.6})$$

where  $\text{Re}[Z_s(\omega_r)]$  and  $\text{Im}[Z_s(\omega_r)]$  are the  $x$  and  $y$  of the signal component at  $\omega_r$ , respectively. Polar coordinates of amplitude and phase are retrieved using the coordinate transforms,

$$r = \sqrt{x^2 + y^2}, \quad (\text{B.7})$$

$$\phi = \tan^{-1}(y/x). \quad (\text{B.8})$$

## B.4 Capacitive Alignment Model Derivation

---

The equation of motion for the dual-tip system is derived in the main text as,

$$m_1 \frac{d^2 z_1}{dt^2} + \beta_{01}^z \frac{dz_1}{dt} + k_{01}^z (z_1 - d_0) = \left( \frac{-\varepsilon_0 A_{ov} V_0^2}{4z_1^2} \right) [1 + \cos(\omega_p t)]. \quad (\text{B.9})$$

Expressing Eq. B.9 in terms of  $z_r = z - d_0$  yields,

$$m_1 \frac{d^2 z_r}{dt^2} + \beta_{01}^z \frac{dz_r}{dt} + k_{01}^z z_r = \left( \frac{-\varepsilon_0 A_{ov} V_0^2}{4(z_r + d_0)^2} \right) [1 + \cos(\omega_p t)], \quad (\text{B.10})$$

and enables further simplification via approximation. Assuming that  $z_r \ll d_0$  the right hand side of Eq. B.10 can be taken to first order using a Taylor series,<sup>1</sup>

$$m_1 \frac{d^2 z_r}{dt^2} + \beta_{01}^z \frac{dz_r}{dt} + k_{e1}^z z_r \simeq \left( \frac{-\varepsilon_0 A_{ov} V_0^2}{4d_0^2} \right) [1 + \cos(\omega_p t)], \quad (\text{B.11})$$

where,

$$k_{e1}^z = k_{01}^z - \left( \frac{\varepsilon_0 A_{ov} V_0^2}{2d_0^3} \right) [1 + \cos(\omega_p t)]. \quad (\text{B.12})$$

This effective spring constant  $k_{e1}^z$  does not cause parametric mixing as it oscillates at  $\omega_p$  therefore its effect can be averaged out over time resulting in  $\langle k_{e1}^z \rangle = k_{01}^z - \varepsilon_0 A_{ov} V_0^2 / 2d_0^3$ . The

---

<sup>1</sup>  $F(z_r) = F(0) + \frac{dF(z_r)}{dz_r} \Big|_0 z_r = \left( \frac{-\varepsilon_0 A_{ov} V_0^2}{4} \right) [1 + \cos(\omega_p t)] \left( \frac{1}{d_0^2} - \frac{2z_r}{d_0^3} \right)$

EoM is then once again approximated to,

$$m_1 \frac{d^2 z_r}{dt^2} + \beta_{01}^z \frac{dz_r}{dt} + \langle k_{e1}^z \rangle z_r \simeq \left( \frac{-\varepsilon_0 A_{ov} V_0^2}{4d_0^2} \right) [1 + \cos(\omega_p t)], \quad (\text{B.13})$$

Defining the constant  $q$  as,

$$q = \left( \frac{-\varepsilon_0 A_{ov} V_0^2}{4d_0^3} \right), \quad (\text{B.14})$$

the effective spring constant can be expressed as,

$$k_{e1}^z = k_{01}^z + 2q [1 + \cos(\omega_p t)], \quad (\text{B.15})$$

$$\langle k_{e1}^z \rangle = k_{01}^z + 2q, \quad (\text{B.16})$$

and the EOM can be again rewritten in the form,

$$m_1 \ddot{z}_r + \beta_{01}^z \dot{z}_r + [\langle k_{e1}^z \rangle + 2q \cos(\omega_p t)] z_r - q [1 + \cos(\omega_p t)] d_0 \simeq 0, \quad (\text{B.17})$$

Equation Eq. B.17 is of the form of the driven damped Mathieu equation,

$$\ddot{z} + 2\kappa \dot{z} + [a - 2q \cos(2t)] z = F(t), \quad (\text{B.18})$$

and has solutions in the limit of small oscillations of [201],

$$z_1 \approx d_0 - |z_1^{off}| - z_{m1} \cos(\omega_p t + \varphi_1) \quad (\text{B.19})$$

where

$$z_1^{off} \approx \frac{\varepsilon_0 A_{ov} V_0^2}{4d_0^2 \langle k_{e1}^z \rangle}, \quad (\text{B.20a})$$

$$z_{m1} \approx \frac{\varepsilon_0 A_{ov} V_0^2}{4d_0^2 \sqrt{(\langle k_{e1}^z \rangle - m_1 \omega_p^2)^2 + (\beta_{01}^z \omega_p)^2}}, \quad (\text{B.20b})$$

$$\varphi_1 \approx \tan^{-1} \left( \frac{\beta_{01}^z \omega_p}{\langle k_{e1}^z \rangle - m_1 \omega_p^2} \right). \quad (\text{B.20c})$$



## Appendix C

# Fast Spectroscopy of Plasmonic Dimer Make/Break Junctions

---

One of the aspects of the microscope platform not discussed in the main text is the capability for fast spectroscopy with 10  $\mu$ s resolution. This was developed in order to measure the initial contact dynamics of plasmonic tip dimers as they come into conductive contact, along with the plasmonics of break junctions formed between the two Au surfaces in a touching tip dimer. Mechanically controllable break junctions (MCBJs) similar to the Au contact formed between tips are well documented and have formed the basis of quantised conductance studies in 3D systems at room temperature (as opposed to the original 2DEG systems) [250–260].

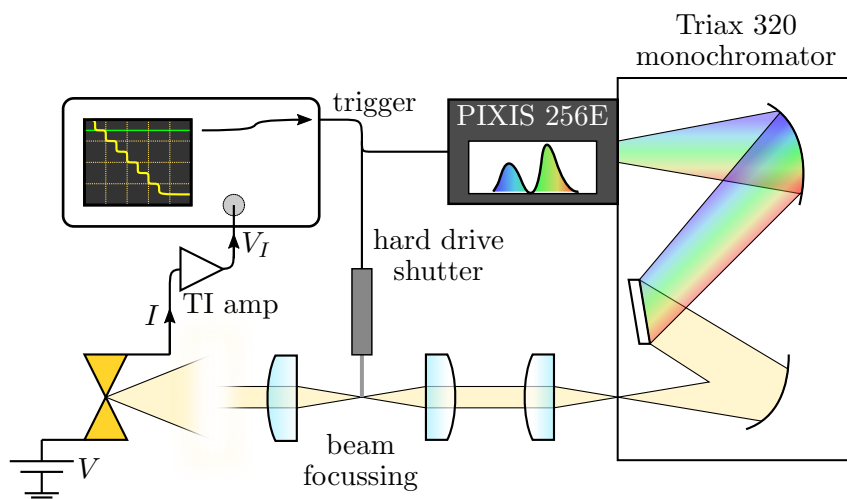


**Figure C.1: Diagram of the fast spectroscopy setup.** The setup consists of a custom shutter, built from a disassembled hard drive, and a monochromator-CCD pair. Kinetics acquisition on the CCD, along with the shutter mechanism, is triggered by fast electrical signals from the tips which are measured on the oscilloscope.

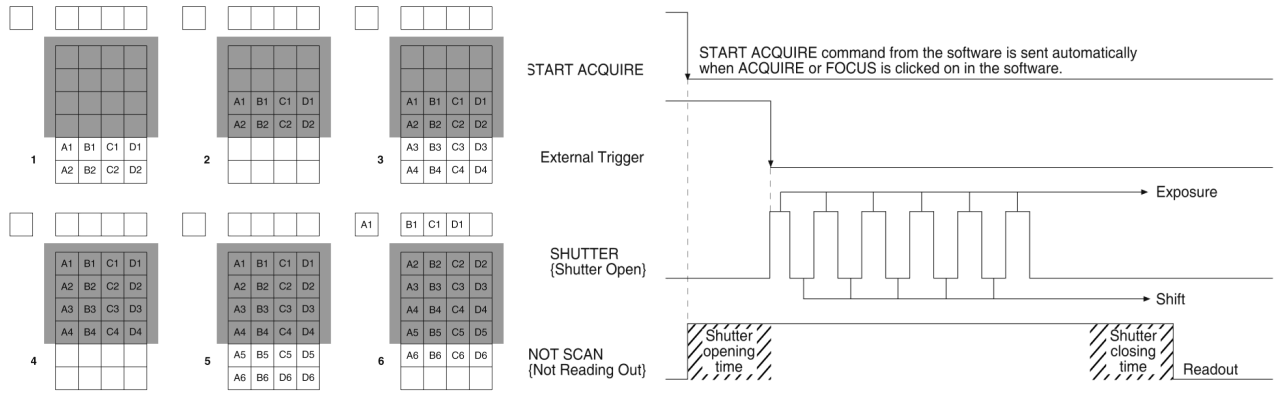


**Figure C.2: Diagram showing kinetics mode acquisition on the CCD.** An exposed region of the CCD is shuffled into a mechanically or optically masked region. Once the whole CCD has been exposed the image is read out. This acquisition process, along with the opening of the fast shutter, is triggered by an external TTL pulse from an oscilloscope. These images are taken from the Princeton Instruments PIXIS CCD manual.

## C.1 Experimental Setup

The experimental setup for fast spectroscopy is shown in Figure C.1. Collimated scattered light from the tips is focussed down onto the end of the shutter blade and then, with the shutter open, reimaged onto the entrance slit of a monochromator (Horiba Yvon Jobin Triax 320). The monochromator is paired with a CCD supporting a kinetics readout mode (Princeton Instruments PIXIS 256E), wherein charge is shuffled down the active CCD area after the single top-most line of pixels is exposed to produce a time-series of spectra. The time interval recorded during time-resolved spectroscopy is given by,

$$t_{\text{range}} = 256(t_{\text{exposure}} + t_{\text{shift}}), \quad (\text{C.1})$$

where  $t_{\text{exposure}}$  is the exposure period of each row of pixels and  $t_{\text{shift}}$  is the time taken to shift all pixels by one row. The shuffle speed is fast ( $9.2\ \mu\text{s}$ ) compared with the readout time meaning it is possible to obtain resolutions around  $10\ \mu\text{s}$  with the complete image readout only once the kinetics process has completed. Kinetics acquisition is therefore good for measuring short-lived, single-shot events, similar in application to a streak camera. A coarse,  $150\ \text{lines mm}^{-1}$  diffraction grating is chosen to disperse the visible spectrum along the top row of the CCD. The fast spectroscopy path from its initial split off point at the beamsplitter is completely tubed to reduce any background noise incident on the sensitive CCD, with an opening only to place the shutter in the beam.

The kinetics sequence is armed at the start of each experiment, waiting for a trigger signal to begin acquisition. To improve the activation time upon receiving the trigger signal

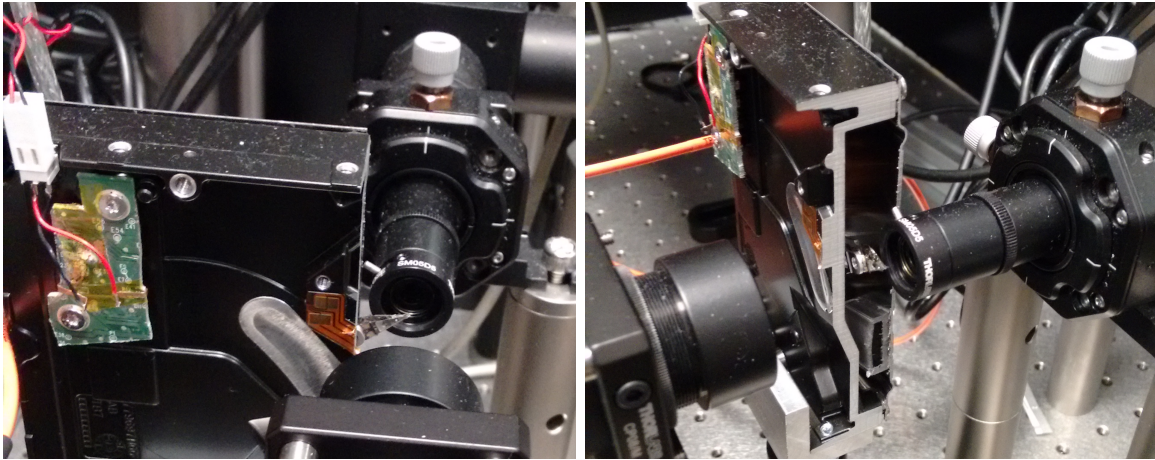


**Figure C.3: Images of the hard drive shutter.** The shutter works by passing a current through the hard drive voice coil, generating a magnetic field which quickly moves the read head via a Lorentz force. This functions as a shutter blade. The shutter blade is placed in the focus between two lenses in order to uncover the focussed beam spot in the shortest possible time. Rise times in this configuration are around 300  $\mu$ s.

non-essential CCD procedures, such as continuous cleaning, are deactivated. The CCD is protected from pre-sequence overexposure by a custom-built fast shutter, constructed using the read head from a disassembled 3.5" computer hard-drive, shown in Figure C.3. The hard drive is mounted onto a 3D translation stage and the shutter blade is aligned in the focus of the scattered light such that the time taken to uncover the beam is minimised. Regular shutters are limited to 8 ms opening times due to solenoid delay and thus the majority of a short,  $\sim$ 10 ms make/break junction event would be missed. Use of the hard-drive voice coil mechanism enables shutter open times of around 300  $\mu$ s, as confirmed using both CCD and photodiode measurements. Currents to the voice coil and their trigger mechanism are provided by an Arduino microcontroller with a motor driver circuit, enabling up to 2 A of current. The fast trigger mechanism is enabled by directly addressing each bit of the circuit and bypassing the standard Arduino functions. These kinds of shutters have been previously developed [261, 262] though not before with the simplicity of using Arduino circuit boards and programming.

The trigger signal to the CCD and shutter is provided by the oscilloscope. The oscilloscope is set to trigger once the tip junction conductance either rises above  $1G_0$  or falls below  $10G_0$ . As tips come into contact or as the contact area between pulled tips is reduced the number of conductance channels discretely changes by  $G_0$ . The trigger signal synchronises the electronic and spectral measurements to facilitate correlation comparisons. The current limiting resistor described in chapter 4.3 was installed primarily to prevent the amplifiers feeding the oscilloscope from overloading, thus causing the break junction event to be missed in the time taken for the amplifiers to reset. To ensure correct triggering and optimum electronic measurements, electrical signals passing through the high bandwidth d.c. circuit are cleaned up

using low pass filters and a multi-stage (transimpedance) amplification process to maintain a 1 MHz bandwidth at a total gain between  $10^4$ – $10^5$ .

## C.2 Performance and Issues in Tip Dimer Scanning Experiments

Both make and break contact events typically last no more than 10 ms in the current system, often occurring more on a 100  $\mu$ s–1 ms time scale. The kinetics mode has a minimum acquisition time of 2.56 ms with a maximum 10  $\mu$ s single spectrum time resolution set by the pixel shift time. The system is trialled using a reflected supercontinuum laser beam with an additional 10  $\mu$ s exposure per row of pixels to give a 5 ms measurement, shown in Figure C.4. The beam is chopped and measured on a photodiode to show the system is working as expected. Similar tests were performed with an electronically modulated diode laser to determine the time resolution of measurements.

Figure C.5 shows an example of a conductance traced measured on a break junction between two tips. The traces shows that as the tip contact breaks, the conductance drops in units of  $G_0$ . Under these circumstances the CTP modes sustained by the tip dimer are expected to undergo a redshift with decreasing conductance (ideally in discrete quantised steps). Make junctions, as opposed to break junctions, showed more success in tips since the jump into contact is generally a single high quality event whereas in break junctions the forces holding

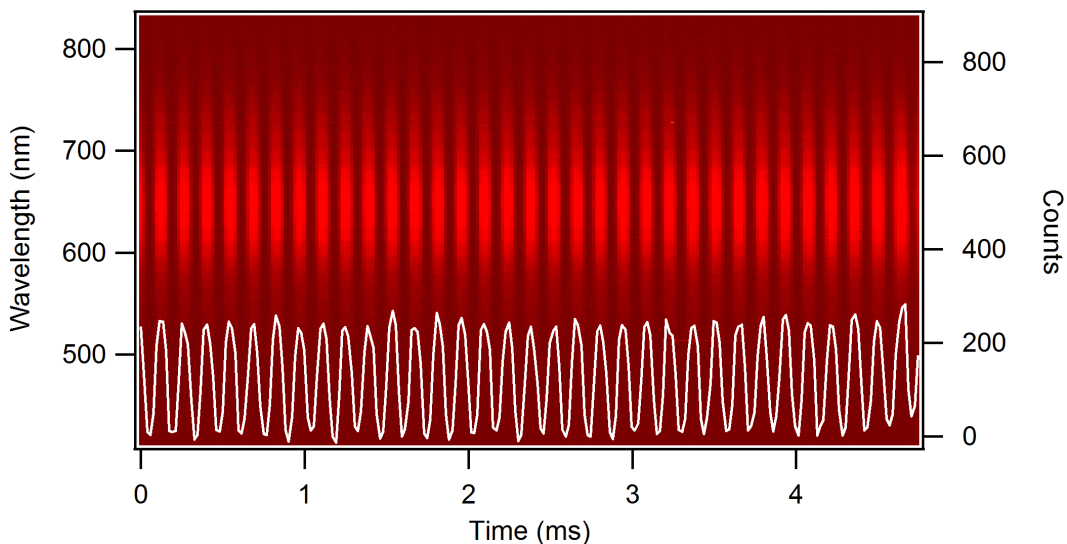


**Figure C.4: Testing of kinetics mode acquisition.** A reflected supercontinuum beam is chopped and measured both with kinetics mode on the CCD and by a photodiode on the oscilloscope. Oscillations in the beam at the chopping frequency are clearly seen in both the spectral image and the superimposed photodiode output over a 5 ms time period.

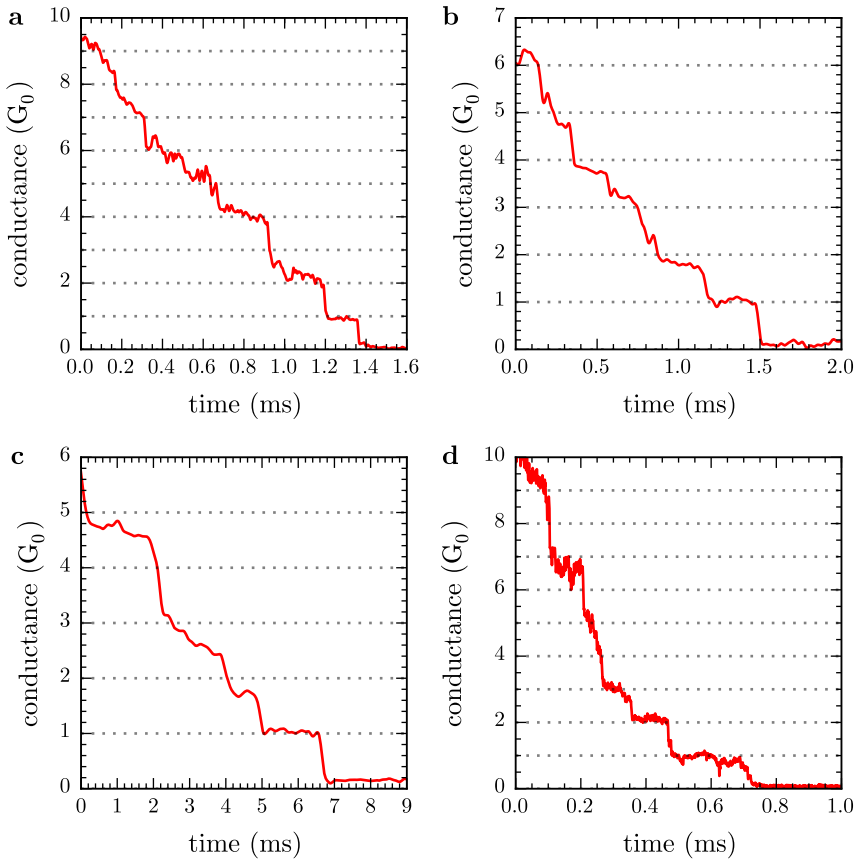


**Figure C.5: Examples of fast conductance measurements on tip dimer break junctions.** During the break the contact conductance drops in units of  $G_0$  until the last atom-atom contact breaks and tips separate.

the tip together and the flexibility of the cantilevers causes issues. Tips often exhibit multiple breaks or changes in conductance as the junction vibrates with the final break occurring only once the gap adhesion forces are overcome. Given the strength of the average tip adhesion (and that it often causes the ball to break from the tip apex) the large amount of pulling force applied to the cantilever leads to a very quick sub- $\mu$ s break event. This is not possible to measure in the given system. Although the make contact event is typically higher quality it is far more difficult to trigger due to operating near the noise floor, often meaning that the  $1G_0$  level is too low to reliably observe.

Though the fast spectroscopy system was engaged in every scan the method provided no useable results. Spectral images contained no detectable signals, as shown in Figure C.6, due to the short exposure times and low supercontinuum laser powers used to prevent damage to tips. Eventually the  $G_0$ -level conductance data was measured using a slow, controlled make junction in a standard spatial scan (shown in Figure 6.6b). For this technique to become useful the length of the break or make contact event needs to be lengthened in order to increase the exposure time per row of pixels on the CCD. This could be achieved through more control of the tip position, i.e. by using stiff tips in a low humidity environment to minimise adhesion and

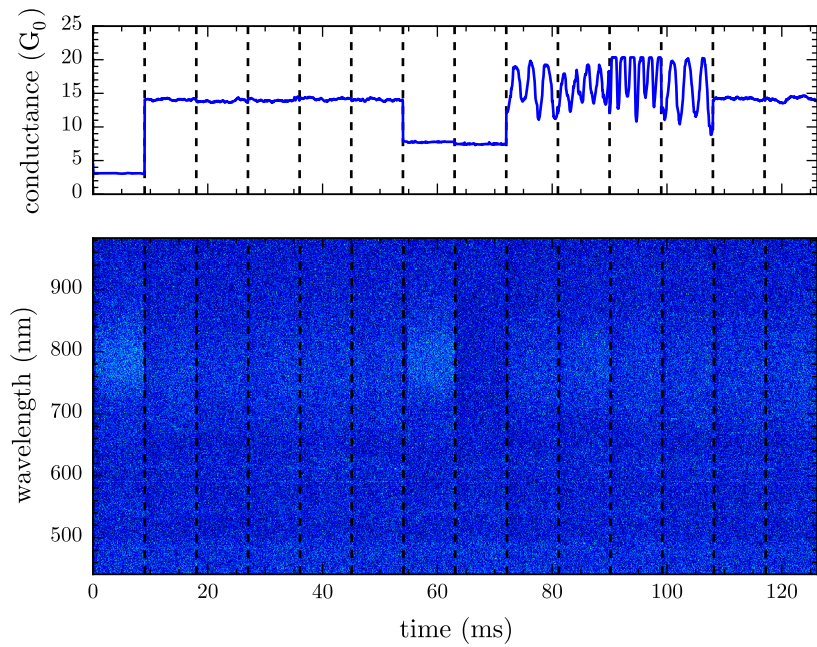


**Figure C.6:** A representative fast scanning measurement from a plasmonic tip dimer. No signal is detectable with such small exposures per spectrum at acceptable power levels.

more controllably break the contact without significantly bending the cantilever. Alternatively, the increased robustness of the electrochemically fabricated plasmonic tips means increased focal intensities could be sustained. By leveraging both of these suggestions in the future, plasmonic MCBJs could be realised as a means of studying conductance at optical frequencies.

# Bibliography

---

- [1] M. Fleischmann, P. J. Hendra, and A. McQuillan, “Raman spectra of pyridine adsorbed at a silver electrode”, *Chemical Physics Letters* **26**, 163–166 (1974).
- [2] D. L. Jeanmaire and R. P. Van Duyne, “Surface raman spectroelectrochemistry: part i. heterocyclic, aromatic, and aliphatic amines adsorbed on the anodized silver electrode”, *Journal of Electroanalytical Chemistry and Interfacial Electrochemistry* **84**, 1–20 (1977).
- [3] E. Ash and G Nicholls, “Super-resolution aperture scanning microscope”, *Nature* **237**, 510–512 (1972).
- [4] D. W. Pohl, W Denk, and M Lanz, “Optical stethoscopy: image recording with resolution  $\lambda/20$ ”, *Applied physics letters* **44**, 651–653 (1984).
- [5] A. Lewis et al., “Development of a 500 Å spatial resolution light microscope: i. light is efficiently transmitted through  $\lambda/16$  diameter apertures”, *Ultramicroscopy* **13**, 227–231 (1984).
- [6] W. D. Pohl, *Optical near-field scanning microscope*, US Patent 4,604,520, 1986.
- [7] A Harootunian et al., “Super-resolution fluorescence near-field scanning optical microscopy”, *Applied Physics Letters* **49**, 674–676 (1986).
- [8] E Betzig et al., “Near-field scanning optical microscopy (nsom)”, in 1988 los angeles symposium–oe/lase’88 (International Society for Optics and Photonics, 1988), pp. 91–99.
- [9] L. Novotny and N. Van Hulst, “Antennas for light”, *Nature Photonics* **5**, 83–90 (2011).
- [10] C. V. Raman, “A new radiation”, *Indian Journal of physics* **2**, 387–398 (1928).
- [11] R Zhang et al., “Chemical mapping of a single molecule by plasmon-enhanced raman scattering”, *Nature* **498**, 82–86 (2013).
- [12] G. Binnig et al., “Surface studies by scanning tunneling microscopy”, *Physical review letters* **49**, 57 (1982).
- [13] G. Binnig, C. F. Quate, and C. Gerber, “Atomic force microscope”, *Physical review letters* **56**, 930 (1986).
- [14] K. J. Savage et al., “Revealing the quantum regime in tunnelling plasmonics”, *Nature* **491**, 574–577 (2012).
- [15] P. Drude, “Zur elektronentheorie der metalle”, *Annalen der Physik* **306**, 566–613 (1900).
- [16] P. B. Johnson and R.-W. Christy, “Optical constants of the noble metals”, *Physical Review B* **6**, 4370 (1972).

- [17] R. Egerton, *Electron energy-loss spectroscopy in the electron microscope* (Springer Science & Business Media, 2011).
- [18] C. Kittel, P. McEuen, and P. McEuen, *Introduction to solid state physics*, Vol. 8 (Wiley New York, 1976).
- [19] A. Otto, “Excitation of nonradiative surface plasma waves in silver by the method of frustrated total reflection”, *Zeitschrift für Physik* **216**, 398–410 (1968).
- [20] E. Kretschmann, “Die bestimmung optischer konstanten von metallen durch anregung von oberflächenplasmaschwingungen”, *Zeitschrift für Physik* **241**, 313–324 (1971).
- [21] R. Wood, “On a remarkable case of uneven distribution of light in a diffraction grating spectrum”, *The London, Edinburgh, and Dublin Philosophical Magazine and Journal of Science* **4**, 396–402 (1902).
- [22] U Fano, “The theory of anomalous diffraction gratings and of quasi-stationary waves on metallic surfaces (sommerfeld’s waves)”, *JOSA* **31**, 213–222 (1941).
- [23] W. A. Murray and W. L. Barnes, “Plasmonic materials”, *Advanced materials* **19**, 3771–3782 (2007).
- [24] S. A. Maier, *Plasmonics: fundamentals and applications* (Springer Science & Business Media, 2007).
- [25] J. D. Jackson, *Classical electrodynamics* (John Wiley & Sons, 1999).
- [26] E Prodan and P. Nordlander, “Plasmon hybridization in spherical nanoparticles”, *The Journal of chemical physics* **120**, 5444–5454 (2004).
- [27] C Sönnichsen et al., “Spectroscopy of single metallic nanoparticles using total internal reflection microscopy”, *Applied Physics Letters* **77**, 2949–2951 (2000).
- [28] J. Krenn et al., “Design of multipolar plasmon excitations in silver nanoparticles”, *Applied Physics Letters* **77**, 3379–3381 (2000).
- [29] J. Mock et al., “Shape effects in plasmon resonance of individual colloidal silver nanoparticles”, *The Journal of Chemical Physics* **116**, 6755–6759 (2002).
- [30] H. Kuwata et al., “Resonant light scattering from metal nanoparticles: practical analysis beyond rayleigh approximation”, *Applied physics letters* **83**, 4625–4627 (2003).
- [31] X. Huang et al., “Cancer cell imaging and photothermal therapy in the near-infrared region by using gold nanorods”, *Journal of the American Chemical Society* **128**, 2115–2120 (2006).
- [32] X. Huang et al., “Plasmonic photothermal therapy (pptt) using gold nanoparticles”, *Lasers in medical science* **23**, 217–228 (2008).
- [33] X. Huang and M. A. El-Sayed, “Gold nanoparticles: optical properties and implementations in cancer diagnosis and photothermal therapy”, *Journal of Advanced Research* **1**, 13–28 (2010).
- [34] C. Noguez, “Surface plasmons on metal nanoparticles: the influence of shape and physical environment”, *The Journal of Physical Chemistry C* **111**, 3806–3819 (2007).
- [35] I. S. Grant and W. R. Phillips, *Electromagnetism* (John Wiley & Sons, 2013).

- [36] C. F. Bohren and D. R. Huffman, *Absorption and scattering of light by small particles* (John Wiley & Sons, 2008).
- [37] S. Berweger et al., “Light on the tip of a needle: plasmonic nanofocusing for spectroscopy on the nanoscale”, *The Journal of Physical Chemistry Letters* **3**, 945–952 (2012).
- [38] P. Bharadwaj, B. Deutsch, and L. Novotny, “Optical antennas”, *Advances in Optics and Photonics* **1**, 438–483 (2009).
- [39] G. Mie, “Beiträge zur optik trüber medien, speziell kolloidaler metallösungen”, *Annalen der physik* **330**, 377–445 (1908).
- [40] F. Huang and J. J. Baumberg, “Actively tuned plasmons on elastomerically driven au nanoparticle dimers”, *Nano letters* **10**, 1787–1792 (2010).
- [41] M. G. Millyard et al., “Stretch-induced plasmonic anisotropy of self-assembled gold nanoparticle mats”, *Applied Physics Letters* **100**, 073101 (2012).
- [42] J. Mertens et al., “Controlling subnanometer gaps in plasmonic dimers using graphene”, *Nano letters* **13**, 5033–5038 (2013).
- [43] R. W. Taylor et al., “Watching individual molecules flex within lipid membranes using sers”, *Scientific reports* **4** (2014).
- [44] N. C. Lindquist et al., “Tip-based plasmonics: squeezing light with metallic nanoprobes”, *Laser & Photonics Reviews* **7**, 453–477 (2013).
- [45] S. A. Maier, P. G. Kik, and H. A. Atwater, “Observation of coupled plasmon-polariton modes in au nanoparticle chain waveguides of different lengths: estimation of waveguide loss”, *Applied Physics Letters* **81**, 1714–1716 (2002).
- [46] T. Atay, J.-H. Song, and A. V. Nurmikko, “Strongly interacting plasmon nanoparticle pairs: from dipole-dipole interaction to conductively coupled regime”, *Nano Letters* **4**, 1627–1631 (2004).
- [47] O. Muskens et al., “Optical scattering resonances of single and coupled dimer plasmonic nanoantennas”, *Optics express* **15**, 17736–17746 (2007).
- [48] R. W. Taylor et al., “Precise subnanometer plasmonic junctions for sers within gold nanoparticle assemblies using cucurbit [n] uril “glue””, *ACS nano* **5**, 3878–3887 (2011).
- [49] L. Herrmann et al., “Self-sifting of chain plasmons: the complex optics of au nanoparticle clusters”, *Optics express* **21**, 32377–32385 (2013).
- [50] T. Okamoto and I. Yamaguchi, “Optical absorption study of the surface plasmon resonance in gold nanoparticles immobilized onto a gold substrate by self-assembly technique”, *The Journal of Physical Chemistry B* **107**, 10321–10324 (2003).
- [51] J. K. Daniels and G. Chumanov, “Nanoparticle-mirror sandwich substrates for surface-enhanced raman scattering”, *The Journal of Physical Chemistry B* **109**, 17936–17942 (2005).
- [52] M. K. Kinnan and G. Chumanov, “Surface enhanced raman scattering from silver nanoparticle arrays on silver mirror films: plasmon-induced electronic coupling as the enhancement mechanism”, *The Journal of Physical Chemistry C* **111**, 18010–18017 (2007).

- [53] S. Mubeen et al., “Plasmonic properties of gold nanoparticles separated from a gold mirror by an ultrathin oxide”, *Nano letters* **12**, 2088–2094 (2012).
- [54] B. de Nijs et al., “Unfolding the contents of sub-nm plasmonic gaps using normalising plasmon resonance spectroscopy”, *Faraday Discussions* (2014).
- [55] I. Romero et al., “Plasmons in nearly touching metallic nanoparticles: singular response in the limit of touching dimers”, *Optics Express* **14**, 9988–9999 (2006).
- [56] E. Hao and G. C. Schatz, “Electromagnetic fields around silver nanoparticles and dimers”, *The Journal of chemical physics* **120**, 357–366 (2004).
- [57] C. E. Talley et al., “Surface-enhanced raman scattering from individual au nanoparticles and nanoparticle dimer substrates”, *Nano Letters* **5**, 1569–1574 (2005).
- [58] U. Kreibig and M. Vollmer, *Optical properties of metal clusters*, Vol. 25 (Springer Berlin, 1995).
- [59] M. Gluodenis and C. A. Foss, “The effect of mutual orientation on the spectra of metal nanoparticle rod-rod and rod-sphere pairs”, *The Journal of Physical Chemistry B* **106**, 9484–9489 (2002).
- [60] W Rechberger et al., “Optical properties of two interacting gold nanoparticles”, *Optics Communications* **220**, 137–141 (2003).
- [61] N. J. Halas et al., “Plasmons in strongly coupled metallic nanostructures”, *Chemical reviews* **111**, 3913–3961 (2011).
- [62] P. K. Jain, W. Huang, and M. A. El-Sayed, “On the universal scaling behavior of the distance decay of plasmon coupling in metal nanoparticle pairs: a plasmon ruler equation”, *Nano Letters* **7**, 2080–2088 (2007).
- [63] X. Ben and H. S. Park, “Size dependence of the plasmon ruler equation for two-dimensional metal nanosphere arrays”, *The Journal of Physical Chemistry C* **115**, 15915–15926 (2011).
- [64] S. Kadkhodazadeh et al., “Scaling of the surface plasmon resonance in gold and silver dimers probed by eels”, *The Journal of Physical Chemistry C* **118**, 5478–5485 (2014).
- [65] P. Nordlander et al., “Plasmon hybridization in nanoparticle dimers”, *Nano Letters* **4**, 899–903 (2004).
- [66] E Prodan et al., “A hybridization model for the plasmon response of complex nanostructures”, *Science* **302**, 419–422 (2003).
- [67] P. Nordlander and E. Prodan, “Plasmon hybridization in nanoparticles near metallic surfaces”, *Nano Letters* **4**, 2209–2213 (2004).
- [68] M.-W. Chu et al., “Probing bright and dark surface-plasmon modes in individual and coupled noble metal nanoparticles using an electron beam”, *Nano letters* **9**, 399–404 (2008).
- [69] A. L. Koh et al., “Electron energy-loss spectroscopy (eels) of surface plasmons in single silver nanoparticles and dimers: influence of beam damage and mapping of dark modes”, *Acs Nano* **3**, 3015–3022 (2009).
- [70] R. Esteban et al., “Bridging quantum and classical plasmonics with a quantum-corrected model”, *Nature Communications* **3**, 825 (2012).

- [71] J. B. Lassiter et al., “Close encounters between two nanoshells”, *Nano letters* **8**, 1212–1218 (2008).
- [72] O Pérez-González et al., “Optical spectroscopy of conductive junctions in plasmonic cavities”, *Nano letters* **10**, 3090–3095 (2010).
- [73] O Pérez-González, N Zabala, and J Aizpurua, “Optical characterization of charge transfer and bonding dimer plasmons in linked interparticle gaps”, *New Journal of Physics* **13**, 083013 (2011).
- [74] C. Tserkezis et al., “Optical response of threaded chain plasmons: from capacitive chains to continuous nanorods”, *Optics express* **22**, 23851–23860 (2014).
- [75] R. Esteban et al., “A classical treatment of optical tunneling in plasmonic gaps: extending the quantum corrected model to practical situations”, *Faraday discussions* **178**, 151–183 (2015).
- [76] D. J. Griffiths, *Introduction to quantum mechanics* (Pearson Education India, 2005).
- [77] J. G. Simmons, “Generalized formula for the electric tunnel effect between similar electrodes separated by a thin insulating film”, *Journal of Applied Physics* **34**, 1793–1803 (1963).
- [78] J. M. Blanco, F. Flores, and R. Pérez, “Stm-theory: image potential, chemistry and surface relaxation”, *Progress in surface science* **81**, 403–443 (2006).
- [79] S. F. Tan et al., “Quantum plasmon resonances controlled by molecular tunnel junctions”, *Science* **343**, 1496–1499 (2014).
- [80] J. Zuloaga, E. Prodan, and P. Nordlander, “Quantum description of the plasmon resonances of a nanoparticle dimer”, *Nano letters* **9**, 887–891 (2009).
- [81] R. Landauer, “Spatial variation of currents and fields due to localized scatterers in metallic conduction”, *IBM Journal of Research and Development* **1**, 223–231 (1957).
- [82] J. A. Scholl et al., “Observation of quantum tunneling between two plasmonic nanoparticles”, *Nano letters* **13**, 564–569 (2013).
- [83] H. Cha, J. H. Yoon, and S. Yoon, “Probing quantum plasmon coupling using gold nanoparticle dimers with tunable interparticle distances down to the subnanometer range”, *ACS nano* **8**, 8554–8563 (2014).
- [84] W. Zhu and K. B. Crozier, “Quantum mechanical limit to plasmonic enhancement as observed by surface-enhanced raman scattering”, *Nature communications* **5** (2014).
- [85] V. Kravtsov et al., “Control of plasmon emission and dynamics at the transition from classical to quantum coupling”, *Nano letters* **14**, 5270–5275 (2014).
- [86] G. Hajisalem, M. S. Nezami, and R. Gordon, “Probing the quantum tunneling limit of plasmonic enhancement by third harmonic generation”, *Nano letters* **14**, 6651–6654 (2014).
- [87] M. Barbry et al., “Atomistic near-field nanoplasmatics: reaching atomic-scale resolution in nano optics”, *Nano letters* (2015).
- [88] F. Benz et al., “Nano optics of molecular-shunted plasmonic nanojunctions”, *Nano letters* **15**, 669–674 (2014).

- [89] L. O. Herrmann et al., "Threading plasmonic nanoparticle strings with light", *Nature communications* **5** (2014).
- [90] R. M. Stöckle et al., "Nanoscale chemical analysis by tip-enhanced raman spectroscopy", *Chemical Physics Letters* **318**, 131–136 (2000).
- [91] M. S. Anderson, "Locally enhanced raman spectroscopy with an atomic force microscope", *Applied Physics Letters* **76**, 3130–3132 (2000).
- [92] N. Hayazawa et al., "Metallized tip amplification of near-field raman scattering", *Optics Communications* **183**, 333–336 (2000).
- [93] B. Pettinger et al., "Surface enhanced raman spectroscopy: towards single molecular spectroscopy", *Electrochemistry* **68**, 942–949 (2000).
- [94] F Zenhausern, M. O'boyle, and H. Wickramasinghe, "Apertureless near-field optical microscope", *Applied Physics Letters* **65**, 1623–1625 (1994).
- [95] F. Zenhausern, Y Martin, and H. Wickramasinghe, "Scanning interferometric apertureless microscopy: optical imaging at 10 angstrom resolution", *Science* **269**, 1083–1085 (1995).
- [96] R Bachelot, P Gleyzes, and A. Boccara, "Near-field optical microscope based on local perturbation of a diffraction spot", *Optics letters* **20**, 1924–1926 (1995).
- [97] B Knoll et al., "Contrast of microwave near-field microscopy", *Applied physics letters* **70**, 2667–2669 (1997).
- [98] B Knoll and F Keilmann, "Scanning microscopy by mid-infrared near-field scattering", *Applied Physics A: Materials Science & Processing* **66**, 477–481 (1998).
- [99] F Keilmann, B Knoll, and A Kramer, "Long-wave-infrared near-field microscopy", *physica status solidi (b)* **215**, 849–854 (1999).
- [100] J. Wessel, "Surface-enhanced optical microscopy", *JOSA B* **2**, 1538–1541 (1985).
- [101] B. Pettinger et al., "Tip-enhanced raman spectroscopy: near-fields acting on a few molecules", *Annual review of physical chemistry* **63**, 379–399 (2012).
- [102] C. Neacsu, G. Steudle, and M. Raschke, "Plasmonic light scattering from nanoscopic metal tips", *Applied Physics B* **80**, 295–300 (2005).
- [103] D Mehtani et al., "Optical properties and enhancement factors of the tips for apertureless near-field optics", *Journal of Optics A: Pure and Applied Optics* **8**, S183 (2006).
- [104] T Wang et al., "Excitation of propagating surface plasmons with a scanning tunnelling microscope", *Nanotechnology* **22**, 175201 (2011).
- [105] L. Novotny and S. J. Stranick, "Near-field optical microscopy and spectroscopy with pointed probes\*", *Annu. Rev. Phys. Chem.* **57**, 303–331 (2006).
- [106] J. Steidtner and B. Pettinger, "High-resolution microscope for tip-enhanced optical processes in ultrahigh vacuum", *Review of Scientific Instruments* **78**, 103104 (2007).
- [107] H. K. Wickramasinghe et al., "Billion-fold increase in tip-enhanced raman signal", *ACS nano* **8**, 3421–3426 (2014).
- [108] N. Hayazawa et al., "Near-field raman scattering enhanced by a metallized tip", *Chemical Physics Letters* **335**, 369–374 (2001).

- [109] B.-S. Yeo et al., “Enhancement of raman signals with silver-coated tips”, *Applied spectroscopy* **60**, 1142–1147 (2006).
- [110] B.-S. Yeo et al., “Towards rapid nanoscale chemical analysis using tip-enhanced raman spectroscopy with ag-coated dielectric tips”, *Analytical and bioanalytical chemistry* **387**, 2655–2662 (2007).
- [111] M. Zhang et al., “Experimental research on the spectral response of tips for tip-enhanced raman spectroscopy”, *Journal of Optics* **15**, 055006 (2013).
- [112] T. Mino, Y. Saito, and P. Verma, “Quantitative analysis of polarization-controlled tip-enhanced raman imaging through the evaluation of the tip dipole”, *ACS nano* **8**, 10187–10195 (2014).
- [113] N. Kumar, A. Rae, and D. Roy, “Accurate measurement of enhancement factor in tip-enhanced raman spectroscopy through elimination of far-field artefacts”, *Applied Physics Letters* **104**, 123106 (2014).
- [114] N. Hayazawa et al., “Focused excitation of surface plasmon polaritons based on gap-mode in tip-enhanced spectroscopy”, *Japanese Journal of Applied Physics* **46**, 7995 (2007).
- [115] A. Taguchi et al., “Controlling the plasmon resonance wavelength in metal-coated probe using refractive index modification”, *Optics express* **17**, 6509–6518 (2009).
- [116] K. Uetsuki et al., “Tunable plasmon resonances in a metallic nanotip–film system”, *Nanoscale* **4**, 5931–5935 (2012).
- [117] R Esteban, R Vogelgesang, and K Kern, “Simulation of optical near and far fields of dielectric apertureless scanning probes”, *Nanotechnology* **17**, 475 (2006).
- [118] W. Zhang, X. Cui, and O. J. Martin, “Local field enhancement of an infinite conical metal tip illuminated by a focused beam”, *Journal of Raman Spectroscopy* **40**, 1338–1342 (2009).
- [119] T. Schmid et al., “Nanoscale chemical imaging using tip-enhanced raman spectroscopy: a critical review”, *Angewandte Chemie International Edition* **52**, 5940–5954 (2013).
- [120] M Zhang, J Wang, and Q Tian, “Tip-enhanced raman spectroscopy mapping with strong longitudinal field excitation”, *Optics Communications* **315**, 164–167 (2014).
- [121] M. I. Stockman, “Nanofocusing of optical energy in tapered plasmonic waveguides”, *Physical review letters* **93**, 137404 (2004).
- [122] D. Pile and D. K. Gramotnev, “Adiabatic and nonadiabatic nanofocusing of plasmons by tapered gap plasmon waveguides”, *Applied Physics Letters* **89**, 041111 (2006).
- [123] S. Berweger et al., “Adiabatic tip-plasmon focusing for nano-raman spectroscopy”, *The Journal of Physical Chemistry Letters* **1**, 3427–3432 (2010).
- [124] J. S. Lee et al., “Superfocusing of electric or magnetic fields using conical metal tips: effect of mode symmetry on the plasmon excitation method”, *Optics express* **19**, 12342–12347 (2011).
- [125] R. M. Roth et al., “Resonant-plasmon field enhancement from asymmetrically illuminated conical metallic-probe tips”, *Optics Express* **14**, 2921–2931 (2006).

- [126] A. Goncharenko et al., “Electric field enhancement by a nanometer-scaled conical metal tip in the context of scattering-type near-field optical microscopy”, *Applied physics letters* **88**, 104101 (2006).
- [127] C. Schäfer et al., “A single particle plasmon resonance study of 3d conical nanoantennas”, *Nanoscale* **5**, 7861–7866 (2013).
- [128] S. Cherukulappurath et al., “Template-stripped asymmetric metallic pyramids for tunable plasmonic nanofocusing”, *Nano letters* **13**, 5635–5641 (2013).
- [129] C. Huber et al., “Optical near-field excitation at commercial scanning probe microscopy tips: a theoretical and experimental investigation”, *Physical Chemistry Chemical Physics* **16**, 2289–2296 (2014).
- [130] C. A. Barrios et al., “Highly stable, protected plasmonic nanostructures for tip enhanced raman spectroscopy”, *The Journal of Physical Chemistry C* **113**, 8158–8161 (2009).
- [131] B. Pettinger et al., “Direct monitoring of plasmon resonances in a tip-surface gap of varying width”, *Physical Review B* **76**, 113409 (2007).
- [132] B. Pettinger et al., “Tip-enhanced raman scattering: influence of the tip-surface geometry on optical resonance and enhancement”, *Surface Science* **603**, 1335–1341 (2009).
- [133] E. Bailo and V. Deckert, “Tip-enhanced raman scattering”, *Chemical Society Reviews* **37**, 921–930 (2008).
- [134] N. Hayazawa, T.-a. Yano, and S. Kawata, “Highly reproducible tip-enhanced raman scattering using an oxidized and metallized silicon cantilever tip as a tool for everyone”, *Journal of Raman Spectroscopy* **43**, 1177–1182 (2012).
- [135] L. Meng et al., “Gold-coated afm tips for tip-enhanced raman spectroscopy: theoretical calculation and experimental demonstration”, *Optics Express* **23**, 13804–13813 (2015).
- [136] B. Ren, G. Picardi, and B. Pettinger, “Preparation of gold tips suitable for tip-enhanced raman spectroscopy and light emission by electrochemical etching”, *Review of Scientific Instruments* **75**, 837–841 (2004).
- [137] C. C. Neacsu et al., “Scanning-probe raman spectroscopy with single-molecule sensitivity”, *Physical Review B* **73**, 193406 (2006).
- [138] T.-a. Yano et al., “Confinement of enhanced field investigated by tip-sample gap regulation in tapping-mode tip-enhanced raman microscopy”, *Applied Physics Letters* **91**, 121101 (2007).
- [139] A. Downes, D. Salter, and A. Elfick, “Finite element simulations of tip-enhanced raman and fluorescence spectroscopy”, *The Journal of Physical Chemistry B* **110**, 6692–6698 (2006).
- [140] C. Blum et al., “Tip-enhanced raman spectroscopy—an interlaboratory reproducibility and comparison study”, *Journal of Raman Spectroscopy* **45**, 22–31 (2014).
- [141] M. B. Raschke and C. Lienau, “Apertureless near-field optical microscopy: tip–sample coupling in elastic light scattering”, *Applied Physics Letters* **83**, 5089–5091 (2003).
- [142] G. Picardi et al., “Comparative study of atomic force mode and tunneling mode tip-enhanced raman spectroscopy”, *The European Physical Journal Applied Physics* **40**, 197–201 (2007).

- [143] A. Wiener et al., “Nonlocal effects in the nanofocusing performance of plasmonic tips”, *Nano letters* **12**, 3308–3314 (2012).
- [144] X. Cui et al., “Tuning the resonance frequency of ag-coated dielectric tips”, *Optics express* **15**, 8309–8316 (2007).
- [145] N. Mauser and A. Hartschuh, “Tip-enhanced near-field optical microscopy”, *Chemical Society reviews* **43**, 1248–1262 (2014).
- [146] C Ropers et al., “Grating-coupling of surface plasmons onto metallic tips: a nanoconfined light source”, *Nano letters* **7**, 2784–2788 (2007).
- [147] C. C. Neacsu et al., “Near-field localization in plasmonic superfocusing: a nanoemitter on a tip”, *Nano letters* **10**, 592–596 (2010).
- [148] P. Uebel et al., “A gold-nanotip optical fiber for plasmon-enhanced near-field detection”, *Applied Physics Letters* **103**, 021101 (2013).
- [149] S. Kharintsev et al., “Plasmonic optical antenna design for performing tip-enhanced raman spectroscopy and microscopy”, *Journal of Physics D: Applied Physics* **46**, 145501 (2013).
- [150] A Weber-Bargioni et al., “Functional plasmonic antenna scanning probes fabricated by induced-deposition mask lithography”, *Nanotechnology* **21**, 065306 (2010).
- [151] M. Fleischer et al., “Gold nanocone near-field scanning optical microscopy probes”, *ACS nano* **5**, 2570–2579 (2011).
- [152] I. Maouli et al., “Optical antennas for tunable enhancement in tip-enhanced raman spectroscopy imaging”, *Applied Physics Express* **8**, 032401 (2015).
- [153] Y. Zou et al., “Surface plasmon resonances of optical antenna atomic force microscope tips”, *Applied Physics Letters* **94**, 171107 (2009).
- [154] A. I. Denisyuk et al., “Tunable optical antennas based on metallic nanoshells with nanoknobs”, *Journal of nanoscience and nanotechnology* **12**, 8651–8655 (2012).
- [155] F. Huth et al., “Resonant antenna probes for tip-enhanced infrared near-field microscopy”, *Nano letters* **13**, 1065–1072 (2013).
- [156] T. Umakoshi et al., “Fabrication of near-field plasmonic tip by photoreduction for strong enhancement in tip-enhanced raman spectroscopy”, *Applied Physics Express* **5**, 052001 (2012).
- [157] Y. Gan, “Invited review article: a review of techniques for attaching micro-and nanoparticles to a probe’s tip for surface force and near-field optical measurements”, *Review of scientific instruments* **78**, 081101 (2007).
- [158] T. Kalkbrenner et al., “A single gold particle as a probe for apertureless scanning near-field optical microscopy”, *Journal of Microscopy* **202**, 72–76 (2001).
- [159] I. Barsegova et al., “Controlled fabrication of silver or gold nanoparticle near-field optical atomic force probes: enhancement of second-harmonic generation”, *Applied Physics Letters* **81**, 3461–3463 (2002).
- [160] O Sqalli et al., “Gold elliptical nanoantennas as probes for near field optical microscopy”, *Journal of applied physics* **92**, 1078–1083 (2002).

- [161] Y. Kawata et al., “The use of capillary force for fabricating probe tips for scattering-type near-field scanning optical microscopes”, *Applied physics letters* **82**, 1598–1600 (2003).
- [162] C.-G. Park et al., “Tip-enhanced raman scattering with a nanoparticle-functionalized probe”, *B. Korean Chem. Soc* **33**, 1748–1752 (2012).
- [163] T Okamoto and I Yamaguchi, “Photocatalytic deposition of a gold nanoparticle onto the top of a sin cantilever tip”, *Journal of microscopy* **202**, 100–103 (2001).
- [164] I. U. Vakarelski and K. Higashitani, “Single-nanoparticle-terminated tips for scanning probe microscopy”, *Langmuir* **22**, 2931–2934 (2006).
- [165] H.-W. Cheng et al., “Characterization of single 1.8-nm au nanoparticle attachments on afm tips for single sub-4-nm object pickup”, *Nanoscale research letters* **8**, 1–10 (2013).
- [166] Y. Tian et al., “Shape-controlled electrodeposition of gold nanostructures”, *The Journal of Physical Chemistry B* **110**, 23478–23481 (2006).
- [167] Y.-C. Yang et al., “Electrochemical growth of gold nanostructures for surface-enhanced raman scattering”, *The Journal of Physical Chemistry C* **115**, 1932–1939 (2011).
- [168] M. Paunovic and M. Schlesinger, *Fundamentals of electrochemical deposition*, 2nd ed., Vol. 45 (John Wiley & Sons, 2006).
- [169] A. J. Bard and L. R. Faulkner, *Electrochemical methods: fundamentals and applications*, 2nd (Wiley New York, 2001).
- [170] L Oniciu and L Mureşan, “Some fundamental aspects of levelling and brightening in metal electrodeposition”, *Journal of Applied Electrochemistry* **21**, 565–574 (1991).
- [171] S Roy, “Electrochemical gold deposition from non-toxic electrolytes”, *ECS Transactions* **16**, 67–72 (2009).
- [172] T. A. Green, “Gold electrodeposition for microelectronic, optoelectronic and microsystem applications”, *Gold Bulletin* **40**, 105–114 (2007).
- [173] “Crc handbook of chemistry and physics”, in, edited by W. M. Haynes (CRC press, 2013).
- [174] Z. Li et al., “Surface properties of platinum thin films as a function of plasma treatment conditions”, *Surface science* **529**, 410–418 (2003).
- [175] P Fuchs, “Low-pressure plasma cleaning of au and ptir noble metal surfaces”, *Applied Surface Science* **256**, 1382–1390 (2009).
- [176] B. Scharifker and G. Hills, “Theoretical and experimental studies of multiple nucleation”, *Electrochimica Acta* **28**, 879–889 (1983).
- [177] L Komsiykska and G Staikov, “ElectrocrySTALLIZATION of au nanoparticles on glassy carbon from hclo 4 solution containing [aucl 4]-”, *Electrochimica Acta* **54**, 168–172 (2008).
- [178] M. E. Hyde and R. G. Compton, “A review of the analysis of multiple nucleation with diffusion controlled growth”, *Journal of Electroanalytical Chemistry* **549**, 1–12 (2003).
- [179] P. V. Dudin, P. R. Unwin, and J. V. Macpherson, “Electrochemical nucleation and growth of gold nanoparticles on single-walled carbon nanotubes: new mechanistic insights”, *The Journal of Physical Chemistry C* **114**, 13241–13248 (2010).

- [180] R. H. Webb, “Confocal optical microscopy”, Reports on Progress in Physics **59**, 427 (1996).
- [181] D. B. Murphy, *Fundamentals of light microscopy and electronic imaging* (John Wiley & Sons, 2002).
- [182] G. Cox and C. J. Sheppard, “Practical limits of resolution in confocal and non-linear microscopy”, Microscopy research and technique **63**, 18–22 (2004).
- [183] O. Hollricher and W. Ibach, “High-resolution optical and confocal microscopy”, in *Confocal raman microscopy* (Springer, 2011), pp. 1–20.
- [184] M. Born and E. Wolf, *Principles of optics: electromagnetic theory of propagation, interference and diffraction of light* (Cambridge university press, 1999).
- [185] T. Wilson and A. Carlini, “Size of the detector in confocal imaging systems”, Optics letters **12**, 227–229 (1987).
- [186] J. L. Hutter and J. Bechhoefer, “Calibration of atomic-force microscope tips”, Review of Scientific Instruments **64**, 1868–1873 (1993).
- [187] T. Senden and W. Ducker, “Experimental determination of spring constants in atomic force microscopy”, Langmuir **10**, 1003–1004 (1994).
- [188] A. Torii et al., “A method for determining the spring constant of cantilevers for atomic force microscopy”, Measurement Science and Technology **7**, 179 (1996).
- [189] J. E. Sader, J. W. Chon, and P. Mulvaney, “Calibration of rectangular atomic force microscope cantilevers”, Review of Scientific Instruments **70**, 3967–3969 (1999).
- [190] R Levy and M Maaloum, “Measuring the spring constant of atomic force microscope cantilevers: thermal fluctuations and other methods”, Nanotechnology **13**, 33 (2002).
- [191] P. J. Cumpson, C. A. Clifford, and J. Hedley, “Quantitative analytical atomic force microscopy: a cantilever reference device for easy and accurate afm spring-constant calibration”, Measurement Science and Technology **15**, 1337 (2004).
- [192] R. S. Gates and M. G. Reitsma, “Precise atomic force microscope cantilever spring constant calibration using a reference cantilever array”, Review of Scientific Instruments **78**, 086101 (2007).
- [193] E. Langlois et al., “Spring constant calibration of atomic force microscopy cantilevers with a piezosensor transfer standard”, Review of Scientific Instruments **78**, 093705 (2007).
- [194] B. Ohler, “Cantilever spring constant calibration using laser doppler vibrometry”, Review of Scientific Instruments **78**, 063701 (2007).
- [195] K. J. Savage et al., “From microns to kissing contact: dynamic positioning of two nano-systems”, Applied Physics Letters **99**, 053110 (2011).
- [196] J. Matey and J Blanc, “Scanning capacitance microscopy”, Journal of Applied Physics **57**, 1437–1444 (1985).
- [197] C. Bugg and P. King, “Scanning capacitance microscopy”, Journal of Physics E: Scientific Instruments **21**, 147 (1988).

- [198] Y Huang, C. Williams, and J Slinkman, “Quantitative two-dimensional dopant profile measurement and inverse modeling by scanning capacitance microscopy”, *Applied physics letters* **66**, 344–346 (1995).
- [199] J. Kopanski, J. Marchiando, and J. Lowney, “Scanning capacitance microscopy measurements and modeling: progress towards dopant profiling of silicon”, *Journal of Vacuum Science & Technology B* **14**, 242–247 (1996).
- [200] P. Girard, “Electrostatic force microscopy: principles and some applications to semiconductors”, *Nanotechnology* **12**, 485 (2001).
- [201] K. J. Savage, “Plasmonic interactions in the quantum tunnelling regime”, PhD thesis (University of Cambridge, 2012).
- [202] J. Tamayo and R Garcia, “Deformation, contact time, and phase contrast in tapping mode scanning force microscopy”, *Langmuir* **12**, 4430–4435 (1996).
- [203] R. Garcia and A. San Paulo, “Attractive and repulsive tip-sample interaction regimes in tapping-mode atomic force microscopy”, *Physical Review B* **60**, 4961 (1999).
- [204] A. San Paulo and R. Garcia, “Unifying theory of tapping-mode atomic-force microscopy”, *Physical Review B* **66**, 041406 (2002).
- [205] S. Lee et al., “Nonlinear dynamics of microcantilevers in tapping mode atomic force microscopy: a comparison between theory and experiment”, *Physical Review B* **66**, 115409 (2002).
- [206] R. A. Schultz et al., “Hyperspectral imaging: a novel approach for microscopic analysis”, *Cytometry* **43**, 239–247 (2001).
- [207] S. J. Leavesley et al., “Hyperspectral imaging microscopy for identification and quantitative analysis of fluorescently-labeled cells in highly autofluorescent tissue”, *Journal of biophotonics* **5**, 67–84 (2012).
- [208] E. K. Hege et al., “Hyperspectral imaging for astronomy and space surveillance”, in *Optical science and technology, spie’s 48th annual meeting* (International Society for Optics and Photonics, 2004), pp. 380–391.
- [209] J. A. Hackwell et al., “Lwir/mwir imaging hyperspectral sensor for airborne and ground-based remote sensing”, in *Spie’s 1996 international symposium on optical science, engineering, and instrumentation* (International Society for Optics and Photonics, 1996), pp. 102–107.
- [210] G. A. Shaw and H.-h. K. Burke, “Spectral imaging for remote sensing”, *Lincoln Laboratory Journal* **14**, 3–28 (2003).
- [211] M. Kim, Y. Chen, P. Mehl, et al., “Hyperspectral reflectance and fluorescence imaging system for food quality and safety”, *Transactions-American Society of Agricultural Engineers* **44**, 721–730 (2001).
- [212] A. Gowen et al., “Hyperspectral imaging—an emerging process analytical tool for food quality and safety control”, *Trends in Food Science & Technology* **18**, 590–598 (2007).
- [213] T. Vo-Dinh, “A hyperspectral imaging system for in vivo optical diagnostics”, *Engineering in Medicine and Biology Magazine, IEEE* **23**, 40–49 (2004).

- [214] M. E. Martin et al., "Development of an advanced hyperspectral imaging (hsi) system with applications for cancer detection", *Annals of biomedical engineering* **34**, 1061–1068 (2006).
- [215] G. Lu and B. Fei, "Medical hyperspectral imaging: a review", *Journal of biomedical optics* **19**, 010901–010901 (2014).
- [216] M. Bashevoy et al., "Hyperspectral imaging of plasmonic nanostructures with nanoscale resolution", *Optics express* **15**, 11313–11320 (2007).
- [217] M. Iga et al., "Development of thin-film tunable band-pass filters based hyper-spectral imaging system applied for both surface enhanced raman scattering and plasmon resonance rayleigh scattering", *Review of Scientific Instruments* **83**, 103707 (2012).
- [218] R. W. Slawson, Z. Ninkov, and E. P. Horch, "Hyperspectral imaging: wide-area spectrophotometry using a liquid-crystal tunable filter", *Publications of the Astronomical Society of the Pacific* **111**, 621–626 (1999).
- [219] N. Gat, "Imaging spectroscopy using tunable filters: a review", in *Aerosense 2000* (International Society for Optics and Photonics, 2000), pp. 50–64.
- [220] J. T. Daly et al., "Tunable narrow-band filter for lwir hyperspectral imaging", in *Symposium on integrated optoelectronics* (International Society for Optics and Photonics, 2000), pp. 104–115.
- [221] T. Okamoto and I. Yamaguchi, "Simultaneous acquisition of spectral image information", *Optics letters* **16**, 1277–1279 (1991).
- [222] T. V. Bulygin and G. N. Vishnyakov, "Spectrotomography: a new method of obtaining spectrograms of two-dimensional objects", in *Analytical methods for optical tomography* (International Society for Optics and Photonics, 1992), pp. 315–322.
- [223] T. Okamoto, A. Takahashi, and I. Yamaguchi, "Simultaneous acquisition of spectral and spatial intensity distribution", *Applied Spectroscopy* **47**, 1198–1202 (1993).
- [224] M. Descour and E. Dereniak, "Computed-tomography imaging spectrometer: experimental calibration and reconstruction results", *Applied Optics* **34**, 4817–4826 (1995).
- [225] S. Grusche, "Basic slit spectroscope reveals three-dimensional scenes through diagonal slices of hyperspectral cubes", *Applied optics* **53**, 4594–4603 (2014).
- [226] A. Sanders et al., "Facile fabrication of spherical nanoparticle-tipped afm probes for plasmonic applications", *Particle & Particle Systems Characterization* **32**, 182–187 (2015).
- [227] M. I. Stockman, "Nanoplasmonics: past, present, and glimpse into future", *Optics express* **19**, 22029–22106 (2011).
- [228] A. Lombardi and L. Weller, "Revealing the near-field plasmonic resonances in single nanostructures using tuneable sers", in preparation (2015).
- [229] J. T. Hugall and J. J. Baumberg, *Physical Review Letters* (2015).
- [230] S. Mahajan et al., "Understanding the surface-enhanced raman spectroscopy “background”", *The Journal of Physical Chemistry C* **114**, 7242–7250 (2009).
- [231] F. G. De Abajo and J Aizpurua, "Numerical simulation of electron energy loss near inhomogeneous dielectrics", *Physical Review B* **56**, 15873 (1997).

- [232] F. G. de Abajo and A. Howie, “Retarded field calculation of electron energy loss in inhomogeneous dielectrics”, *Physical Review B* **65**, 115418 (2002).
- [233] J. T. Hugall, J. J. Baumberg, and S. Mahajan, “Disentangling the peak and background signals in surface-enhanced raman scattering”, *The Journal of Physical Chemistry C* **116**, 6184–6190 (2012).
- [234] Y. Gan, “Atomic and subnanometer resolution in ambient conditions by atomic force microscopy”, *Surface Science Reports* **64**, 99–121 (2009).
- [235] M. Holmberg et al., “Nanobubble trouble on gold surfaces”, *Langmuir* **19**, 10510–10513 (2003).
- [236] Y. Song et al., “The origin of the “snap-in” in the force curve between afm probe and the water/gas interface of nanobubbles”, *ChemPhysChem* **15**, 492–499 (2014).
- [237] Q. Zhong et al., “Fractured polymer/silica fiber surface studied by tapping mode atomic force microscopy”, *Surface Science Letters* **290**, L688–L692 (1993).
- [238] P. Hansma et al., “Tapping mode atomic force microscopy in liquids”, *Applied Physics Letters* **64**, 1738–1740 (1994).
- [239] C. A. Putman et al., “Tapping mode atomic force microscopy in liquid”, *Applied physics letters* **64**, 2454–2456 (1994).
- [240] J. Lambe and S. McCarthy, “Light emission from inelastic electron tunneling”, *Physical Review Letters* **37**, 923 (1976).
- [241] R. Berndt, J. K. Gimzewski, and P. Johansson, “Inelastic tunneling excitation of tip-induced plasmon modes on noble-metal surfaces”, *Physical review letters* **67**, 3796 (1991).
- [242] P. Bharadwaj, A. Bouhelier, and L. Novotny, “Electrical excitation of surface plasmons”, *Physical review letters* **106**, 226802 (2011).
- [243] S. Divitt, P. Bharadwaj, and L. Novotny, “The role of gap plasmons in light emission from tunnel junctions”, *Optics express* **21**, 27452–27459 (2013).
- [244] F. Ye et al., “Optical and electrical mappings of surface plasmon cavity modes”, *Nanophotonics* **3**, 33–49 (2014).
- [245] B. Van Wees et al., “Quantized conductance of point contacts in a two-dimensional electron gas”, *Physical Review Letters* **60**, 848 (1988).
- [246] D. Wharam et al., “One-dimensional transport and the quantisation of the ballistic resistance”, *Journal of Physics C: solid state physics* **21**, L209 (1988).
- [247] F. H. Koppens, D. E. Chang, and F. J. Garcia de Abajo, “Graphene plasmonics: a platform for strong light–matter interactions”, *Nano letters* **11**, 3370–3377 (2011).
- [248] J. Christensen et al., “Graphene plasmon waveguiding and hybridization in individual and paired nanoribbons”, *ACS nano* **6**, 431–440 (2011).
- [249] J. Chen et al., “Optical nano-imaging of gate-tunable graphene plasmons”, *Nature* **487**, 77–81 (2012).
- [250] J. N. Armstrong et al., “Channel saturation and conductance quantization in single-atom gold constrictions”, *Physical Review B* **82**, 195416 (2010).

- [251] J. Costa-Krämer et al., “Conductance quantization in nanowires formed between micro and macroscopic metallic electrodes”, *Physical Review B* **55**, 5416 (1997).
- [252] J. Costa-Krämer, N Garcia, and H. Olin, “Conductance quantization histograms of gold nanowires at 4 k”, *Physical Review B* **55**, 12910 (1997).
- [253] J. Costa-Krämer, “Conductance quantization at room temperature in magnetic and nonmagnetic metallic nanowires”, *Physical Review B* **55**, R4875 (1997).
- [254] U. Landman et al., “Reversible manipulations of room temperature mechanical and quantum transport properties in nanowire junctions”, *Physical review letters* **77**, 1362 (1996).
- [255] D. Natelson, “Mechanical break junctions: enormous information in a nanoscale package”, *ACS nano* **6**, 2871–2876 (2012).
- [256] V. Rodrigues, T. Fuhrer, and D. Ugarte, “Signature of atomic structure in the quantum conductance of gold nanowires”, *Physical review letters* **85**, 4124 (2000).
- [257] V Rodrigues et al., “Quantum conductance in silver nanowires: correlation between atomic structure and transport properties”, *Physical Review B* **65**, 153402 (2002).
- [258] C Sabater et al., “Mechanical annealing of metallic electrodes at the atomic scale”, *arXiv preprint arXiv:1205.4612* (2012).
- [259] M. R. Sørensen, M. Brandbyge, and K. W. Jacobsen, “Mechanical deformation of atomic-scale metallic contacts: structure and mechanisms”, *Physical Review B* **57**, 3283 (1998).
- [260] I. Yanson et al., “Atomic-size oscillations in conductance histograms for gold nanowires and the influence of work hardening”, *Physical review letters* **95**, 256806 (2005).
- [261] L. Maguire, S Szilagyi, and R. Scholten, “High performance laser shutter using a hard disk drive voice-coil actuator”, *Review of Scientific Instruments* **75**, 3077 (2004).
- [262] R. Scholten, “Enhanced laser shutter using a hard disk drive rotary voice-coil actuator”, *Review of scientific instruments* **78**, 026101 (2007).



# List of Symbols

---

$a$	radius of a spherical particle [m]
$\alpha$	polarisability [ $C\text{ m}^2\text{ V}^{?1}$ ]
<b>B</b>	magnetic field strength/magnetic flux density [T]
$c$	speed of light, $2.99 \times 10^8 \text{ m s}^{-1}$
<b>D</b>	electric displacement field
$d$	dimer gap separation [m]
$d_p$	confocal pinhole diameter [m]
$\delta_m$	electromagnetic skin depth [m]
<b>E</b>	electric field [ $V\text{ m}^{-1}$ ]
$E_0$	incident electric field [ $V\text{ m}^{-1}$ ]
$E^\circ$	standard electrochemical potential [V]
$\varepsilon$	complex relative permittivity, $\varepsilon = \varepsilon_1 + i\varepsilon_2$ , also known as a dielectric function of a material
$\varepsilon_0$	permittivity of free space, $8.854\,187\,82 \times 10^{-12} \text{ m}^{-3} \text{ kg}^{-1} \text{ s}^4 \text{ A}^2$
$G$	conductance [S] or [ $\Omega^{-1}$ ]
$\gamma$	coefficient of damping [ $s^{-1}$ ]
<b>H</b>	magnetic field [ $A\text{ m}^{-1}$ ]
$I$	current [A]
<b>J</b>	current density [ $A\text{ m}^{-2}$ ]
$\mathbf{J}_{\text{ext}}$	external current density [ $A\text{ m}^{-2}$ ]
$\mathbf{J}_{\text{int}}$	internal current density [ $A\text{ m}^{-2}$ ]
$\mathbf{J}_{\text{tot}}$	total current density [ $A\text{ m}^{-2}$ ]
$k$	cantilever spring constant [ $N\text{ m}^{-1}$ ]
$k$	magnitude of the wavevector [ $\text{m}^{-1}$ ]
<b>k</b>	wavevector [ $\text{m}^{-1}$ ]
$k_0$	magnitude of the photonic wavevector, $\omega/c$ [ $\text{m}^{-1}$ ]
$l$	degree of spherical harmonic (multipolar mode)
<b>M</b>	magnetisation/magnetic dipole moment per unit volume [ $A\text{ m}^{-2}$ ]
$m$	mass [kg]
$m_l$	order of spherical harmonic of degree $l$
$\mu$	relative permeability
$\mu_0$	permeability of free space, $1.256\,637\,06 \times 10^6 \text{ m kg s}^{-2} \text{ A}^{-2}$
$n$	number density of electrons [ $\text{m}^{-3}$ ]

$\tilde{n}$	complex refractive index, $\tilde{n} = n + i\kappa$
$\omega$	angular frequency, $2\pi f$ [rad $^{-1}$ ]
$\omega_p$	plasma frequency [rad]
$\mathbf{P}$	polarisation/electric dipole moment per unit volume [C m $^{-2}$ ]
$\varphi$	electrostatic potential [V]
$Q$	quality factor of a resonance
$\mathbf{r}$	spatial vector with components $(x, y, z)$ or $(r, \theta, \phi)$ depending on coordinate system [m]
$r_{\text{lateral}}$	lateral optical resolution, i.e. the minimum resolvable distance between two features [m]
$\rho_{\text{ext}}$	external volume charge density [C m $^{-3}$ ]
$\rho_{\text{int}}$	internal volume charge density [C m $^{-3}$ ]
$\rho_{\text{tot}}$	total volume charge density [C m $^{-3}$ ]
$\sigma$	conductivity [S m $^{-1}$ ]
$\sigma$	surface charge density [C m $^{-2}$ ]
$\sigma_{\text{abs}}$	absorption cross section [m $^2$ ]
$\sigma_{\text{ext}}$	extinction cross section, $\sigma_{\text{abs}} + \sigma_{\text{scat}}$ [m $^2$ ]
$\sigma_{\text{scat}}$	scattering cross section [m $^2$ ]
$t$	time [s]
$\tau$	relaxation time [s]
$u$	displacement of the free electron gas from equilibrium under an applied field [m]
$V$	voltage or potential difference [V]
$v$	velocity [m s $^{-1}$ ]

# Acronyms

---

Notation	Description
2DEG	2D electron gas
a-SNOM	apertureless scanning near-field optical microscopy
AFM	atomic force microscopy
BDP	bonding hybridised dipolar plasmon
BEM	boundary element method
BF	bright-field
CTP	charge transfer plasmon
DF	dark-field
DFT	density functional theory
DI	de-ionised
DSO	digital storage oscilloscope
EELS	electron energy loss spectroscopy
EM	electromagnetic
EMI	electromagnetic interference
FDTD	finite-difference time-domain
FIB	focussed ion beam
FWHM	full-width half-maximum
IMI	insulator-metal-insulator
IR	infrared
LSP	localised surface plasmon
LSPP	localised surface plasmon polariton
MIM	metal-insulator-metal
MNP	metallic nanoparticle
NA	numerical aperture
NPoM	nanoparticle-on-mirror
ODE	ordinary differential equation
PSD	position sensitive detector
PSF	point spread function
QCM	quantum corrected model
s-SNOM	scattering scanning near-field optical microscopy
SAM	surface-assembled monolayer
SBDP	screened bonding dipolar plasmon

---

<b>Notation</b>	<b>Description</b>
SCM	scanning capacitance microscopy
SDF	supercontinuum dark-field
SEM	scanning electron microscopy
SERS	surface-enhanced Raman scattering
SHE	standard hydrogen electrode
SMU	source-meter unit
SNOM	scanning near-field optical microscopy
SP	surface plasmon
SPM	scanning probe microscopy
SPP	surface plasmon polariton
STM	scanning tunnelling microscopy
TE	transverse electric
TENOM	tip-enhanced near-field optical microscopy
TERS	tip-enhanced Raman scattering
TIR	total internal reflection
TM	transverse magnetic
UV	ultraviolet